UNIVERSITY OF CALIFORNIA

Los Angeles

**Advanced Imaging and Bioengineering Approaches to Cardiovascular Disease**

Dissertation submitted in partial satisfaction of the requirements for the degree of

Doctor of Philosophy in Molecular, Cellular, and Integrative Physiology

by

RENÉ RUPEN SEVAG PACKARD

2016

**ABSTRACT OF THE DISSERTATION**

Advanced Imaging and Bioengineering Approaches to Cardiovascular Disease

by

René Rupen Sevag Packard

Doctor of Philosophy in Molecular, Cellular, and Integrative Physiology

University of California, Los Angeles, 2016

Professor Tzung Hsiai, Chair

Light Sheet Fluorescence Microscopy enables multi-dimensional and multi-scale imaging via illuminating specimens with a separate thin sheet of laser. It allows rapid plane illumination for reduced photo-damage and superior axial resolution and contrast. By combining our approach with tissue clearing techniques, we reveal the entire cardiac structures and hypertrabeculation of adult zebrafish hearts in response to doxorubicin chemotherapy treatment. We incorporate light-sheet fluorescent microscopy and pulsed-wave Doppler ultrasound to unravel the 3D architecture and electromechanical coupling of doxorubicin-induced cardiac injury and regeneration in the adult zebrafish model. 3-month old zebrafish were injected intraperitoneally with doxorubicin followed by imaging at 3, 30, and 60 days post-injection. We observed an initial decrease in myocardial and endocardial cavity volume at day 3, followed by ventricular remodeling and hypertrabeculation at day 30, and normalization at day 60. Doxorubicin-injected fish developed ventricular diastolic dysfunction evidenced by elevated E/A ratios at day 30, normalizing at day 60. Myocardial performance indexes were also elevated at day 30 in the doxorubicin group, indicating worsening of global cardiac function, followed by normalization at day 60. qRT-PCR to investigate the pathways involved revealed up-regulation of Notch signaling genes, particularly the ligand Jagged1 and target gene HEY2 at days 30 and 60. Treatment with the γ-secretase inhibitor DAPT to inhibit Notch signaling attenuated restoration of ventricular function,

demonstrated by persistence of abnormal E/A ratios and myocardial performance indexes at day 60, thereby implicating Notch pathways in the cardiac regeneration process. Our results suggest that doxorubicin-induced cardiac injury leads to ventricular remodeling, followed by activation of Notch signaling to promote hypertrabeculation and restoration of cardiac function.

Next, we developed and studied invasive, and non-invasive imaging approaches to characterize atherosclerotic plaques. Four-point electrode systems are commonly used for electric impedance measurements of biomaterials and tissues. We introduced a 2-point system to reduce electrode polarization for heterogeneous measurements of vascular wall. Presence of endoluminal oxidized low density lipoprotein (oxLDL) and lipids alters the electrochemical impedance that can be measured by electrochemical impedance spectroscopy (EIS). We developed a catheter-based 2-point micro-electrode configuration for intravascular deployment in New Zealand White rabbits. An array of 2 flexible round electrodes, 240 μm in diameter and separated by 400 μm was microfabricated and mounted on an inflatable balloon catheter for EIS measurement of the oxLDL-rich lesions developed as a result of high-fat diet-induced hyperlipidemia. Upon balloon inflation, the 2-point electrode array conformed to the arterial wall to allow deep intraplaque penetration via alternating current. The frequency sweep from 10 – 300 kHz generated an increase in capacitance, providing distinct changes in both impedance ($\Omega$) and phase ($\phi$) in relation to varying degrees of intraplaque lipid burden in the aorta. Aortic endoluminal EIS measurements were compared with epicardial fat tissue and validated by intravascular ultrasound and immunohistochemistry for plaque lipids and foam cells. Thus, we demonstrate a new approach to quantify endoluminal EIS via a 2-point stretchable electrode strategy.

In the next study, a new absolute quantitation of myocardial blood flow (MBF) method with the novel positron emission tomography (PET) ^{18}F-Flurpiridaz radiopharmaceutical was developed, taking advantage of its early kinetics and high first-pass extraction by the myocardium. We

performed the first in human measurements of MBF in 7 normal subjects and 8 patients with documented coronary artery disease (CAD). PET images with time-activity curves were acquired at rest and during adenosine stress. In normal subjects, regional MBF between coronary artery territories did not differ significantly, leading to a mean global MBF of 0.73 mL/min/g at rest and 2.53 mL/min/g during stress, with a mean global myocardial flow reserve (MFR) of 3.70. CAD vascular territories with <50% stenosis demonstrated a mean MBF of 0.73 at rest and 2.02 during stress, leading to a mean MFR of 2.97. CAD vascular territories with ≥50% stenosis exhibited a mean MBF of 0.86 at rest and 1.43 during stress, leading to a mean MFR of 1.86. Differences in stress MBF and MFR between normal and CAD territories, as well as between <50% and ≥50% stenosis vascular territories, were significant. The significant decrease in stress MBF and ensuing MFR in CAD territories allows a clear distinction between vascular territories exhibiting stress-inducible myocardial ischemia and those with normal perfusion using ^{18}F-Flurpiridaz PET.

In the last study, we studied the ability of fractional flow reserve by computerized tomography (FFR-CT) to predict subsequent coronary revascularization. FFR-CT provides non-invasive functional assessment of the hemodynamic significance of coronary artery stenosis. We determined the FFR-CT values, receiver operator characteristic curves and predictive ability of FFR-CT for *actual* standard of care guided coronary revascularization. Consecutive outpatients who underwent coronary CT angiography (coronary CTA) followed by invasive angiography over a 24-month period from 2012-2014 were identified, sent for FFR-CT analysis, and results stratified by coronary artery calcium (CAC) scores. Coronary CTA studies were re-interpreted in a blinded manner, and baseline FFR-CT values obtained retrospectively. Therefore, results did not interfere with clinical decision-making. Median FFR-CT values were 0.70 in revascularized (n=69) and 0.86 in not revascularized (n=138) coronary arteries. Using clinically established significance cutoffs of FFR-CT ≤0.80 and coronary CTA ≥70% stenosis for the prediction of clinical decision making and subsequent coronary revascularization, the positive predictive values were 74% and

88%, and negative predictive values 96% and 84%, respectively.  The area under the curve (AUC) for all studied territories was 0.904 for coronary CTA, 0.920 for FFR-CT, and 0.941 for coronary CTA combined with FFR-CT.  With increasing CAC scores, the AUC decreased for coronary CTA but remained higher for FFR-CT.  The addition of FFR-CT provides a complementary role to coronary CTA and increases the ability of a CT-based approach to identify subsequent standard of care guided coronary revascularization.

The dissertation of René Rupen Sevag Packard is approved.


Linda L. Demer

James N. Weiss

Johannes Czernin

Tzung Hsiai, Committee Chair


University of California, Los Angeles

2016

# DEDICATION

*To Ani Karine, Loris Tovmas, and Nairi Alice Zabel.*

*I love you more than anything.*

# TABLE OF CONTENTS

# LIST OF FIGURES AND TABLES

# ACKNOWLEDGMENTS

*Pour cent histoires mortes, il demeure tout de même une ou deux histoires vivantes.*

*Jean-Paul Sartre – La nausée (1938)*

John Wooden, a true UCLA legend, quoted in his final years:

*I am now in my eighth decade and I would like to be able to tell you that I lived up to my Dad's creed, but I more like the fellow who said:*

> *I am not what I ought to be,*
>
> *Not what I want to be,*
>
> *Not what I am going to be,*
>
> *But I am thankful that*
>
> *I am better than I used to be.*

In my case, this journey would not have been possible without UCLA, the Division of Cardiology, and the STAR (Specialty Training and Advanced Research) program. It has been a remarkable 5-year fellowship training indeed, and I will always look back to these formative years with fondness.

There are too many people for me to thank, too many people who have taught me so much, but I would like to acknowledge the most salient ones:

Dr. Tzung K. Hsiai, my PhD mentor, himself a graduate of the STAR program, has been an unbelievable source of inspiration, a mentor in the true sense of the term who is selfless, always supportive, always available, and with extremely high expectations which are inspiring to his trainees. It is in large part thanks to his relentless support, expert advice, and superior laboratory

Dr. Linda L. Demer for providing invaluable guidance when I needed to re-orient my basic research and PhD training to find a more ideal complement between my experimental and clinical research interests in cardiovascular imaging.  I will never forget everything Dr. Demer did to put me back on track to complete my PhD training and for introducing me to my mentor Dr. Hsiai. Having originally conceived the STAR program 25 years ago in 1991, and initiated it in 1993 together with Dr. Alan M. Fogelman in the Department of Medicine at UCLA, Dr. Demer via the STAR program was the primary reason I wanted to join UCLA for my cardiology fellowship.

Dr. Johannes Czernin for helping me structure cardiac imaging training during fellowship, advising me early on to pursue cardiac PET imaging research with Dr. Maddahi, and encouraging me to expand further to cardiac CT.

Dr. James N. Weiss, Dr. Alan M. Fogelman, and Dr. Gregory A. Brent for their unwavering support during my transition from fellow to faculty in the physician-scientist track of the Department of Medicine and Division of Cardiology at UCLA.

The leadership of the Department of Molecular, Cellular, and Integrative Physiology (MCIP):  Dr. Mark A. Frye, Dr. James G. Tidball, and Yesenia Rayos, for their support and advice.

Dr. François Mach who was the first to initiate me to cardiovascular research while I was a student at the Faculty of Medicine at the University of Geneva, Switzerland.

Dr. Peter Libby and Dr. Andrew H. Lichtman with whom I pursued vascular biology research at Harvard University.

My friends, old and new, who are an integral part of the fabric of my life:  Serge Ulrich, Juan Sepulveda, David Jobé, William Marconi, Gil Viry, Gina Rossi, Thanh Lam, Thibaud Kössler, Paul Klauser, Julien Zimmermann, Guillaume Racloz, Vincent Gillioz, Michael Lauterbach, Viviane Rocha, Fabrice Schneider, Stephanie Schulte, Ara Nazarian, Raffi Simonian, Edwin Avanessian, Ara Rostomian, Seepan Parseghian, and Areg Bagdasarian.

My parents Vahé and Pauline, who sacrificed everything to give me the best possible education.

My grandmothers Alice and Zabel, without whom I would not have pursued an academic track.

My aunt and uncle Lusnar and Aram, whose support and love have been constant.

Most important of all – my wife Ani, who has always been there in the good times as well as the challenging ones.  In those moments, she often believed more in me than I did in myself.  I hope to make her, our son Loris, and our daughter Nairi, proud.

A question that may arise upon reading this dissertation, is: "How are the individual Chapters interconnected?" In reality, the present body of work is divided into two main overarching themes:

1. Light sheet fluorescent imaging for functional studying and quantitative analysis of experimental models of disease, in particular chemotherapy-induced cardiomyopathy (Chapters 1 – 2).

2. Characterization of atherosclerotic plaques using:
   a) novel bioengineering approaches and invasive sensors in experimental models (Chapters 3 – 4),
   b) nuclear cardiology (Chapter 5 – 7),
   c) cardiac computerized tomography (Chapters 8 – 9).

I hope the reader will find this dissertation both enjoyable and instructive.

**CURRICULUM VITAE**

## Education

2016        Ronald Reagan UCLA Medical Center
            David Geffen School of Medicine, University of California, Los Angeles
            Los Angeles, California
            *Fellowship, Division of Cardiology*
            *STAR (Specialty Training and Advanced Research) Program*

2011        University Hospitals of Cleveland Case Medical Center
            Case Western Reserve University School of Medicine
            Cleveland, Ohio
            *Residency, Department of Internal Medicine*

2009        Brigham and Women's Hospital, Harvard Medical School
            Boston, Massachusetts
            *Cardiovascular Biology Research Fellowship.  Laboratory of Peter Libby, MD*

2004        Faculty of Medicine, University of Geneva
            Geneva, Switzerland
            *Federal Degree of Medicine, with Thesis (MD).  Advisor: François Mach, MD*
            Dissertation Title:  *Atorvastatin Treatment and Vaccination Efficacy*

1999        Music Theory, Conservatory of Geneva
            Geneva, Switzerland
            *Diplôme de Culture Musicale (Degree of Musical Culture), Magna Cum Laude*

1997        Piano, Conservatory of Lausanne
            Vaud, Switzerland
            *Diplôme de Virtuosité, Summa Cum Laude*
            *First Prize with Special Commendation from the Jury*

1996        Voltaire College
            Geneva, Switzerland
            *Maturité Fédérale, Section Scientifique (Bachelor of Science), Cum Laude*

## Publications

Packard R.R.S., Schlegel S., Senouf D., Burger F., Sigaud P., Perneger T., Siegrist C.-A., Mach F.
Atorvastatin treatment and vaccination efficacy
*Journal of Clinical Pharmacology* 2007 Aug; 47(8): 1022-1027.

Packard R.R.S., Libby P.
Inflammation in atherosclerosis: from vascular biology to biomarker discovery and risk prediction
*Clinical Chemistry* 2008 Jan; 54(1): 24-38.

Packard R.R.S., Maganto-García E., Gotsman I., Tabas I., Libby P., Lichtman A.H.
CD11c$^+$ dendritic cells maintain antigen processing, presentation capabilities, and CD4$^+$ T-cell priming efficacy under hypercholesterolemic conditions associated with atherosclerosis
*Circulation Research* 2008 Oct; 103(9): 965-973.

Packard R.R.S., Libby P.
Atherosclerosis
In Offermans S., Rosenthal W., editors.
*Encyclopedia of Molecular Pharmacology, 2$^{nd}$ Edition*. Heidelberg: Springer, 2008, p. 224-229.

Packard R.R.S., Lichtman A.H., Libby P.
Innate and adaptive immunity in atherosclerosis
*Seminars in Immunopathology* 2009 Jun; 31(1): 5-22.

Packard R.R.S., Huang S.-C., Dahlbom M., Czernin J., Maddahi J.
Absolute quantitation of myocardial blood flow in human subjects with or without myocardial ischemia using dynamic Flurpiridaz F18 positron emission tomography
*The Journal of Nuclear Medicine* 2014 Sep; 55(9): 1438-1444.

Maddahi J., Packard R.R.S.
Cardiac PET perfusion tracers: current status and future directions
*Seminars in Nuclear Medicine* 2014 Sep; 44(5): 333-343.

Lee J.*, Packard R.R.S.*, Hsiai T.K. * Equal contribution
Blood flow modulation of vascular dynamics
*Current Opinion in Lipidology* 2015 Oct; 26(5): 376-383.

Fei P.*, Lee J.*, Packard R.R.S.*, Sereti K.I., Xu H., Ma J., Ding Y., Kang H., Chen H., Sung K., Kulkarni R., Ardehali R., Kuo C.-C.J., Xu X., Ho C.-M., Hsiai T.K. * Equal contribution
Cardiac light-sheet fluorescent microscopy for multi-scale and rapid imaging of architecture and function
*Scientific Reports* 2016 Mar 3; 6: 22489.

Packard R.R.S., Karlsberg R.P.
Integrating FFR$_{CT}$ into routine clinical practice: a solid PLATFORM or slippery slope?
*Journal of the American College of Cardiology* 2016 Aug 2; 68(5): 446-449.

Packard R.R.S.*, Zhang X.*, Luo Y.*, Ma T., Jen N., Ma J., Demer L.L, Zhou Q., Sayre J.W., Li R., Tai Y.-C., Hsiai T.K. * Equal contribution
Two-point stretchable electrode array for endoluminal electrochemical impedance spectroscopy measurements of lipid-laden atherosclerotic plaques
*Annals of Biomedical Engineering* 2016 Sep; 44(9): 2695-2706.

Packard R.R.S., Li D., Budoff M.J., Karlsberg R.P.
Fractional flow reserve by computerized tomography and subsequent coronary revascularization
*European Heart Journal – Cardiovascular Imaging. Manuscript in press.*

Maddahi J., Packard R.R.S.
PET should replace SPECT in cardiac imaging for diagnosis and risk assessment of patients with known or suspected CAD - Pro
*Journal of Nuclear Cardiology. Manuscript in press*.

**INTRODUCTION TO THE CHAPTERS**

**Chemotherapy-induced cardiomyopathy**

Heart failure afflicts nearly 5 million people in the United States, and an additional 550,000 new cases are diagnosed each year [1]. Despite current regimens, cardiotoxicity of chemotherapeutic agents remains an important clinical problem [2]. These treatments can adversely affect the heart in an array of ways, including myocardial ischemia, arrhythmia or pericardial disease [2]. While treatment-related impairment of cardiac function can be either transient or irreversible, the most frequent complication remains heart failure [2] [3]. This can manifest itself either as diastolic dysfunction progressing to heart failure with preserved ejection fraction, decreased systolic function leading to depressed ejection fraction, or both. The emerging interests and growing understanding of this problem led to the new field of cardio-oncology [4].

Anthracyclines, such as doxorubicin (Doxo), are a cornerstone of chemotherapeutic strategies in various cancers such as breast cancer, lymphoma, sarcoma and pediatric leukemia [5]. Their widespread use, however, is currently limited mostly by anthracycline-induced cardiotoxicity [6] leading to a reduction in optimal dose delivery and duration of treatment in certain patients [5]. Direct evidence of cardiomyocyte death following anthracycline treatment is provided by elevation of troponin levels following treatment [7]. Cardiotoxicity due to anthracycline treatment is clinically quantified by changes in ejection fraction [5]. The primary mechanism underlying anthracycline-induced cardiomyopathy is cell death, both by activation of apoptotic pathways and necrosis mediated by topoisomerase-II$\beta$ in cardiomyocytes [8] [9]. Generation of excess reactive oxygen species (ROS) by electron exchange with the anthracycline quinone moiety has been established for decades [5]. The ROS induce mitochondrial damage, release of cytochrome c and activation of caspases 9 and 3 leading to cellular deoxyribonucleic acid (DNA) fragmentation.

Previously the exclusive domain of developmental biology, the zebrafish *(Danio rerio)* is now increasingly used as a vertebrate model to provide valuable insights into cardiovascular disease

[10] [11] [12] and cancer [13]. Despite having only 1 atrium and 1 ventricle connected by 1 atrioventricular valve, the zebrafish electrocardiogram patterns are very similar to those observed in humans, with sequential atrial and ventricular depolarization and repolarization [14] [15]. Importantly, zebrafish hearts have a complete regenerative capacity following injury which is deficient in humans [16] [17] which may pave the way for novel therapeutic pathways and approaches. In zebrafish, regenerating myocardium electrically couples with uninjured myocardium [18]. Adult zebrafish provide a conserved vertebrate model for human cardiomyopathies to elucidate the cardioprotective effect of inhibiting target of rapamycin (TOR) signaling in response to doxorubicin (Doxo)-induced cardiotoxicity [19]. Embryonic zebrafish further enable visualization of myofibrillar microarchitecture as a model to study ErbB2 signaling, a component of the Notch pathway, in response to the breast cancer chemotherapy target HER2/NEU [20].

4D (3D + time) imaging to recapitulate the zebrafish endocardium requires fast tissue scanning and high axial resolution. For these reasons, we have developed in-house Light-Sheet Fluorescent Microscopy (LSFM), also known as Selective Plane Illumination Microscopy (SPIM), to capture the endocardial trabecular network. We have further investigated the electrical and mechanical attributes of regenerating myocardium in adult zebrafish by utilizing microelectrocardiogram (μECG) and high-frequency ultrasonic transducers [21] [22] [23] [24]. To assess ventricular function during repair, we synchronize μECG signals with an ultrasound pulsed-wave (PW) Doppler to interrogate cardiac hemodynamics [17]. We further developed analysis of ventricular inflow tract Doppler signals to determine isovolumic contraction and relaxation times, ejection times and calculation of the myocardial performance index [25].

In this context, we interface SPIM with high-frequency PW Doppler transducers to study the 3D architecture, electrical and mechanical coupling of Doxo-induced cardiac injury and repair. We hypothesize that Doxo-induced cardiomyopathy develops ventricular remodeling, followed by

activation of Notch-mediated endocardial trabeculation to regain contractile function in an adult zebrafish model of heart regeneration.

**Imaging of zebrafish hearts in 3D with high spatial, temporal, and axial resolution by laser light-sheet microscopy**

One approach used in zebrafish systems relies on super-resolution microscopes known as light sheet microscopes or single plane illumination microscopy (SPIM) [26]. These provide a unique combination of capabilities, including high spatial and temporal resolution, high signal-to-noise-ratio and low level of photobleaching [26]. Whereas initially used almost exclusively in transparent tissues, essentially zebrafish and fly embryos [27], the advent of chemical clearing techniques have allowed for the progressive adaptation of this powerful imaging tool to larger tissues and adult organisms [28] [29] [30]. The high-resolution images can visualize elements as small as 1 $\mu$m, enabling precise determination of tissue, cellular and subcellular processes.

Contrary to conventional wide-field and confocal microscopes which use the same lens for excitation of the fluorophore and collection of emitted fluorescence, these are separate events in light sheet microscopy where the detection lens is arranged at a 90° angle relative to the emission lens [28]. In addition, optical sectioning is obtained by placement of a pinhole in front of the intensity detector, permitting only the observed plane to be illuminated and excited, decreasing photobleaching, and in the case of live animal imaging, phototoxicity [28]. While fluorescence microscopy techniques have become increasingly developed in terms of resolution, speed and penetration, they remain limited to thin and transparent samples [31]. Current fluorescent imaging techniques are limited by their intrinsic depth penetration and z-resolution [32]. Images acquired by conventional microscopy techniques incur significant background noise due to out-of-focus illumination, and low axial resolution due to a large depth of field. Confocal laser scanning microscopy uses a pin-hole to eliminate the out-of focus excitation to improve the axial resolution.

However, the dynamic range and penetration depth are significantly reduced due to ~95% blockage of fluorescence.

To address these optical challenges, light sheet microscopy applies 2 separate sets of lenses for illumination and detection through its selective plane excitation (laser light sheets) and offers numerous optical advances to study anthracycline-induced cardiotoxicity:    1) deep axial resolution, 2) large dynamic range, 3) rapid data acquisition, 4) 3D organ structure reconstruction, and 5) reduced photobleaching.  In our light sheet microscopy setup, a low numerical aperture objective lens is combined with a cylindrical lens to generate a light sheet for scanning across the sample.  A stack of images is acquired by moving the sample in a stepwise fashion along the detection axis.  As a result, the z-axial resolution of the sample is dominated by the illumination side that will not be limited by the objective of the detection lens.  Furthermore, the low magnification lens allows for a large field of view and a wide dynamic range without compromising the axial resolution.  Thus, our light sheet fluorescent microscopy system introduces high-speed data acquisition in which thousands of images in different colors are acquired within a short period (< hours).  For these reasons, stacks of images can be recorded in a few seconds, allowing high repetition rates in time-lapse recording of live embryos.

We optimized the benzyl alcohol–benzyl benzoate (BABB, also known as Murray's clear) [33] optical clearing protocols.  Briefly, hearts will be placed in a phosphate buffered saline 1x solution to remove retained blood, paraformaldehyde 4% for fixation, agarose 1.5% for embedding, multiple ethanol steps for dehydration and BABB for lipid removal.  In optics, the refractive index is a dimensionless number describing how light propagates through a given medium.  As light exits a medium, it may also change its propagation direction, being bent (refracted) in proportion to the refractive index.  To prevent this phenomenon, we need to match as closely as possible the refractive indexes of the sample, surrounding media and tube.  In our case, BABB was used for

clearing, leading to a refractive index change of the tissue to that of BABB (index 1.51). BABB will also be used as an immersion liquid and the sample placed in a special glass tube (index 1.53) to match the refractive indexes. This prevented refraction, and loss of fluorescent signal, from occurring.

Following precise manual set-up with multiple verifications of the exact location of each crucial element of the laser imaging system, a fully automated image acquisition was implemented using a customized LabVIEW program. To quantify changes in global myocardial volume, compact and trabeculated myocardium, we use Amira software (FEI Visualization Sciences Group) to reconstruct the 3D cardiac volume.

**Determining cardiac functional phenotypes in response to doxorubicin via high-frequency ultrasonic transducers**

We apply an ultrasound array imaging system with the use of pulsed wave (PW) Doppler, high-frequency ultrasonic array 30 MHz transducers [21] [34] [35] to obtain ventricular inflow hemodynamics in zebrafish, similar to those obtained in humans in the Echocardiography lab. To assess ventricular function in response to Doxo treatment, we synchronize micro-electrocardiogram (μECG) signals with high-frequency ultrasound pulsed-wave (PW) Doppler to interrogate cardiac hemodynamics. The detection of μECG signals are performed via micro-needles customized to give free access to the array transducer. For ECG acquisition, signals are amplified 10,000-fold (1700 Differential Amplifier, A-M Systems), and filtered between 0.1 and 500 Hz at a cut-off frequency of 60 Hz. Wavelet transform and thresholding techniques is used to enhance signal-to-noise ratios (Matlab, MathWorks) for the individual ECG recording as previously reported [22]. A trigger signal generated from the ultrasound system is sent to the ECG recording system to synchronize acquisitions. μECG signals allow identification of PW Doppler signals of passive (early [E] wave velocity) and active ventricular filling (atrial [A] wave velocity) during diastole. The

6

ratio of these 2 waves, the E/A ratio, allows determination of diastolic function. Contrary to these measures which are dependent on the angle $\theta$ of the transducer beam with the flow of blood [36] and hence prone to variability, measurement of various temporal segments of the cardiac cycle are independent of ultrasound signal angulation. These measures – isovolumic contraction time (IVCT), ejection time (ET) across the bulboventricular valve and isovolumic relaxation time (IVRT) determine the myocardial performance index (MPI) as follows: MPI = (IVCT + IVRT) / ET. MPI constitutes an integrated measure of systolic and diastolic function, with increases in MPI values indicating a worsening of cardiac function. Under the guidance of B-mode imaging, Doppler gate (window) is positioned downstream from the atrioventricular (AV) valve in the ventricular inflow region to interrogate inflow velocities. The pulse repetition frequency (PRF) for PW Doppler is set to 9.5 kHz. PW Doppler signals are recorded for the control and Doxo groups for ~3 seconds, and stored for further off-line analysis using Matlab [37].

**Notch signaling as a possible mechanism underlying myocardial repair in response to doxorubicin-mediated injury**

During development, the myocardium differentiates into 2 layers, an outer compact zone and an inner trabeculated zone. Mutations in this genetic program result in congenital heart defects [38]. Trabeculae form a network of branching outgrowths from the ventricular wall [39]. A significant reduction in trabeculation is usually associated with ventricular compact zone deficiencies (known as hypoplastic ventricle), whereas hypertrabeculation (non-compaction) is closely associated with left ventricular non-compaction [40]. Previous studies have revealed the critical role of Notch signaling in the proliferation and differentiation of cardiac trabeculation [38,41]. Hemodynamic shear stress, which is altered in the setting of cardiac remodeling observed in chemotherapy, induces endocardial stretch and strain during ventricular loading, which in turn is implicated in intracellular Notch signaling. The Notch pathway mediates differentiation and proliferation of trabecular myocytes [40,41,42,43]. Mutations in Notch pathway regulator MIB1 (mindbomb homolog 1), which

encodes an E3 ubiquitin ligase to promote endocytosis of the Notch ligands Delta and Jagged, cause left ventricular non-compaction cardiomyopathy [44]. Notch activation by delta-like ligand 1 (DLL1) or delta-like ligand 4 (DLL4) in the endocardial cell results in transcription of ephrin B2 (EPHB2), which in turn regulates neuregulin (NRG1) [38]. As a secreted factor, NRG1 signals to adjacent cells to promote their differentiation into trabecular myocytes. In a parallel pathway, Notch activity in the endocardium also activates bone morphogenetic protein 10 (BMP10) expression in the adjacent myocytes, promoting their proliferation [38]. In response to epi- or endocardial injury, Notch signaling regulates cardiomyocyte proliferation during zebrafish heart regeneration [45]. In this context, we sought to determine Notch signaling pathways underlying myocardial repair in response to Doxo treatment and to modulate these pathways using chemical inhibitors. We hypothesize that Doxo-induced cardiomyopathy regains contractile function via Notch-mediated trabecular cardiomyocyte proliferation in a zebrafish model of heart regeneration.

**Invasive and non-invasive approaches to assess atherosclerotic vascular disease**

In addition to metabolic [46], environmental [47], microbiotal [48], and genetic [49,50] mechanisms at play, atherosclerosis is recognized as a chronic inflammatory disease involving both the innate and adaptive arms of immunity which modulate lesion initiation, progression, and potential late complications [51,52,53]. Thrombosis often complicates physical disruption of the protective collagen-rich fibrous cap overlying the atheroma, exposing circulating clotting factors to pro-coagulants expressed within lesions as a result of inflammatory activation and initiation of the coagulation cascade and ensuing clinical symptoms [51,52]. Despite a broad array of available pharmacological and procedural interventions, atherosclerosis remains the leading cause of death and disability in the developed world [54].

In this setting, considerable research and clinical efforts of preventive cardiovascular medicine have been geared towards identifying high-risk atherosclerotic plaques and high-risk patients [55]

8

[56]. To help address these challenges, we conducted studies both in a translational animal model of atherosclerosis [57] and in humans [58] [59]. These studies detailed below involved the microfabrication of an electrochemical impedance spectroscopy sensor for intra-arterial deployment and underlying plaque characterization *in vivo* [57], the biomathematical modeling and determination of $^{18}$F-flurpiridaz positron emission tomography (PET) absolute myocardial blood flow quantitation in control subjects and patients with coronary artery disease [58], and the assessment of fractional flow reserve by computerized tomography (FFR-CT) based on computational fluid dynamics principles as a strategy to predict patients undergoing clinically indicated coronary revascularization procedures [59].

**Invasive electrochemical impedance spectroscopy to characterize atherosclerotic plaques**

Currently, fractional flow reserve, intravascular ultrasound or optical coherence tomography are limited to anatomic and hemodynamic characteristics of atherosclerotic plaques [60]. Despite the advent of computerized tomographic (CT) angiography, high resolution magnetic resonance imaging [61], intravascular ultrasound, near-infrared fluorescence [62], and time-resolved laser-induced fluorescence spectroscopy [63], real-time interrogation of metabolically active, lipid-rich plaques remains an unmet clinical need. Electrochemical impedance spectroscopy (EIS) measures charges stored in tissues by electrical impedance developed in response to applied alternating current. EIS is the macroscopic representation of the electric field and current density distribution within the experimented samples. Fat-free tissue is known to be a viable electrical conductor for its high water and electrolytes content. However, fat tissue is anhydrous and thus, a poor conductor. The high lipid content, including negatively charged active lipids such as oxidized low density lipoprotein (oxLDL) [64] and foam cells present in the plaque change the endoluminal electrochemical properties that can be measured by EIS [65] [66] [67].

We previously developed concentric bipolar microelectrode sensors (diameter = 300 μm) and introduced balloon-inflatable electrodes to measure EIS signals from non-homogeneous tissue composition, non-planar endoluminal surface, and non-uniform electric current distribution of the atherosclerotic lesions [68] [69]. With our novel EIS design and microfabrication [57], we introduce a 2-point configuration to avoid separate current paths and common-mode signals that confound measured data [70]. The 2-point configuration with flexible round electrodes (diameter = 240 μm) enables deep intraplaque penetration by alternating current, allowing for quantification of atherosclerotic plaques from the thoracic to distal abdominal aortas in the New Zealand White rabbit model. We quantified and validated EIS signals both *in vivo* and *ex vivo* in relation to epicardial fat tissue, and recapitulated the frequency range from 10 – 300 kHz in which distinct capacitive and phase changes revealed low, intermediate and high oxLDL-rich lesions. Thus, we demonstrate a new generation of balloon-inflatable 2-point microelectrodes as a reliable, safe and robust approach to complement diagnostic angiography [57]. Our findings provide a basis for future pre-clinical studies to determine the EIS sensor either as a stand-alone catheter or packaged with other modalities such as intravascular ultrasound [60].

## ^{18}F-flurpiridaz positron emission tomography for the absolute quantitation of myocardial blood flow

The importance of absolute quantitation of myocardial blood flow (MBF) expressed as mL/min/g of myocardium, above and beyond relative perfusion imaging, has been well established and is progressively entering routine clinical practice [71] [72] [73]. ^{13}N-ammonia coronary flow reserve (CFR), expressed as the ratio of stress to rest MBF, increases diagnostic sensitivity [74] and has a strong association with prognosis [75] [76]. [82]Rb-chloride MBF and CFR correctly detects 3-vessel CAD [77] and predicts adverse cardiovascular events [78] beyond relative perfusion [79] [80]. Most importantly, absolute quantitation of MBF with [82]Rb-chloride is a strong and independent predictor of cardiac

mortality in patients with known or suspected CAD, providing incremental risk stratification over established clinical variables and relative perfusion [81].

$^{18}$F-flurpiridaz is a novel PET radiopharmaceutical with a half-life of 108 minutes and is a structural analog of the insecticide pyridaben, a known inhibitor of the mitochondrial complex-1 of the electron transport chain [82]. The first-pass extraction fraction of $^{18}$F-flurpiridaz by the myocardium is elevated – 94% – and flow-independent over a wide range of conditions [83], implying a linear relationship between uptake and MBF [84]. In comparison, $^{13}$N-ammonia has an extraction fraction of 82% at rest and $^{82}$Rb-chloride one of 42% with a significant roll-off phenomenon, i.e. low extraction at high flows [85].

The elevated extraction fraction of $^{18}$F-flurpiridaz over a wide range of flow rates makes it an optimal candidate for absolute MBF quantitation. We employed a quantitation method that utilizes the early kinetics of myocardial uptake of the tracer, taking advantage of the high first-pass extraction fraction [83] with no requirement for compartmental modeling as is the case for currently available PET tracers. Our method depends only on the dynamic images of the first 90 seconds and is thus less sensitive to patient movement [58]. We applied this quantitative method to normal subjects with low likelihood of myocardial ischemia and CAD patients with stress-inducible myocardial ischemia, providing MBF data over a wide range of conditions [58]. In CAD patients, diseased vascular segments had significantly lower MBF in response to adenosine stress and thus a reduced CFR compared to controls. Interestingly, CAD vascular segments with <50% stenosis exhibited stress MBF and CFR values between those from vascular segments with ≥50% stenosis and those from normal subjects. Consistent with previous reports, this suggests that despite being labeled as angiographically non-significant, these territories are not normal and exhibit hemodynamic and metabolic abnormalities. Previously suggested mechanisms include abnormalities of endothelium-dependent and/or smooth muscle cell-dependent vasomotion, with

these patients being at increased risk of future cardiovascular events [71]. Our first-in-human results create the foundation for future studies of MBF quantitation with $^{18}$F-flurpiridaz in larger populations and subgroups of interest, such as patients with metabolic abnormalities but clinically silent CAD.

**Fractional flow reserve by coronary computerized tomography angiography to determine the hemodynamic significance of coronary lesions non-invasively**

Coronary computed tomography angiography (CTA) is being used increasingly in patient care despite the highest standard ever set for adoption of a noninvasive imaging test for diagnosing coronary artery disease (CAD). Recent analyses from the SCOT-HEART (Scottish Computed Tomography of the HEART) trial, which randomized patients to standard of care with or without coronary CTA [86], demonstrated that following a coronary CTA, invasive angiograms are significantly more likely to show obstructive lesions, and appropriate therapy to be initiated, associated with halving of myocardial infarction occurrence [87]. Combined with the recent PROMISE (Prospective Multicenter Imaging Study for Evaluation of Chest Pain) trial [88], these data support this expanding role for coronary CTA in CAD management [89]. Furthermore, coronary CTA may be used to monitor coronary plaque progression [90] [91] and has an increasing role in patients with acute chest pain [92] presenting to the emergency department [93]. These studies and others have fueled the proposal that coronary CTA is a highly competitive or superior modality as a gatekeeper to invasive angiography [94] [95].

Complementing this role of coronary CTA, considerable effort has been devoted to assess the physiologic significance of stenosis burden by different CT-based approaches, of which fractional flow reserve CT (FFR-CT) is the most rigorously studied [96] [97] [98] [99]. FFR-CT computation is based on calculations of coronary flow and pressure fields from anatomic data, in particular construction of an anatomic model of the coronary arteries, a mathematical model of coronary physiology to

derive boundary conditions representing cardiac output, aortic pressure, microcirculatory resistance, and their combination with fluid dynamics principles which relate to conservation of mass and balance of momentum [100] [101].

We determined baseline FFR-CT values in patients undergoing coronary revascularization and those treated with optimal medical therapy, establishing significant differences in median values (0.70 vs. 0.86, respectively) [59]. A comparison of accepted and routinely used clinical significance cutoffs of FFR-CT ≤ 0.80 and coronary CTA stenosis ≥ 70% highlighted important different behaviors of these 2 tests. Indeed, a coronary CTA approach had a significant positive predictive value and positive likelihood ratio, indicating that in the presence of an angiographically significant stenosis, the odds of having a downstream revascularization were high, reflecting the ability of coronary CTA to identify high-risk patients. In contrast, an FFR-CT approach had a significant negative predictive value and negative likelihood ratio, supporting the hypothesis that in the presence of a hemodynamically insignificant FFR-CT value > 0.80, the odds of having downstream revascularization were low, thereby reflecting the ability of FFR-CT to exclude high-risk patients. Our results suggest that coronary CTA combined with FFR-CT allows individual patient-level, artery-specific decision making, thereby enhancing the gatekeeping function of coronary CTA and increasing the diagnostic and therapeutic yield of invasive coronary angiography.

**REFERENCES**

**1.**      Mortality GBD and Causes of Death Collaborators. Global, regional, and national age-sex specific all-cause and cause-specific mortality for 240 causes of death, 1990-2013: a systematic analysis for the Global Burden of Disease Study 2013. *Lancet*. 2014.

**2.**      Ewer MS and Ewer SM. Cardiotoxicity of anticancer treatments: what the cardiologist needs to know. *Nature Reviews Cardiology*. 2010;7:564-75.

**3.**      Ewer MS and Ewer SM. Cardiotoxicity of anticancer treatments. *Nature Reviews Cardiology*. 2015;12:547-58.

**4.**      Albini A, Pennesi G, Donatelli F, Cammarota R, De Flora S and Noonan DM. Cardiotoxicity of anticancer drugs: the need for cardio-oncology and cardio-oncological prevention. *Journal of the National Cancer Institute*. 2010;102:14-25.

**5.**      Vejpongsa P and Yeh ET. Prevention of anthracycline-induced cardiotoxicity: challenges and opportunities. *Journal of the American College of Cardiology*. 2014;64:938-45.

**6.**      Swain SM, Whaley FS and Ewer MS. Congestive heart failure in patients treated with doxorubicin: a retrospective analysis of three trials. *Cancer*. 2003;97:2869-79.

**7.**      Cardinale D, Sandri MT, Martinoni A, et al. Myocardial injury revealed by plasma troponin I in breast cancer treated with high-dose chemotherapy. *Annals of Oncology*. 2002;13:710-5.

**8.**      Zhang YW, Shi J, Li YJ and Wei L. Cardiomyocyte death in doxorubicin-induced cardiotoxicity. *Archivum Immunologiae et Therapia Experimentalis (Warsz)*. 2009;57:435-45.

**9.**      Zhang S, Liu X, Bawa-Khalfe T, Lu LS, Lyu YL, Liu LF and Yeh ET. Identification of the molecular basis of doxorubicin-induced cardiotoxicity. *Nature Medicine*. 2012;18:1639-42.

**10.**     Campbell JM, Hartjes KA, Nelson TJ, Xu X and Ekker SC. New and TALENted genome engineering toolbox. *Circulation Research*. 2013;113:571-87.

**11.**     Kim JD, Lee HW and Jin SW. Diversity is in my veins: role of bone morphogenetic protein signaling during venous morphogenesis in zebrafish illustrates the heterogeneity within endothelial cells. *Arteriosclerosis, Thrombosis, and Vascular Biology*. 2014;34:1838-45.

**12.**     Santoro MM. Antiangiogenic cancer drug using the zebrafish model. *Arteriosclerosis, Thrombosis, and Vascular Biology*. 2014;34:1846-53.

**13.**     White R, Rose K and Zon L. Zebrafish cancer: the state of the art and the path forward. *Nature Reviews Cancer*. 2013;13:624-36.

**14.**     Sedmera D, Reckova M, deAlmeida A, Sedmerova M, Biermann M, Volejnik J, Sarre A, Raddatz E, McCarthy RA, Gourdie RG and Thompson RP. Functional and morphological evidence for a ventricular conduction system in zebrafish and Xenopus hearts. *American Journal of Physiolology - Heart and Circulatory Physiology*. 2003;284:H1152-60.

**15.**     Milan DJ, Jones IL, Ellinor PT and MacRae CA. In vivo recording of adult zebrafish electrocardiogram and assessment of drug-induced QT prolongation. *American Journal of Physiolology - Heart and Circulatory Physiology*. 2006;291:H269-73.

**16.**     Poss KD, Wilson LG and Keating MT. Heart regeneration in zebrafish. *Science*. 2002;298:2188-90.

**17.**     Lee J, Cao H, Kang BJ, et al. Hemodynamics and ventricular function in a zebrafish model of injury and repair. *Zebrafish*. 2014;11:447-54.

**18.**     Kikuchi K, Holdway JE, Werdich AA, et al. Primary contribution to zebrafish heart regeneration by gata4(+) cardiomyocytes. *Nature*. 2010;464:601-5.

**19.**     Ding Y, Sun X, Huang W, et al. Haploinsufficiency of target of rapamycin attenuates cardiomyopathies in adult zebrafish. *Circulation Research*. 2011;109:658-69.

**20.**     Reischauer S, Arnaout R, Ramadass R and Stainier DY. Actin binding GFP allows 4D in vivo imaging of myofilament dynamics in the zebrafish heart and the identification of Erbb2 signaling as a remodeling factor of myofibril architecture. *Circulation Research*. 2014;115:845-56.

**21.**     Sun L, Lien CL, Xu X and Shung KK. In vivo cardiac imaging of adult zebrafish using high frequency ultrasound (45-75 MHz). *Ultrasound in Medicine and Biology*. 2008;34:31-9.

**22.**     Sun P, Zhang Y, Yu F, et al. Micro-electrocardiograms to study post-ventricular amputation of zebrafish heart. *Annals of Biomedical Engineering*. 2009;37:890-901.

**23.**      Yu F, Huang J, Adlerz K, et al. Evolving cardiac conduction phenotypes in developing zebrafish larvae: implications to drug sensitivity. *Zebrafish*. 2010;7:325-31.

**24.**      Yu F, Li R, Parks E, Takabe W and Hsiai TK. Electrocardiogram signals to assess zebrafish heart regeneration: implication of long QT intervals. *Annals of Biomedical Engineering*. 2010;38:2346-57.

**25.**      Tei C, Ling LH, Hodge DO, et al. New index of combined systolic and diastolic myocardial performance: a simple and reproducible measure of cardiac function--a study in normals and dilated cardiomyopathy. *Journal of Cardiology*. 1995;26:357-66.

**26.**      Keller PJ and Dodt HU. Light sheet microscopy of living or cleared specimens. *Current Opinion in Neurobiology*. 2012;22:138-43.

**27.**      Pantazis P and Supatto W. Advances in whole-embryo imaging: a quantitative transition is underway. *Nature Reviews Molecular Cell Biology*. 2014;15:327-39.

**28.**      Stelzer EH. Light-sheet fluorescence microscopy for quantitative biology. *Nature Methods*. 2014;12:23-6.

**29.**      Reynaud EG, Peychl J, Huisken J and Tomancak P. Guide to light-sheet microscopy for adventurous biologists. *Nature Methods*. 2014;12:30-4.

**30.**      Keller PJ, Ahrens MB and Freeman J. Light-sheet imaging for systems neuroscience. *Nature Methods*. 2014;12:27-9.

**31.**      Huisken J and Stainier DY. Selective plane illumination microscopy techniques in developmental biology. *Development*. 2009;136:1963-75.

**32.**      Huisken J, Swoger J, Del Bene F, Wittbrodt J and Stelzer EH. Optical sectioning deep inside live embryos by selective plane illumination microscopy. *Science*. 2004;305:1007-9.

**33.**      Dent JA, Polson AG and Klymkowsky MW. A whole-mount immunocytochemical analysis of the expression of the intermediate filament protein vimentin in Xenopus. *Development*. 1989;105:61-74.

**34.** Hu C, Zhang L, Cannata JM, Yen J and Shung KK. Development of a 64 channel ultrasonic high frequency linear array imaging system. *Ultrasonics*. 2011;51:953-9.

**35.** Cannata JM, Williams JA, Zhang L, Hu CH and Shung KK. A high-frequency linear ultrasonic array utilizing an interdigitally bonded 2-2 piezo-composite. *IEEE Transactions on Ultrasonics, Ferroelectrics, and Frequency Control*. 2011;58:2202-12.

**36.** Nagueh SF, Appleton CP, Gillebert TC, et al. Recommendations for the evaluation of left ventricular diastolic function by echocardiography. *Journal of the American Society of Echocardiography.* 2009;22:107-33.

**37.** Aydin N, Fan L and Evans DH. Quadrature-to-directional format conversion of Doppler signals using digital methods. *Physiological Measurement*. 1994;15:181-99.

**38.** High FA and Epstein JA. The multifaceted role of Notch in cardiac development and disease. *Nature Reviews Genetics*. 2008;9:49-61.

**39.** Peshkovsky C, Totong R and Yelon D. Dependence of cardiac trabeculation on neuregulin signaling and blood flow in zebrafish. *Development Dynamics*. 2011;240:446-56.

**40.** Zhang W, Chen H, Qu X, Chang CP and Shou W. Molecular mechanism of ventricular trabeculation/compaction and the pathogenesis of the left ventricular noncompaction cardiomyopathy (LVNC). *American Journal of Medical Genetics Part C Seminars in Medical Genetics*. 2013;163C:144-56.

**41.** Grego-Bessa J, Luna-Zurita L, del Monte G, et al. Notch signaling is essential for ventricular chamber development. *Developmental Cell*. 2007;12:415-29.

**42.** Liu J, Bressan M, Hassel D, et al. A dual role for ErbB2 signaling in cardiac trabeculation. *Development*. 2010;137:3867-75.

**43.** Culver JC and Dickinson ME. The effects of hemodynamic force on embryonic development. *Microcirculation*. 2010;17:164-78.

**44.** Luxan G, Casanova JC, Martinez-Poveda B, et al. Mutations in the NOTCH pathway regulator MIB1 cause left ventricular noncompaction cardiomyopathy. *Nature Medicine*. 2013;19:193-201.

**45.** Zhao L, Borikova AL, Ben-Yair R, et al. Notch signaling regulates cardiomyocyte proliferation during zebrafish heart regeneration. *Proceedings of the National Academy of Sciences of the United States of America*. 2014;111:1403-8.

**46.** Demer LL and Tintut Y. Inflammatory, metabolic, and genetic mechanisms of vascular calcification. *Arteriosclerosis, Thrombosis, and Vascular Biology*. 2014;34:715-23.

**47.** Cosselman KE, Navas-Acien A and Kaufman JD. Environmental factors in cardiovascular disease. *Nature Reviews Cardiology*. 2015;12:627-42.

**48.** Tang WH and Hazen SL. The contributory role of gut microbiota in cardiovascular disease. *The Journal of Clinical Investigation*. 2014;124:4204-11.

**49.** Kathiresan S and Srivastava D. Genetics of human cardiovascular disease. *Cell*. 2012;148:1242-57.

**50.** Bennett BJ, Davis RC, Civelek M, et al. Genetic Architecture of Atherosclerosis in Mice: A Systems Genetics Analysis of Common Inbred Strains. *PLoS Genetics*. 2015;11:e1005711.

**51.** Packard RR and Libby P. Inflammation in atherosclerosis: from vascular biology to biomarker discovery and risk prediction. *Clinical chemistry*. 2008;54:24-38.

**52.** Packard RR, Lichtman AH and Libby P. Innate and adaptive immunity in atherosclerosis. *Seminars in Immunopathology*. 2009;31:5-22.

**53.** Libby P, Lichtman AH and Hansson GK. Immune effector mechanisms implicated in atherosclerosis: from mice to humans. *Immunity*. 2013;38:1092-104.

**54.** Mozaffarian D, Benjamin EJ, Go AS, et al. Heart Disease and Stroke Statistics-2015 Update A Report From the American Heart Association. *Circulation*. 2015;131:E29-E322.

**55.** Naghavi M, Libby P, Falk E, et al. From vulnerable plaque to vulnerable patient: a call for new definitions and risk assessment strategies: Part I. *Circulation*. 2003;108:1664-72.

56.     Naghavi M, Libby P, Falk E, et al. From vulnerable plaque to vulnerable patient: a call for new definitions and risk assessment strategies: Part II. *Circulation*. 2003;108:1772-8.

57.     Packard RR, Zhang X, Luo Y, et al. Two-Point Stretchable Electrode Array for Endoluminal Electrochemical Impedance Spectroscopy Measurements of Lipid-Laden Atherosclerotic Plaques. *Annals of Biomedical Engineering*. 2016;44:2695-706.

58.     Packard RR, Huang SC, Dahlbom M, Czernin J and Maddahi J. Absolute quantitation of myocardial blood flow in human subjects with or without myocardial ischemia using dynamic flurpiridaz F 18 PET. *Journal of Nuclear Medicine.* 2014;55:1438-44.

59.     Packard RR, Li D, Budoff MJ and Karlsberg RP. Fractional flow reserve by computerized tomography and subsequent coronary revascularization. *European Heart Journal Cardiovascular Imaging*. 2016. In Press.

60.     Bourantas CV, Garcia-Garcia HM, Naka KK, et al. Hybrid intravascular imaging: current applications and prospective potential in the study of coronary atherosclerosis. *Journal of the American College of Cardiology*. 2013;61:1369-78.

61.     Worthley SG, Helft G, Fuster V, et al. A novel nonobstructive intravascular MRI coil: in vivo imaging of experimental atherosclerosis. *Arteriosclerosis, Thrombosis, and Vascular Biology*. 2003;23:346-50.

62.     Jaffer FA, Vinegoni C, John MC, et al. Real-time catheter molecular sensing of inflammation in proteolytically active atherosclerosis. *Circulation*. 2008;118:1802-9.

63.     Marcu L, Fishbein MC, Maarek JM and Grundfest WS. Discrimination of human coronary artery atherosclerotic lipid-rich lesions by time-resolved laser-induced fluorescence spectroscopy. *Arteriosclerosis, Thrombosis, and Vascular Biology*. 2001;21:1244-50.

64.     Sevanian A, Hwang J, Hodis H, et al. Contribution of an in vivo oxidized LDL to LDL oxidation and its association with dense LDL subpopulations. *Arteriosclerosis, Thrombosis, and Vascular Biology.* 1996;16:784-93.

65.     Konings MK, Mali WP and Viergever MA. Development of an intravascular impedance

catheter for detection of fatty lesions in arteries. *IEEE Transactions on Medical Imaging*. 1997;16:439-46.

**66.**     Streitner I, Goldhofer M, Cho S, et al. Electric impedance spectroscopy of human atherosclerotic lesions. *Atherosclerosis*. 2009;206:464-8.

**67.**     Streitner I, Goldhofer M, Cho S, et al. Cellular imaging of human atherosclerotic lesions by intravascular electric impedance spectroscopy. *PloS One*. 2012;7:e35405.

**68.**     Yu F, Lee J, Jen N, et al. Elevated electrochemical impedance in the endoluminal regions with high shear stress: implication for assessing lipid-rich atherosclerotic lesions. *Biosensors & Bioelectronics*. 2013;43:237-44.

**69.**     Cao H, Yu F, Zhao Y, et al. Stretchable electrochemical impedance sensors for intravascular detection of lipid-rich lesions in New Zealand White rabbits. *Biosensors & Bioelectronics*. 2014;54:610-6.

**70.**     Grimnes S and Martinsen OG. Sources of error in tetrapolar impedance measurements on biomaterials and other ionic conductors. *J Phys D Appl Phys*. 2007;40:9-14.

**71.**     Schindler TH, Schelbert HR, Quercioli A and Dilsizian V. Cardiac PET imaging for the detection and monitoring of coronary artery disease and microvascular health. *JACC Cardiovascular Imaging*. 2010;3:623-40.

**72.**     Johnson NP and Gould KL. Integrating Noninvasive Absolute Flow, Coronary Flow Reserve, and Ischemic Thresholds Into a Comprehensive Map of Physiological Severity. *JACC Cardiovascular Imaging*. 2012;5:430-440.

**73.**     Gould KL, Johnson NP, Bateman TM, et al. Anatomic versus physiologic assessment of coronary artery disease. Role of coronary flow reserve, fractional flow reserve, and positron emission tomography imaging in revascularization decision-making. *Journal of the American College of Cardiology*. 2013;62:1639-53.

**74.**     Fiechter M, Ghadri JR, Gebhard C, et al. Diagnostic value of 13N-ammonia myocardial perfusion PET: added value of myocardial flow reserve. *Journal of Nuclear Medicine*.

2012;53:1230-4.

**75.** Tio RA, Dabeshlim A, Siebelink HMJ, et al. Comparison Between the Prognostic Value of Left Ventricular Function and Myocardial Perfusion Reserve in Patients with Ischemic Heart Disease. *Journal of Nuclear Medicine*. 2009;50:214-219.

**76.** Herzog BA, Husmann L, Valenta I, et al. Long-term prognostic value of 13N-ammonia myocardial perfusion positron emission tomography added value of coronary flow reserve. *Journal of the American College of Cardiology*. 2009;54:150-6.

**77.** Parkash R, deKemp RA, Ruddy TD, et al. Potential utility of rubidium 82 PET quantification in patients with 3-vessel coronary artery disease. *Journal of Nuclear Cardiology.* 2004;11:440-9.

**78.** Fukushima K, Javadi MS, Higuchi T, et al. Prediction of short-term cardiovascular events using quantification of global myocardial flow reserve in patients referred for clinical 82Rb PET perfusion imaging. *Journal of Nuclear Medicine.* 2011;52:726-32.

**79.** Ziadi MC, Dekemp RA, Williams KA, et al. Impaired myocardial flow reserve on rubidium-82 positron emission tomography imaging predicts adverse outcomes in patients assessed for myocardial ischemia. *Journal of the American College of Cardiology*. 2011;58:740-8.

**80.** Farhad H, Dunet V, Bachelard K, et al. Added prognostic value of myocardial blood flow quantitation in rubidium-82 positron emission tomography imaging. *European Heart Journal Cardiovascular Imaging*. 2013;14:1203-10.

**81.** Murthy VL, Naya M, Foster CR, et al. Improved cardiac risk assessment with noninvasive measures of coronary flow reserve. *Circulation*. 2011;124:2215-24.

**82.** Yalamanchili P, Wexler E, Hayes M, et al. Mechanism of uptake and retention of F-18 BMS-747158-02 in cardiomyocytes: a novel PET myocardial imaging agent. *Journal of Nuclear Cardiology*. 2007;14:782-8.

**83.** Huisman MC, Higuchi T, Reder S, et al. Initial characterization of an 18F-labeled myocardial perfusion tracer. *Journal of Nuclear Medicine*. 2008;49:630-6.

**84.** Yu M, Guaraldi MT, Mistry M, et al. BMS-747158-02: a novel PET myocardial perfusion

21

imaging agent. *Journal of Nuclear Cardiology.* 2007;14:789-98.

**85.**     Maddahi J and Packard RR. Cardiac PET perfusion tracers: current status and future directions. *Seminars in Nuclear Medicine*. 2014;44:333-43.

**86.**     Scot-Heart Investigators. CT coronary angiography in patients with suspected angina due to coronary heart disease (SCOT-HEART): an open-label, parallel-group, multicentre trial. *Lancet*. 2015;385:2354-2354.

**87.**     Williams MC, Hunter A, Shah ASV, et al. Use of Coronary Computed Tomographic Angiography to Guide Management of Patients With Coronary Disease. *Journal of the American College of Cardiology*. 2016;67:1759-1768.

**88.**     Douglas PS, Hoffmann U, Patel MR, et al. Outcomes of anatomical versus functional testing for coronary artery disease. *The New England Journal of Medicine*. 2015;372:1291-300.

**89.**     Fordyce CB, Newby DE and Douglas PS. Diagnostic Strategies for the Evaluation of Chest Pain: Clinical Implications From SCOT-HEART and PROMISE. *Journal of the American College of Cardiology*. 2016;67:843-52.

**90.**     Zeb I, Li D, Nasir K, Malpeso J, et al. Effect of statin treatment on coronary plaque progression - a serial coronary CT angiography study. *Atherosclerosis*. 2013;231:198-204.

**91.**     Sandfort V, Lima JA and Bluemke DA. Noninvasive Imaging of Atherosclerotic Plaque Progression: Status of Coronary Computed Tomography Angiography. *Circulation Cardiovascular Imaging*. 2015;8:e003316.

**92.**     Nieman K and Hoffmann U. Cardiac computed tomography in patients with acute chest pain. *European Heart Journal*. 2015;36:906-14.

**93.**     Cheezum MK and Blankstein R. Coronary computed tomographic angiography: its role in emergency department triage. *Circulation*. 2014;130:2052-6.

**94.**     Karlsberg RP, Budoff MJ, Thomson LE, Friedman JD and Berman DS. Reduction in downstream test utilization following introduction of coronary computed tomography in a cardiology practice. *The International Journal of Cardiovascular Imaging*. 2010;26:359-66.

**95.**     Shaw LJ, Hausleiter J, Achenbach S, et al. Coronary Computed Tomographic Angiography as a Gatekeeper to Invasive Diagnostic and Surgical Procedures. *Journal of the American College of Cardiology*. 2012;60:2103-2114.

**96.**     Koo BK, Erglis A, Doh JH, et al. Diagnosis of ischemia-causing coronary stenoses by noninvasive fractional flow reserve computed from coronary computed tomographic angiograms. Results from the prospective multicenter DISCOVER-FLOW (Diagnosis of Ischemia-Causing Stenoses Obtained Via Noninvasive Fractional Flow Reserve) study. *Journal of the American College of Cardiology*. 2011;58:1989-97.

**97.**     Nakazato R, Park HB, Berman DS, et al. Noninvasive fractional flow reserve derived from computed tomography angiography for coronary lesions of intermediate stenosis severity: results from the DeFACTO study. *Circulation Cardiovascular Imaging*. 2013;6:881-9.

**98.**     Norgaard BL, Leipsic J, Gaur S, et al. Diagnostic performance of noninvasive fractional flow reserve derived from coronary computed tomography angiography in suspected coronary artery disease: the NXT trial (Analysis of Coronary Blood Flow Using CT Angiography: Next Steps). *Journal of the American College of Cardiology*. 2014;63:1145-55.

**99.**     Douglas PS, De Bruyne B, Pontone G, et al. 1-Year Outcomes of FFRCT-Guided Care in Patients With Suspected Coronary Disease The PLATFORM Study. *Journal of the American College of Cardiology*. 2016;68:435-445.

**100.**     Taylor CA, Fonte TA and Min JK. Computational fluid dynamics applied to cardiac computed tomography for noninvasive quantification of fractional flow reserve: scientific basis. *Journal of the American College of Cardiology*. 2013;61:2233-41.

**101.**     Min JK, Taylor CA, Achenbach S, et al. Noninvasive Fractional Flow Reserve Derived From Coronary CT Angiography: Clinical Data and Scientific Principles. *JACC Cardiovascular Imaging*. 2015;8:1209-22.

**CHAPTER ONE**

**Cardiac light-sheet fluorescent microscopy for multi-scale and rapid imaging of architecture and function**

Fei P.*, Lee J.*, <u>Packard R.R.S.</u>*, Sereti K.I., Xu H., Ma J., Ding Y., Kang H., Chen H., Sung K., Kulkarni R., Ardehali R., Kuo C.-C.J., Xu X., Ho C.-M., Hsiai T.K. * Equal contribution

Original article, published in *Scientific Reports* 2016 Mar 3; 6: 22489.

Manuscript reproduced with permission.

**ABSTRACT**

Light Sheet Fluorescence Microscopy (LSFM) enables multi-dimensional and multi-scale imaging via illuminating specimens with a separate thin sheet of laser. It allows rapid plane illumination for reduced photo-damage and superior axial resolution and contrast. We hereby demonstrate cardiac LSFM (c-LSFM) imaging to assess the functional architecture of zebrafish embryos with a retrospective cardiac synchronization algorithm for four-dimensional reconstruction (3-D space + time). By combining our approach with tissue clearing techniques, we reveal the entire cardiac structures and hypertrabeculation of adult zebrafish hearts in response to doxorubicin treatment. By integrating the resolution enhancement technique with c-LSFM to increase the resolving power under a large field-of-view, we demonstrate the use of low power objective to resolve the entire architecture of large-scale neonatal mouse hearts, revealing the helical orientation of individual myocardial fibers. Therefore, our c-LSFM imaging approach provides multi-scale visualization of architecture and function to drive cardiovascular research with translational implication in congenital heart diseases.

**INTRODUCTION**

The advent of three-dimensional imaging of biological organisms and tissues provides a paradigm shift to interface optical imaging with cardiovascular research. Unraveling cardiac morphogenesis, regeneration, differentiation and proliferation require deep tissue penetration to visualize the dynamic events with high spatiotemporal and depth resolution. While modern light microscopy techniques, such as wide-field microscopy and confocal scanning microscopy, have enabled spatial resolution to image intracellular organelles, insufficient axial resolution and noticeable photo-damage remain a challenge. The 3-D post-imaging reconstruction and stitching for large sample size renders the imaging processes laborious and prolonged[1-3]. The advent of Optical Coherence Tomography (OCT) and Optical Projection Tomography (OPT) has enabled 3-D and non-invasive imaging of large specimens. OCT allows imaging of living samples by light sectioning through coherence[4,5] and OPT operates on a similar principle with X-ray computed tomography to image chick embryos with intermediate sizes at high resolution. However, OCT is limited from fluorescent imaging due to the lack of coherence, and OPT is limited by its spatial resolution and recording rate[6]. Recently, the use of micro-Computed Tomography (CT) with intrinsic resolution limit (15-45 $\mu$m) has provided high spatial and temporal resolution for imaging newborn (<3.5 mm) and fetal mouse hearts (<2 mm) with routine operation (<35 min) for congenital heart disease[7]. In addition, micro–Magnetic Resonance Image (MRI) has allowed for live imaging of mouse brain with high spatial resolution (30x30x60 $\mu$m) and compatible scanning acquisition time (<45 min)[8]. Both micro-CT and micro–MRI are limited from tracking the fluorescently labeled live zebrafish and neonatal hearts for cardiac development, injury and repair. In this context, Light Sheet Fluorescence Microscopy is an emerging imaging modality for multi-dimensional, -scale, and -channel visualization of cardiac architecture and physiology accompanied by rapid and precise tracking of multi-fluorescently labeled intracellular, cellular or tissue components from several microns to millimeters[9-11].

Light Sheet Fluorescence Microscopy (LSFM) has allowed for high speed, precise tracking of multi-fluorescently labeled cells or tissues of interests within a complex and dynamic cardiovascular environment[10,11].  Unlike conventional wide-field and laser scanning microscopy, LSFM applies two separate optical paths for plane illumination and fluorescence detection. Instead of wide-field excitation or point scanning in which the excitation path is parallel to the detection path, LSFM selectively illuminates an ultra-thin plane of the sample via a sheet of light orthogonal to the detection path.  By providing sharp and in-focus excitation along the axial direction, LSFM reduces the photon burden to the sample, enhances the image contrast via eliminating out-of-focus contamination, and improves the axial resolution under a large field-of-view.  With its numerous structure variants, including Selective Plane Illumination Microscopy (SPIM), Multidirectional SPIM (m-SPIM), Digitally Scanned Light Sheet Microscopy (DSLM), Objective-Coupled Planar Microscopy (OCPI), Oblique Plane Microscope (OPM), and Bessel-Beam-based Light Sheet Microscopy, being widely developed in recent years, LSFM is on the verge of becoming a predominant visualization technique for a broad range of life science research[12-16].  Ahrens *et al*. demonstrated functional imaging of neurons at nearly one-second resolution[17].  Schmid *et al.* further measured endothelial cell migration patterns and tissue remodeling in the early endoderm[18].  LSFM is uniquely powerful for multi-scale imaging to unravel developmental milestones over a dynamic range of length and time scales.

Here, we developed a cardiac LSFM (c-LSFM) system to image various cardiac architectures ranging from hundreds of microns to several millimeters.  To image rapid cardiac contraction from a large region-of-interest (ROI), we integrated several optimization algorithms with the c-LSFM system to enhance temporal and spatial resolution.  When imaging a contracting embryonic zebrafish heart, the 2-D plane images obtained from the conventional LSFM significantly improved demarcation of the cardiac boarders for computational fluid dynamics and myocardial strain studying.  However, we further enhanced the temporal resolution to reconstruct the rapidly

27

contracting 4-D embryonic zebrafish hearts (3-D spatial and time domain) by integrating a retrospective gating algorithm with the c-LSFM system. Next, we introduced a resolution-enhancement technique to offset the decreased spatial resolution from the low numerical aperture (N.A.) and low magnification of the detection lenses; thereby, allowing for imaging macro-scale neonatal mouse hearts with high spatial resolution under a large field-of-view (FOV). We further achieved cellular resolution to uncover the helical orientation of individual myocardial fibers, as well as the bi- and tri-cuspid valves, muscular ridges and trabecular network. In this context, we have built on the established SPIM principle for tunable c-LSFM imaging to uncover cardiac architecture, development and remodeling otherwise challenging with existing imaging modalities. We introduced a widely tunable c-LSFM system for high-speed, large-FOV, and long-term multi-scale imaging ranging from zebrafish model to the higher vertebrate with translational implication to studying congenital heart diseases in the mouse models.

**METHODS**

**Ethics statement**

Zebrafish and mice were maintained in accordance with UCLA Institutional Animal Care and Use Committee (IACUC) protocols, under a project license also approved by the UCLA IACUC.

**Preparation of the Transgenic and Mutant Zebrafish Lines**

In compliance with the UCLA IACUC protocols, transgenic *Tg*(*cmlc2:gfp*) lines were raised in the UCLA Zebrafish Core facility. *Cmlc2* is expressed with gfp, and is cardiomyocyte-specific[32]. To maintain optical clearance of the embryos, the medium was supplemented with 0.003% phenylthiourea (PTU) to suppress pigmentation at 20 hpf[33]. *Tg*(*cmlc2:gfp*) embryos were anesthetized in 0.05% tricaine[34,35] and immersed in 0.5 % low-melt agarose at 37°C from 50 to 100 hpf. This procedure allowed for imaging myocardial movement prior to agarose solidification. The embryos immersed in low-melt agarose were transferred to a fluorinated ethylene propylene (FEP) tube (Refractive Index (RI): ~1.33) to provide optical clarity for fluorescence detection. The FEP tube was immersed in a water chamber (water RI: ~1.33) connected to the LSFM system. The samples were allowed to rotate in the x-y-z directions via an automated device.

**Doxorubicin (DOX) Treatment to Adult Zebrafish Hearts**

Transgenic zebrafish *Tg(cmlc2:GFP)* lines with gpf-labeled cardiac myosin light chain were used to allow visualization of the 3-D cardiac structural reorganization in response to DOX, an anthracycline agent of chemotherapy. The aforementioned optical clearing technique enabled the gfp signal to remain unquenched. Adult fish following DOX injection were imaged by LSFM at 30 days following injection. Images were analyzed using ImageJ and Amira softwares, allowing delineation of the volumes of interest.

**Murine heart preparation**

In compliance with the UCLA IACUC protocols, *αMHC*[Cre] (B6.FVB-*Tg*(*Myh6-cre*)2182Mds/J) and *TdTomato* (B6;129S6-*Gt(ROSA)26Sor*[tm9(CAG-tdTomato)Hze]/J) mice were obtained from the Jackson laboratory (ME, USA).  To readily identify cardiomyocytes based on intrinsically expressed fluorescent proteins, we generated a double transgenic mouse model (*αMHC*[Cre]*;TdTomato*) in which cardiomyocytes were indelibly marked by TdTomato.  Hearts were harvested from one to three days old *αMHC*[Cre]*;TdTomato* mice.  Prior to extraction, hearts were stopped in diastole by injection of KCl (3M) followed by washing with 1X PBS.  The tissue was subsequently fixed in 4% paraformaldehyde for 2 hours, followed by three washes with 1X PBS.

**Optical Clearing of Myocardium**

The agarose gel containing the heart samples (adult zebrafish heart or neo-natal mouse hearts) was dehydrated by immersing the gel into 40, 60, 80 and 100% ethanol at room temperature, for 10 to 30 minutes sequentially.  Next, the agarose gel with the samples was immersed into a BABB solution (1:2 benzyl alcohol:benzyl benzoate) for 30 to 120 minutes, to remove the lipid components from the cell membranes and replace them with BABB solution.  Then the refractive index of chemically treated tissue was perfectly matched with that of BABB (RI ~1.51).  The optical clearing greatly reduced scattering from thick cardiac tissues and enabled light transmission through the entire transparent heart.

**4-D Imaging of Embryonic Zebrafish Hearts**

We incorporated post-computation with c-LSFM to study the cardiac mechanics of live embryonic zebrafish hearts.  Living *Tg*(*cmlc:gfp*) fish embryos were selected for 4-D visualization of *cmlc*-labeled myocardium.  As the light-sheet sectioned a thin layer of the beating heart at a certain z depth, the sCMOS camera (Hamamatsu ORCA flash 4.0) continuously recorded the dynamic plane images of this layer (depth) for 4 to 5 cardiac cycles at a high frame rate of ~ 100 fps.  Every 300 frames were acquired from each z layer in response to the relatively fast heart rate (~2 bps)

of zebrafish embryos. We reiterated this process for each z layer till the light-sheet scanned through the entire heart[36]. A retrospective synchronization algorithm was applied to the non-gated LSFM dataset, followed by computational synchronization of the cardiac cycles at different z layers[10,36]. Finally, we sequentially reconstructed the multiple 3-D structures from systole to diastole during a cardiac cycle to generate a "3-D beating heart" in both spatial and time domains **(Fig. S5, S7)**.

There are four sequentially executed image processing steps to reconstruct the zebrafish beating heart. These are period determination, relative shift determination, absolute shift determination and post-processing. First, period determination is designed to estimate an accurate heart rate. In short, we iterate through a set of estimated period hypotheses, and back-project all samples into the first period with respect to the hypotheses. By comparing the samples at the same spatial location, we evaluate each of the period hypotheses. The best hypotheses will be selected accordingly. Second, relative shift determination aimed at aligning the starting sample of each individual image sequences. Starting from a number of relative shift hypotheses, we adopted a quadratic cost function to measure the alignment. By maximizing the alignment, we select the best possible relative shift for each image sequence with respect to the other sequences. Third, absolute shift determination targeted to obtain the absolute shift of each individual image sequence with respect to the first sequence. We use the relative shift result, and calculate a weighted averaged shift for each slice respectively. Finally, we post-process the images by resampling each image sequence with respect to period, truncate image sequence to align the starting sample, and remove noise.

**Confocal Microscopy**

Zeiss LSM 5 PASCAL was used to compare the image resolution and acquisition speed against c-LSFM. After clearing 120dpf zebrafish heart, we placed it on a coverslip and imaged with a 10X/0.3 air objective lens.

**Quantification of Cardiac Mechanics**

To assess changes in ventricular function during cardiac development, volumetric dimension throughout the cardiac cycle was acquired by LSFM at 100 hpf using a sCMOS camera. Captured images were used for segmentation to create a 2-D moving boundary with 600 nodes[37]. The nodes were guided to provide cardiac wall motion as previously described[37]. Matlab (Mathworks, Natick, MA, USA) was used to calculate the global longitudinal strain rates based on changes in displacement ($D$) between two time frames[38].

$$\text{Strain rate} = \frac{dD}{dt} \approx \frac{D_2 - D_1}{time\ step},$$

where $D_1$ denotes the early stage and $D_2$ the later stage at a time-step of 0.05 seconds. Based on LSFM images coupled with non-gated 4-D synchronization computational algorithm[10,36], changes in end systolic (ESV) and end diastolic volume (EDV) were determined by the Amira imaging software (FEI software, Hillsboro, OR)[38].

**RESULTS**

**Implementation of Cardiac Light-Sheet Fluorescence Microscopy (c-LSFM)**

The workflow of c-LSFM was characterized by the orthogonal optical paths and multi-dimensional reconstruction of multi-scale cardiac structures with high resolution **(Fig. 1)**. The optical setting is based on Selective Plane Illumination Microscopy (SPIM)[19]. In the plane illumination path, the combination of a cylindrical lens together with an objective line focused the collimated beam into a hyperbolic light sheet with tunable parameters for illuminating cardiac structures **(Fig. 1a)**. The orthogonal detection path collected the correspondingly excited fluorescence signals under various magnifications ranging from 2X to 20X. To cater the need of frequent switch of detection objectives for various sizes of cardiac samples, we use the long working distance air detection objective combined with post resolution enhancement to replace the water sealing design in original SPIM and improve the convenience of operation. When the heart scanned through the light sheet along the z direction, the sCMOS camera (Hamamatsu, ORCA flash 4.0) located at the terminal end of the detection path simultaneously recorded a stack of 2-D plane images along different z depths **(Fig. 1b)**. At each z depth, only the thinly illuminated plane emitted fluorescence; thus, the captured frames were free of out-of-focus excitation and had high axial resolution. The plane illumination mode and high-frame rate of sCMOS camera allowed completion of the entire 3-D scanning and data acquisition within a few minutes. While the single view scanning was commonly applied for the vast majority of our cardiac specimens, multiple view scanning was an alternative to image the high-scattering cardiac tissues. The multi-view fusion technique restored the entire cardiac architecture from the computationally acquired multi-view dataset[20]. Finally, a spline interpolation and an iterative 3-D deconvolution were subsequently applied to the reconstructed image stack to compensate for the under-sampling of camera and remove the image blurs **(Fig. 1c, d)**. As a result, a 3-D "digital heart" was reconstructed in the last step to provide visualized output with high spatiotemporal resolution and high dynamic range.

**Calibration of light-sheets for multi-scale imaging**

In our c-LSFM system, the light-sheet profile was widely tunable for multiple-scale cardiac samples. Typically, three light-sheet configurations were generated to illuminate the embryonic zebrafish heart (100-150 $\mu$m), adult zebrafish heart (500-1500 $\mu$m), and neo-natal mouse heart (3000-5000 $\mu$m) **(Fig. 2a)**. To provide a uniform plane illumination across the entire sample, the confocal region of the light sheet was finely tuned to cover the sample's transverse dimension **(Fig. 2b, S1)**. Within a certain size of lateral confocal region, the axial extent of axial resolution of the light sheet was also determined by the property of Gaussian beam **(Fig. 2a)**. To characterize the generated light sheets, we used a monochrome CCD profiler to sequentially acquire the projections of the light sheets along their propagation. The extent of axial projection was directly imaged at the waist of the light sheet by the profiler, and the confocal range was further reconstructed by stacking the projections. The thickness of the light sheet, defined as the axial full width at half maximum (FWHM) value of the beam waist, was measured at ~5 $\mu$m for the embryonic zebrafish heart (i), ~9 $\mu$m for the adult zebrafish heart (ii), and ~ 18 $\mu$m for the neo-natal mouse heart (iii) **(Fig. 2a)**. The lateral confocal ranges with respect to these three axial extents were profiled **(Fig. 2b, i - iii)**. The detection objectives were 20X/0.5 for the embryonic zebrafish heart, 10X/0.3 for the adult zebrafish heart, and 4X/0.13 for the neonatal mouse heart to capture the full region-of-interest (ROI). Once the thickness of the light-sheet for excitation and the objective lens for detection were determined, we obtained the lateral and axial resolution for each configuration by measuring the point spread function (PSF). We imaged the fluorescent point source (polystyrene beads, average size ~400 nm) by applying the aforementioned 3 light-sheet configurations, and demonstrated the lateral and axial resolution of the c-LSFM system for the individual configurations by measuring the FWHMs from x-y, x-z, and y-z plane images **(Fig. 2c)**. Under the macro configuration, we further compared the results before and after the

34

resolution enhancement was applied **(Fig. 2c, III and IV)**. The resolved FWHMs of the point source were reduced from ~4.5 $\mu$m to ~2 $\mu$m laterally and from ~18 $\mu$m to ~10 $\mu$m axially.

**Functional analyses of zebrafish embryos**

The global longitudinal strain rate is defined as the shortening of a defined global longitudinal length over time. We measured the strain rates at 100 hours post fertilization (hpf) over the cardiac cycle period **(Fig. 3a)**. We applied high frame-rate acquisition and acquired multiple image sequences to improve the spatial and temporal resolution in response to variable cardiac cycles[10]. The 4-D synchronized LSFM post-image processing allowed analysis of the instantaneous changes in ventricular volume in living zebrafish embryos in the x-y, y-z, and x-z planes **(Fig. 3b, S2)**, from which we quantified the mean stroke volume (4.1 x $10^5$ $\mu m^3$) and ejection fraction (74.5%) **(Table S1)**. At 100 hpf, we revealed the prominent trabecular network that provides oxygenation and nutrition to the myocardium to enhance cardiac contractile function[21].

**Doxorubicin-induced cardiac injury in adult zebrafish**

By integrating tissue clearing technique with c-LSFM, we were able to implement rapid 3-D imaging of the intact adult zebrafish hearts without cryostat sectioning. The fast BABB (1:2 benzyl alcohol:benzyl benzoate mixture) clearing technique rendered the entire hearts translucent with preservation of the fluorescently-labeled tissues of interest. The combination of sustained fluorescent signal from the transgenic *Tg*(*cmlc:gfp*) green fluorescent protein–labeled cardiomyocyte light-chain (cmlc) and the high detection efficiency of the c-LSFM system allowed for rapid light-sheet scanning of the entire hearts within 1 minute, followed by high resolution 3-D reconstruction using Amira visualization software. We demonstrated the coronal, sagittal, and transverse plane images of a wild-type heart at 120 days post fertilization (dpf), revealing the

trabecular network and atrioventricular valve (AV) **(Fig. 4a)**.  The volumetric rendering of the heart was achieved by stacking 500 z-slices together, allowing for 3-D visualization and quantification of functional phenotypes from various image views **(Fig. 4a)**.  Prior to doxorubicin (DOX) injection, the trabecular network appeared compact in association with a small ventricular cavity.  Following chemotherapy injection at 90 dpf, adult zebrafish developed an accentuated trabecular network and an enlarged ventricle at 120 dpf in comparison with the wild-type **(Fig. 4b)**.  We further validated these findings by quantifying the occupancy ratio of the myocardium to the entire heart as ~65% in wild-type fish versus ~52% in DOX-injected fish **(Fig. 4c)**.  As a corollary, the volume ratio of the ventricle cavity was ~27% versus ~41% **(Fig. 4d)**.  These findings suggest that the c-LSFM system unravels hypertrabeculation as a new phenomenon of myocardial response to injury and repair.


**Cardiac LSFM (c-LSFM) to image neonatal mouse architecture**

We further calibrated the light-sheet configuration to image the neonatal mouse heart with a size in the range of several millimeters.  A 15 μm light-sheet sectioning plus a 4X/0.13 detection lens were applied to image the entire sample with a large FOV.  By stacking the recorded z slices into a volume (600 slices with 6 μm in the step size), we demonstrated the reconstructed sagittal and transverse planes, as well as the original coronal planes, to reveal the 4-chamber cardiac structures **(Fig. 5a)**.  The volumetric renderings of the reconstructed "digital heart" further revealed the 3-D morphology with high axial and spatial resolution.  By cropping and rotating the 3-D heart, we highlighted the bicuspid, tricuspid, and pulmonic valves, the trabecular network in the atrial appendages, as well as the myocardial fiber orientation **(Fig. 5b, c)**.


However, the space-bandwidth product of our c-LSFM system was limited by the use of a low power objective lens (4X/0.13) and relatively raw voxel sampling under large FOV (1.625 x 1.625 x 8 μm in case of normal sampling).  Thus, the lateral and axial resolution prior to post-imaging

processing appeared insufficient to resolve the cellular details, such as a single myocardial fiber under a large FOV.  For this reason, we implemented deep over-scanning of the sample and applied a resolution enhancement processing based on the over-scanned data to increase the space band-width product.  First, to reduce the information loss from under-sampling as much as possible, we ran an over-scanning of 3 μm step size (being 6 times smaller than the light sheet thickness) in the axial direction during image acquisition and scaled up the obtained 3-D image 3 times at lateral direction using b-spline interpolation.  Then, we deconvolved the pre-processed 3-D image with measured 3-D point-spread-function of the optical system (interpolated to the same voxel spacing with the image data), to further recover the image from blurring and substantially enhance the resolution.  The iterative 3-D deconvolution conducted in this work was run on the open source ImageJ platform using its "parallel iterative deconvolution" plugin, "3-D iterative deconvolution" module.  We selected the MRNSD (Modified Residual Norm Steepest Descent) or WPL (Wiener Filter Preconditioned Landweber) option, which are both non-negatively constrained algorithms, with appropriate preconditioning parameters to solve the final resolution-enhanced output **(Fig. S3)**.  During computation, we set the max number of iteration (e.g., 50) and mean delta threshold (e.g., 0.01) to determine the convergence.  In most cases, the 3-D deconvolution could be completed within 20 iterations and generated the final deblurred output. In **Fig. 6c**, the top panels (i) show the raw c-LSFM imaging with blurred cellular structure.  The middle panels reveal enhanced resolution to map the cardiac architecture at the cellular resolution.  Upon zooming into the left ventricular wall, the volumetric rendering unraveled the myocardial fibers with diameter < 10 μm.  In the lower panels, images illuminated by the 9 μm light-sheet and detected by the 10X/0.3 objective lens were compared with the upper and middle panels.  This comparison demonstrated the super-resolved cardiac architecture with the use of a lower magnification lens to achieve a resolving power superior to those of higher magnification. We further demonstrated this enhanced imaging capability to reveal the distinct helical orientation of cardiomyocyte fibers in the ventricular and septal walls, as well as the muscular ridges and

trabeculation in the left atrial appendage **(Fig. 6)**. Overall, by integrating our c-LSFM with resolution-enhancement computation, we decoupled limited resolution from the large FOV and achieved cellular resolving power over a meso-scale specimen.

**DISCUSSION**

The main contribution of our in-house c-LSFM system lies in its multi-scale and rapid cardiac imaging with high axial and temporal resolution to uncover cardiac developmental structures in both zebrafish embryos and neonatal mice as well as revealing ventricular changes in response to chemotherapy-induced cardiotoxicity. The application of optical clearing of the adult cardiac samples for c-LSFM, followed by the post-enhancement algorithms, revealed 3-D hypertrabeculation in response to doxorubicin-induced injury in zebrafish hearts (hundreds of microns) and valvular structures and helical orientation of cardiomyocyte fibers in the ventricular walls of the neonatal mouse hearts (a few millimeters) **(Fig. S4)**. We quantified the time-dependent contractile function of zebrafish embryos at 100 hpf. We visualized the neonatal cardiac architecture by using a low power magnification to resolve cellular structures otherwise challenging with existing micro-CT imaging modalities[7]. We distinguished bicuspid from tricuspid valves, and unraveled trabecular networks; thereby, providing anatomical, functional, and pathophysiological phenotypes to drive the future investigation of cardiac injury, repair, and development.


Unlike the conventional Selective Plane Illumination Microscopy (SPIM), our c-LSFM system was designed to accommodate multi-scale cardiac samples[22,23]. SPIM requires the illumination and detection lenses being sealed into a water chamber in which the samples are in close alignment with a short working distance; whereas our c-LSFM system applies a long working distance and non-water dipping objectives. In addition, the large working space allows for scanning of entire macro-size samples, and the integration of the resolution enhancement technique decouples the requirements for high numerical aperture (N.A.), water-dipping objectives for high resolution, and the large space-bandwidth product. Moreover, avoiding the need to seal the objectives in the water chamber enables frequent changes of objectives for various sample conditions and

dimensions. Based on the optical principle of SPIM, we have developed a tunable c-LSFM system for multi-scale and rapid cardiac light-sheet imaging.

When imaging a large sized cardiac structure, such as the neonate mouse heart, the raw LSFM data obtained under a low magnification and a large field-of-view setting were subject to significant image blurring caused by (1) limited optical power (the small N.A. of the detection objective and thick illuminating light-sheet), and (2) insufficient digital readout (under-sampling from the camera). This image blurring generated an unsatisfactory resolution to distinguish the fine cellular structures. To address this issue, we implemented a step-by-step image processing to recover the 3-D sacrificed spatial resolution over the entire volume-of-view. To reduce the information loss from under-sampling, we performed 4 to 8 times over-scanning (the step size is 4-8 times smaller than the light-sheet thickness) along the axial direction during image acquisition, followed by scaling up the obtained 3-D image by 2- to 4-times at lateral direction using b-spline interpolation. To further de-blur the image and to substantially enhance the resolution, we deconvolved the pre-processed 3-D image with the measured 3-D point-spread-function of the optical system (that was interpolated to the same voxel spacing with the image data). The iterative 3-D deconvolution was run on the ImageJ platform using its "parallel iterative deconvolution" plugin, and "3-D iterative deconvolution" module. We chose the MRNSD (Modified Residual Norm Steepest Descent) or WPL (Wiener Filter Preconditioned Landweber) option, both of which are non-negatively constrained algorithms, with appropriate preconditioning parameters to solve the final resolution-enhanced output. During computation, we set the max number of iteration (e.g., 50) and mean delta threshold (e.g., 0.01) to determine the convergence. In most cases, the 3-D deconvolution could be completed within 20 iterations. We further provided image dataset prior to and post 4-D synchronization algorithm. Prior to synchronization, image dataset from $Z_1$, $Z_2$ $Z_3$, and $Z_4$ at same time point are in a different cardiac cycle. However, post 4-D synchronization, $Z_1$, $Z_2$ $Z_3$, and $Z_4$ are synchronized at same time point **(Fig. S5)**. Therefore, 3-D images at each

time point permitted analysis of cardiac mechanics based on time-dependent volume changes **(Table S1)**.

While the 4-D synchronized beating zebrafish heart was reported (Mickoleit, *et al*. "High-resolution reconstruction of the beating zebrafish heart." *Nature Methods* (2014)), we performed additional 4-D functional analysis of cardiac mechanics by time-dependent 3-D volume change based on our resolution enhancement algorithm; thereby, uncovering 4-D *in vivo* physiological parameters, including end-diastolic volume, end-systolic volume, stoke volume, ventricular ejection fraction, heart rate, and cardiac output. We have added the detailed analyses of cardiac mechanics derived from c-LSFM imaging in **Table S1**.

In addition, we applied retrospective synchronization algorithms and resolution-enhancement post-processing to the raw c-LSFM datasets to enhance spatial and temporal resolution. Our c-LSFM system is capable of capturing the beating embryonic zebrafish (3-D space + time) and meso-scale neonate mouse hearts. While the current cardiac cycle synchronization and spatial resolution enhancement algorithms were separately implemented to the beating and isolated hearts, we anticipate further resolution enhancement in 4-D images by fusion of these two algorithms in future investigations.

Unlike the transparent zebrafish embryos, light-sheet imaging of adult zebrafish and neonatal mouse hearts entails significant light scattering due to large size and non-homogeneous samples. The current approach to visualize completely opaque hearts is to perform cryostat sectioning, followed by confocal scanning which necessitates manual and precise sectioning of the samples. The sectioned slices need to be placed on microscopy glass slides for individual imaging over several hours of neonatal mouse samples, and the individually acquired images need to be 'stitched' together. In this context, the use of confocal microscopy is theoretically feasible to

generate 3-D and high-resolution architecture; however, the sample preparation, acquisition time, and data processing warrant a rapid and multi-scale light-sheet strategy for both living embryos and large-sized samples. Without sectioning mid-size samples such as the 120 dpf adult zebrafish heart, c-LSFM provides superior axial resolution on visualizing the cardiac trabecular network that is not able to be clearly discerned by confocal axially **(Fig. S6)**. Besides the advantage of better axial resolution for imaging large samples, c-LSFM further shows outstanding acquisition speed advantages of plane illumination over confocal's point scan. In our control experiment, the acquisition rate of c-LSFM is ~209 mega pixels per second (8 s for 2048*2048*400 volumetric image) *versus* 0.19 mega pixels per second of confocal (1800 s for 1024*1024*322 volumetric image). Along with the high scanning speed, the c-LSFM also has high fluorescence detection efficiency which is over 90%, due to its wide-field detection. In contrast, confocal blocks most of the excited fluorescence for out-of-focus planes (95-97% under 1 Airy unit) and thus has a very poor detection efficiency as well as higher rate of photo-bleaching.

We have further minimized optical scattering which commonly occurs in myocardial imaging. In addition to applying tissue clearing, we performed rapid plane-by-plane scanning to attenuate photo-bleaching. Following pre-processing and re-construction with both image analysis software and our post-processing algorithms, the acquired series of virtual sections (as opposed to the manually sectioned heart slices by the confocal approach) have allowed for precise 3-D re-construction of the cardiac structures. In particular, internal anatomic cardiac structures, such as valves and trabeculation, are clearly visualized. Similar to the fluorescence microscopy techniques, sub-cellular organelles of interest may be labeled prior to sacrificing the animals (e.g. transgenic zebrafish lines with green fluorescent protein-labeled *cmlc*) or may be targeted by fluorophore-labeled antibodies to specific epitopes. Intrinsically occurring auto-fluorescence from elastin and/or collagen as well as NADPH (nicotinamide adenine dinucleotide phosphate) in cardiomyocytes may bypass the need for fluorescent labeling. Despite optical clearing with

BABB, streaking artifacts can remain from local absorption or scattering of the non-homogeneous sample **(Fig. 5a)**. The streaking artifacts can be eliminated by incorporating bilateral even plane illumination to engender a thinner pivoting light sheet[24]. Thus, our c-LSFM is capable of performing optical sectioning in an intact heart for 3-D visualization and analysis of a structure of interest from various views.

Adaptive optics may be considered to enhance our c-LSFM system. Adaptive optics was first derived from Astronomy to rectify the light paths that are scattered by the atmosphere into a clear image, and has been widely used in biological imaging for recovering the signals from severely scattered tissues. Several techniques, such as Optical Phase Conjugation, Digital Optical Phase Conjugation, Wavefront Reversion, have been invented to refocus the scattered light for deep tissue penetration. The adaptive optics is designed to address the turbid medium in which the vast majority of components are beyond the ballistic regime. In our work, the zebrafish embryo heart is highly transparent without significant scattering observed. Both the adult zebrafish and neonatal mouse hearts are opaque. To visualize ultra-structures such as valves and trabecular formation, we chemically cleared the heart samples, rendering them transparent for laser penetration into the entire tissue and for fluorescent signal collection without scattering. Thus, our focus is to establish the application of LSFM for visualizing both anatomy and function/physiology of transparent and scattering-free cardiac samples with high spatial-temporal and depth resolution.

Using the c-LSFM strategy, we observed that doxorubicin treatment, an anthracycline class of chemotherapeutic agent, induced an enlarged ventricular cavity but cardiac hypertrabeculation in an attempt to provide oxygenation and nutrition to the myocardium for maintenance of cardiac contractile function[21]. Besides the adult zebrafish hearts, our c-LSFM has further provided the axial resolution to elucidate the 3-D helical architecture of cardiomyocytes in association with the

programmed perinatal changes of cardiac mechanics for coordinated cardiac contractile function[25]. Cardiomyocyte architecture has been visualized by 3-D fiber tracking and quantified by measuring helix angle via diffusion-weighted magnetic resonance imaging (MRI) in fetal, neonatal, and adult pig hearts[26]. The helical architecture of cardiomyocytes was observed as early as the mid-gestational period, and postnatal changes of cardiomyocyte architecture were observed from postnatal day 1 to 14 in the septum and right ventricular free wall[26]. The transmural gradient of cardiomyocyte orientation undergoes progressive changes during cardiac development in response to mechanical workload[27]. Superior to the contrast-enhanced microcomputed tomography (micro-CT) imaging[7], our c-LSFM elucidated the distinct orientation of cardiomyocyte fibers, muscular ridges and trabeculation in the left atrial appendage, as well as papillary muscle in the left ventricle **(Fig. 6)**[28]. Thus, a c-LSFM strategy opens a new avenue to unravel functional and structural phenotypes in genetically engineered mouse models otherwise challenging with micro-CT or fetal echocardiography[29], to elucidate lineage tracing of cardiomyocyte blasts[30] and patterns of mesenchymal-endothelial transition for neovascularization[31].

**FIGURES**
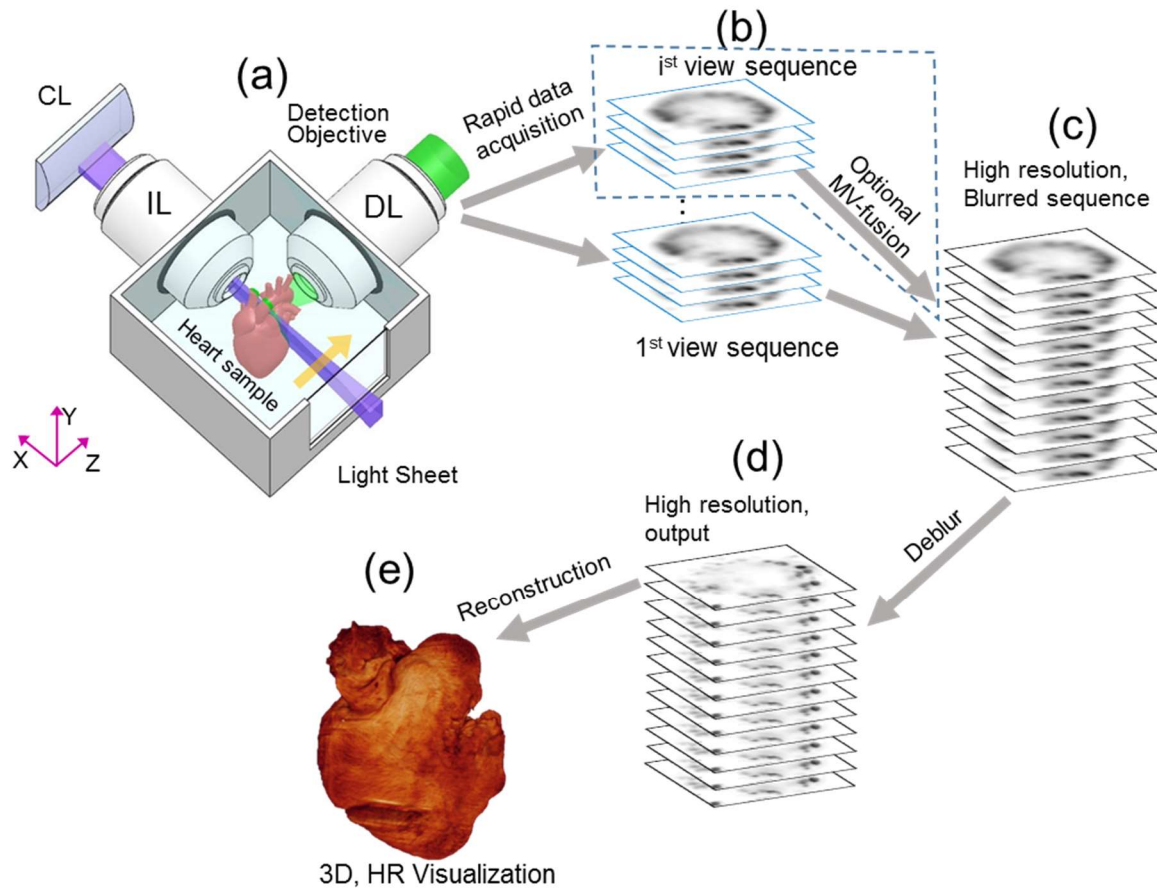


**Figure 1**.  Implementation of cardiac Light-Sheet Fluorescence Microscopy (LSFM).

(**a**) The optical setting of LSFM.  A laser beam (purple) is collected and focused by the beam expander to optimize the beam size.  A cylindrical lens (CL) converts the laser beam to a sheet of laser light to illuminate a thin layer of the sample.  The sample is mounted at the intersection of the illumination lens (IL) and detection lens (DL).  The illuminated 2-D layer (fluorescent detection in green) is captured by the high-frame rate CMOS camera.  The illumination axis is orthogonal to the detection axis, and the illumination optics is designed to illuminate a very thin volume around the focal plane of the detection objective.  The configurations of light-sheet illumination and fluorescence detection are highly tunable to accommodate for various heart

samples.  (**b**) The plane fluorescent images at different axial (z) depths are sequentially captured by the camera (**c**)-(**d**).  For non-transparent fetal mouse hearts, multi-view (MV) techniques are applied to rotate the samples for multi-view imaging, followed by registering and fusing these views into a 3-D cardiac architecture.  An iterative deconvolution technique is applied to the blurred sequence for high resolution.  (**e**) A digitally reconstructed heart is accomplished by stacking the deconvolved images.
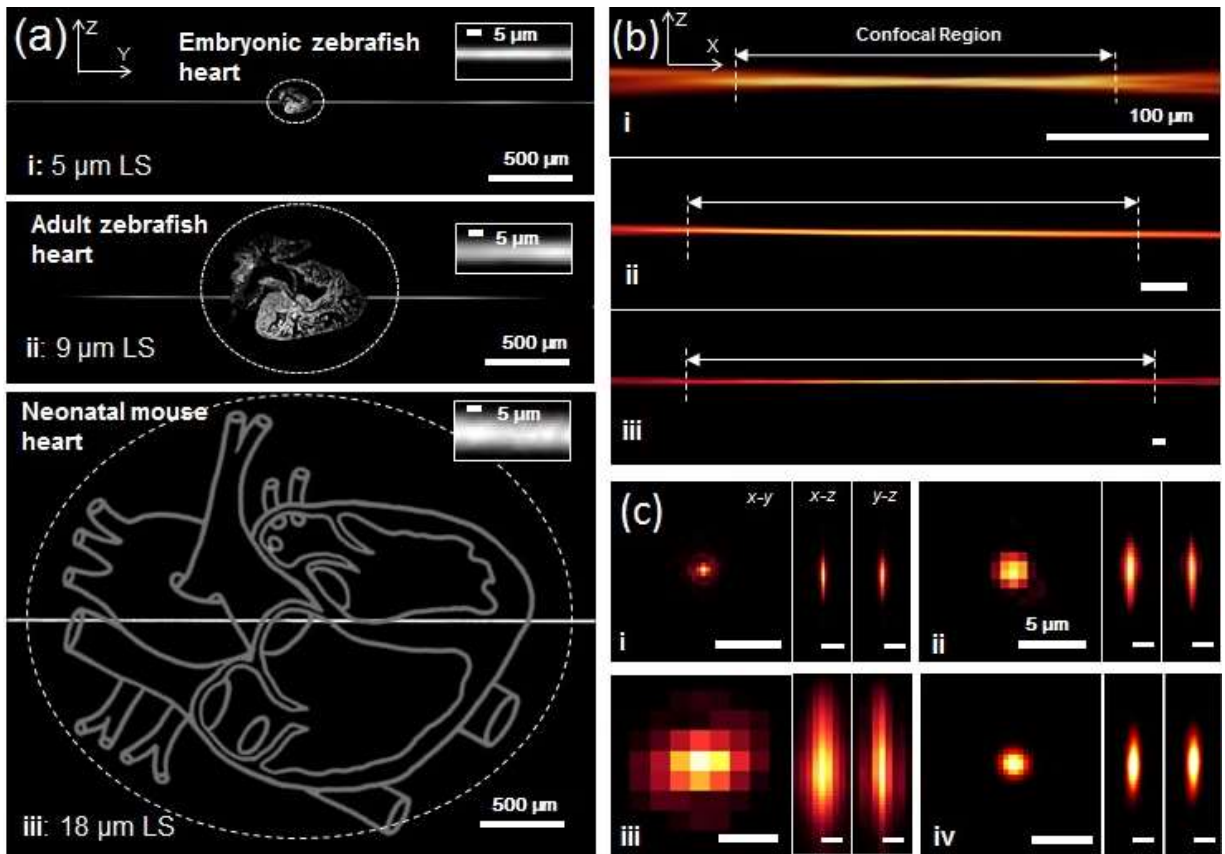
**Figure 2**. Light-sheet profiles for reconstructing cardiac architecture.

**(a)** The axial confinement of the light-sheet (LS) was used for sectioning the (**i**) embryonic zebrafish, (**ii**) adult zebrafish, and (**iii**) neonatal mouse hearts. The small aperture of the slit reduced the beam width to render the waist of laser sheet less focused and wider (shown in the inserts). LS: light sheets. **(b)** The changes in Rayleigh Range corresponded to the area available for light-sheet sectioning. The double-headed arrow line indicates the Rayleigh range (confocal region), in which the light-sheet is considered to be uniform. The scale bars are 100 μm in length for the sub-images in (**i**), (**ii**), and (**iii**). **(c)** Imaging a 400 nm fluorescent bead (sub-resolution point source) was compared with the (**i**) 5μm light-sheet (LS) detected by the 20X/0.5 detection objective (DO), (**ii**) 9 μm LS by 10X/0.3 DO, (**iii**) 18 μm LS by 4X/0.13 DO, and (**iv**) 18 μm LS by 4X/0.13 DO, with resolution enhancement applied. The FWHM extent of image blurring from the point source in the x-y, x-z and y-z plane reflects the lateral and axial resolution.
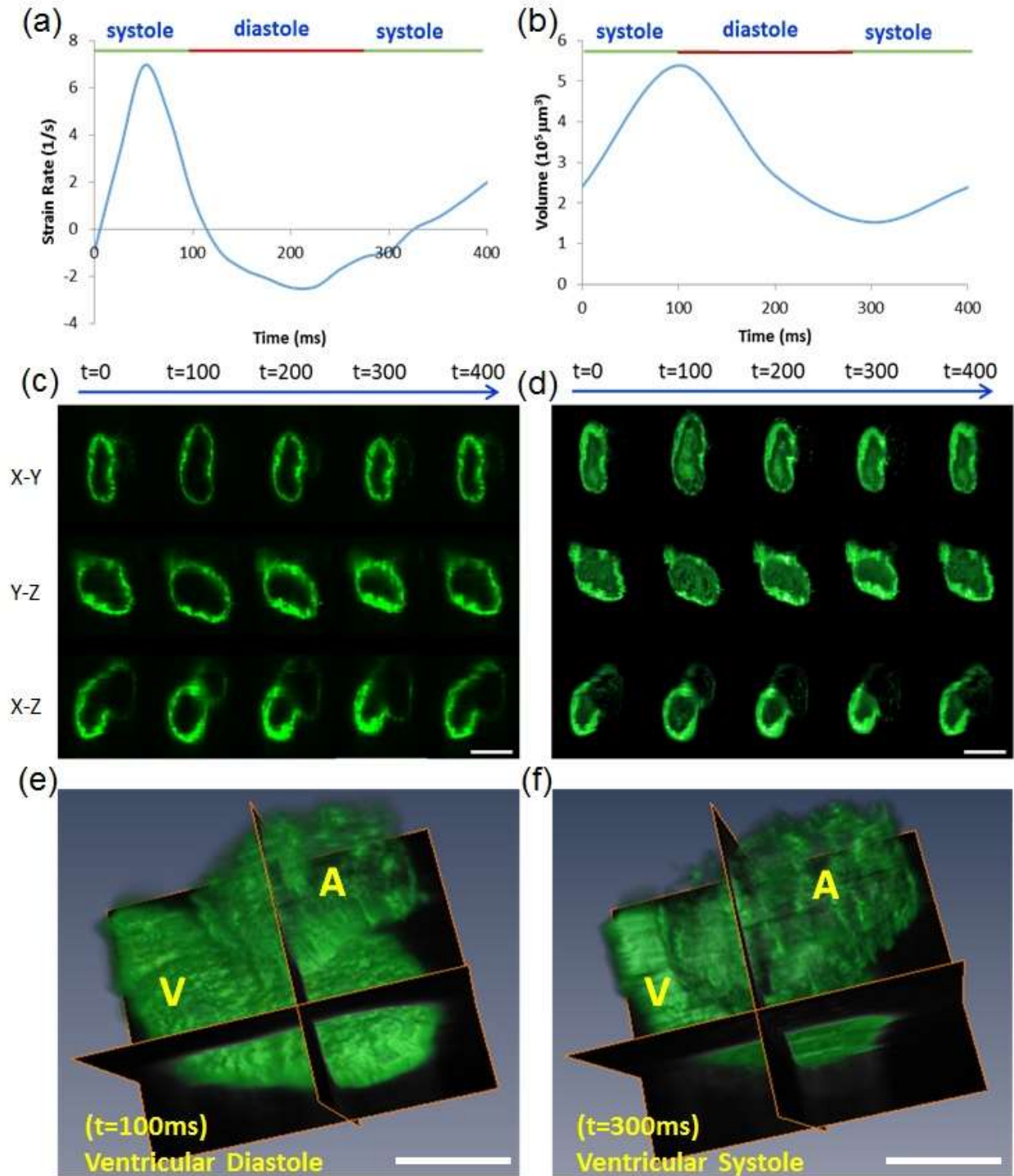
**Figure 3.** 4-D synchronized images to quantify global longitudinal strain rates and volume change of the ventricle at 100 hours post fertilization (hpf).

**(a)** Changes in global longitudinal strain rates were quantified during the entire cardiac cycle. **(b)** The ventricular volume was measured in terms of EDV at $95.4 \times 10^5$ $\mu m^3$ and ESV at $1.5 \times 10^5$ $\mu m^3$, respectively. **(c)** LSFM images captured the zebrafish hearts in the x-y, x-z, and y-z planes during the cardiac cycle. **(d)** 4-D synchronized LSFM-acquired images revealed endocardial trabeculation in the x-y, x-z, and y-z plane during the cardiac cycle. **(e-f)** 4-D zebrafish cardiac motion was captured during ventricular diastole and systole. A: Atrium, V: Ventricle. Scale bar: 50μm.
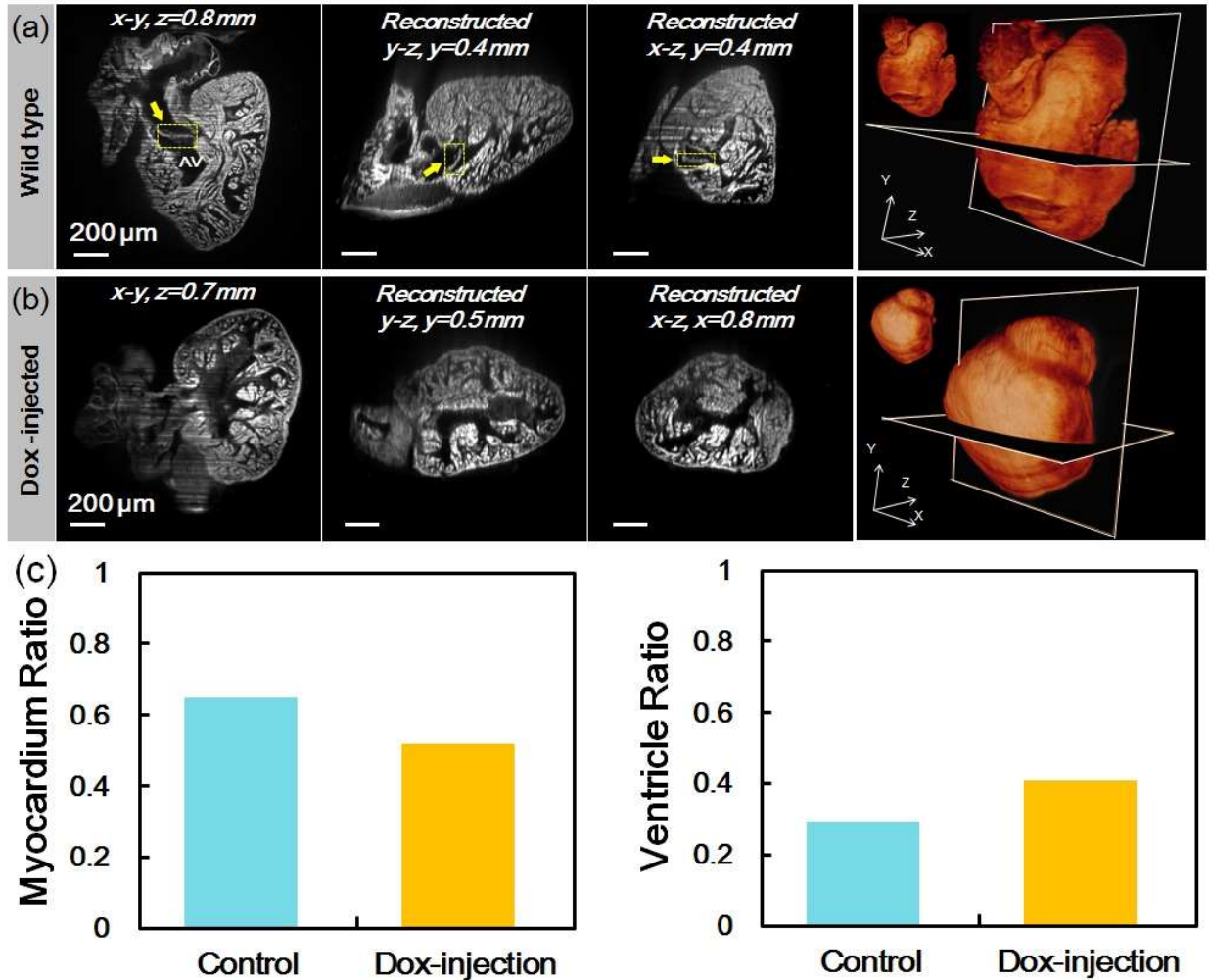
**Figure 4**. Rapid 3-D images to recapitulate trabeculated network in response to doxorubicin (Dox) treatment in the adult zebrafish.

**(a)** A representative wild-type zebrafish heart at 120 dpf. The coronal, sagittal and transverse planes of the heart displayed a compact trabecular network. The atrioventricular valve (AV) was identified (yellow arrows). Scale bars are 200 µm in length. In the rightmost column, a 3-D rendering of the "digital heart" was reconstructed by stacking 500 slices of plane images in volume. The 3-D structure of the "digital heart" can be assessed by arbitrary cropping. **(b)** A representative Dox-injected zebrafish heart at 120 dpf. The endocardial cavity appeared enlarged and the trabecular network was accentuated. **(c)** The quantified volume ratios of the myocardium (left) and the ventricle cavity (right) in the whole heart.

50
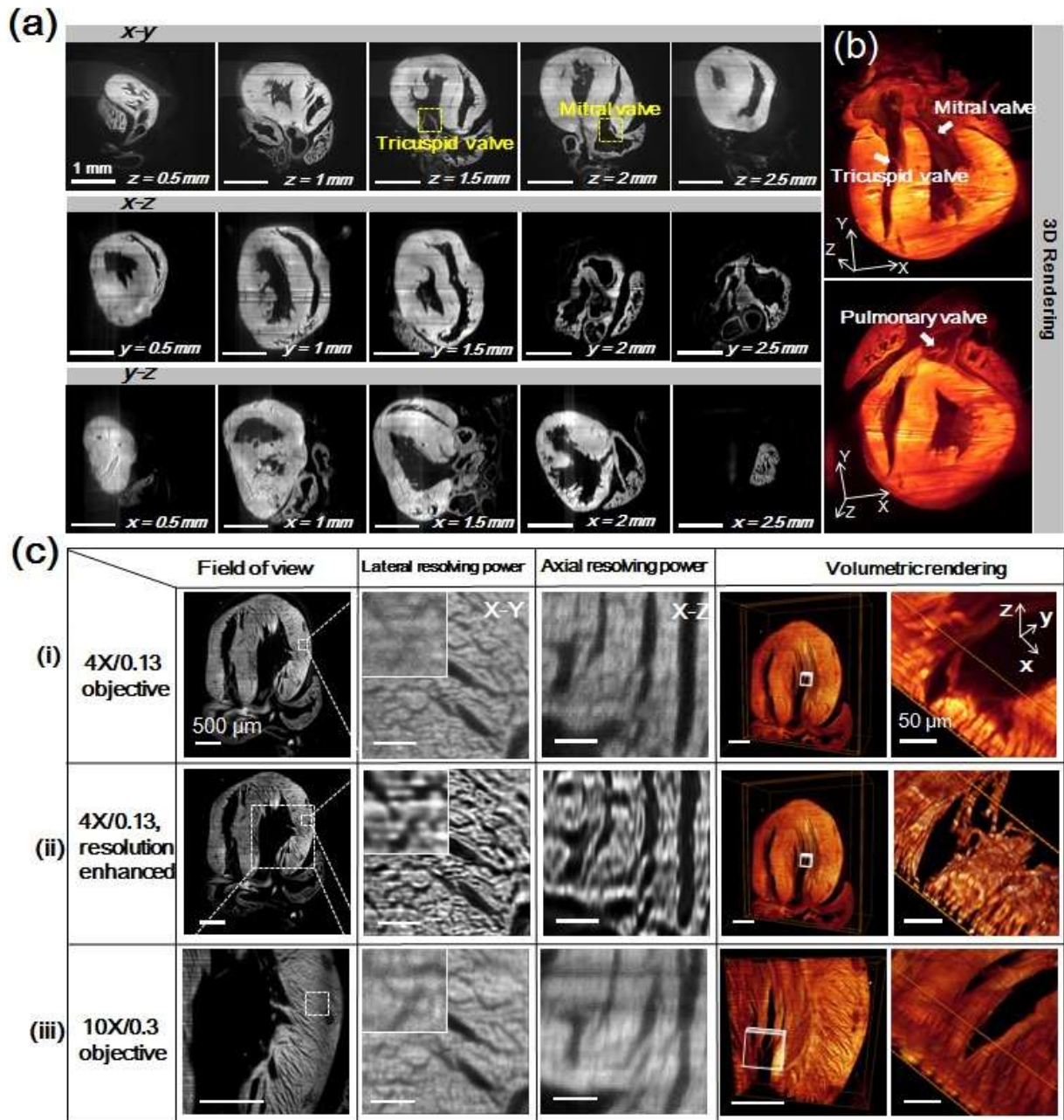
**Figure 5.** Cardiac LSFM (c-LSFM) imaging of a 1-day neonate mouse heart with enhanced cellular resolution.

**(a)** The coronal, sagittal, and transverse planes at different depths uncover 3-D architecture. Scale bars are 1 mm in length in all of the sub-graphs. **(b)** The boxes were cropped from the volume rendering of the reconstructed "digital heart" to reveal the endocardial architecture. **(c)**

The cardiac architecture is compared with the (**i**) 18 μm light-sheet and 4X/0.13 objective, (**ii**) 4x/0.13 resolution enhanced images, and (**iii**) 9 μm light-sheet and 10X/0.3 objective. Magnification from left to right reveals the field of view, lateral, and axial resolving power, followed by the volumetric rendering effects of 3 configurations. Myocardial orientation was resolved in detail in the resolution-enhanced c-LSFM group. All scale bars are 500 μm, except for 50 μm in the rightmost column.
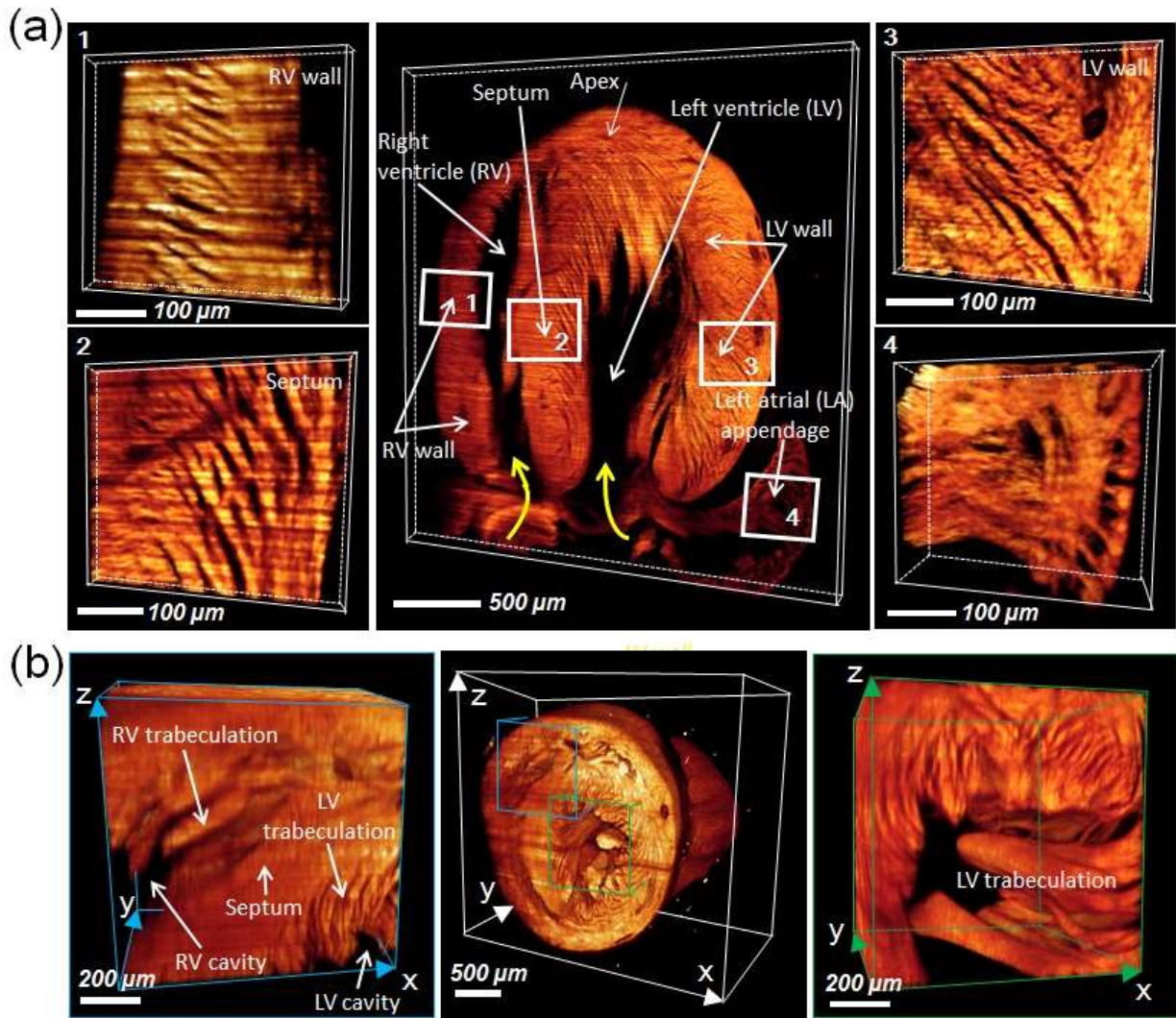
**Figure 6.** High resolution architecture of neonatal mouse hearts.

**(a)** 3-D LSFM revealed the distinct helical organization of individual cardiomyocyte fibers from the right ventricular wall to septum to left ventricular walls (zones 1, 2, and 3), providing insights into the mechanics of ventricular contraction in RV vs. LV. Endocardial structure of the left atrial appendage revealed the muscular ridge and muscular trabeculation (zone 4). The yellow curved arrows indicate the orientation of cardiomyocyte fibers. **(b)** Ultrastructure in the RV (zone 1) and LV cavity (zone 2) unravel trabeculation/papillary muscle (zone 1). LV: left ventricle; RV: right ventricle; LA: left atrium.
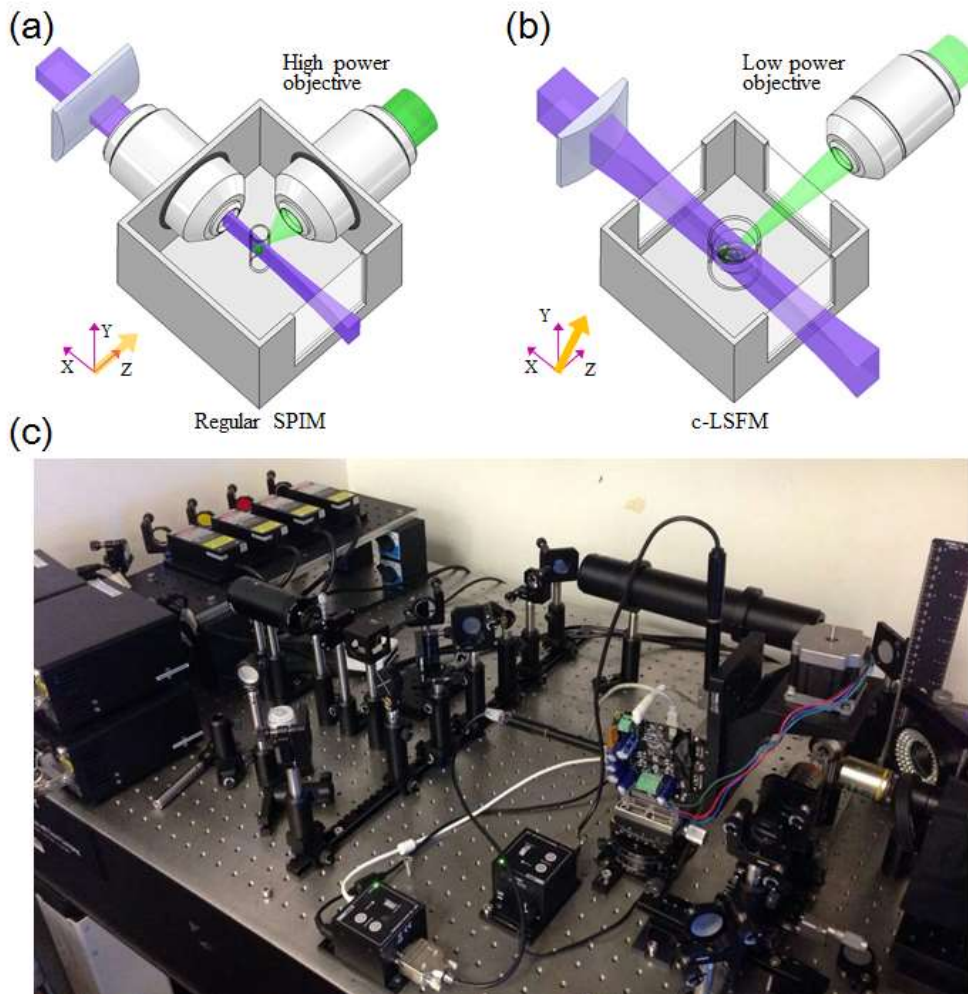
**Figure S1**. The schematic diagram of cardiac-LSFM (c-LSFM) modality.

**(a)** The regular SPIM seals two high power, water immersion lenses into a water chamber, aligning them nearby the small sample, for both illumination and detection.  **(b)** In contrast, the c-LSFM system uses low power, long working distance, air objectives with ample room between the sample and the front pupil of objective.  **(c)** The photograph of the c-LSFM system shows that on one hand, the large sizes of the cardiac structures necessitate a large working space for scanning of entire samples as well as convenience of operation.  On the other hand, the involvement of the resolution enhancement technique substantially decouples the need of high

N.A., water dipping objectives from the high resolution, large space-bandwidth product. Furthermore, eliminating the sealing of the objectives into a water chamber additionally benefits the frequent changes in immersing mediums for different samples.  Therefore, the c-LSFM modality we specially designed is very efficient in performing trans-scale cardiac light sheet imaging conveniently.
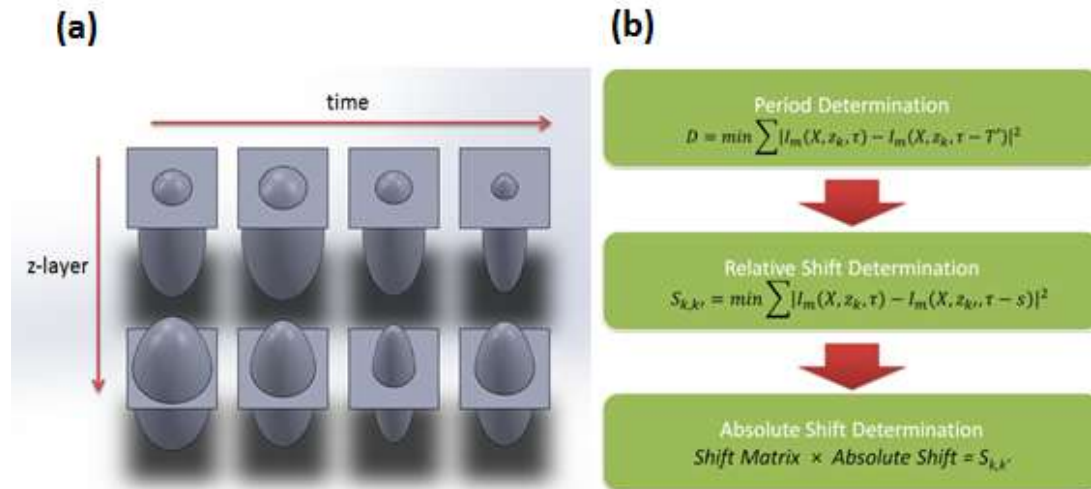
**Figure S2**. 4-D zebrafish beating heart reconstruction methods.

**(a)** When scanning in a single layer, cardiac contraction is time-dependent.  While moving in the z-axis to scan the following z layer, we captured time-dependent contraction images from each layer from top to bottom of the heart.  **(b)** For proper synchronization, heartbeat period was determined by frame.  We iterated through a set of hypothesized periods and back-projected all samples into the first period with respect to the hypotheses.  After back-projection, we compared samples at a same spatial location but from different periods and evaluated each of the period hypotheses.  The best hypotheses were selected accordingly.  Relative shift determination aimed at aligning the starting sample of each individual image sequence.  The heart may not be in the same contraction state at the beginning of all sequences when we start taking images at each z layer.  Starting from a number of relative shift hypotheses, we adopted a quadratic cost function to measure the alignment.  The cost function is calculated via measuring the similarity between two hypothetically aligned images from two adjacent image sequences with respect to the relative shift hypotheses.   By maximizing the alignment, we select the best possible relative shift hypothesis for each image sequence with respect to the other sequences.   Absolute shift determination targeted to obtain the absolute shift of each individual image sequence with respect to the first sequence.  In the previous step, relative shift between any close-by image sequences

are obtained. We recursively calculate relative shift between the current image sequence and an early sequence until obtaining the relative shift with respect to the first image sequence. The above process is applied to every image sequence, and all such processes can be compactly implemented by one matrix multiplication.
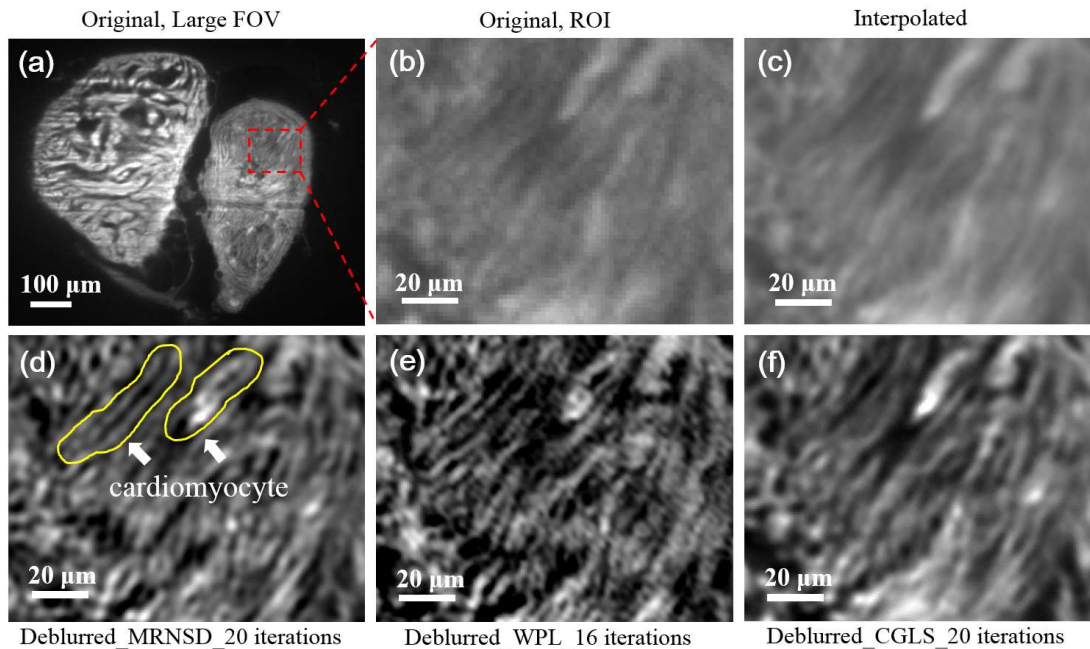
**Figure S3.** Post-image processing of adult zebrafish heart with resolution enhancement by different deconvolution techniques.

(a) Zebrafish atrium and ventricle are visualized on one section of raw image. (b) The individual cardiomyocytes were unresolvable from the selected region-of-interest from the atrium due to the optics blurring and under-sampling by the camera. (c) The image was first scaled up with 3X b-spline interpolation to partially recover the information loss from incomplete sampling. (d), (e) and (f) illustrate the interpolated images deblurred by iterative MRNSD, WPL and CGLS deconvolution, respectively. The WPL algorithm generates most effective deblurring to recover sharp and high frequency signals. However, it also generates image discontinuity, likely due to the application of wiener filter. The CGLS algorithm appears to be mild, generating the least degree of deblurring. Of the three resolution enhancement algorithms, the MRNSD method provides optimal trade-off between the resolution enhancement and information preservation.
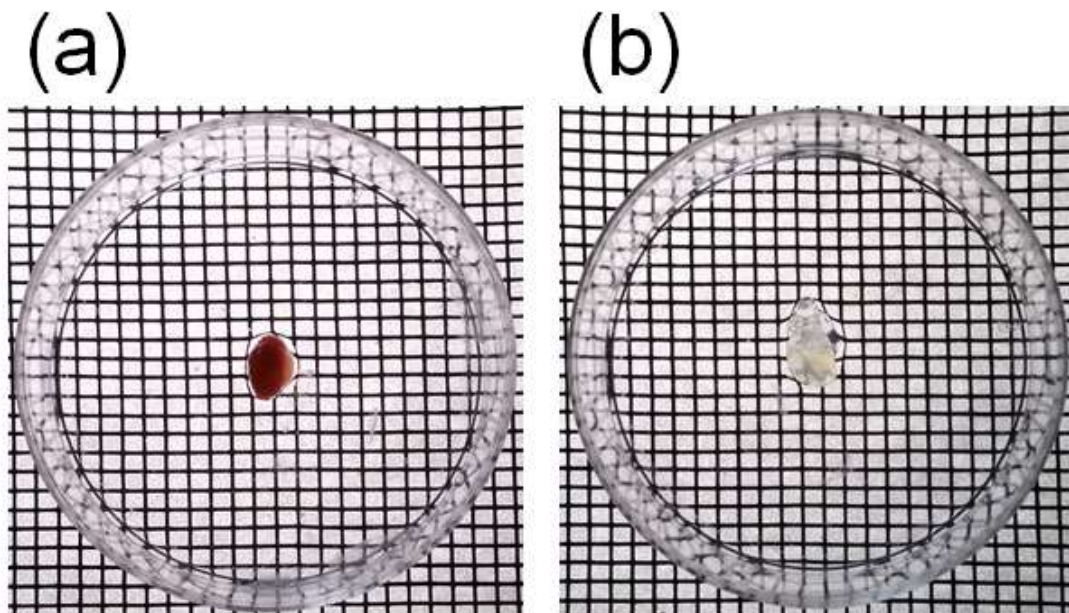
**Figure S4.** The day 1 neonatal mouse hearts before and after BABB clearing.

**(a)** Photograph of the raw isolated hearts. **(b)** Photograph of the cleared heats treated by a rapid BABB clearing. BABB chemical clearing of the tissue is fast and potent. We optically cleared the day 1 neonatal mouse heart with 2 hours serial ethanol dehydration followed by 2 hours benzyl alcohol-benzyl benzoate clearing. Compared to the raw hearts that were completely opaque before clearing **(a)**, the treated hearts showed significantly reduced scattering and became highly translucent on a scale board.
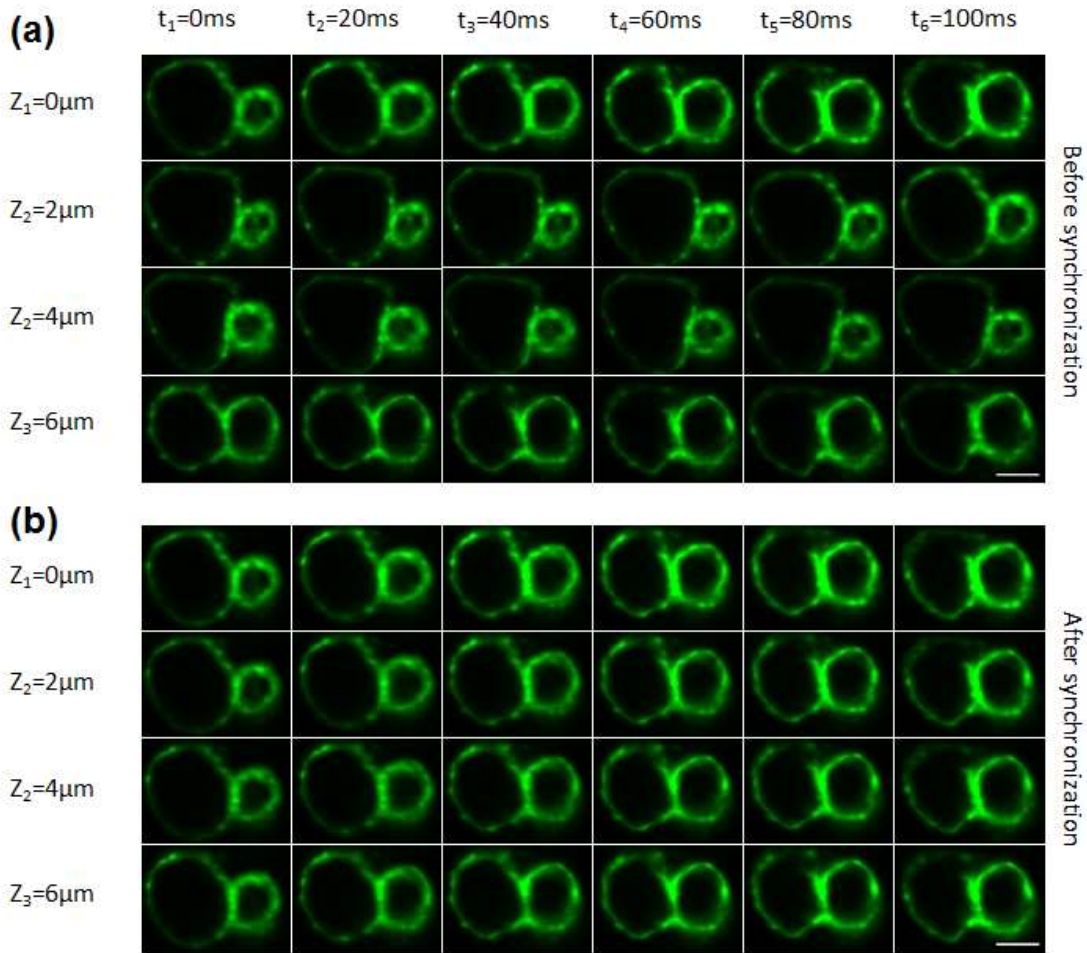
**Figure S5.** Comparison between prior to and post 4-D synchronization algorithm.

(a) Before synchronization, zebrafish cardiac contractions at different Z positions were not in the same stage. (b) After synchronization, all Z positions were synchronized in the same cardiac contraction stage. Therefore, stacked images for 3-D reconstruction at certain time points were obtained and provided volume information. Scale bar = 50$\mu$m.
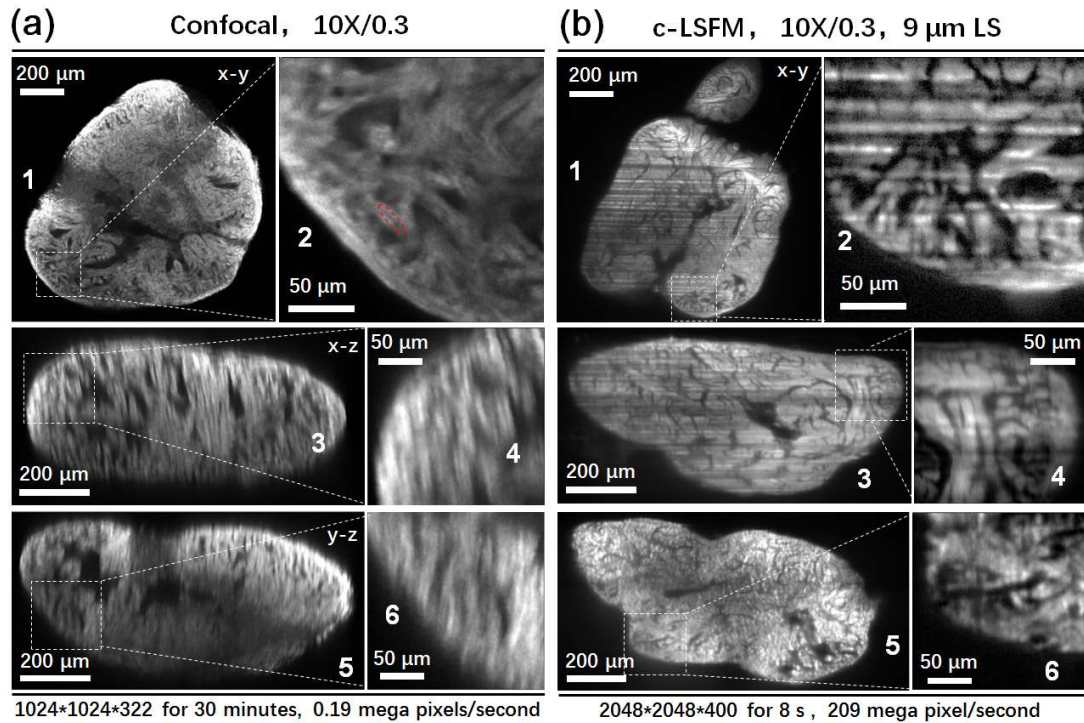
**Figure S6.** Imaging comparison between c-LSFM and confocal microscopy using 120 dpf zebrafish hearts.

(a) The original x-y plane image, reconstructed x-z and y-z plane images obtained from confocal data. (b) The original x-y plane image, reconstructed x-z and y-z plane images obtained from c-LSFM data. The zoomed-in images shown in the right columns (2, 4, 6) indicate the lateral and axial resolving powers of confocal and c-LSFM.

| # of heartbeats | 10 beats | 10 beats | 5 beats | 10 beats | 10 beats |
|---|---|---|---|---|---|
| Z resolution | 2μm | 4μm | 2μm | 2μm | 2μm |
| Frame rate | 50fps | 100fps | 100fps | 100fps | 200fps |
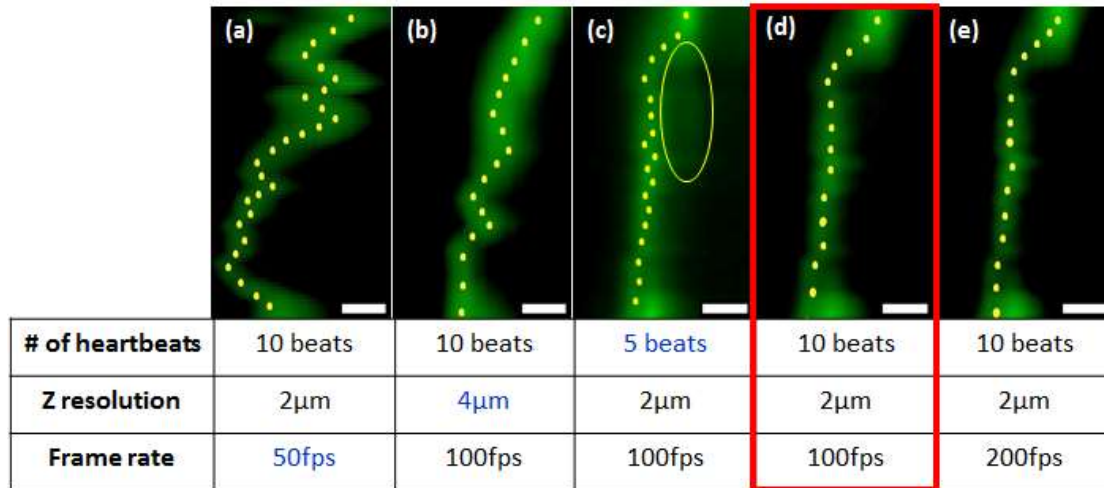
**Figure S7.** Comparison of 4-D synchronized images with a combination of 3 different parameters. (a & b) Both low frame rate and low z resolution were inadequately synchronized. Both images demonstrated a crinkled pattern in the cardiac wall. (c) Reducing the capturing number to 5 heartbeats (cardiac cycles) revealed similar synchronization with capturing 10 beats. However, negligible artifact appeared behind the wall (yellow circle). (d & e) Increasing the frame rate to 200fps revealed identical image quality to that of 100fps. Therefore, we selected (d) as the optimal combination for 4-D synchronized imaging parameters. Scale bar = 10μm.

| | |
|---|---|
| End-Diastolic Volume ($10^5 \mu m^3$) | $5.5 \pm 0.6$ |
| End-Systolic Volume ($10^5 \mu m^3$) | $1.4 \pm 0.5$ |
| Stroke Volume ($10^5 \mu m^3$/beat) | $4.1 \pm 0.5$ |
| Ejection Fraction (%) | $74.5 \pm 5.6$ |
| Heart Rate (bpm) | $164 \pm 20$ |
| Cardiac Output ($10^5 \mu m^3$/min) | $672.4 \pm 15$ |

**Table S1.** Analysis of cardiac mechanics in 4dpf zebrafish from 4-D in vivo imaging.

**REFERENCES**

**1.**      Huang, B., Bates, M. & Zhuang, X. Super-resolution fluorescence microscopy. *Annual review of biochemistry* 78, 993-1016 (2009).

**2.**      Gustafsson, M. G. Surpassing the lateral resolution limit by a factor of two using structured illumination microscopy. *Journal of microscopy* 198, 82-87 (2000).

**3.**      Gustafsson, M. G. Nonlinear structured-illumination microscopy: wide-field fluorescence imaging with theoretically unlimited resolution. *Proceedings of the National Academy of Sciences of the United States of America* 102, 13081-13086 (2005).

**4.**      Yelbuz, T. M., Choma, M. A., Thrane, L., Kirby, M. L. & Izatt, J. A. Optical coherence tomography: a new high-resolution imaging technology to study cardiac development in chick embryos. *Circulation* 106, 2771-2774 (2002).

**5.**      Sharpe, J. *et al.* Optical projection tomography as a tool for 3D microscopy and gene expression studies. *Science* 296, 541-545 (2002).

**6.**      Pampaloni, F., Reynaud, E. G. & Stelzer, E. H. The third dimension bridges the gap between cell culture and live tissue. *Nature reviews. Molecular cell biology* 8, 839-845 (2007).

**7.**      Kim, A. J. *et al.* Microcomputed tomography provides high accuracy congenital heart disease diagnosis in neonatal and fetal mice. *Circulation. Cardiovascular imaging* 6, 551-559 (2013).

**8**.      Baltes, C., Radzwill, N., Bosshard, S., Marek, D. & Rudin, M. Micro MRI of the mouse brain using a novel 400 MHz cryogenic quadrature RF probe. *NMR in biomedicine* 22, 834-842 (2009).

**9**.      Keller, P. J., Schmidt, A. D., Wittbrodt, J. & Stelzer, E. H. Reconstruction of zebrafish early embryonic development by scanned light sheet microscopy. *Science* 322, 1065-1069 (2008).

**10.**      Mickoleit, M. *et al.* High-resolution reconstruction of the beating zebrafish heart. *Nature methods* 11, 919-922 (2014).

**11**.     Scherz, P. J., Huisken, J., Sahai-Hernandez, P. & Stainier, D. Y. High-speed imaging of developing heart valves reveals interplay of morphogenesis and function. *Development* 135, 1179-1187 (2008).

**12**.     Keller, P. J., Schmidt, A. D., Wittbrodt, J. & Stelzer, E. H. Reconstruction of zebrafish early embryonic development by scanned light sheet microscopy. *Science* 322, 1065-1069 (2008).

**13.**     Huisken, J., Swoger, J., Del Bene, F., Wittbrodt, J. & Stelzer, E. H. Optical sectioning deep inside live embryos by selective plane illumination microscopy. *Science* 305, 1007-1009 (2004).

**14**.     Planchon, T. A. *et al.* Rapid three-dimensional isotropic imaging of living cells using Bessel beam plane illumination. *Nature methods* 8, 417-423 (2011).

**15**.     Holekamp, T. F., Turaga, D. & Holy, T. E. Fast three-dimensional fluorescence imaging of activity in neural populations by objective-coupled planar illumination microscopy. *Neuron* 57, 661-672 (2008).

**16**.     Zong, W. *et al.* Large-field high-resolution two-photon digital scanned light-sheet microscopy. *Cell research* 25, 254-257 (2015).

**17**.     Freeman, J. *et al.* Mapping brain activity at scale with cluster computing. *Nature methods* 11, 941-950 (2014).

**18**.     Schmid, B. *et al.* High-speed panoramic light-sheet microscopy reveals global endodermal cell dynamics. *Nature communications* 4, 2207 (2013).

**19**.     Huisken, J. & Stainier, D. Y. Selective plane illumination microscopy techniques in developmental biology. *Development* 136, 1963-1975 (2009).

**20**.     Swoger, J., Verveer, P., Greger, K., Huisken, J. & Stelzer, E. H. Multi-view image fusion improves resolution in three-dimensional microscopy. *Optics express* 15, 8029-8042 (2007).

**21**.     Sedmera, D., Pexieder, T., Vuillemin, M., Thompson, R. P. & Anderson, R. H. Developmental patterning of the myocardium. *The Anatomical record* 258, 319-337 (2000).

**22**.     Huisken, J., Swoger, J., Del Bene, F., Wittbrodt, J. & Stelzer, E. H. Optical sectioning deep inside live embryos by selective plane illumination microscopy. *Science* 305, 1007-1009 (2004).

**23**.    Greger, K., Swoger, J. & Stelzer, E. Basic building units and properties of a fluorescence single plane illumination microscope. *Rev Sci Instrum* 78, 023705 (2007).

**24**.    Huisken, J. & Stainier, D. Y. Even fluorescence excitation by multidirectional selective plane illumination microscopy (mSPIM). *Optics letters* 32, 2608-2610 (2007).

**25.**    Pijnappels, D. A., Gregoire, S. & Wu, S. M. The integrative aspects of cardiac physiology and their implications for cell-based therapy. *Annals of the New York Academy of Sciences* 1188, 7-14 (2010).

**26**.    Zhang, L. *et al.* Cardiomyocyte architectural plasticity in fetal, neonatal, and adult pig hearts delineated with diffusion tensor MRI. *American journal of physiology. Heart and circulatory physiology* 304, H246-252 (2013).

**27**.    Garrido, L., Wedeen, V. J., Kwong, K. K., Spencer, U. M. & Kantor, H. L. Anisotropy of water diffusion in the myocardium of the rat. *Circ Res* **74**, 789-793 (1994).

**28**.    Cabrera, J. A., Ho, S. Y., Climent, V. & Sanchez-Quintana, D. The architecture of the left lateral atrial wall: a particular anatomic region with implications for ablation of atrial fibrillation. *Eur Heart J* 29, 356-362 (2008).

**29.**    Liu, X. *et al.* Interrogating congenital heart defects with noninvasive fetal echocardiography in a mouse forward genetic screen. *Circulation. Cardiovascular imaging* 7, 31-42 (2014).

**30.**    Jain, R. *et al.* HEART DEVELOPMENT. Integration of Bmp and Wnt signaling by Hopx specifies commitment of cardiomyoblasts. *Science* 348, aaa6071 (2015).

**31**.    Ubil, E. *et al.* Mesenchymal-endothelial transition contributes to cardiac neovascularization. *Nature* 514, 585-590 (2014).

**32**.    Shin, J. T. *et al.* Human-zebrafish non-coding conserved elements act in vivo to regulate transcription. *Nucleic acids research* 33, 5437-5445 (2005).

**33**. Kaufmann, A., Mickoleit, M., Weber, M. & Huisken, J. Multilayer mounting enables long-term imaging of zebrafish development in a light sheet microscope. *Development* 139, 3242-3247 (2012).

**34**. Hove, J. R. *et al.* Intracardiac fluid forces are an essential epigenetic factor for embryonic cardiogenesis. *Nature* 421, 172-177 (2003).

**35**. Stoletov, K. *et al.* Vascular lipid accumulation, lipoprotein oxidation, and macrophage lipid uptake in hypercholesterolemic zebrafish. *Circ Res* 104, 952-960 (2009).

**36**. Liebling, M., Forouhar, A. S., Gharib, M., Fraser, S. E. & Dickinson, M. E. Four-dimensional cardiac imaging in living embryos via postacquisition synchronization of nongated slice sequences. *Journal of biomedical optics* 10, 054001 (2005).

**37**. Lee, J. *et al.* Moving domain computational fluid dynamics to interface with an embryonic model of cardiac morphogenesis. *PloS one* 8, e72924 (2013).

**38.** Mayet, J. *et al.* Improvement in midwall myocardial shortening with regression of left ventricular hypertrophy. *Hypertension* 36, 755-759 (2000).

**CHAPTER TWO**

**3-dimensional light-sheet fluorescent microscopy and high-frequency ultrasonic transducers to characterize doxorubicin-induced cardiac injury and regeneration**

Packard R.R.S.*, Beebe T.*, Kang B., Fei P., Ding Y., Jen N., Ma J., Shih Y.-H., Ding Y., Xu X., Hsiai T.K. * Equal contribution

**ABSTRACT**

Anthracyclines such as doxorubicin are a cornerstone of chemotherapeutic strategies in various cancers. Their widespread use, however, is currently limited by anthracycline-induced cardiotoxicity. We propose to incorporate light-sheet fluorescent microscopy and pulsed-wave Doppler ultrasound to unravel the 3D architecture and electromechanical coupling of doxorubicin-induced cardiac injury and regeneration in the adult zebrafish model. 3-month old zebrafish were injected intraperitoneally with doxorubicin (20 $\mu$g/g body weight) followed by imaging at 3, 30, and 60 days post-injection. We observed an initial decrease in myocardial and endocardial cavity volume at day 3, followed by ventricular remodeling and hypertrabeculation at day 30, and normalization at day 60 ($P<0.05$, n=5). Doxorubicin-injected fish developed ventricular diastolic dysfunction evidenced by elevated E/A ratios at day 30, normalizing at day 60 ($P<0.05$, n=11-20). Myocardial performance indexes were also elevated at day 30 in the doxorubicin group, indicating worsening of global cardiac function, followed by normalization at day 60 ($P<0.05$, n=9-19). qRT-PCR to investigate the pathways involved revealed up-regulation of Notch signaling genes, particularly the ligand Jagged1 and target gene HEY2 at days 30 and 60 ($P<0.05$, n=5). Treatment with the γ-secretase inhibitor DAPT to inhibit Notch signaling attenuated restoration of ventricular function, demonstrated by persistence of abnormal E/A ratios and myocardial performance indexes at day 60 ($P<0.05$, n=7-12), thereby implicating Notch pathways in the cardiac regeneration process. Our results suggest that doxorubicin-induced cardiac injury leads to ventricular remodeling, followed by activation of Notch signaling to promote hypertrabeculation and restoration of cardiac function.

**INTRODUCTION**

Cardiotoxicity of chemotherapeutic agents remains an unmet clinical challenge[1] with the most frequent complication remaining cardiomyopathy leading to heart failure[2]. Injured myocardium undergoes apoptosis leading to fibrosis[2,3], whereas zebrafish *(Danio rerio)* possess a capacity to undergo regression in fibrosis and regeneration of myocardium in injured hearts[4]. Despite having a two-chambered heart, the zebrafish cardiac action potential and electrocardiogram (ECG) patterns are similar to those of humans for atrial activation (P-waves), ventricular depolarization (QRS complexes) and repolarization (T-waves)[5,6], thus representing a viable vertebrate model for cardiac injury and repair[4]. In adult zebrafish, regenerating myocardium electrically couples with uninjured myocardium[7], providing a conserved cardiomyopathy model to elucidate the cardioprotective effect of inhibiting target of rapamycin (TOR) signaling in response to doxorubicin (Doxo)-induced cardiotoxicity[8].

To characterize the ultra-structural and functional changes in Doxo-induced cardiomyopathy, we have developed the Light-Sheet Fluorescent Microscope (LSFM) for rapid image acquisition with high spatial resolution and depth penetration. Current routinely used light microscopy techniques such as confocal microscopy are confined to imaging thin and transparent samples[9] with background noise from out-of-focus illumination, limited depth penetration and low axial resolution due to a large depth of field[9]. The advent of LSFM offers deep axial resolution with a large dynamic range of length and time scales, rapid data acquisition and reduced photobleaching via a thin sheet of laser light for selective illumination of the sample in the focal plane of the detection system[9-11]. The application of linear scanning via single plane excitation further allows for a high resolution at low magnification with objective lenses from 1X – 10X[12]. As a result, sub-micron spatial resolution is achieved from a large sample volume (~10 mm$^3$) to provide multi-scale imaging from sub-micron to millimeter scales[12]. In addition to the cost savings compared to high magnification optics, the low magnification lenses allow for a large working distance between the

samples and illuminating/detecting lenses for non-planar imaging of live samples[13]. Thus, cardiac LSFM provides the axial resolution and depth penetration needed to unravel endocardial trabecular networks in response to anthracycline-induced cardiotoxicity[12].

To elucidate electromechanical coupling in the injured and regenerating myocardium, we have integrated micro-electrocardiogram (µECG) with high-frequency pulsed-wave (PW) Doppler to interrogate cardiac hemodynamics[5,14,15]. Synchronizing µECG with PW Doppler signals allowed identification of passive (early [E]-wave velocity) and active (atrial [A]-wave velocity) ventricular filling to determine E/A ratios and monitor ventricular diastolic dysfunction[16]. The PW Doppler signals further enabled us to establish the myocardial performance index by determining ventricular inflow tract isovolumic contraction and relaxation times as well as ejection times[17].

In this context, the paralleled advances of light-sheet fluorescence microscopy and high-frequency ultrasonic transducers unravel the 3D architecture and electromechanical coupling of Doxo-induced cardiac injury and regeneration. Our results suggest that Doxo-induced cardiac injury develops ventricular remodeling, followed by activation of Notch signaling to promote endocardial hypertrabeculation to restore contractile function.

**METHODS**

**Research Design**

All animal studies were performed in compliance with the IACUC protocol approved by the UCLA Office of Animal Research.  Experiments were conducted in adult 3-month old zebrafish **(Fig. 1)**. A one-time 5 $\mu$L injection of doxorubicin (Sigma) at a dose of 20 $\mu$g/g of body weight by intraperitoneal route (Nanofil 10 $\mu$L syringe, 34 gauge beveled needle, World Precision Instruments) or of a control vehicle (Hank's Balanced Salt Solution) was performed at day 0. Previous reports examined the therapeutic window of doxorubicin, establishing severe (> 70%) mortality within 1 week only of treatment at a dose of 50 µg/g of body weight[8].  A dose of 20 $\mu$g/g of body weight on the other hand was demonstrated to produce a more acceptable balance between a robust cardiac phenotype following anthracycline chemotherapy, however in the setting of a much lower mortality of ~30% at day 60[8] which was replicated in the current study. At days 3, 30 and 60 following therapy, zebrafish were analyzed *in vivo* by high-frequency ultrasound or harvested under microscopic guidance, the hearts removed and chemically cleared prior to *ex vivo* light sheet microscopy, or mRNA isolated.

**3D Image Acquisition by Light-Sheet Fluorescent Microscopy**

Imaging was performed using a custom-built light-sheet fluorescent microscope (LSFM) in the Cardiovascular Engineering Laboratory at UCLA.  The workflow of LSFM was characterized by the orthogonal optical paths and multi-dimensional reconstruction of cardiac structures with high spatial resolution **(Fig. 2)**.  The detailed optical setting is based on the Selective Plane Illumination Microscopy (SPIM) imaging modality[18].  In the plane illumination path, the combination of a cylindrical lens (focal length = 50 mm, LJ1695RM-A, Thorlabs) together with a 4X/0.13 objective (Plan Fluor, Nikon) line-focused the collimated laser beam (405 nm, 473 nm, 532 nm and 589 nm) into a hyperbolic light sheet with tunable parameters to illuminate the zebrafish heart **(Fig.**

**2).** Images were captured using a sCMOS (Scientific Complementary Metal Oxide Semiconductor) camera (ORCA Flash 4.0 V2, Hamamatsu). Compared to conventional wide-field microscopy, the plane illumination mode of our system enables high axial resolution imaging without disturbance from out-of-focus fluorescence. Following precise alignment of the LSFM system, a fully automated image acquisition was implemented using a customized LabVIEW program.

**3D Image Processing and Reconstruction**

A spline interpolation and an iterative 3D deconvolution were subsequently applied to the reconstructed image stack to compensate for the under-sampling of camera and remove the image blurs. As a result, a 3D "digital zebrafish heart" was reconstructed in the last step to provide visualized output with high spatiotemporal resolution and high dynamic range. In the present study, we used zebrafish which were cardiac myosin light chain-green fluorescent protein (*cmlc2-gfp*) transgenic to visualize the cardiac ventricle and precisely assess myocardial architectural fate and 3D structural reorganization after chemotherapy. To quantify changes in cardiac volumes of interest, all of the raw data were processed to remove stationary noise, including stripes, by a plugin termed variational stationary noise remover in Fiji[19]. The 3D rendering and image segmentation were processed by Amira 6.1 (FEI Software). 3D endocardial cavity volumes and 3D total heart volumes were measured, and 3D myocardial volumes calculated (myocardial volume = total heart volume – endocardial cavity volume) **(Fig. 3)**.

**Chemical Clearing**

We optimized the benzyl alcohol–benzyl benzoate (BABB, also known as Murray's clear)[20] optical clearing protocol. Following microsurgical isolation, hearts were placed in a phosphate buffered saline 1x solution to remove retained blood, paraformaldehyde 4% for fixation, agarose 1.5% for

embedding, sequential ethanol steps (40% - 60% - 80% - 100%) for dehydration and BABB (with a BA:BB ratio of 1:2) for lipid removal and refractive index matching.

**µECG Acquisition**

The detection of µECG signals was performed via micro-needles (AD Instruments). The sedated fish (in 0.02% Tricaine) were placed in a damp sponge ventral-side-up **(Fig. 4)**. For ECG acquisition, the working electrode was positioned closely above the ventricle between the gills while the reference electrode was placed close to the tail. The signals were amplified 10,000-fold (1700 Differential Amplifier, A-M Systems), and filtered between 0.1 and 500 Hz at a cut-off frequency of 60 Hz. Wavelet transform and thresholding techniques were used to enhance signal-to-noise ratios (Matlab, MathWorks) for the individual ECG recording[5].

**Cardiac Functional Phenotypes via High-Frequency Ultrasonic Transducers**

Sedated fish were secured on a test-bed immersed in diluted Tricaine (0.02%) for 10-15 minutes and placed ventral side facing upward. The array transducer was mounted on a mechanical positioner placed vertically above the ventral side of the zebrafish at a distance of ~6 mm. The µECG electrodes are customized in order to give free access to the array transducer. A trigger signal generated from the ultrasound system is sent to the µECG recording system to synchronize acquisitions. Under the guidance of B-mode imaging, a Doppler gate (window) was positioned downstream from the atrioventricular (AV) valve in the ventricular inflow region to interrogate inflow velocities. The pulse repetition frequency (PRF) for pulsed wave (PW) Doppler was set to 9.5 kHz and the estimated Doppler angle was ~0° given the blood flow of the zebrafish cardiac chambers are in the dorsal-ventral direction. PW Doppler signals were recorded for the control and Doxo groups for ~3 seconds, and stored for further off-line analysis using Matlab[21]. To interrogate cardiac hemodynamics, we applied µECG signals to allow identification of PW Doppler signals of passive (early [E] wave velocity) and active (atrial [A] wave velocity) ventricular filling

74

during diastole **(Fig. 5 a, b)**.  Contrary to these measures which are dependent on the angle $\theta$ of the transducer beam with the flow of blood[22] and hence prone to variability, measurement of various temporal segments of the cardiac cycle are independent of ultrasound signal angulation. These measures – isovolumic contraction time (IVCT), ejection time (ET) across the bulboventricular valve, and isovolumic relaxation time (IVRT) – determine the myocardial performance index (MPI) as follows:  MPI = (IVCT + IVRT) / ET **(Fig. 5 c, d)**[17].  MPI constitutes an integrated measure of systolic and diastolic function, with increases in MPI values indicating a worsening of cardiac function.

## Notch Signaling Following Chemotherapy

Extracted hearts were grinded with RNA lysis buffer, total RNA isolated (Qiagen) and cDNA synthetized.  We tested the involvement of key components of Notch pathways in our cardiomyopathy model:  receptor (Notch 1b), ligands (Delta-like ligand 4, Jagged 1, Jagged 2) and downstream effectors and targets (HEY1, HEY2, and Neuregulin1).  6 zebrafish hearts were pooled for each n with a total of n=5 per condition and per time-point and expression levels determined by quantitative RT-PCR normalized to baseline expressions at day 0 prior to treatment **(Fig. 6a)**.

## Notch Inhibition in Adult Zebrafish

Following Doxo IP injections, adult zebrafish were treated with the γ-secretase inhibitor DAPT (SelleckChem) at 10 µM in fish water overnight for 3 times a week over 60 days **(Fig. 6b)**.  The DAPT solution was made fresh at the beginning of each week and was filtered after each treatment.  Ventricular function was assessed at 3, 30, and 60 days post-injection as described above.

**Statistical Analyses**

All values are expressed as means ± standard errors of the mean. Statistical comparisons between 2 groups were performed using Student's t-test and $P$-values < 0.05 considered significant.

**RESULTS**

**Cardiac light-sheet fluorescent microscopy**

The intact heart was positioned orthogonally between the illumination and detection objectives **(Fig. 2a)** which permits selective plane illumination and fluorescent excitation. Axial images were acquired **(Fig. 2b)** and areas of interest such as endocardial cavity **(Fig. 2c-e)** and total heart volumes **(Fig. 2f-h)** determined with post-imaging 3D reconstructions. The thickness of the light-sheet on the focus is appr. 2 $\mu$m. The orthogonal detection path collected the plane-excited fluorescence signals under a fairly large field-of-view using a 4X/0.13 objective. When the heart scanned through the light-sheet along the z direction, the sCMOS camera located at the terminal end of the detection path simultaneously recorded a stack of 2D plane images along different z depths. The sCMOS camera pixel size is 6.5 $\mu$m x 6.5 $\mu$m. With a 4X objective the pixel size became 6.5/4 = 1.625 $\mu$m x 1.625 $\mu$m. Sequential images were rapidly acquired in a step-wise manner with an incremental size (z-step) of 3 $\mu$m. Furthermore, the high-frame rate of the sCMOS camera (up to 100 frames per second with 2048 x 2048 pixels per image) allowed completion of the entire 3D scanning and data acquisition within tens of seconds. In this study, the exposure time of each image was 20 msec. Our imaging approach allows us to obtain an entire set of raw data in < 15 sec.

**3D ventricular remodeling and hypertrabeculation**

At days 3, 30 and 60 following chemotherapy treatment, control fish developed a thick, homogeneous layer of myocardium **(Fig. 3a)**, whereas Doxo-injected fish developed an initial decrease in both myocardial and endocardial cavity volumes at day 3, followed by ventricular remodeling and hypertrabeculation at day 30 **(Fig. 3b)**, indicated by a significant decrease in the volume occupied by the myocardial layer and conversely a significant increase in the endocardial cavity volume ($P$<0.05, n=5) **(Fig. 3c)**. The ventricular remodeling normalized to the control

configuration at day 60, demonstrating the capability of LSFM to monitor cardiac ultrastructural changes at the 3D level.

## Dynamics of electromechanical coupling

To assess ventricular function in response to Doxo treatment, we synchronized micro-electrocardiogram (µECG) signals with blood flow velocities in zebrafish hearts measured using a high-frequency ultrasound array imaging system with 30 MHz 256-element linear array transducer[14,23,24]. Doxo-injected fish developed worsening of ventricular diastolic function **(Fig. 4)** illustrated by an elevation of E/A ratios at day 30 ($P$<0.05, n=11-20) which normalized at day 60 **(Fig. 5a, b)**. As a corollary, Doxo-treated fish developed an elevated myocardial performance index – an integrated measure of both systolic and diastolic function – indicating worsening of global cardiac function at day 30 ($P$<0.05, n=9-19), followed by normalization at day 60 **(Fig. 5c, d)**. This myocardial performance index normalization supports that zebrafish harbor the regenerative capacity to restore chemo-induced systolic and diastolic dysfunction.

## Doxo-mediated Notch pathway activation

In response to Doxo injection, Notch-related genes were transactivated in adult zebrafish hearts **(Fig. 6a)**. In particular, Jagged 1 and HEY 2 mRNA expressions were up-regulated at days 30 and 60 ($P$<0.05, n=5). This observation implicates Notch pathways underlying cardiac regeneration following Doxo treatment.

## Notch inhibition to attenuate regeneration

To test the role of Notch signaling underlying restoration of ventricular architecture and function, we inhibited the cleavage and release of Notch intracellular domain (NICD) with the γ-secretase inhibitor DAPT following Doxo injection **(Fig. 6b)**. Ventricular diastolic dysfunction as measured by elevated E/A ratios was observed at day 30 similar to the absence of DAPT ($P$<0.01, n=11),

but did not normalize by day 60 (**Fig. 6c**, *P*<0.05, n=7-10).  Similarly, myocardial performance index was elevated at day 30 (*P*<0.01, n=12-14) and remained elevated at day 60 (*P*<0.01, n=8-12), indicating impaired cardiac function persisted through 60 days post-injury **(Fig. 6d)**.  This attenuation of functional recovery implicates Notch signaling as a key mechanism in cardiac regeneration following Doxo-induced injury.

**DISCUSSION**

The present body of work seeks to apply the novel light-sheet imaging and high-frequency ultrasonic transducer to elucidate anthracycline-induced cardiac injury and regeneration in the adult zebrafish model[25]. There currently is a paucity of robust and reproducible imaging tools in the adult zebrafish model for the accurate and quantitative study of cardiac structure and function. Super-resolution microscopes known as light-sheet microscopes or single plane illumination microscopes (SPIM)[11] provide a unique combination of capabilities, including high spatial and temporal resolution, high signal-to-noise-ratio and low level of photobleaching[10]. Whereas initially used almost exclusively in transparent tissues, primarily zebrafish and fly embryos, the advent of chemical clearing techniques have allowed for multi-scale imaging of hearts from zebrafish embryos (hundreds of microns) to adult zebrafish and neonatal mice (several millimeters)[12]. More routinely used animal imaging techniques such as micro-CT (X-ray computerized tomography) have rapid acquisition scans of a few seconds with a spatial resolution as low as 4.6 $\mu m$[26]. Micro-MRI (magnetic resonance imaging) images demonstrate superior soft tissue contrast compared to micro-CT scans, however at the expense of a lower spatial resolution (~60 $\mu m$) and poor temporal resolution (minutes to hours)[27]. Moreover, molecular biomarker-based contrast agent development for micro-CT or -MRI has been proposed[28], but is not routinely available at present. Both micro-CT and micro-MRI are thus limited from tracking fluorescently labeled zebrafish hearts for cardiac injury and regeneration. By contrast, micro-PET (positron emission tomography) imaging systems permit molecular tracking with radiolabeled immunological probes[29,30], however with a spatial resolution of ~1.5 mm that remains insufficient for small structures such as the zebrafish heart[31].

Modern light microscopy techniques have superior spatial resolution with the ability to track fluorescently labeled molecules of interest. Confocal scanning microscopy has a spatial

resolution allowing imaging of intracellular organelles, however insufficient axial resolution, poor

depth penetration, poor temporal resolution, and noticeable photo-damage[11].  Moreover, the 3D

image reconstruction and stitching process is laborious and not amenable to the analysis of a

very large number of samples.  LSFM on the other hand has sub-micron spatial resolution with

deep penetration into tissues, high temporal resolution (a few seconds) and near-real time 3D

image reconstruction[12].  The application of two separate sets of orthogonal lenses for illumination

and fluorescence detection through selective plane excitation via laser light-sheet further reduces

the photon burden to the sample, enhances the image contrast by eliminating out-of-focus

contamination and reducing background noise, and improves the axial resolution under a large

field-of-view[10-12].

In this context, we assessed the effects of Doxo chemotherapy on cardiac 3D architecture by

LSFM, myocardial function by high-frequency ultrasound imaging, and Notch pathway expression

patterns, by determining the time-course and sequence of cardiac recovery and functional

regeneration in adult zebrafish.   Anthracyclines such as Doxo are a cornerstone of

chemotherapeutic strategies in various cancers such as breast cancer, lymphoma, sarcoma and

pediatric leukemia[32].  Their widespread use, however, is currently limited mostly by anthracycline-

induced cardiotoxicity leading to a reduction in optimal dose delivery and duration of treatment in

certain patients[32].

Previously the exclusive domain of developmental biology, the zebrafish is now increasingly used

to provide valuable insights into cardiovascular disease[33] and cancer[34].  Despite having only 1

atrium and 1 ventricle connected by 1 atrioventricular valve, the zebrafish electrocardiogram

patterns are very similar to those observed in humans, with sequential atrial and ventricular

depolarization and repolarization[35].  Importantly, zebrafish hearts have a complete regenerative

capacity following injury[4,16], which is deficient in humans, and may pave the way for novel therapeutic pathways and approaches.

Our LSFM results illustrate Doxo-induced changes in 3D cardiac architecture and remodeling. This was visualized by a decrease in the total myocardial volume and an increase in endocardial cavity volume in the chemotherapy group. We observed peak phenotypes at days 3 and 30 post-chemotherapy with normalization over the subsequent 60-day experimental time-point. Reciprocally, we determined a peak in cardiac trabeculation formation at the 30-day time-points when the heart is responding to acute injury prior to undergoing normalization of its architecture by day 60.

We demonstrated the integration of light-sheet fluorescent microscopy with high-frequency PW Doppler to uncover cardiac architecture and function in response to anthracycline-induced cardiac toxicity followed by the repair and regeneration process in an adult zebrafish model[4,16], with translational implication to chemo-induced cardiomyopathy[25]. We elucidated the hemodynamic and functional phenotypes of Doxo-induced injury via synchronized micro-electrocardiographic and high-frequency ultrasound based interrogation of cardiac ventricular inflow. We assessed a reliable PW Doppler technique to obtain ventricular inflow hemodynamics in zebrafish, similar to those obtained in humans in the Echocardiography lab[14]. Our observations are of physiologic relevance and suggest an adaptation of cardiac function following exposure to the cardiotoxic agent. The progressive restoration of normal cardiac function parallels hypertrabeculation – a feature previously described in zebrafish hearts following surgical amputation[4] or cryo-injury[16].

We assessed Notch signaling as a possible mechanism underlying myocardial repair in response to Doxo-mediated injury. During development, the myocardium differentiates into 2 layers, an outer compact zone and an inner trabeculated zone. Mutations in this genetic program result in

congenital heart defects[36]. Previous studies have revealed the critical role of Notch signaling in the proliferation and differentiation of cardiac trabeculation[36,37]. Notch activation in the endocardial cell results in transcription of ephrin B2 (EPHB2), which in turn regulates neuregulin (NRG1)[36]. As a secreted factor, NRG1 signals to adjacent cells to promote their differentiation into trabecular myocytes. In this context, we determined Notch signaling pathways underlying myocardial repair in response to Doxo treatment and demonstrated enhanced transcriptional expression of Notch ligands (DLL4) and downstream effectors (HEY2). Treatment with the γ-secretase inhibitor DAPT to inhibit the cleavage and release of NICD attenuated myocardial repair following doxorubicin-mediated injury, further corroborating the key role of Notch signaling in this recovery.

In humans, myocardial injury often results in scar tissue formation and loss of ventricular function. Unlike humans, zebrafish have the capacity to replace scar tissue following injury. We interfaced chemical clearing mediated light-sheet fluorescent imaging with high-frequency PW Doppler transducers to study the 3D architecture and cardiac hemodynamics, thereby advancing imaging approaches of Doxo-induced cardiac injury and repair. We observed that following Doxo treatment, the myocardium undergoes a profound remodeling due to chemotherapy induced necrosis and apoptosis leading to cardiac injury[1,2,32]. Doxo treatment initially reduced diastolic and global ventricular function, and we hypothesize that Doxo-induced cardiomyopathy regains contractile and relaxation functions via Notch-mediated trabecular myocyte proliferation to restore cardiac function in an adult zebrafish model of heart regeneration with translational therapeutic implications[38].

**FIGURES**
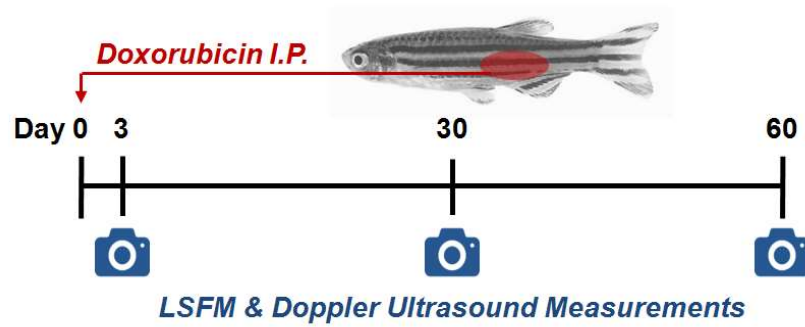


**Figure 1.** Doxorubicin Treatment and Imaging Timeline.

Adult fish were injected with doxorubicin intraperitoneally at day 0, followed by Light-Sheet Fluorescent Microscopy (LSFM) and Doppler ultrasound measurements at 3, 30, and 60 days post-injection.
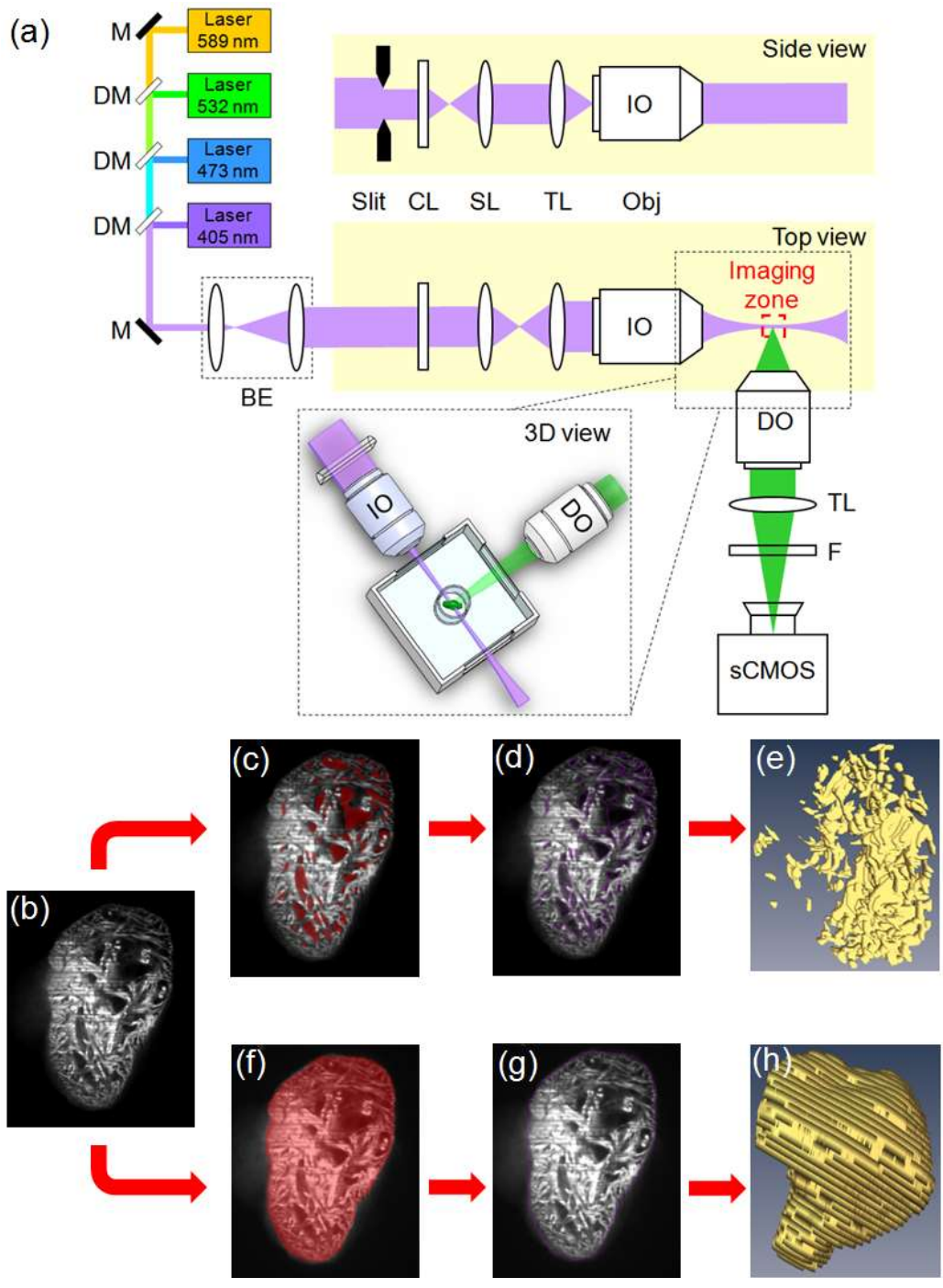
**Figure 2.** Light-Sheet Imaging and 3D Reconstruction.

**(a)** Collimated lasers are transmitted through a line focusing cylindrical lens and an illumination objective (CL+IO), to generate a light-sheet sectioning the sample. The detection arm includes

an objective lens (DO) positioned orthogonally to the illumination path for fluorescence detection. The detection axis needs to exactly conjugate the illuminated plane with the camera CMOS plane. 3D reconstruction was accomplished using a 7-step process. **(b)** Step 1: Axial image – example of 1 of 50 axial images analyzed. **(c)** Step 2: Endocardial cavity identification. **(d)** Step 3: Endocardial cavity segmentation. **(e)** Step 4: 3D endocardial cavity image reconstruction. **(f)** Step 5: total heart volume outer counter delineation. **(g)** Step 6: total heart volume outer contour segmentation. **(h)** Step 7: 3D total heart volume image reconstruction. **Legend.** BE: beam expander. CL: cylindrical lens. DM: dichroic mirror. DO: detection objective. F: filter. IO: illumination objective. M: mirror. Obj: objective. sCMOS: scientific complementary metal oxide semiconductor. SL: scan lens. TL: tube lens.
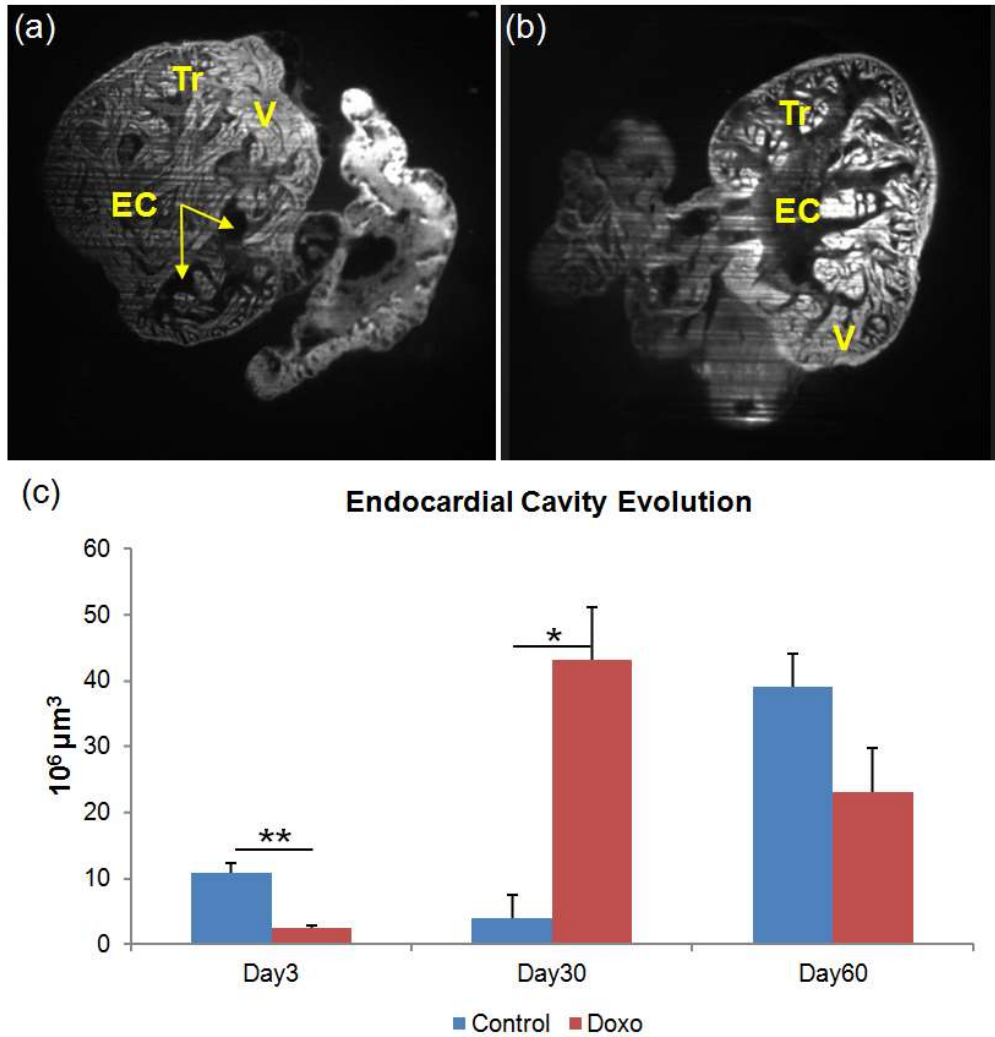
**Figure 3.** Cardiac Architecture Following Doxorubicin Treatment.

Adult zebrafish hearts were harvested at days 3, 30 and 60 following treatment with doxorubicin or control vehicle. **(a)** Control hearts demonstrate preserved architecture with a central cavity surrounded by homogenous, thick ventricular myocardium. **(b)** Doxorubicin-treated hearts demonstrate cardiac remodeling leading to trabeculation formation and relative paucity of myocardium. **(c)** Results demonstrate an initial decrease in heart cavity volume (day 3) following acute cardiac toxicity with loss of myocardial mass (data not shown) followed by cardiac remodeling leading to enlargement of endocardial cavity volume (day 30) with normalization, similar to previously reported cardiac regeneration (day 60). N=5 fish per group and per time-

point.  * *P*<0.05, ** *P*<0.01.  **Legend.**  EC: Endocardial Cavity.  Tr: trabeculation formation.  V: ventricular myocardium.
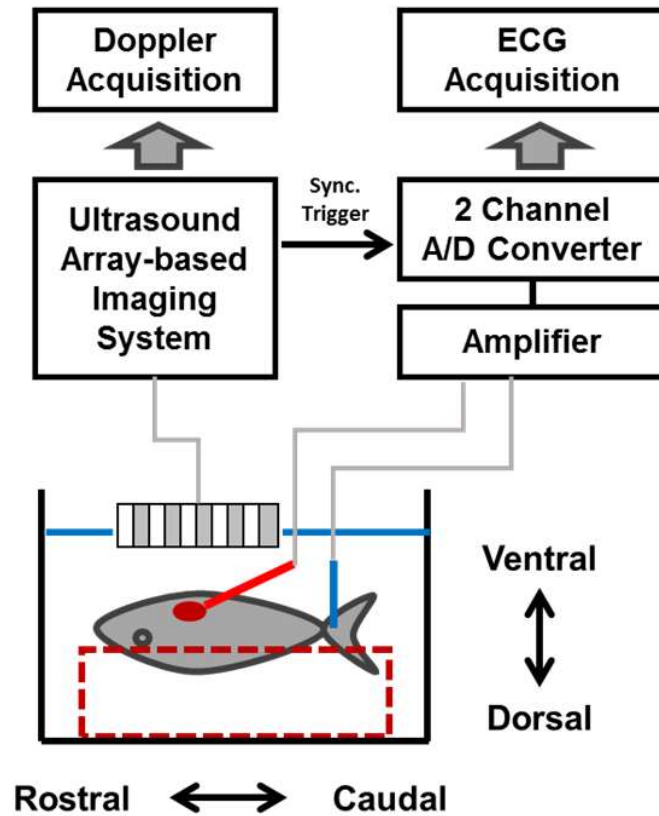
**Figure 4.** High-Frequency Pulsed Wave Doppler Ultrasonic Setup.

Simultaneous measurements of μECG and Doppler signals were obtained *in vivo* in adult

zebrafish hearts. **Legend.** ECG: electrocardiogram. Sync: synchronized.
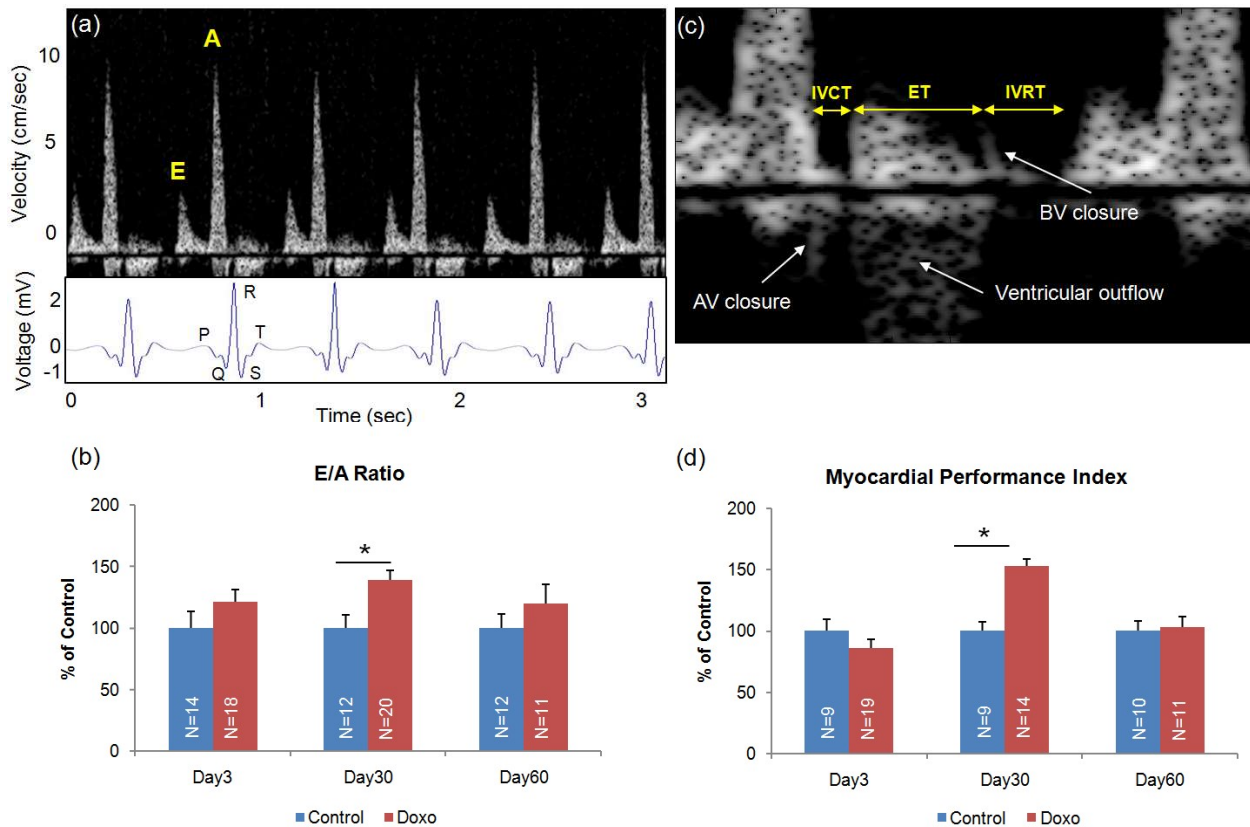
**Figure 5.** Diastolic Function and Myocardial Performance Index (MPI) by Micro-Echocardiography Following Doxorubicin Treatment.

**(a)** ECG signals were co-registered for synchronization with Doppler measurements of ventricular blood inflow. **(b)** E/A wave ratios were measured at days 3, 30 and 60 after treatment with control vehicle or Doxo and normalized to control values. E/A reference ratios in control fish remained constant over time. Following Doxo treatment, there was a rise in E/A ratios at day 30 followed by normalization at day 60. **(c)** Illustration of MPI determination with IVCT, ET and IVRT times. **(d)** MPI parameters were measured at days 3, 30 and 60 after treatment with control vehicle or Doxo and normalized to control values. MPI values in control fish remained constant over time. Following Doxo treatment, there was a rise in MPI at day 30 followed by normalization at day 60. *$P<0.01$. **Legend.** AV: atrioventricular. BV: bulboventricular. ET: ejection time. IVCT: isovolumic contraction time. IVRT: isovolumic relaxation time.
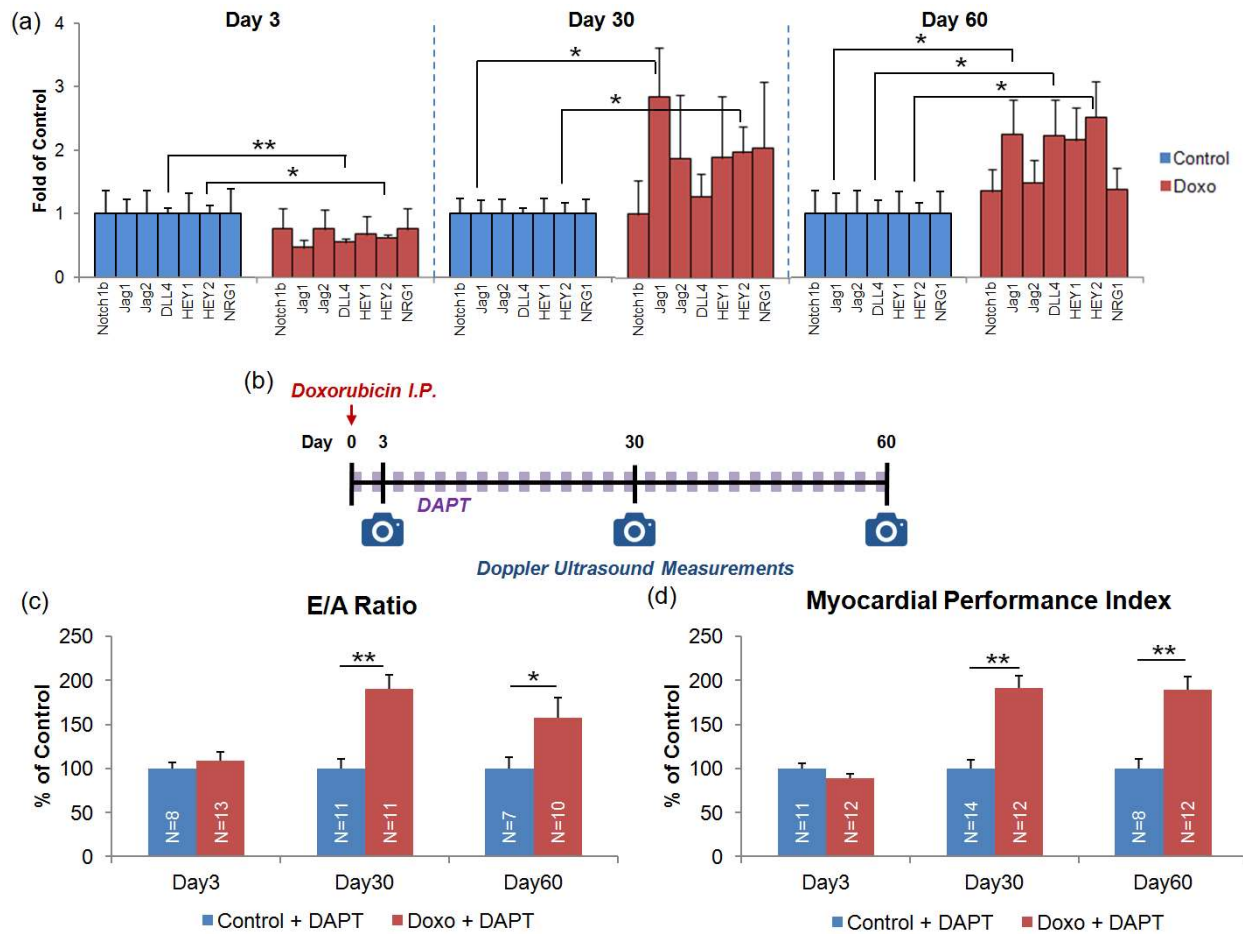
**Figure 6.** Notch Signaling and Doxorubicin Treatment.

6 zebrafish hearts were pooled for each sample with a total of n=5 per condition and per time-point following Doxo or control vehicle injection at days 3, 30 and 60, and mRNA expression levels determined. **(a)** We demonstrate increased expression in the Doxo treated group with statistical significance in the Notch ligand JAG1 and downstream effector Hey2 at day 30 and day 60 and in DLL4 at day 60. Treating zebrafish with 10 µM Notch-signaling-inhibitor DAPT **(b)** following doxorubicin injection inhibited the normalization of **(c)** E/A ratio and **(d)** MPI at day 60 observed in the absence of DAPT. *$P<0.05$, **$P<0.01$. **Legend.** DLL4: Delta-like ligand 4. Jag1: Jagged 1. Jag2: Jagged 2. NRG1: Neuregulin 1.

91

## REFERENCES

1.      Thavendiranathan P, Wintersperger BJ, Flamm SD and Marwick TH. Cardiac MRI in the assessment of cardiac injury and toxicity from cancer chemotherapy: a systematic review. *Circulation Cardiovascular imaging*. 2013;6:1080-91.

2.      Lenneman CG and Sawyer DB. Cardio-Oncology: An Update on Cardiotoxicity of Cancer-Related Treatment. *Circulation research*. 2016;118:1008-20.

3.      Albini A, Pennesi G, Donatelli F, Cammarota R, De Flora S and Noonan DM. Cardiotoxicity of anticancer drugs: the need for cardio-oncology and cardio-oncological prevention. *J Natl Cancer Inst*. 2010;102:14-25.

4.      Poss KD, Wilson LG and Keating MT. Heart regeneration in zebrafish. *Science*. 2002;298:2188-90.

5.      Sun P, Zhang Y, Yu F, Parks E, Lyman A, Wu Q, Ai L, Hu CH, Zhou Q, Shung K, Lien CL and Hsiai TK. Micro-electrocardiograms to study post-ventricular amputation of zebrafish heart. *Ann Biomed Eng*. 2009;37:890-901.

6.      Zhang X, Beebe T, Jen N, Lee CA, Tai Y and Hsiai TK. Flexible and waterproof micro-sensors to uncover zebrafish circadian rhythms: The next generation of cardiac monitoring for drug screening. *Biosensors & bioelectronics*. 2015;71:150-7.

7.      Kikuchi K, Holdway JE, Werdich AA, Anderson RM, Fang Y, Egnaczyk GF, Evans T, Macrae CA, Stainier DY and Poss KD. Primary contribution to zebrafish heart regeneration by gata4(+) cardiomyocytes. *Nature*. 2010;464:601-5.

8.      Ding Y, Sun X, Huang W, Hoage T, Redfield M, Kushwaha S, Sivasubbu S, Lin X, Ekker S and Xu X. Haploinsufficiency of target of rapamycin attenuates cardiomyopathies in adult zebrafish. *Circulation research*. 2011;109:658-69.

9.      Huisken J, Swoger J, Del Bene F, Wittbrodt J and Stelzer EH. Optical sectioning deep inside live embryos by selective plane illumination microscopy. *Science*. 2004;305:1007-9.

10.     Keller PJ and Dodt HU. Light sheet microscopy of living or cleared specimens. *Curr Opin*

*Neurobiol*. 2012;22:138-43.

**11.** Stelzer EH. Light-sheet fluorescence microscopy for quantitative biology. *Nature methods*. 2014;12:23-6.

**12.** Fei P, Lee J, Packard RR, Sereti KI, Xu H, Ma J, Ding Y, Kang H, Chen H, Sung K, Kulkarni R, Ardehali R, Kuo CC, Xu X, Ho CM and Hsiai TK. Cardiac Light-Sheet Fluorescent Microscopy for Multi-Scale and Rapid Imaging of Architecture and Function. *Scientific reports*. 2016;6:22489.

**13.** Lee J, Fei P, Packard RR, Kang H, Xu H, Baek KI, Jen N, Chen J, Yen H, Kuo CJ, Chi NC, Ho CM, Li R and Hsiai TK. 4-Dimensional light-sheet microscopy to elucidate shear stress modulation of cardiac trabeculation. *The Journal of clinical investigation*. 2016;126:1679-90.

**14.** Sun L, Lien CL, Xu X and Shung KK. In vivo cardiac imaging of adult zebrafish using high frequency ultrasound (45-75 MHz). *Ultrasound Med Biol*. 2008;34:31-9.

**15.** Yu F, Li R, Parks E, Takabe W and Hsiai TK. Electrocardiogram signals to assess zebrafish heart regeneration: implication of long QT intervals. *Ann Biomed Eng*. 2010;38:2346-57.

**16.** Lee J, Cao H, Kang BJ, Jen N, Yu F, Lee CA, Fei P, Park J, Bohlool S, Lash-Rosenberg L, Shung KK and Hsiai TK. Hemodynamics and ventricular function in a zebrafish model of injury and repair. *Zebrafish*. 2014;11:447-54.

**17.** Tei C, Ling LH, Hodge DO, Bailey KR, Oh JK, Rodeheffer RJ, Tajik AJ and Seward JB. New index of combined systolic and diastolic myocardial performance: a simple and reproducible measure of cardiac function--a study in normals and dilated cardiomyopathy. *J Cardiol*. 1995;26:357-66.

**18.** Greger K, Swoger J and Stelzer EH. Basic building units and properties of a fluorescence single plane illumination microscope. *The Review of scientific instruments*. 2007;78:023705.

**19.** Schindelin J, Arganda-Carreras I, Frise E, Kaynig V, Longair M, Pietzsch T, Preibisch S, Rueden C, Saalfeld S, Schmid B, Tinevez JY, White DJ, Hartenstein V, Eliceiri K, Tomancak P and Cardona A. Fiji: an open-source platform for biological-image analysis. *Nature methods*. 2012;9:676-82.

20.     Dent JA, Polson AG and Klymkowsky MW. A whole-mount immunocytochemical analysis of the expression of the intermediate filament protein vimentin in Xenopus. *Development*. 1989;105:61-74.

21.     Aydin N, Fan L and Evans DH. Quadrature-to-directional format conversion of Doppler signals using digital methods. *Physiol Meas*. 1994;15:181-99.

22.     Nagueh SF, Appleton CP, Gillebert TC, Marino PN, Oh JK, Smiseth OA, Waggoner AD, Flachskampf FA, Pellikka PA and Evangelista A. Recommendations for the evaluation of left ventricular diastolic function by echocardiography. *J Am Soc Echocardiogr*. 2009;22:107-33.

23.     Hu C, Zhang L, Cannata JM, Yen J and Shung KK. Development of a 64 channel ultrasonic high frequency linear array imaging system. *Ultrasonics*. 2011;51:953-9.

24.     Cannata JM, Williams JA, Zhang L, Hu CH and Shung KK. A high-frequency linear ultrasonic array utilizing an interdigitally bonded 2-2 piezo-composite. *IEEE Trans Ultrason Ferroelectr Freq Control*. 2011;58:2202-12.

25.     Kobayashi I, Ono H, Moritomo T, Kano K, Nakanishi T and Suda T. Comparative gene expression analysis of zebrafish and mammals identifies common regulators in hematopoietic stem cells. *Blood*. 2010;115:e1-9.

26.     Smith DB, Bernhardt G, Raine NE, Abel RL, Sykes D, Ahmed F, Pedroso I and Gill RJ. Exploring miniature insect brains using micro-CT scanning techniques. *Scientific reports*. 2016;6.

27.     Baltes C, Radzwill N, Bosshard S, Marek D and Rudin M. Micro MRI of the mouse brain using a novel 400 MHz cryogenic quadrature RF probe. *Nmr Biomed*. 2009;22:834-842.

28.     Zhou Z, Qutaish M, Han Z, Schur RM, Liu Y, Wilson DL and Lu ZR. MRI detection of breast cancer micrometastases with a fibronectin-targeting contrast agent. *Nature communications*. 2015;6:7984.

29.     Wu AM. Antibodies and antimatter: the resurgence of immuno-PET. *Journal of nuclear medicine*. 2009;50:2-5.

30.     Su H, Gorodny N, Gomez LF, Gangadharmath U, Mu F, Chen G, Walsh JC, Szardenings

K, Kolb HC and Tamarappoo B. Noninvasive molecular imaging of apoptosis in a mouse model of anthracycline-induced cardiotoxicity. *Circulation Cardiovascular imaging*. 2015;8:e001952.

**31.** Goertzen AL, Bao QN, Bergeron M, Blankemeyer E, Blinder S, Canadas M, Chatziioannou AF, Dinelle K, Elhami E, Jans HS, Lage E, Lecomte R, Sossi V, Surti S, Tai YC, Vaquero JJ, Vicente E, Williams DA and Laforest R. NEMA NU 4-2008 Comparison of Preclinical PET Imaging Systems. *Journal of Nuclear Medicine*. 2012;53:1300-1309.

**32.** Vejpongsa P and Yeh ET. Prevention of anthracycline-induced cardiotoxicity: challenges and opportunities. *J Am Coll Cardiol*. 2014;64:938-45.

**33.** Campbell JM, Hartjes KA, Nelson TJ, Xu X and Ekker SC. New and TALENted genome engineering toolbox. *Circulation research*. 2013;113:571-87.

**34.** White R, Rose K and Zon L. Zebrafish cancer: the state of the art and the path forward. *Nat Rev Cancer*. 2013;13:624-36.

**35.** Sedmera D, Reckova M, deAlmeida A, Sedmerova M, Biermann M, Volejnik J, Sarre A, Raddatz E, McCarthy RA, Gourdie RG and Thompson RP. Functional and morphological evidence for a ventricular conduction system in zebrafish and Xenopus hearts. *American journal of physiology Heart and circulatory physiology*. 2003;284:H1152-60.

**36.** High FA and Epstein JA. The multifaceted role of Notch in cardiac development and disease. *Nat Rev Genet*. 2008;9:49-61.

**37.** Zhang W, Chen H, Qu X, Chang CP and Shou W. Molecular mechanism of ventricular trabeculation/compaction and the pathogenesis of the left ventricular noncompaction cardiomyopathy (LVNC). *Am J Med Genet C Semin Med Genet*. 2013;163C:144-56.

**38.** Andersson ER and Lendahl U. Therapeutic modulation of Notch signalling--are we there yet? *Nat Rev Drug Discov*. 2014;13:357-78.

**CHAPTER THREE**


**Blood flow modulation of vascular dynamics**


Lee J.*, Packard R.R.S.*, Hsiai T.K. * Equal contribution

**ABSTRACT**

Blood flow is intimately linked with cardiovascular development, repair, and dysfunction. The current review will build on the fluid mechanical principle underlying hemodynamic shear forces, mechanotransduction, and metabolic effects. Pulsatile flow produces both time- ($\partial\tau/\partial t$) and spatial-varying shear stress ($\partial\tau/\partial x$) to modulate vascular oxidative stress and inflammatory response with pathophysiological significance for atherosclerosis. The characteristics of hemodynamic shear forces; namely, steady laminar ($\partial\tau/\partial t = 0$), pulsatile, (PSS: unidirectional forward flow) and oscillatory shear stress (OSS: bidirectional with a near net 0 forward flow) modulate mechanosignal transduction to influence metabolic effects on vascular endothelial function. Atheroprotective PSS promotes anti-oxidant, anti-inflammatory, and anti-thrombotic responses, whereas atherogenic OSS induces NADPH oxidase–JNK signaling to increase mitochondrial superoxide production, protein degradation of superoxide dismutase, and post-translational protein modifications of LDL particles in the disturbed flow-exposed regions of vasculature. In the era of tissue regeneration, shear stress has been implicated in re-activation of developmental genes; namely, Wnt and Notch signaling, for vascular development and repair. Blood flow imparts a dynamic continuum from vascular development to atherosclerosis to repair. Augmentation of PSS confers atheroprotection and re-activation of developmental signaling pathways for regeneration.

**INTRODUCTION**

Atherosclerosis is a systemic disease; however, its manifestations tend to be eccentric and focal. Detection of atherosclerotic lesions prone to rupture is of clinical importance in the management of patients for acute heart attack or stroke. In addition to genetic predisposition and epigenetic factors, the pathogenesis is modulated by a combination of biochemical and hemodynamic factors. Hemodynamic force, such as wall shear stress on the endothelial cells, modulates inflammatory and metabolic effects in the vascular system [1]. At the lateral walls of bifurcations, disturbed flow, including oscillatory flow (bidirectional and axially misaligned flow), is considered to be an inducer of oxidative stress favoring the initiation of atherosclerosis, whereas in the medial walls of bifurcations, pulsatile flow (unidirectional and axially aligned flow) down-regulates inflammatory cytokines, adhesion molecules, and oxidative stress [2-4] **(Fig. 1)**. In this review, we focus on how fluid shear stress imparts both metabolic and mechanical effects on vascular endothelial function to influence vascular remodeling with clinical implication in arterial restenosis after angioplasty [5-7].

**Fluid mechanical principle of hemodynamic shear forces**

Fluid shear stress is generated by the frictional force by virtue of the viscosity that acts tangentially on the endoluminal surface. In the case of Couette flow, the fluid is embedded between two parallel plates separated by a displacement H. Shear force is applied to move the upper plate with velocity $U$ while the lower plate is fixed. Shear stress ($\tau$) is defined as the slope of tangential velocity ($du/dy$), and is proportional to the dynamic viscosity ($\mu$).

$$\mu\frac{U}{2H} \approx \mu\frac{du}{dy}|_{y=-H} = \tau$$

At a constant pressure (P) throughout the fluid domain, the equation of fluid motion known as Navier-Stokes equation is defined as follows:

$$\frac{dP}{dx} = 0, \qquad \mu\frac{d^2u}{dy^2} = 0$$

When the upper plate at $y = H$ is moving with velocity $U$ ($U_{top} = U$), and the lower plate at $y = -H$ is fixed ($U_{bottom} = 0$), fluid motion is linearly defined as **(Fig. 2a)**:

$$u = \frac{U}{2}\left(\frac{y}{H} + 1\right)$$

In the case of Poiseuille flow, both the upper and lower plates are fixed. The Navier-Stoke equation for 2-D blood flow at a constant pressure applied throughout the fluid domain is defined as:

$$\frac{dP}{dx} = \text{constant} \neq 0, \qquad \mu\frac{d^2u}{dy^2} = \frac{dP}{dx}$$

The velocity profile is parabolic; that is, the velocity is maximal at the center, and zero at the wall or $y = \pm H$ for the non-slip flow **(Fig. 2b)**.

$$u = \frac{1}{2\mu}\frac{dP}{dx}(y^2 - H^2)$$

In the case of 3-D Poiseuille flow in the blood vessel, fluid shear stress at steady state ($d\tau/dt = 0$) is directly proportional to the flow rate of blood ($Q$) and dynamic viscosity ($\mu$), and inversely proportional to the cube of arterial radius ($R$).

$$\tau = \frac{4\mu Q}{R^3}$$

Therefore, a small change in diameter significantly influences wall shear stress.

Fully developed Poiseuille blood flow seldom occurs in the arterial system due to the non-Newtonian blood flow, in which the dynamic viscosity ($\mu$) is not constant. Branching points in the presence of pulsatile flow prevents fully developed flow. For this reason, disturbed flow, including oscillatory flow, preferentially and geometrically occurs in the lateral wall of branching points **(Fig. 1)**. This atherogenic flow promotes vascular oxidative stress and inflammatory responses to initiate atherosclerosis [8].

**Spatial variations in hemodynamic shear stress**

In the arterial system, the greater aortic curvature and the lateral walls of bifurcating regions are prone to develop endothelial dysfunction **(Fig. 1e)**. Oscillatory shear stress (OSS) in the aortic arch or bifurcation induces oxidative stress via nicotinamide adenine dinucleotide phosphate (NADPH)-oxidase enzyme system production of cytosolic superoxide ($O_2^-$), and up-regulates atherogenic gene expression, including nuclear factor- kB (NF-$\kappa$B)-mediated adhesion molecules and chemokines [9]. In these regions **(Fig. 2c-e)**, the time-averaged shear stress and pressure are relatively low as compared to the straight regions or the greater curvature. As fluid flows from high to lower pressure regions, blood flow tends to divert towards the lower pressured regions where the inertia force retards the fluid motion, giving rise to flow separation known as eddies. Therefore, OSS develops downstream or in the post-stenotic regions, where the time-averaged shear stress is low, promoting inflammatory responses. In contrast, high shear stress develops

upstream in the pre-stenotic regions, where the "shoulder" of the plaque is susceptible to fluid and mechanical mismatch or Von Mises stress to destabilize the plaque and induce rupture [10]. Thus, hemodynamic shear stress is low in post-stenotic but high in pre-stenotic regions [11]. The combination of OSS and low mean shear stress favors atherogenesis, whereas pulsatile and high shear stress confers protection [12]. These combined effects explain why atherosclerotic plaques grow in the shoulder regions, which are also the most inflammatory active and vulnerable to rupture although lesions are most prominent at the throat overlying the necrotic core.  Despite the highest shear force occurring at the narrowing or the throat of stenotic lesions, OSS and low mean shear stress in post-stenotic regions increase the residence time for LDL and favor inflammatory cells, including monocytes, to transmigrate to the subendothelial layer and increase lesion size.

In the throat of stenotic lesions, the high shear stress caused by narrowing of the plaque  presents an opportunity for shear-activated nanotherapeutic thrombolytic agents to treat stenotic plaques [13].  Micro-aggregates of nanoparticles were recapitulated in the mouse model in which tissue plasminogen-coated nanoparticles disintegrate into nano-scale components in response to high fluid shear stress, leading to rapid clot dissolution in a mesenteric injury model to restore blood flow [13]. Although nanotoxicity remains a translational barrier, the integration of nanotherapeutics with hemodynamic shear force presents a promising direction to address post-stenotic lesion growth.

Despite improvement in imaging modalities such as intravascular ultrasound or magnetic resonance angiography to visualize anatomic structures, detecting areas of flow separation or low shear stress in post-stenotic regions remains challenging.   Given the limitations in real-time prediction of rupture-prone regions, Ai *et al.* demonstrated flow reversal in a 3-D eccentric stenotic model by high frequency ultrasonic transducer (45 MHz) [14]. By interfacing

microelectromechanical system (MEMS) thermal sensors with the high-frequency pulsed wave Doppler ultrasound, real-time assessment of changes in fluid shear stress upstream, downstream, and at the throat of the stenosis was validated by both computational fluid dynamics (CFD) codes and the ultrasound-acquired flow profiles. Furthermore, post-stenotic regions are prone to vascular oxidative stress and inflammatory responses, features of clinical relevance [14]. In this context, the advent of micro shear stress sensors holds promise to identify vascular regions of flow reversal with high spatial and temporal resolution [15-17]. In corollary, the application of shear-activated nanotherapeutic particles opens a new area of nanomedicine to address atherosclerotic lesions in the regions of flow separation or reversal when the blood flows though the lesser curvature of the aortic arch or the lateral wall of bifurcations. On the other hand, exercise-augmented pulsatile shear stress (PSS) up-regulates atheroprotective genes, including endothelial nitric oxide synthase (eNOS) [18-22], conferring cardioprotection.

**Shear stress-mediated mechanotransduction**

Shear stress imparts both metabolic and mechanical effects on vascular endothelial cells (EC) [23]. A complex flow profile develops at the arterial bifurcations; namely, flow separation and migrating stagnation points, creating low and oscillating shear stress **(Fig. 2c-e)**. In response to fluid shear stress, transmembrane proteins (including G-protein, Lectin-like oxidized LDL receptor-1 [LOX-1 receptor], Toll-like receptor, and caveolin) [24-26], junctional proteins [27], and subendothelial mechanosensors (integrin) [28] are considered to be the mechano-receptors that transmit shear forces to mechano-signal transduction **(Fig. 3)**. In addition to mechanosensing, EC sense shear stress via deformation of the cell surface which leads to the activation of transmembrane ion channels [29, 30], realignment of endothelial cytoskeleton [31-33], and transmission of intracellular signaling pathways to modulate gene expressions [34-38].

At the lateral walls of bifurcations, disturbed flow, including oscillatory flow is considered to be an inducer of oxidative stress. OSS-activated NADPH oxidase enzyme system promotes superoxide ($O_2\cdot^-$) production. In the presence of superoxide dismutase (SOD), $O_2\cdot^-$ is converted to hydrogen peroxide ($H_2O_2$) and hydroxyl radicals ($\cdot OH$). These two reactive oxygen species (ROS) promote LDL oxidation, NF-κB-mediated adhesion molecule and matrix metalloproteinase (MMP) expression to destabilize atherosclerotic lesions. In parallel, $O_2\cdot^-$ reacts with NO· at a rapid diffusion-limited rate to form peroxynitrite ($ONOO^-$) as a substrate to lipid oxidation and nitrotyrosine formation [3, 6, 39-42]. OSS further up-regulates NADPH oxidase-dependent receptors for advanced glycation endproducts (RAGE) as an inflammatory mediator in diabetes [43]. In contrast, in the medial wall of bifurcations, pulsatile flow (PSS) down-regulates oxidative stress and inflammatory responses, but up-regulates eNOS and antioxidant expression to promote vasodilatory, anti-inflammatory, anti-oxidative and anti-thrombotic properties [2, 44*]. Furthermore, PSS or laminar flow (steady flow at $d\tau/dt = 0$) decreases RAGE expression and attenuates RAGE signaling to inhibit NF-κB translocation to the nuclei [45].

**Shear stress modulation of low density lipoprotein (LDL) post-translational modifications**

The post-translational modifications of LDL particles initiate and modulate the progression of atherosclerosis. Myeloperoxidase (MPO), present in phagocytes such as macrophages, is released in response to oxidative stress and inflammatory responses. MPO produces hypochlorous acid by the reaction of $H_2O_2$ and chloride ions [46]. While this key reaction contributes significantly to the antimicrobial activity of phagocytes [47], a large body of evidence now supports oxidation of LDL by the MPO-$H_2O_2$-chloride system as a harbinger in the development of atherosclerosis [48*].

In addition to cytosolic ROS production, OSS induces mitochondrial $O_2^-$ production [49]. OSS activates NADPH oxidase-ROS-JNK signaling, leading to an increase in mitochondrial $O_2^-$ production [50-52], whereas PSS increases eNOS activities and mitochondrial membrane potential ($\Delta\Psi_m$) accompanied with an increase in Mn-SOD activities [53, 54]. Furthermore, oxLDL activates JNK to promote Mn-SOD ubiquitination and protein degradation [50-52]. Using a targeted proteomic approach, we have gained mechanistic insights into shear-modulated relative ratios of reactive oxygen species (ROS) and reactive nitrogen species (RNS), leading to $ONOO^-$ formation and specific post-translational nitration in the $\alpha$ and $\beta$ helices of the apoB100 protein [53, 55, 56]; namely, $\alpha$-1 ($Tyr^{144}$), $\alpha$-2 ($Tyr^{2524}$), $\beta$-2 ($Tyr^{3295}$), $\alpha$-3 ($Tyr^{4116}$), and $\beta$-2 ($Tyr^{4211}$) [53]. Nitration leads to Apolipoprotein-B100 unfolding, and the modified particles are endocytosed by the scavenger receptors LOX-1, CD36 and SR-A (scavenger receptor-A), further contributing to the progression of atherosclerosis [57]. Similarly, high-performance liquid chromatography analyses of EC exposed to OSS demonstrates increased expression of the catalytic subunits of NADPH oxidase gp91phox or Nox4 with an ensuing increase in $O_2^-$ production [3]. In contrast, pulsatile shear stress (PSS) up-regulates eNOS expression accompanied with NO· production, further conferring an atheroprotective role to attenuate post-translational oxidative and nitrative modifications of LDL particles [3] [40].

**Shear stress regulation of inflammatory cell recruitment**

Oscillatory flow induces up-regulation of adhesion molecules and cytokines, allowing monocyte/endothelial interactions central to atherosclerosis over a dynamic range of shear stress, as demonstrated with high spatial and temporal resolution using micro-electro-mechanical systems (MEMS) sensors [39]. Indeed, EC exposed to low shear stress and flow reversal respond to inflammatory stimuli with increased monocyte binding [58], an effect mediated in part by the endothelial expression of ICAM-1 (intercellular adhesion molecule-1) [59] and release of the

central atherogenic chemokine MCP-1 (monocyte chemoattractant protein-1) [60].

The transcription factor Krüppel-like factor 2 (KLF2) is an atheroprotective molecule induced by statin [61] and resveratrol [62] therapy. Recently, shear stress-induced KLF2 expression has been implicated in regulating endothelial metabolism [44**]. KLF2 is selectively induced in vascular EC exposed to the biomechanics of atheroprotected regions of the vasculature [63, 64]. Laminar shear stress reduced endothelial glycolysis by repressing the expression of phosphofructokinase-2/fructose-2,6-bisphosphatase-3 (PFKFB3) in a KLF2-dependent manner to maintain the quiescent metabolic state of EC and to inhibit angiogenesis. KLF2 further confers anti-inflammatory, anti-thrombotic, and anti-oxidative properties. In response to disturbed flow, particular biochemical stimuli, including cytokines, high glucose, and oxidative stress, KLF2 expression are reduced, resulting in an increase in glycolysis and angiogenesis [65**]. In human carotid arteries, the induction of KLF2 results in the regulation of endothelial transcriptional programs controlling inflammation, thrombosis, vascular tone, and blood vessel development [63]. KLF2, therefore, serves as a mechano-sensitive and athero-protective transcription factor [63]. However, the underlying mechanisms whereby shear stress regulates cellular metabolism, including glycolysis and mitochondrial redox state, to maintain endothelial homeostasis remains to be explored.

**Shear stress regulation of atherothrombosis**

The most common complication of atherosclerosis is fibrous cap rupture leading to plaque thrombosis and clinical manifestation of acute coronary syndromes or stroke. The biomechanical properties of plaque mineralization were recapitulated in *in vitro* or *in silico* models. When cultures of calcifying vascular cells (CVC), a subpopulation of smooth muscle cells that spontaneously mineralize, are subjected to increasing magnitude in pulsatile shear stress, calcification does not increase plaque vulnerability to fluid shear stress, but may contribute a slight stabilization [66].

Destabilization of atherosclerotic plaques occur in the presence of active metabolic states; namely, oxidized lipids and activated MMP are released by macrophages [4]. Disturbed flow or extreme high shear stress also regulates the expression of tissue factor, also known as factor III, to initiate the coagulation cascade following plaque rupture and subsequent thrombotic events [67].

**Shear stress modulation of vascular development and repair**

In the era of stem cell and regenerative medicine, hemodynamic shear stress provides a biomechanical cure to modulate the microenvironment for vascular differentiation and repair. The transcription factor Runx1 (Runt-related transcription factor 1) is a master regulator of hematopoiesis [68]. Hemodynamic shear forces increase the expression of Runx1 in CD41$^+$c-Kit$^+$ hematopoietic progenitor cells, thus augmenting their colony-forming potential [68]. Additionally, shear force-mediated mechanotransduction is implicated in the differentiation of stem cells to EC [69-71], and modulates hematopoietic and multilineage engraftment potential during embryogenesis [72**]. The effects on hematopoiesis are mediated in part by a cascade downstream of wall shear stress to regulate calcium efflux and to activate the prostaglandin E$_2$-cyclic adenosine monophosphate-protein (AMP) kinase A signaling axis [72**].

Steady laminar shear stress was further demonstrated to affect pluripotency, as well as germ specification to the mesodermal, endodermal, and ectodermal lineages, as indicated by gene expression of OCT4, T-BRACHY, AFP, and NES in mouse embryonic cells [73]. OSS induces directional reorganization of F-actin to mediate the fate choice of mesenchymal stem cells (MSCs) through the regulation of the β-catenin/Wnt signaling pathway in a time-dependent manner [74*]. OSS also activates angiopoietin-2 (Ang-2) expression critical to angiogenesis via canonical β-catenin/Wnt signaling in human aortic EC [75*]. Low and disturbed flow patterns up-regulate Notch1 expression in EC with translational implication for arteriovenous identity [76]. Steady shear

stress induces VEGF-Notch signaling pathway to increase expression of the arterial endothelial marker EphrinB2, but down-regulates the venous endothelial marker EphB4 in murine embryonic stem (ES) cells [77]. Thus, the hemodynamic cue in the vascular microenvironment modulates vascular differentiation and proliferation.

**CONCLUSION**

Shear stress imparts both metabolic and mechanical effects on vascular EC, with a clinical implication in the focal and eccentric nature of atherosclerotic plaques. Physiologic shear stress up-regulates vasodilators, antioxidant enzymes, and tissue plasminogen activator (tPA) to confer atheroprotective responses, whereas oscillatory shear stress induces vasoconstriction, growth factors, and adhesion molecules to prime atherogenic responses. PSS increases endothelial mitochondrial membrane potential ($\Delta\Psi_m$) accompanied by a decrease in mitochondrial superoxide production (mtO$_2^-$), whereas OSS oxidized LDL increase mtO$_2^-$ production to promote apoptotic pathways. Recently, shear stress-reactivated developmental Wnt-Ang-2 signaling in mature vascular EC was implicated in vascular formation and repair. Shear stress-activated VEGF-Notch signaling regulates the fate of arteriovenous differentiation. In this context, the spatial ($\partial\tau/\partial x$) and temporal ($\partial\tau/\partial t$) variations in shear stress largely determine the focal nature of vascular oxidative stress and pro-inflammatory states. While sedentary life-style promotes flow separation and disturbed flow, exercise-augmented pulsatile shear stress remains a timeless therapeutic strategy for maintaining endothelial homeostasis.
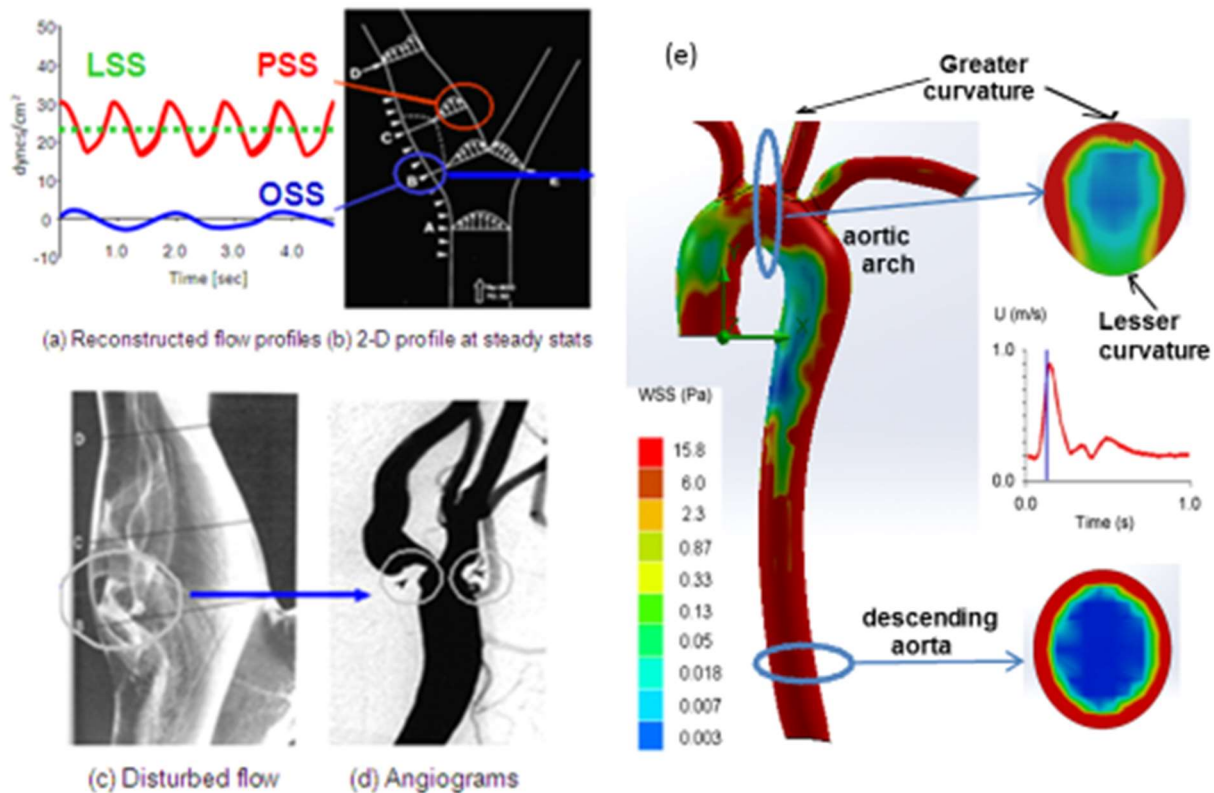
**Figure 1.** (a) Shear stress profiles at the lateral and medial walls of arterial bifurcations. (b) Pulsatile shear stress (PSS) occurs at the medial wall (red circle), whereas oscillating flow (OSS) occurs at the migrating stagnation point of the lateral wall (blue circle). (c) Flow separation and disturbed flow develops at the lateral wall. (d) Angiogram supports the predilection sites for atherosclerosis. (e) Spatial variations in wall shear stress profiles at an instantaneous moment in systole. The magnitude of wall shear stress is relatively high in the ascending aorta, greater curvature, and descending aorta. Cross-section at the aortic arch reveals an eccentric distribution of high shear stress in the greater curvature but low in the lesser curvature. Cross-section from the descending aorta reveals concentric high shear stress.
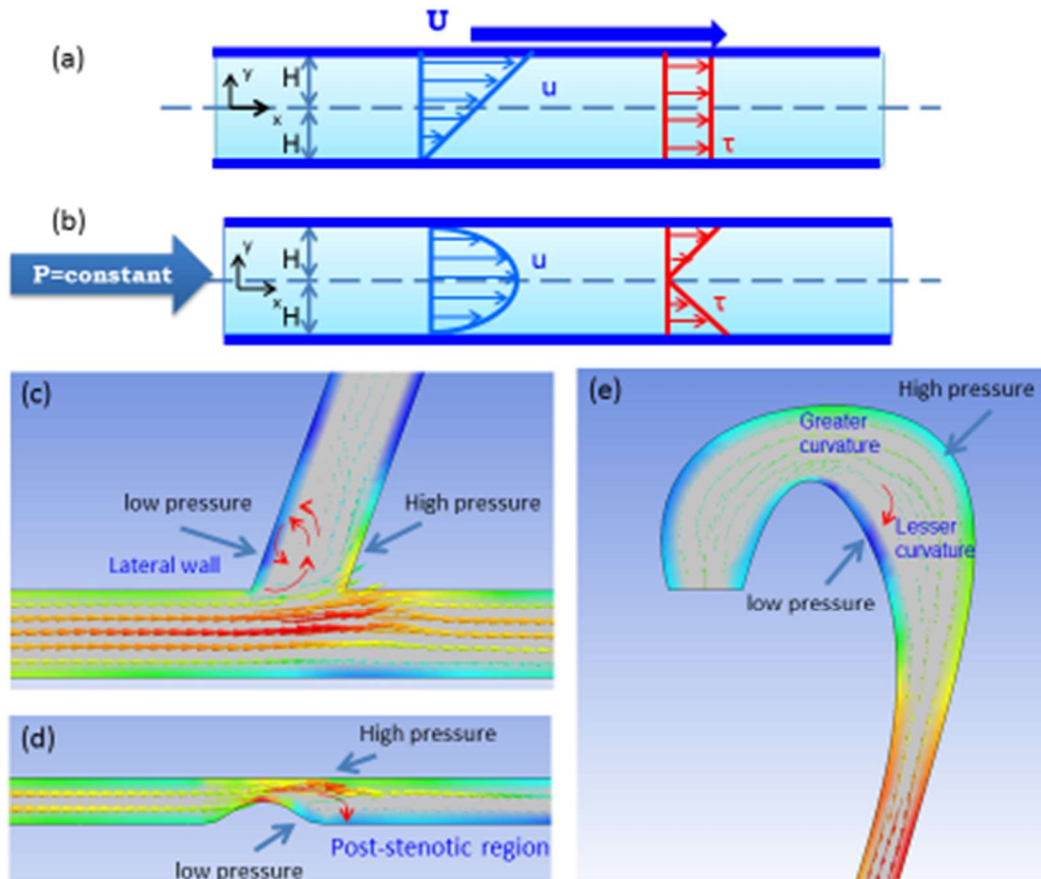
**Figure 2.** Comparison between Couette and Poiseuille flow.

(a) When top plate moves with velocity U and bottom plate is fixed, fluid motion (Navier-Stoke Equation) shows a linear profile. Also, shear stress profile shows the constant profile. (b) When constant pressure is applied to fluid which is trapped between two fixed plates, fluid motion shows a parabolic flow. Shear stress profile shows a linear profile. Anatomic variation promotes low reversal occurring from the high pressured to low pressured regions. (c) In the bifurcated region, low pressure develops at the lateral wall of bifurcation, lesser curvature, and the post-stenotic region. (d) In the wake of post-stenotic region, low pressure promotes flow separation and flow reversal. (e) In aortic arch, Greater curvature has higher pressure than the lesser curvature.
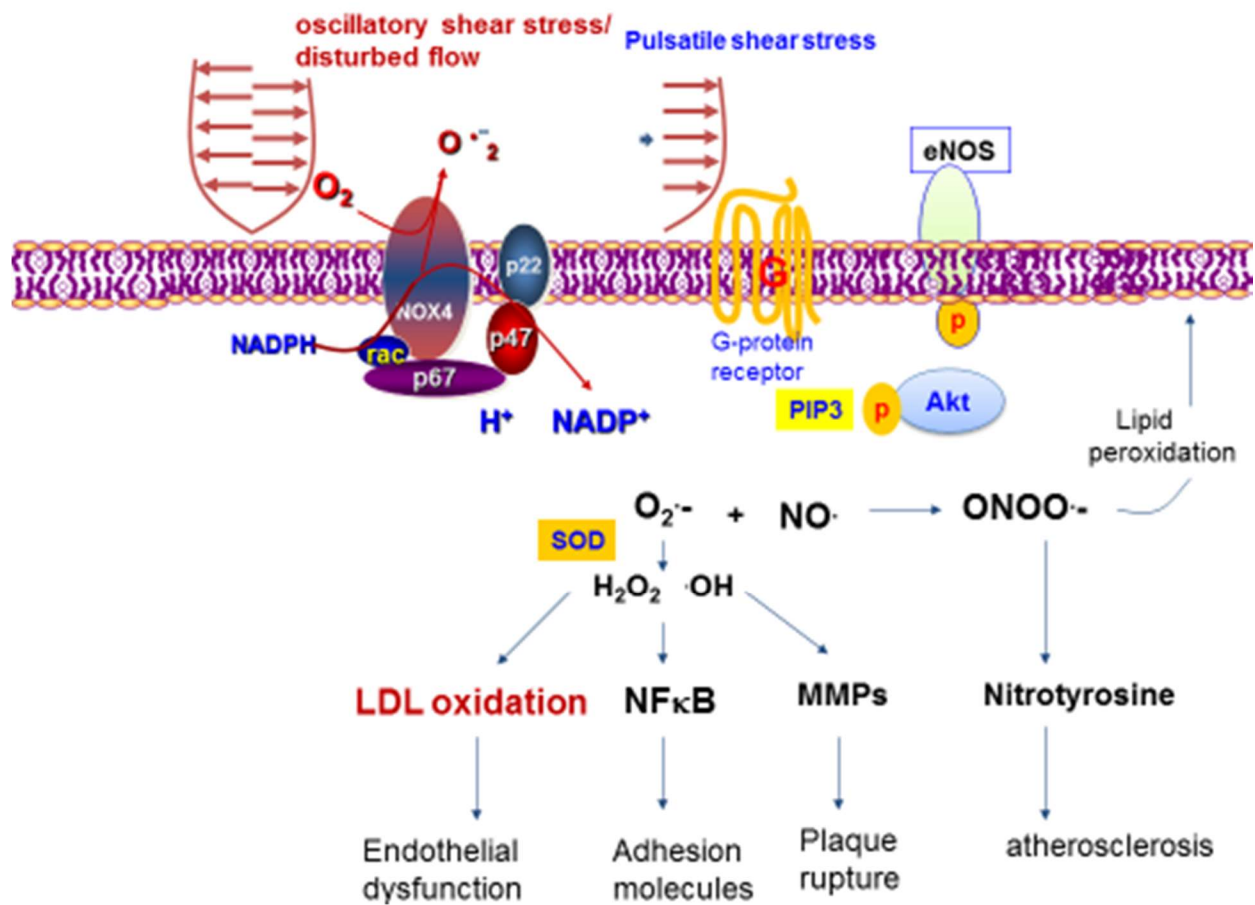
**Figure 3.** Oscillatory shear stress mediated mechanotransduction signal modulates inflammatory responses, whereas pulsatile shear stress activates G-protein and PIP3-AKT pathway, leading to phosphoyrrylation of eNOS.

**REFERENCES**

1.      Madamanchi NR, Vendrov A, Runge MS. Oxidative stress and vascular disease. *Arteriosclerosis, thrombosis, and vascular biology* 2005; 25:29-38.

2.      Harrison D, Griendling KK, Landmesser U *et al.* Role of oxidative stress in atherosclerosis. *The American journal of cardiology* 2003; 91:7A-11A.

3.      Hwang J, Ing MH, Salazar A *et al.* Pulsatile versus oscillatory shear stress regulates NADPH oxidase subunit expression: implication for native LDL oxidation. *Circ Res* 2003; 93:1225-1232.

4.      Li R, Mittelstein D, Lee J *et al.* A dynamic model of calcific nodule destabilization in response to monocyte- and oxidized lipid-induced matrix metalloproteinases. American journal of physiology. *Cell physiology* 2012; 302:C658-665.

5.      Stone PH, Coskun AU, Kinlay S *et al.* Effect of endothelial shear stress on the progression of coronary artery disease, vascular remodeling, and in-stent restenosis in humans: in vivo 6-month follow-up study. *Circulation* 2003; 108:438-444.

6.      Takabe W, Jen N, Ai L *et al.* Oscillatory shear stress induces mitochondrial superoxide production: implication of NADPH oxidase and c-Jun NH2-terminal kinase signaling. *Antioxidants & redox signaling* 2011; 15:1379-1388.

7.      Cheng C, Tempel D, van Haperen R *et al.* Shear stress-induced changes in atherosclerotic plaque composition are modulated by chemokines. *The Journal of clinical investigation* 2007; 117:616-626.

8.      Yu F, Lee J, Jen N *et al.* Elevated electrochemical impedance in the endoluminal regions with high shear stress: implication for assessing lipid-rich atherosclerotic lesions. *Biosensors & bioelectronics* 2013; 43:237-244.

9.      Jen N, Yu F, Lee J *et al.* Atrial fibrillation pacing decreases intravascular shear stress in a New Zealand white rabbit model: implications in endothelial function. *Biomechanics and modeling in mechanobiology* 2013; 12:735-745.

10.    Cheng C, Tempel D, van Haperen R *et al.* Atherosclerotic lesion size and vulnerability are determined by patterns of fluid shear stress. *Circulation* 2006; 113:2744-2753.

11.    Sadeghi MR, Shirani E, Tafazzoli-Shadpour M, Samaee M. The effects of stenosis severity on the hemodynamic parameters-assessment of the correlation between stress phase angle and wall shear stress. *Journal of biomechanics* 2011; 44:2614-2626.

12.    Thim T, Hagensen MK, Horlyck A *et al.* Wall shear stress and local plaque development in stenosed carotid arteries of hypercholesterolemic minipigs. *Journal of cardiovascular disease research* 2012; 3:76-83.

13.    Korin N, Kanapathipillai M, Matthews BD *et al.* Shear-activated nanotherapeutics for drug targeting to obstructed blood vessels. *Science* 2012; 337:738-742.

14.    Ai L, Zhang L, Dai W *et al.* Real-time assessment of flow reversal in an eccentric arterial stenotic model. *Journal of biomechanics* 2010; 43:2678-2683.

15.    Yu H, Ai L, Rouhanizadeh M *et al.* Flexible polymer sensors for in vivo intravascular shear stress analysis. *Journal of Microelectromechanical Systems* 2008; 17:1178-1186.

16.    Ai L, Yu H, Dai W *et al.* Real-time intravascular shear stress in the rabbit abdominal aorta. *IEEE Transactions on Biomedical Engineering* 2009; 56:1755-1764.

17.    Yu F, Ai L, Dai W *et al.* MEMS thermal sensors to detect changes in heat transfer in the pre-atherosclerotic regions of fat-fed New Zealand white rabbits. *Annals of biomedical engineering* 2011; 39:1736-1744.

18.    Davies PF, Polacek DC, Handen JS *et al.* A spatial approach to transcriptional profiling: mechanotransduction and the focal origin of atherosclerosis. *Trends in biotechnology* 1999; 17:347-351.

19.    Garcia-Cardena G, Comander JI, Blackman BR *et al.* Mechanosensitive endothelial gene expression profiles: scripts for the role of hemodynamics in atherogenesis? *Annals of the New York Academy of Sciences* 2001; 947:1-6.

20.    Libby P. Coronary artery injury and the biology of atherosclerosis: inflammation,

thrombosis, and stabilization. *The American journal of cardiology* 2000; 86:3J-8J; discussion 8J-9J.

**21.** Corson MA, James NL, Latta SE *et al.* Phosphorylation of endothelial nitric oxide synthase in response to fluid shear stress. *Circ Res* 1996; 79:984-991.

**22.** Moncada S. Adventures in vascular biology: a tale of two mediators. Philosophical transactions of the Royal Society of London. *Series B, Biological sciences* 2006; 361:735-759.

**23.** Glagov S, Zarins C, Giddens DP, Ku DN. Hemodynamics and atherosclerosis. Insights and perspectives gained from studies of human arteries. *Archives of pathology & laboratory medicine* 1988; 112:1018-1031.

**24.** Makino A, Prossnitz ER, Bunemann M *et al.* G protein-coupled receptors serve as mechanosensors for fluid shear stress in neutrophils. *American journal of physiology. Cell physiology* 2006; 290:C1633-1639.

**25.** Murase T, Kume N, Korenaga R *et al.* Fluid shear stress transcriptionally induces lectin-like oxidized LDL receptor-1 in vascular endothelial cells. *Circ Res* 1998; 83:328-333.

**26.** Wang P, Zhu F, Tong Z, Konstantopoulos K. Response of chondrocytes to shear stress: antagonistic effects of the binding partners Toll-like receptor 4 and caveolin-1. *FASEB journal*: official publication of the Federation of American Societies for Experimental Biology 2011; 25:3401-3415.

**27.** Tarbell JM. Shear stress and the endothelial transport barrier. *Cardiovascular research* 2010; 87:320-330.

**28.** Urbich C, Walter DH, Zeiher AM, Dimmeler S. Laminar shear stress upregulates integrin expression: role in endothelial cell adhesion and apoptosis. *Circ Res* 2000; 87:683-689.

**29.** Nilius B, Droogmans G. Ion channels and their functional role in vascular endothelium. *Physiological reviews* 2001; 81:1415-1459.

**30.** Brakemeier S, Kersten A, Eichler I *et al.* Shear stress-induced up-regulation of the intermediate-conductance Ca(2+)-activated K(+) channel in human endothelium. *Cardiovascular*

*research* 2003; 60:488-496.

**31.** McCue S, Noria S, Langille BL. Shear-induced reorganization of endothelial cell cytoskeleton and adhesion complexes. *Trends in cardiovascular medicine* 2004; 14:143-151.

**32.** Davies PF, Robotewskyj A, Griem ML. Quantitative studies of endothelial cell adhesion. Directional remodeling of focal adhesion sites in response to flow forces. *The Journal of clinical investigation* 1994; 93:2031-2038.

**33.** Helmke BP, Goldman RD, Davies PF. Rapid displacement of vimentin intermediate filaments in living endothelial cells exposed to flow. *Circ Res* 2000; 86:745-752.

**34.** Loufrani L, Dubroca C, You D *et al.* Absence of dystrophin in mice reduces NO-dependent vascular function and vascular density: total recovery after a treatment with the aminoglycoside gentamicin. *Arterioscler Thromb Vasc Biol* 2004; 24:671-676.

**35.** Rizzo V, Morton C, DePaola N *et al.* Recruitment of endothelial caveolae into mechanotransduction pathways by flow conditioning in vitro. *American journal of physiology. Heart and circulatory physiology* 2003; 285:H1720-1729.

**36.** Osawa M, Masuda M, Kusano K, Fujiwara K. Evidence for a role of platelet endothelial cell adhesion molecule-1 in endothelial cell mechanosignal transduction: is it a mechanoresponsive molecule? *The Journal of cell biology* 2002; 158:773-785.

**37.** Cowan DB, Lye SJ, Langille BL. Regulation of vascular connexin43 gene expression by mechanical loads. *Circ Res* 1998; 82:786-793.

**38.** Gudi S, Huvar I, White CR *et al.* Rapid activation of Ras by fluid flow is mediated by Galpha(q) and Gbetagamma subunits of heterotrimeric G proteins in human endothelial cells. *Arterioscler Thromb Vasc Biol* 2003; 23:994-1000.

**39.** Hsiai TK, Cho SK, Wong PK *et al.* Monocyte recruitment to endothelial cells in response to oscillatory shear stress. *FASEB journal*: official publication of the Federation of American Societies for Experimental Biology 2003; 17:1648-1657.

**40.** Hsiai TK, Hwang J, Barr ML *et al.* Hemodynamics influences vascular peroxynitrite

formation: Implication for low-density lipoprotein apo-B-100 nitration. *Free radical biology & medicine* 2007; 42:519-529.

41.     Takabe W, Li R, Ai L *et al.* Oxidized low-density lipoprotein-activated c-Jun NH2-terminal kinase regulates manganese superoxide dismutase ubiquitination: implication for mitochondrial redox status and apoptosis. *Arterioscler Thromb Vasc Biol* 2010; 30:436-441.

42.     Brennan ML, Wu W, Fu X *et al.* A tale of two controversies: defining both the role of peroxidases in nitrotyrosine formation in vivo using eosinophil peroxidase and myeloperoxidase-deficient mice, and the nature of peroxidase-generated reactive nitrogen species. *The Journal of biological chemistry* 2002; 277:17415-17427.

43.     DeVerse JS, Bailey KA, Jackson KN, Passerini AG. Shear stress modulates RAGE-mediated inflammation in a model of diabetes-induced metabolic stress. *American journal of physiology. Heart and circulatory physiolog*y 2012; 302:H2498-2508.

44.     Sun X, Feinberg MW. Regulation of endothelial cell metabolism: just go with the flow. *Arterioscler Thromb Vasc Biol* 2015; 35:13-15.

45.     Ha CH, Kim S, Chung J *et al.* Inhibitory effect of soluble RAGE in disturbed flow-induced atherogenesis. *International journal of molecular medicine* 2013; 32:373-380.

46.     Klebanoff SJ. Myeloperoxidase: friend and foe. *Journal of leukocyte biology* 2005; 77:598-625.

47.     Arnhold J, Flemmig J. Human myeloperoxidase in innate and acquired immunity. *Archives of biochemistry and biophysics* 2010; 500:92-106.

48.     Delporte C, Boudjeltia KZ, Noyon C *et al.* Impact of myeloperoxidase-LDL interactions on enzyme activity and subsequent posttranslational oxidative modifications of apoB-100. *Journal of lipid research* 2014; 55:747-757.

49.     Li R, Jen N, Yu F, Hsiai TK. Assessing mitochondrial redox status by flow cytometric methods: vascular response to fluid shear stress. *Current protocols in cytometry* 2011; Chapter 9:Unit9 37.

**50.** Takabe W, Li R, Ai L *et al.* Oxidized Low-Density Lipoprotein-Activated c-Jun NH2-Terminal Kinase Regulates Manganese Superoxide Dismutase Ubiquitination: Implication for Mitochondrial Redox Status and Apoptosis. *Arteriosclerosis, Thrombosis, and Vascular Biology* 2010; 30:436-441.

**51.** Jen N, Takabe W, Li R *et al.* Oscillatory fluid shear stress-induced JNK activation via NADPH oxidase implicates mitochondrial superoxide production in endothelial cells. *The FASEB Journal* 2010; 24:784.713.

**52.** Takabe W, Jen N, Ai L *et al.* Oscillatory Shear Stress Induces Mitochondrial Superoxide Production: Implication of NADPH Oxidase and c-Jun NH2-terminal Kinase Signaling. *Antioxidants & redox signaling* 2011; 15:1379-1388.

**53.** Hsiai TK, Hwang J, Barr ML *et al.* Hemodynamics influences vascular peroxynitrite formation: Implication for low-density lipoprotein apo-B-100 nitration. *Free Radical Biology and Medicine* 2007; 42:519-529.

**54.** Li R, Beebe T, Cui J *et al.* Pulsatile shear stress increased mitochondrial membrane potential: Implication of Mn-SOD. *Biochemical and Biophysical Research Communications* 2009; 388:406-412.

**55.** Ai L, Rouhanizadeh M, Wu JC *et al.* Shear stress influences spatial variations in vascular Mn-SOD expression: implication for LDL nitration. *American Journal of Physiology- Cell Physiology* 2008; 294:C1576-C1585.

**56.** Hamilton RT, Asatryan L, Nilsen JT *et al.* LDL protein nitration: Implication for LDL protein unfolding. *Archives of biochemistry and biophysics* 2008; 479:1-14.

**57.** Honda HM, Hsiai T, Wortham CM *et al.* A complex flow pattern of low shear stress and flow reversal promotes monocyte binding to endothelial cells. *Atherosclerosis* 2001; 158:385-390.

**58.** Nagel T, Resnick N, Atkinson WJ *et al.* Shear stress selectively upregulates intercellular adhesion molecule-1 expression in cultured human vascular endothelial cells. *The Journal of clinical investigation* 1994; 94:885-891.

59.     Hsiai TK, Cho SK, Reddy S *et al.* Pulsatile flow regulates monocyte adhesion to oxidized lipid-induced endothelial cells. *Arteriosclerosis, thrombosis, and vascular biology* 2001; 21:1770-1776.

60.     Parmar KM, Nambudiri V, Dai G *et al.* Statins exert endothelial atheroprotective effects via the KLF2 transcription factor. *The Journal of biological chemistry* 2005; 280:26714-26719.

61.     Gracia-Sancho J, Villarreal G, Jr., Zhang Y, Garcia-Cardena G. Activation of SIRT1 by resveratrol induces KLF2 expression conferring an endothelial vasoprotective phenotype. *Cardiovascular research* 2010; 85:514-519.

62.     Parmar KM, Larman HB, Dai G *et al.* Integration of flow-dependent endothelial phenotypes by Kruppel-like factor 2. *The Journal of clinical investigation* 2006; 116:49-58.

63.     Wu W, Xiao H, Laguna-Fernandez A *et al.* Flow-Dependent Regulation of Kruppel-Like Factor 2 Is Mediated by MicroRNA-92a. *Circulation* 2011; 124:633-641.

64.     Doddaballapur A, Michalik KM, Manavski Y *et al.* Laminar shear stress inhibits endothelial cell metabolism via KLF2-mediated repression of PFKFB3. *Arterioscler Thromb Vasc Biol* 2015; 35:137-145.

65.     Lin TC, Tintut Y, Lyman A *et al.* Mechanical response of a calcified plaque model to fluid shear force. *Annals of biomedical engineering* 2006; 34:1535-1541.

66.     Lin MC, Almus-Jacobs F, Chen HH *et al.* Shear stress induction of the tissue factor gene. *The Journal of clinical investigation* 1997; 99:737-744.

67.     Adamo L, Naveiras O, Wenzel PL *et al.* Biomechanical forces promote embryonic haematopoiesis. *Nature* 2009; 459:1131-1135.

68.     Yamamoto K, Sokabe T, Watabe T *et al.* Fluid shear stress induces differentiation of Flk-1-positive embryonic stem cells into vascular endothelial cells in vitro. *American journal of physiology. Heart and circulatory physiology* 2005; 288:H1915-1924.

69.     Obi S, Yamamoto K, Shimizu N *et al.* Fluid shear stress induces arterial differentiation of endothelial progenitor cells. *Journal of applied physiology* 2009; 106:203-211.

**70.**     Toh YC, Voldman J. Fluid shear stress primes mouse embryonic stem cells for differentiation in a self-renewing environment via heparan sulfate proteoglycans transduction. *FASEB journal*: official publication of the Federation of American Societies for Experimental Biology 2011; 25:1208-1217.

**71.**     Diaz MF, Li N, Lee HJ *et al.* Biomechanical forces promote blood development through prostaglandin E2 and the cAMP-PKA signaling axis. *The Journal of experimental medicine* 2015; 212:665-680.

**72.**     Wolfe RP, Leleux J, Nerem RM, Ahsan T. Effects of shear stress on germ lineage specification of embryonic stem cells. *Integrative biology*: quantitative biosciences from nano to macro 2012; 4:1263-1273.

**73.**     Kuo YC, Chang TH, Hsu WT *et al.* Oscillatory shear stress mediates directional reorganization of actin cytoskeleton and alters differentiation propensity of mesenchymal stem cells. *Stem cells* 2015; 33:429-442.

**74.**     Li R, Beebe T, Jen N *et al.* Shear stress-activated Wnt-angiopoietin-2 signaling recapitulates vascular repair in zebrafish embryos. *Arterioscler Thromb Vasc Biol* 2014; 34:2268-2275.

**75.**     Jahnsen ED, Trindade A, Zaun HC *et al.* Notch1 is pan-endothelial at the onset of flow and regulated by flow. *PLoS One* 2015; 10:e0122622.

**76.**     Masumura T, Yamamoto K, Shimizu N *et al.* Shear stress increases expression of the arterial endothelial marker ephrinB2 in murine ES cells via the VEGF-Notch signaling pathways. *Arterioscler Thromb Vasc Biol* 2009; 29:2125-2131.

**CHAPTER FOUR**

**Two-point stretchable electrode array for endoluminal electrochemical impedance spectroscopy measurements of lipid-laden atherosclerotic plaques**

Packard R.R.S.*, Zhang X.*, Luo Y.*, Ma T., Jen N., Ma J., Demer L.L, Zhou Q., Sayre J.W., Li R., Tai Y.-C., Hsiai T.K. * Equal contribution

**ABSTRACT**

Four-point electrode systems are commonly used for electric impedance measurements of biomaterials and tissues. We introduce a 2-point system to reduce electrode polarization for heterogeneous measurements of vascular wall. Presence of endoluminal oxidized low density lipoprotein (oxLDL) and lipids alters the electrochemical impedance that can be measured by electrochemical impedance spectroscopy (EIS). We developed a catheter-based 2-point micro-electrode configuration for intravascular deployment in New Zealand White rabbits. An array of 2 flexible round electrodes, 240 μm in diameter and separated by 400 μm was microfabricated and mounted on an inflatable balloon catheter for EIS measurement of the oxLDL-rich lesions developed as a result of high-fat diet-induced hyperlipidemia. Upon balloon inflation, the 2-point electrode array conformed to the arterial wall to allow deep intraplaque penetration via alternating current (AC). The frequency sweep from 10 – 300 kHz generated an increase in capacitance, providing distinct changes in both impedance ($\Omega$) and phase ($\phi$) in relation to varying degrees of intraplaque lipid burden in the aorta. Aortic endoluminal EIS measurements were compared with epicardial fat tissue and validated by intravascular ultrasound and immunohistochemistry for plaque lipids and foam cells. Thus, we demonstrate a new approach to quantify endoluminal EIS via a 2-point stretchable electrode strategy.

**INTRODUCTION**

Electrochemical impedance spectroscopy (EIS) measures charges stored in tissues by electrical impedance (Z) developed in response to applied alternating current (AC). EIS is the macroscopic representation of the electric field and current density distribution within the experimented samples. Such distribution can be described with Maxwell's equations, which, under the quasi-electrostatic limit, reduces to [5]:

$$\nabla \cdot (\sigma^* \nabla \varphi) = 0, \tag{1}$$

where $\sigma^* = \sigma_T + j\omega\varepsilon_T$, and $\sigma_T$ and $\varepsilon_T$ represent the conductivity and permittivity of the sample, respectively, $\omega$ is the angular frequency, $j = \sqrt{-1}$, $\varphi$ denotes the voltage distribution. Current density, $\vec{J} = \sigma^*\vec{E}$, is calculated with known distribution of electric field, $\vec{E}$. Finally, impedance of the sample, $Z$, based on Maxwell's equations, is expressed as:

$$Z = \frac{\Delta\varphi}{\int_S \vec{J} \cdot \mathrm{d}S}, \tag{2}$$

where $S$ denotes the electrode-tissue interface area, $\Delta\varphi$ represents the voltage difference across the two measuring electrodes.


Fat-free tissue is known to be a viable electrical conductor for its high water (approximately 73%) and electrolytes (ions and proteins) content. However, fat tissue is anhydrous and thus, a poor conductor. The high lipid content, including negatively charged active lipids such as oxidized low density lipoprotein (oxLDL) [27] and foam cells present in the plaque change the endoluminal electrochemical properties that can be measured by EIS [17, 28, 29, 30].


The application of microelectrode sensor measures the non-Faraday impedance due to the interface capacitance and non-homogeneities of fatty streaks or pre-atherosclerotic lesions that harbor oxLDL and foam cell infiltrates. Suselbeck *et al.* measured intravascular EIS using a linear

4-electrode configuration microelectrode ($2 \times 10^5$ µm in length) [30]. Our group further reduced the sensor surface area by 2,000-fold using the concentric bipolar microelectrode sensors (300 µm in diameter) [4, 36] and introduced the balloon-inflatable bipolar electrodes to measure EIS signals from non-homogeneous tissue composition, non-planar endoluminal surface, and non-uniform electric current distribution of the atherosclerotic lesions [4].

We hereby introduce a 2-point configuration to avoid separate current paths and common-mode signals that confound measured data [13]. The 2-point configuration with flexible round electrodes (Ø 240 µm, **Fig. 1**) enabled deep intraplaque penetration by AC current, allowing for quantification of oxLDL-rich plaque from the thoracic to distal abdominal aortas in the NZW rabbit model. We biased an input peak-to-peak AC voltage of 50 mV and a sweeping frequency from 10 to 300 kHz to the 2-point electrodes. We quantified and validated EIS signals both *in vivo* and *ex vivo* in relation to epicardial fat tissue, and recapitulated the frequency range from 10 – 300 kHz in which distinct capacitive and phase changes revealed low, intermediate and high oxLDL-rich lesions. Thus, we demonstrated a simplified 2-point electrode design to enhance detection of lipid-laden plaques.

**METHODS**

**EIS sensor deployment, device assembly and microfabrication**

We fabricated an EIS sensor with several microelectrodes in an array **(Fig. 1a)**.  In the present study, we always utilized the same 2 middle electrodes highlighted with red circles.  We present a 3D rendering of the deployment of our EIS sensor with the balloon in grey, plaque in green and vessel wall segment in blue **(Fig. 1b)**.  This is followed by a 2D side-view of the device showing where the microelectrodes are placed and a 2D cross-sectional view of the device in contact with an atherosclerotic plaque segment with electric fields generated between the microelectrodes.

A 20 cm long plastic catheter with a dilatation medical balloon (Vention Medical, NH) sleeved on from one end was used for *in vivo* delivery of the sensor, while the other end was connected with a mechanical pump to control the balloon dilatation.  Miniature holes were punched on the catheter sidewall covered by the balloon for air delivery **(Fig. 1b)**.  The flexible sensor, after connecting the contact pads with metal wires using conductive epoxy, was fixed on the surface of the balloon by silicone adhesive (Henkel, CT).  An insulating heat-shrink tube was used to wrap the wires and secure their positions alongside the catheter.  These wires are conveniently connected with normal electrical cables to interface with measuring instruments as illustrated by the assembled EIS sensor with close-up view showing the flexible electrodes attached on the balloon.

The fabrication process of the flexible EIS sensors started with a parylene-C (PAC) thin film (5 µm) deposition onto a normal silicon wafer treated with hexamethyldisilazane (HMDS, 3 min) for adhesion promotion **(Fig. 1c)**.  Subsequently, a layer of Au/Ti (200nm/20nm) was deposited and selectively removed through chemical wet etching based on a lithographically-defined pattern. Another layer of PAC (5 µm) was deposited as an insulating barrier, followed by exposure of the sensing electrodes and contact pads area via reactive ion etching (RIE).  The final device footprint

was defined by further etching through the PAC thin film.  The PAC sensor was peeled off from the wafer and used for assembly.

**Equivalent circuit diagram for the paired electrode sensor**

The current design can be modeled with the following equivalent circuit to demonstrate the constant phase element (CPE) in association with non-ideal double layer capacitance at the electrode/tissue interface **(Fig. 2a)**.  The electrode-tissue interface impedance of both sensing electrodes is considered as a constant phase element:

$$\text{(CPE)} \; Z_{CPA} = \frac{1}{Y(j\omega)^a} \; , \qquad\qquad (3)$$

where $Y$ denotes the nominal capacitance value, and *a* is a constant between 0 and 1, corresponding to non-ideal interface effects.  The impedance of measured tissue is modeled as paralleled $R_T$ and $C_T$, representing both resistive and capacitive elements within the tissue, depending on material composition and structural variation.  Moreover, the Bode plot of the equivalent circuit model is depicted based on a network analysis similar to Grimnes *et al.* [13] **(Fig. 2b)**.  The values of each electrical component in the Bode plot are adapted from our previous study [34] and are as follows: $Y$=100nS, $R_T$=1k$\Omega$, $C_T$=10pF, $a$=0.8.  As illustrated, the phase gradually rises towards zero degree as the frequency increases, indicating a diminishment in the interfering capacitive effect within the system, particularly at the electrode/tissue interface. Hence, impedance values at higher frequencies have a superior ability to reveal the distinctive characteristics of interrogated samples.

**Animal studies**

All animal studies were performed in compliance with the IACUC protocol approved by the UCLA Office of Animal Research.  Rabbit experiments were conducted in the UCLA translational research imaging center (TRIC) lab.  Analyses were conducted in n=5 control rabbits fed a chow

diet and n=3 age-matched high-fat fed NZW male rabbits [26].  High-fat animals were placed on a 1.5% cholesterol and 6.0% peanut oil diet (Harlan laboratory) for 9 weeks prior to harvesting. Animals were anesthetized with isofluorane gas, endotracheally intubated and placed on a mechanical ventilator.  Blood pressure and heart rate were monitored continuously by a non-invasive paw cuff as well as an intra-arterial sensor.  A femoral cut-down was performed and a 4-French arterial sheath placed in the common femoral artery.  Under fluoroscopic guidance (Siemens Artis Zeego with robotic arm) and iodinated contrast dye injection, the EIS sensor was advanced to the abdominal aorta for live interrogation.  *In vivo* and *ex vivo* measurements were obtained in the abdominal aorta between the renal artery bifurcation and also proximal to the aortic bifurcation.  Following animal harvesting, *ex vivo* measurements were conducted in various segments with differing levels of lipid burden in the descending thoracic aorta and abdominal aorta at the level of the renal arteries.  Three replicates were performed at each interrogation site. Thus, for each animal, measurements were obtained at 3 anatomic sites:  1. descending thoracic aorta, 2. abdominal aorta at the level of the renal arteries, and 3. abdominal aorta proximal to the aortic bifurcation.  In the high-fat fed animals, these 3 anatomic sites correspond to areas with: 1. severe plaque, 2. moderate plaque, and 3. mild plaque, respectively.  AC signals with peak-to-peak voltages of 50 mV and frequencies ranging from 1000 Hz to 300 kHz were delivered at each site.  The impedance magnitude and the phases of the impedances were acquired at 10 data points per frequency decade.

**EIS measurements in aortas**

Angiograms were obtained during fluoroscopy to document vessel anatomy and verify appropriate advancement of the EIS sensor.  Measurements were obtained in control rabbit aortas and in various segments of the high-fat fed rabbit aortas.  Different anatomical segments exhibited varying degrees of atherosclerosis, with the most prominent being the thoracic aorta.  Segments that were analyzed were the descending thoracic aorta (severe plaque), abdominal aorta at the

126

level of the renal artery bifurcation (moderate plaque), and abdominal aorta proximal to the aortic bifurcation (mild plaque).  Results were compared to plaque burden as assessed by lipid content and inflammatory activation by macrophage.  The catheter-based balloon-inflatable EIS sensor was deployed *in vivo*.  The balloon was inflated to 10 psi (pounds per square inch) to allow for optimal endoluminal contact.

**Microfabrication and deployment of high-frequency IVUS**

$PbMg_{1/3}Nb_{2/3}O_3$-$PbTiO_3$ (PMN-PT) single crystal, with its superior piezoelectric properties, served as the functional element of the IVUS transducer used in this study [19].  The general fabrication process previously reported was modified to fabricate the four-layered IVUS transducer [23].  The IVUS transducer was then inserted into customized probe housing (a stainless steel tube one window; OD: 1 mm; length: 2 mm).  The coaxial cable was covered by the flexible torque coil to ensure accurate and smooth translation of torque to the distal end over a large distance and through tortuous curves.  During experiments, the probe was inserted into a sheath to avoid cross-contamination between probe and arterial segments.  Saline solution was filled in the sheath before experiments.  For the IVUS imaging system, a Panametrics PR5900 pulser/receiver (Olympus NDT, Kennewick, WA) was used for pulse generation and signal detection with 26 dB gain and 10~100 MHz band-pass filter.  The ultrasonic radio frequency data was fed into the 12 bit digitizer and digitized at a sampling rate of 400 MHz.  The acquired IVUS signal was processed, displayed and saved simultaneously by custom built software [24].  The system has a frame rate of 20 frames per second with 1000 A-lines per frame.  A custom built rotary joint device was used for motion control and signal coupling from the rotational part to the stationary part.  All these components were fixed to a translational stepper motor with pull-back capability.  To evaluate the general performance of the IVUS transducer and imaging system, the pulse-echo testing was performed.  The measured center frequency of the IVUS transducer was 39 MHz with a fractional bandwidth of 45%.

**Histology**

A portion of each aorta was fixed in 4% paraformaldehyde, embedded in paraffin and serially sectioned at 5 $\mu$m for histological analyses. Lipids were identified by hematoxylin and eosin staining and macrophages by F4/80 staining (monoclonal rat anti-mouse antibody, Invitrogen).

**Statistical and correlation analyses**

Statistical analysis was performed using analysis of variance with multiple comparisons adjustment for this study design. Since the assumption of homogeneity of variance was violated as evidenced by a significant Levene's test [18] in most cases, the Brown-Forsythe test [2] was systematically used to determine significance across groups. Dunnett's test [9] was used for multiple comparisons given this statistical approach does not depend on homogeneity of variances and corrects for multiple testing. IBM SPSS version 20 was used to perform the analysis. A *P*-value < 0.05 was considered significant. Spearman's correlation was determined as follows:

$$r = 1 - \frac{6\Sigma d_i^2}{n(n^2 - 1)} \tag{4}$$

where *r* = Spearman correlation, $d_i$ = difference between ranks, *n* = sample size.

**RESULTS**

**EIS measurements by the 2-point configuration**

The catheter-based balloon-inflatable 2-point configuration was deployed *in vivo*. The frequency sweep revealed similar impedance profiles in the frequency range 1 – 10 kHz, consistent with a more resistive pattern in tissues **(Fig. 3a)**. However, significant differences in impedance appeared in the frequency range 10 – 300 kHz, consistent with a more capacitive behavior of the arteries ($P < 0.05$, Brown-Forsythe test). The EIS measurements revealed a baseline impedance of 12 k$\Omega$ at 10 kHz, 5.6 k$\Omega$ at 100 kHz, and 5.2 k$\Omega$ at 300 kHz in control arteries. EIS increased in the presence of oxLDL-rich lesions. At an intermediate frequency of 10 kHz, the magnitude of the impedance increased to 12.5 k$\Omega$, 13 k$\Omega$ and 14 k$\Omega$ in the abdominal aorta with mild plaque, the abdominal aorta at the renal artery bifurcation with moderate plaque and the descending thoracic aorta with severe plaque, respectively. At a high frequency of 300 kHz, the magnitude of the impedance increased further to 5.9 k$\Omega$, 7 k$\Omega$ and 8.4 k$\Omega$ in arterial segments with mild, moderate and severe plaque, respectively. As a corollary, a decrease in phase was observed in the lower frequency range, indicating a longer delay between voltage input and current output which progressively increased in the higher frequency range ($P < 0.05$ from 1.5 – 125 kHz, Brown-Forsythe test) **(Fig. 3b)**. *Ex vivo* studies were conducted in explanted aortic segments, demonstrating a high correlation with *in vivo* measurements with a Spearman $r = 0.9732$ ($P < 0.0001$) **(Fig. 3c)**. Thus, the 2-point configuration allowed for EIS measurements to quantify the degrees of plaque burden.

**Validation with intravascular ultrasound (IVUS) and immunohistochemistry**

To validate the EIS measurements, we performed IVUS and histology to assess the underlying atherosclerotic lesions. Visualization of atherosclerotic plaques of varying burden was performed by IVUS to confirm underlying plaque severity **(Fig. 4a, b)**. The IVUS and EIS measurements

were not obtained simultaneously, but sequentially with different catheters to avoid interference between the two transducers. Atherosclerotic plaques were further identified by hematoxylin and eosin (H & E) staining, and the oxLDL-laden macrophage/foam cells were detected by F4/80 immunohistochemistry staining **(Fig. 4c-j)** to support the elevated EIS values **(Fig. 3a)**. Control aortas were free of oxLDL-rich lesions or macrophages, validating the low EIS values **(Fig. 3a)**.

**EIS measurements of epicardial fat tissue in comparison with aortic segments**

To further characterize the 2-point configuration, we obtained EIS measurements from *ex vivo* epicardial fat tissue and compared these to aortic segments **(Fig. 5)**. No differences were observed in epicardial fat tissue between control and high fat fed animals. Impedance profiles were significantly higher in epicardial fat tissue compared to aortic segments throughout the frequency sweep from 1 kHz – 300 kHz ($P < 0.05$, Brown-Forsythe test). Post-hoc multiple testing analyses further illustrated significant differences between control aortas and combined atherosclerotic plaque segments from 10 – 300 kHz ($P < 0.05$, Dunnett test). These findings corroborate the capability of the simplified 2-point configuration to distinguish tissues exhibiting varying lipid burden by intravascular EIS measurements.

**Two-point electrode configuration**

One of the critical issues for the 4-point EIS design is the existence of the negative sensitivity field [13]. The formulation of the sensitivity field ($S$) of a tetrapolar configuration has been detailed in previous works [12] and can be written as

$$S = \frac{J_1 \cdot J_2}{I^2}, \tag{5}$$

where $J_1$ and $J_2$ are the current density at the current injection electrode pair and the voltage measuring electrode pair, respectively, and $I$ denotes the actual current being injected.

As seen in Eq. 5, the dot product of $J_1$ and $J_2$ can possibly become a negative value in certain regions of the targeted tissue, indicating a reverse correlation between the local conductivity change within the tissue and the overall impedance value. Consequently, the impedance measurement can no longer genuinely represent the real local conductivity variation and thus fails to recognize regions of different plaque severity. Once shifted to a 2-point design, $J_1$ and $J_2$ represent the same current density flowing across the two electrodes in use and the dot product between the two will always remain positive.

We have highlighted characteristics of EIS sensors with different numbers of electrodes in **Table 1**, and illustrate lower maximum relative variability (defined as standard deviation/mean), an indicator of higher SNR, with the current sensor design. Compared to the concentric design, the 2-point configuration generated a higher SNR for its high common mode rejection ratio (CMRR) as a result of symmetrical electrode-tissue contact area. In addition, under the same input current, the electrode pair with larger separation (2-point) provides a higher electrical potential (higher resistivity due to larger dimension) allowing penetration into the deeper tissues with robust signals, rendering the data more reliable. We compare the previous concentric design with the current design in terms of input voltage, sweeping frequency, impedance and maximum relative variation in **Table 2**. EIS by 2-point configuration was most sensitive in detecting vascular tissue compositions at 10 – 300 kHz while the concentric bipolar configuration was sensitive at 100-300 kHz.

The 2-point design further reduces the number of unknown variables from 6 to 4 in the equivalent circuit [36], reducing simulation and calculation. The 4 unknown variables required in both the 2-point and concentric bipolar designs are: 1) resistive and 2) capacitive elements of the tissue as represented by: $R_T$ and $C_T$, the constant phase element of the electrode-tissue interface in the

counter electrode (CE): $Z_{CPA} = \frac{1}{Y(j\omega)^a}$ , where 3) $Y$ denotes the nominal capacitance value, and 4) $a$ the constant of the surface property of the electrodes ranging from 0 to 1 corresponding to non-ideal interface effects.  The additional 2 unknowns specific to the previous concentric design are 1) double layer capacitance $C_{DL2}$ and 2) charge transfer resistance, $R_{CT2}$, both arising from working electrode-tissue interface.

**DISCUSSION**

The main contribution to endoluminal assessment of atherosclerotic plaque we present is the design and fabrication of balloon inflatable 2-point electrodes for EIS measurements of oxLDL-rich plaque. We characterize the stretchable sensors in terms of distinct changes in impedance and phase spectra in response to balloon inflation pressure. Our 2-point approach represents an advancement to the previously proposed linear 4-point electrode arrays [28, 29, 30], which preclude detection of small and non-homogeneous lesions. Thus, we demonstrate a simplified 2-point electrode configuration to advance the electrochemical impedance measurements for intraplaque lipid-laden lesions.

Atherosclerosis is a chronic inflammatory disease with involvement of both innate and adaptive immune pathways [21]. The atherosclerotic plaque involves a complicated interplay between lipid metabolism, inflammation, macrophage activation and collagen breakdown, and the rupture of atherosclerotic plaques remains a leading cause of mortality in developed countries [20]. Currently, fractional flow reserve (FFR), IVUS or optical coherence tomography (OCT) are limited to anatomic and hemodynamic characteristics of atherosclerotic plaques [1]. Despite the advent of computerized tomographic (CT) angiography, high resolution magnetic resonance imaging (MRI) [31], intravascular ultrasound (IVUS), near-infrared fluorescence (NIRF) [15], and time-resolved laser-induced fluorescence spectroscopy [25], real-time interrogation of metabolically active, lipid-rich plaques remains an unmet clinical need. However, none of the above modalities assess intraplaque lipid and oxidized LDL content as has been proposed with EIS. Importantly, oxidized low density lipoprotein (oxLDL) induces transformation of macrophages to lipid-laden foam cells [3]. Furthermore, growing evidence supports that oxLDL and thin-cap fibroatheromas (TCFA) rich in macrophage/foam cells are prone to mechanical stress and destabilization [8, 11, 37]. Others and our group have further demonstrated the hemodynamic shear forces on metabolically active lesions in athero-prone regions [32, 36]. The safety and relatively simple deployment of an invasive

133

EIS sensor merit further consideration in experimental and translational studies, either alone or combined with other invasive modalities such as IVUS.

When comparing our 2-point sensor with previous 3-point and 4-point linear arrays **(Table 1)**, the maximum relative variability was higher (i.e. more variability and hence less stable EIS results) by 50% in 3-point sensors and by 150% in 4-point sensors.  In addition, when comparing our linear 2-point sensor with the concentric bipolar electrodes **(Table 2)**, the maximum relative variability was the same, however the major advances of the current 2-point design allow for deep tissue penetration for intraplaque burden assessment **(Fig. 1b)**.  The spacing between the two concentric electrodes was 100 $\mu$m, confining current traveling to the fibrous cap area; whereas the spacing between the 2-point round electrodes is 400 µm, allowing for deep current penetration in the frequency band 10 – 100 kHz with high SNR.

Also, the contact impedance between the two concentric bipolar electrodes varies due to the different electrode area, giving rise to different voltage drops at each double layer and introducing common mode noise into the detected signal.  This reduction in noise rejection capacity results in a decrease in SNR.  Moreover, the 2-point design reduced the unknown variables from 6 for the concentric bipolar electrodes to 4 as simulated by the equivalent circuit **(Fig. 2)**.

Our flexible and 2-point electrodes were mounted on an inflatable balloon for endoluminal EIS quantification of lipid burden.  EIS quantifies the intrinsic electrochemical properties of tissues; namely water content, electrolyte concentration, vascular calcification and cholesterol/lipid content which influence the changes in impedance.  Sites of mild, moderate and severe atherosclerotic plaque burden in previously described specific segments of the aorta [16] were verified by fluoroscopy and IVUS for gross anatomy, by histology for lipid presence, and by

immunohistochemistry for foam cells or macrophages.  We applied AC current to the lesions and recorded impedance, Z, to determine electrochemical properties.  EIS takes advantage of the vascular tissues that store and dissipate charges [4, 34, 35, 36].  In addition to the capability of EIS to differentiate oxLDL-rich from oxLDL-free lesions [34, 35] we further demonstrated that endoluminal EIS signals are independent of blood viscosity and flow rate as evidence by the high Spearman correlation between *in vivo* and *ex vivo* EIS signals **(Fig. 3c)**.  Of note, the overall 3D geometry of vessels undergoes changes due to the loss of residual stresses during resection, leading to some modification in the endoluminal area over which stretchable sensor apposition was performed and impedance interrogation conducted.  Despite this limitation, we observed a highly significant correlation between *in vivo* and *ex vivo* measurements.  EIS signals of epicardial fat with a distinct impedance spectrum further support our 2-point design to quantify lipid-rich tissues.

Intravascular EIS assessment by deployment of linear 4-point microelectrode array (2 cm long) via balloon catheter was demonstrated in NZW rabbits [17, 28, 30].  To address EIS signals in human coronary arteries, we previously designed concentric microelectrodes (300 μm in diameter) that were conformal to the non-planar endoluminal surface and non-uniform electric current distribution.  Distinct from the large surface area of the 4-point design, the concentric bipolar microelectrodes afforded a 2,000-fold reduction in size for intravascular deployment in the mice and rabbit models [36].  To further simplify the concentric bipolar design for EIS interrogation in humans, we have re-configured to a 2-point, paired electrode design (highlighted in **Fig. 1a**). Compared to the concentric design [4], 2-point configuration provides a larger separation between the electrode pair (400 ☐m), allowing for deep current traveling into the intraplaque lipid core to achieve significant tissue impedance disparities.  Moreover, these symmetric electrode pairs provide a common mode rejection capability to reject the unwanted input signals from the wanted difference signals.

The gold paired electrodes are well embedded in a layer of insulating PAC film to minimize current drift and cross-talks **(Fig. 1)**. The limited exposed areas for endoluminal contact circumvent potential short circuit. The EIS measurement is conducted at room temperature within the operating range in the Gamry system (0~70 °C) to prevent current drifts. To predict the potential cross-talk (parasitic capacitance), we performed the open circuit impedance, $Z_P$, measurement between the two metal wires to have a quantitative estimation of the potential parasitic capacitance $C_P$. ($Z_P = \frac{1}{j\omega C_P}$; see **Fig. 6**). Impedance values arising from the parasitic capacitance is on the order of 10 kOhm at ~300 kHz in comparison with the measured tissue impedance of 1 kOhm at ~300 kHz. For this reason, the equivalent impedance of parasitic capacitance is 10 times the measurement impedance, minimizing current drift and cross-talk under physiologic conditions.

The high-frequency range indicates that real-time EIS quantification with the decreased phase delay supports the reliable intravascular strategy. An inductor circuit was used for voltage application and subsequent current generation to quantify plaque burden. When inductors (or capacitors) are involved in an AC circuit, the peaks in voltage and current are not synchronized. The fraction of a period difference between the peaks expressed in degrees is the phase difference of ≤ 90°. Our data indicate that there was a significant phase delay of ~ -70° in the low frequency range and a decrease in phase delay to ~ -10° in the highest frequencies. As a result, high frequency range shortens the duration of time lag between voltage application and current generation. The EIS impedance profiles obtained were significantly different over the 10 – 300 kHz frequency sweep, with high impedance in the severe plaque area of the descending thoracic aorta, intermediate impedance in the moderate plaque area of the proximal abdominal aorta, and low impedance in the mild plaque area of the distal abdominal aorta. These results support the application of EIS to quantify intraplaque lipid burden in real time. Previous histological analysis

of aortic atherosclerosis in the rabbit model agreed with severe, moderate, and mild degrees of lipid burden in the thoracic, proximal abdominal and distal abdominal aorta, respectively [16].

Flexible electronics is an emergent intravascular approach for pre-clinical models. Surface flexible hybrid electronics embedded in Polydimethylsiloxane (PDMS) and adhered to the skin have been tested for electrocardiogram and temperature monitoring [33]. Implantable flexible electrode arrays have been embedded in Parylene C (PAC) for its bio-compatibility [6] and investigated for retina implants to restore vision [7]. We have quantified the Young's modulus, or elastic modulus, defined as the ratio of stress to strain of the stretchable paired microelectrodes mounted on inflatable balloons [4]. Since the Young's modulus of nylon for the balloon is 2.7~4.8 GPa [14], matching with that of PAC (3.2 GPa) [22] to minimize strain mismatch, the 2-point electrodes affixed onto the non-compliant balloon (Venture Medical, USA) withstood the inflated balloon at 10 pounds per square inch (psi) or ~69 KPa for optimal endoluminal contact. In fact, the applied stress at 10 psi was well below the tensile stress at 58 MPa of PAC. Furthermore, the Young's modulus of the blood vessel ranges from 0.2 – 0.6 MPa [10] resulting in < 35% deformation in the normal direction of blood flow. Thus, the flexible and stretchable 2-point design provides safe endoluminal contact.

Our 2-point sensor discriminates areas with no plaque (controls), mild plaque (abdominal aorta proximal to the aortic bifurcation), moderate plaque (abdominal aorta at the level of the renal arteries) and severe plaque (descending thoracic aorta), thereby detecting by EIS observations previously made by histology in experimental rabbits [16]. In humans, the intravascular assessment of coronary arteries with differing levels of intraplaque lipid burden has reached clinical use [1]. Additional studies in humans have established that plaques with larger lipid and oxLDL area are more prone to vulnerability and rupture with ensuing clinical events such as myocardial infarction

[11]. These comparisons with pathology observations in humans provide the basis for future studies to establish the ability of EIS to distinguish stable from vulnerable atherosclerotic plaques.

In conclusion, the 2-point EIS design represents a diagnostic and preventive strategy to identify lipid-rich plaques for targeted therapy and for longitudinal follow-up in response to pharmacological intervention. We demonstrate a new generation of balloon-inflatable 2-point microelectrodes as a simple, reliable, safe and robust approach to complement diagnostic angiography. Our findings provide a basis for future pre-clinical studies to determine the EIS sensor either as a stand-alone catheter or packaged with other modalities such as IVUS [1].

**FIGURES AND TABLES**

| Reference | Design | Sample condition | Input voltage (mV) | Sweeping frequency (Hz) | Impedance (Ω) | Maximum relative variability |
|---|---|---|---|---|---|---|
| Yu et al.[35] | 3-point | *in vitro* | 10 | 0.1k-300k | 20k-500k | ~0.15 |
| Streitner et al.[28] | 4-point | *in vitro* | 10 | 1k, 10k, 100k | 0.3k-1k | ~0.25 |
| Presented work | 2-point | *in vivo* | 50 | 1k-300k | 4k-60k | ~0.1 |

**Table 1.**  Comparison of EIS sensors with different numbers of electrodes.

Maximum relative variability: standard deviation / mean.

| Reference | Design | Sample condition | Input voltage (mV) | Sweeping frequency (Hz) | Impedance ($\Omega$) | Maximum relative variability |
|---|---|---|---|---|---|---|
| Yu et al.[36] | Concentric | *in vitro* | 10 | 10k-100k | 1.1k-2.1k | ~0.1 |
| Cao et al.[4] | Concentric | *in vivo* | 10 | 1k-300k | 7k-100k | ~0.1 |
| Presented work | Linear | *in vivo* | 50 | 1k-300k | 4k-60k | ~0.1 |

**Table 2.** Comparison of different 2-point EIS sensors.

Maximum relative variability: standard deviation / mean.
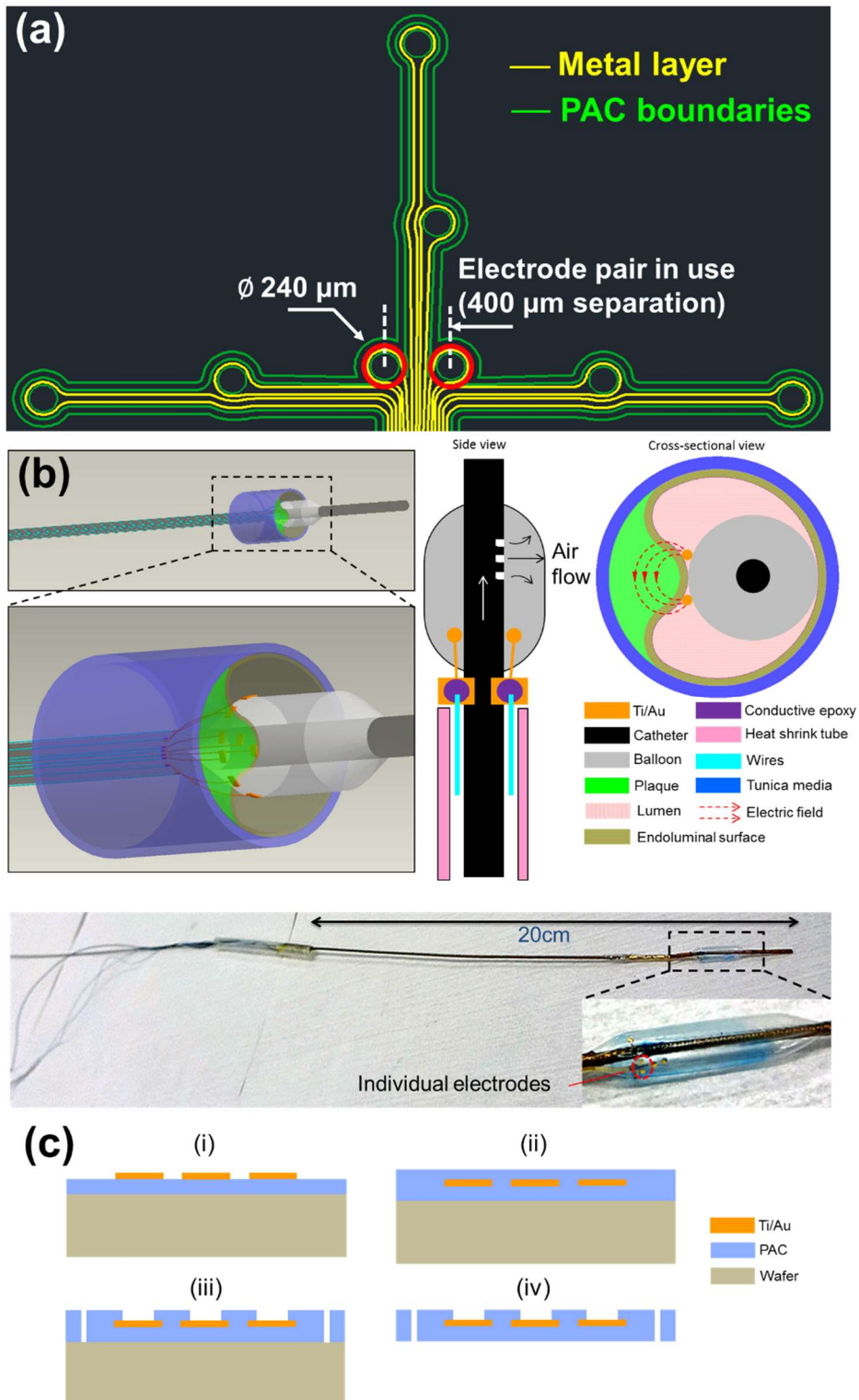
**Figure 1.** **(a)** Design schematic of an array of individually addressable impedance sensing electrodes. A set of eight round electrodes (∅ 240 μm) was implemented. The electrode pair

situated in the center (400 μm separation) and highlighted in red was selected for measurements throughout the study.  **(b)** 3D rendering of the deployed EIS sensor in contact with a plaque, and 2D side-view of the device illustrating microelectrode placement with adjacent 2D cross-sectional view illustrating apposition and contact of the electrodes on the inflated balloon with the endoluminal surface covering an atherosclerotic plaque.  Generated electric fields between the 2 microelectrodes are illustrated.  An image of the actual EIS sensor with close-up view of flexible electrodes attached on the inflated balloon is provided.  **(c)** Schematics of the microfabrication process of the flexible PAC electrodes (i-iv).
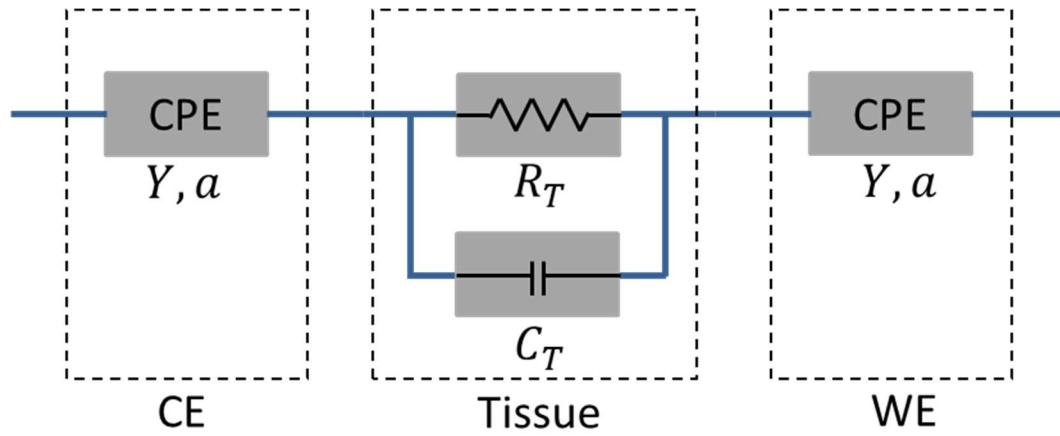
**Figure 2.** **(a)** Equivalent circuit diagram for the paired electrode sensor. *a*: constant between 0 and 1, corresponding to non-ideal interface effects between electrodes and tissues. CE: counter electrode. *WE*: working electrode. *CPE*: constant phase element. $Y$: nominal capacitance value. $R_T$: resistive element. $C_T$: capacitive element.
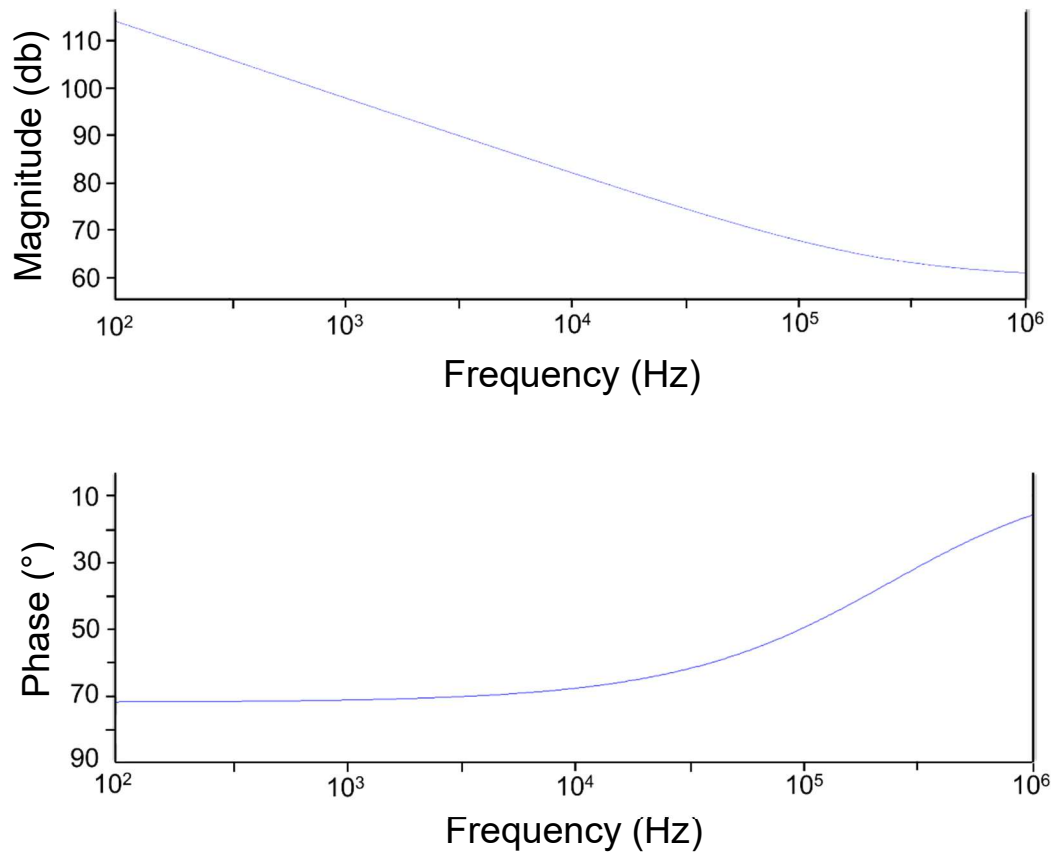
**Figure 2.** **(b)** The Bode plot for the equivalent circuit model with component values: $Y$=100nS.

$R_T$=1kΩ. $C_T$=10pF. $a$=0.8.
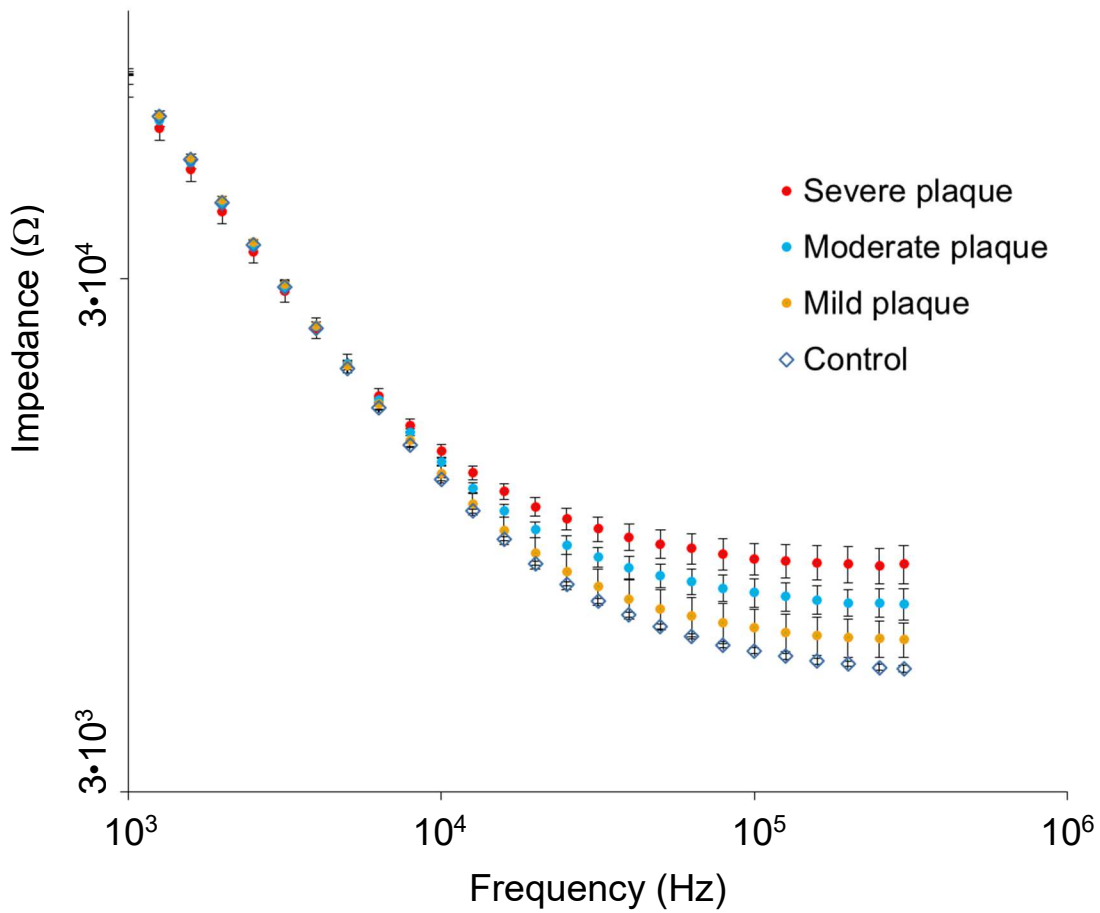
**Figure 3.** **(a)** Impedance magnitude in control aortas and aortic segments with mild, moderate and severe plaque are depicted in logarithmic scale. $P < 0.05$ in the frequency range 10 – 300 kHz for impedance profiles, Brown-Forsythe test. Data presented as means ± standard errors of the mean.
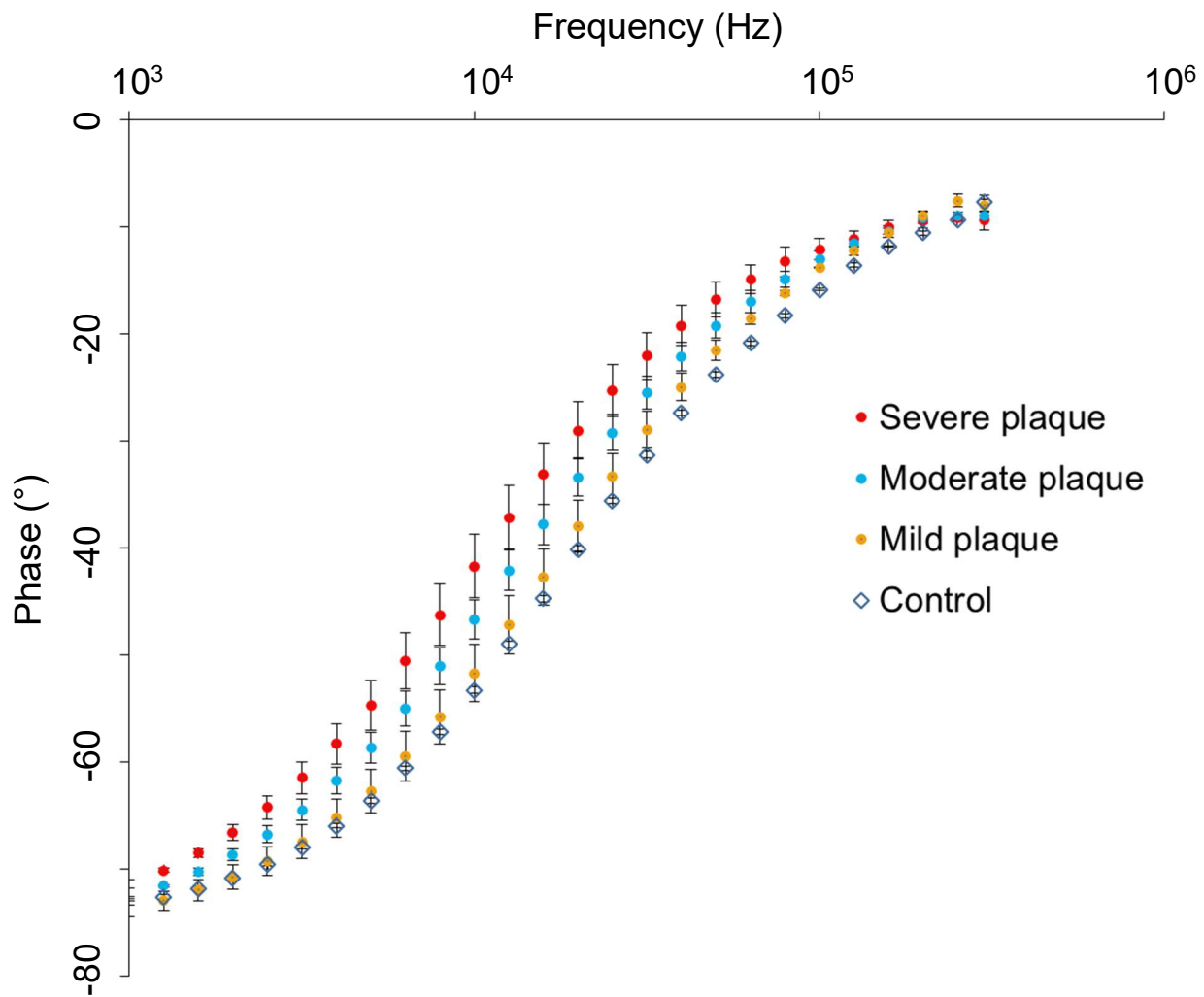
**Figure 3**.  **(b)** Phase spectra in control aortas and aortic segments with mild, moderate and severe

plaque are depicted in logarithmic scale.  *P* < 0.05 in the frequency range 1.5 – 125 kHz for phase

spectra, Brown-Forsythe test.  Data presented as means ± standard errors of the mean.
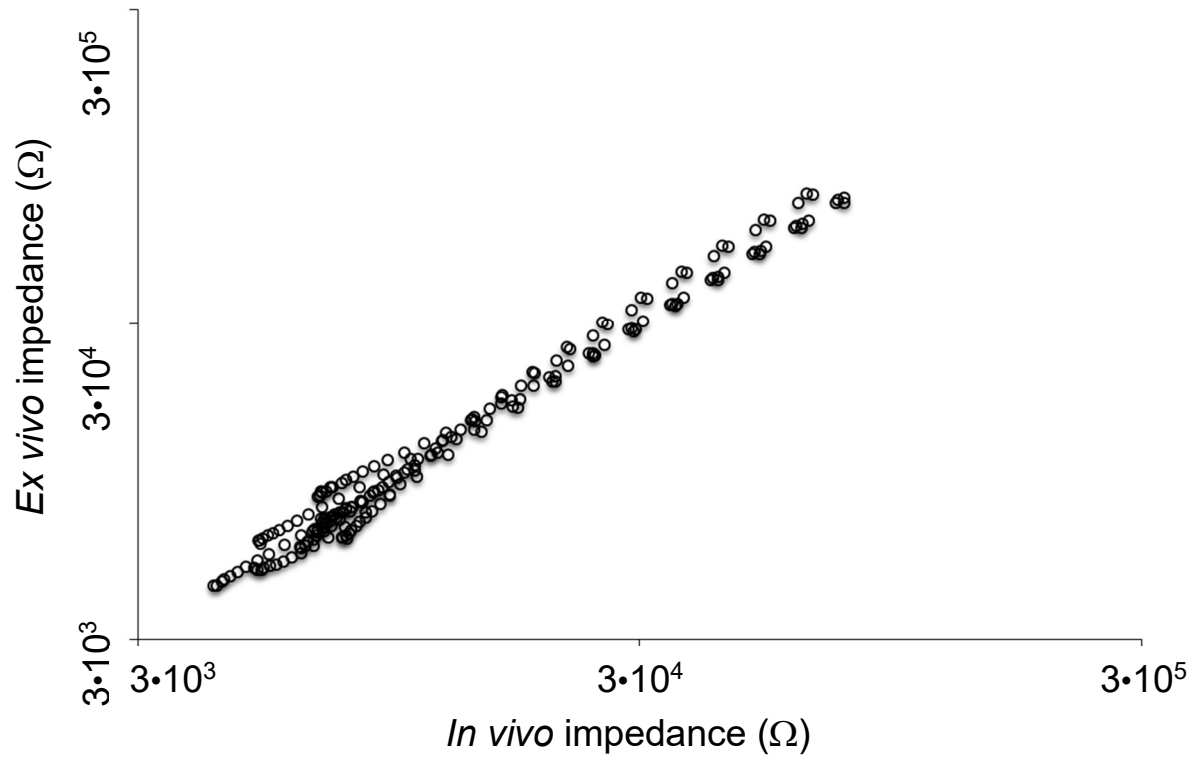
**Figure 3**. **(c)** *In vivo* vs. *ex vivo* correlation of impedance spectra obtained from identical aortic segments with the EIS sensor.  Spearman test *r* = 0.9732, *P* < 0.0001.
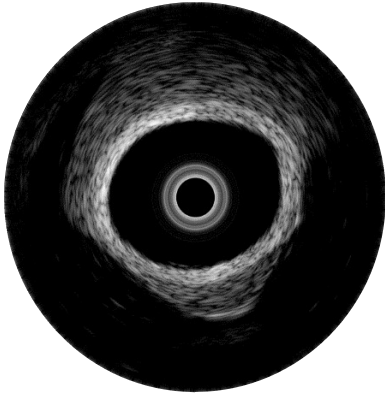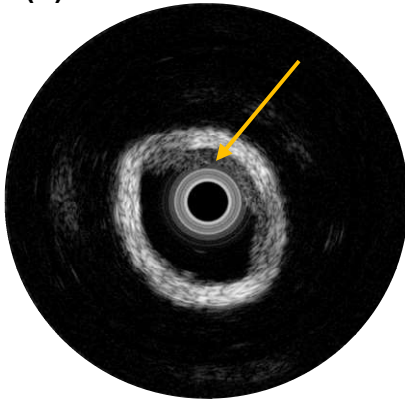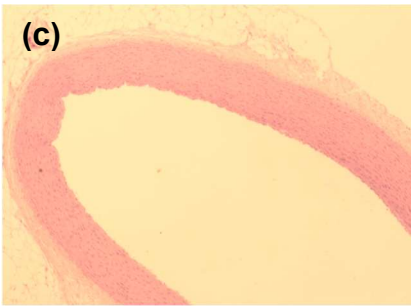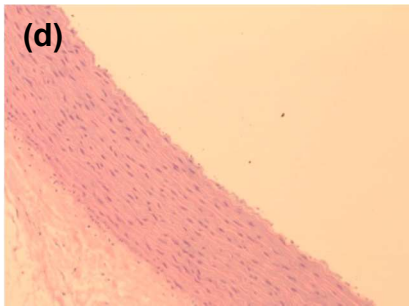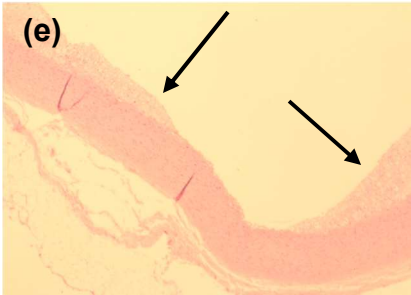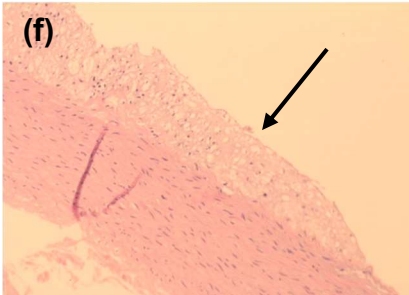
**Figure 4.** Example of intravascular ultrasound measurements obtained in a control aorta **(a)** and from a segment with atherosclerotic plaque **(b)**. The yellow arrow is pointing towards the atherosclerotic plaque. Histologic analysis of control aortas at 4x **(c)** and 10x **(d)** magnification demonstrate absence of subendothelial lipid deposits, whereas subendothelial lipid content characteristic of plaques in atherosclerotic lesions (black arrows) are readily identified in animals fed a high fat diet at 4x **(e)** and 10x **(f)**. Immunohistochemical analysis of macrophage infiltration demonstrates their absence in control aortas at 4x **(g)** and 10x **(h)** whereas a robust presence (green arrows) is documented in atherosclerotic aortic segments from animals fed a high fat diet at 4x **(i)** and 10x **(j)**. Yellow arrows: plaque identified by IVUS. Black arrow: plaque identified by histology. Green arrows: macrophages identified by immunohistochemistry.
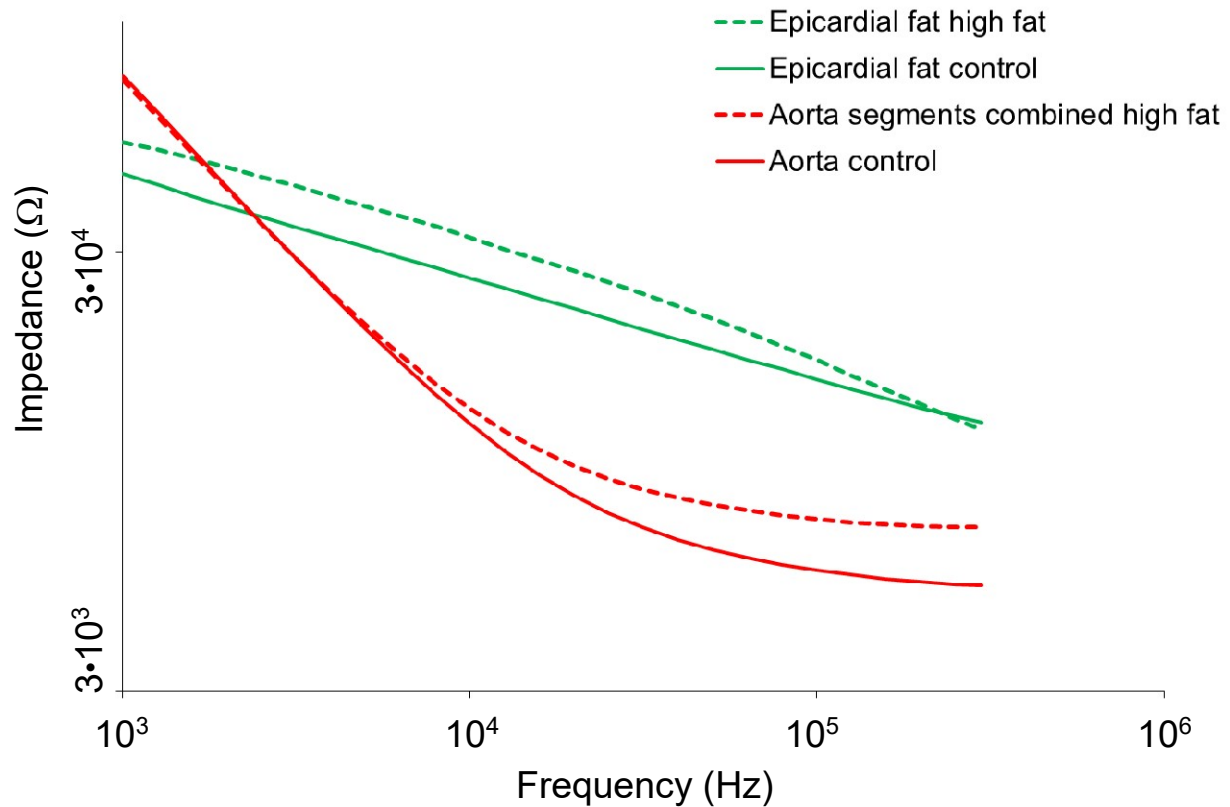
**Figure 5.** Representation of combined EIS impedance spectra from aortas and epicardial fat. Control aortas, atherosclerotic aortas displayed as the mean value of all analyzed segments from various levels of the arterial tree and superimposed profiles of epicardial fat tissue demonstrate stark contrasts in EIS profiles and tissue impedance signatures across the frequency sweep. *P* < 0.05 throughout the frequency sweep from 1 kHz – 300 kHz in epicardial fat tissue compared to aortic segments, Brown-Forsythe test. *P* < 0.05 between control aortas and combined atherosclerotic plaque segments in the frequency range 10 – 300 kHz, Dunnett test.
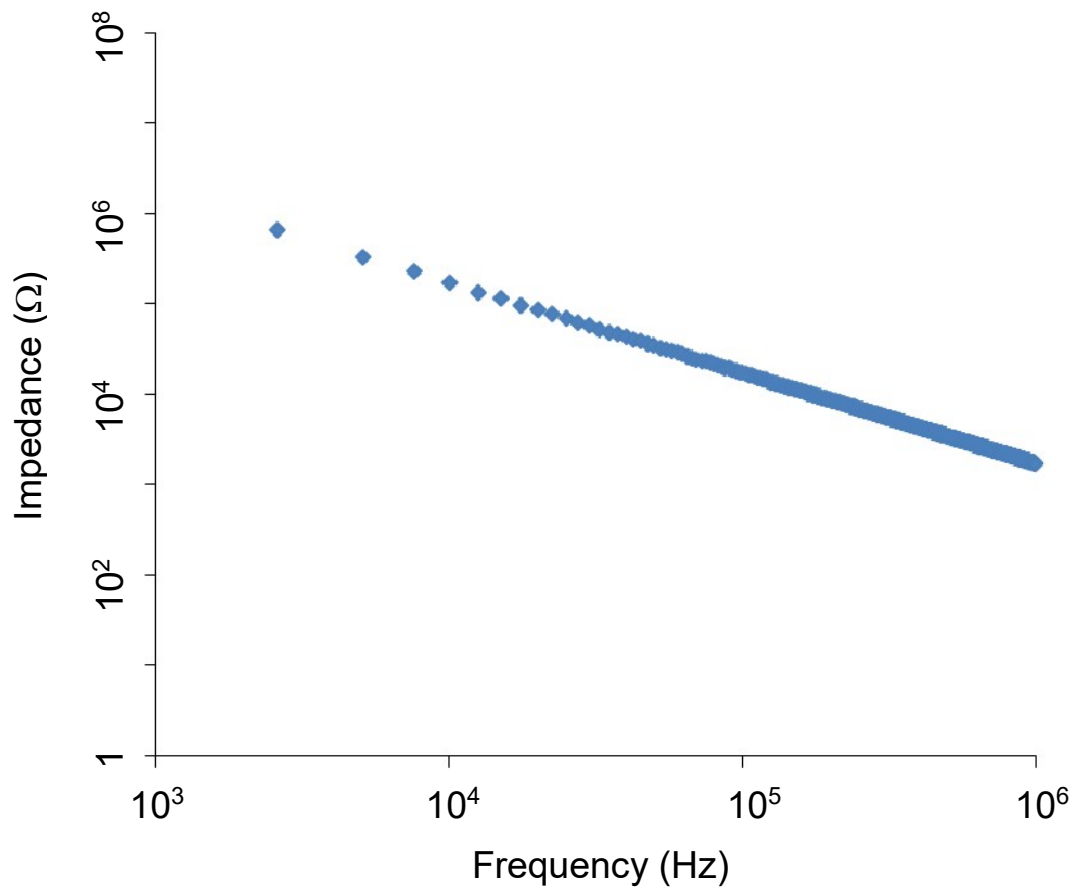
**Figure 6 (a)** Open circuit measurement of impedance magnitude between the two metal wires allows a quantitative estimation of the potential parasitic capacitance. Impedance values arising from the parasitic capacitance are on the order of 10 kOhm at 300 kHz.
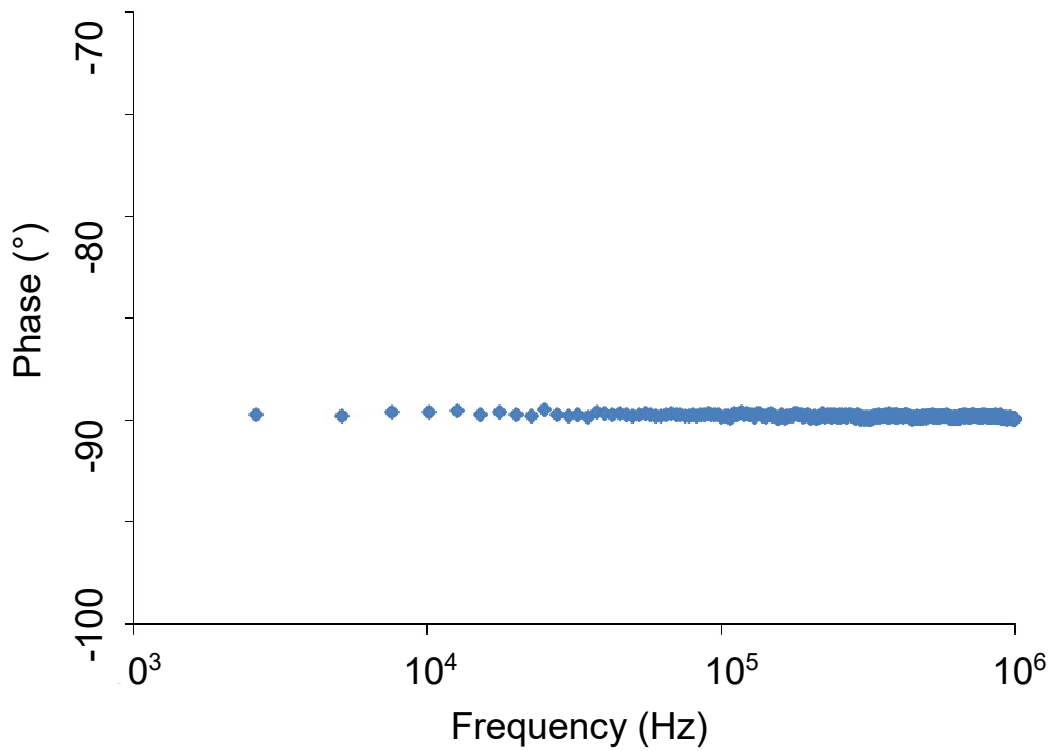
**Figure 6 (b)** Open circuit measurement of phase spectra between the two metal wires allows a quantitative estimation of the potential parasitic capacitance. Impedance values arising from the parasitic capacitance are on the order of 10 kOhm at 300 kHz.

# REFERENCES

**1.** Bourantas, C.V., Garcia-Garcia, H.M., Naka, K.K., Sakellarios, A., Athanasiou, L., Fotiadis, D.I., Michalis, L.K., Serruys, P.W. Hybrid intravascular imaging: current applications and prospective potential in the study of coronary atherosclerosis. *J Am Coll Cardiol*. 61:1369-1378, 2013.

**2.** Brown, M.B., Forsythe, A.B. Robust tests for equality of variances. *J Am Stat Assoc.* 69:364-367, 1974.

**3.** Brown, M.S., Goldstein, J.L. Lipoprotein metabolism in the macrophage: implications for cholesterol deposition in atherosclerosis. *Annu Rev Biochem*. 52:223-261, 1983.

**4.** Cao, H., Yu, F., Zhao, Y., Scianmarello, N., Lee, J., Dai, W., Jen, N., Beebe, T., Li, R., Ebrahimi, R., Chang, D.S., Mody, F.V., Pacella, J., Tai, Y.C., Hsiai, T. Stretchable electrochemical impedance sensors for intravascular detection of lipid-rich lesions in New Zealand White rabbits. *Biosens Bioelectron*. 54:610-616, 2014.

**5.** Castellanos, A., Ramos, A., González, A., Green, N.G., Morgan, H. Electrohydrodynamics and dielectrophoresis in microsystems: scaling laws. *J Phys D Appl Phys.* 36:2584-2597, 2003.

**6.** Chang, J.H., Huang, R., Tai Y.C. High-density 256-channel chip integration with flexible parylene pocket. *IEEE 16th International Conference on Solid-State Sensors, Actuators and Microsystems.* 378 – 381, 2011.

**7.** Chang, J.H., Liu Y., Kang D., Tai Y.C. Reliable packaging for parylene-based flexible retinal implant. *IEEE 17th International Conference on Solid-State Sensors, Actuators and Microsystems.* 2612 – 2615, 2013.

**8.** Chinetti-Gbaguidi, G., Baron, M., Bouhlel, M.A., Vanhoutte, J., Copin, C., Sebti, Y., Derudas, B., Mayi, T., Bories, G., Tailleux, A., Haulon, S., Zawadzki, C., Jude, B., Staels, B. Human atherosclerotic plaque alternative macrophages display low cholesterol handling but high phagocytosis because of distinct activities of the PPARgamma and LXRalpha pathways. *Circ Res*. 108:985-995, 2011.

**9.**     Dunnett, C.W. A multiple comparison procedure for comparing several treatments with a control. *J Am Stat Assoc.* 50:1096-1121, 1955.

**10.**     Ebrahimi, A.P. Mechanical properties of normal and diseased cerebrovascular system. *J Vasc Interv Neurol*. 2:155-162, 2009.

**11.**     Ehara, S., Ueda, M., Naruko, T., Haze, K., Itoh, A., Otsuka, M., Komatsu, R., Matsuo, T., Itabe, H., Takano, T., Tsukamoto, Y., Yoshiyama, M., Takeuchi, K., Yoshikawa, J., Becker, A.E. Elevated levels of oxidized low density lipoprotein show a positive relationship with the severity of acute coronary syndromes. *Circulation*. 103:1955-1960, 2001.

**12.**     Geselowitz, D.B. An application of electrocardiophic lead theory to impedance plethysmography. *IEEE Trans Bio-Med Eng*. 18:38-41, 1971.

**13.**     Grimnes, S., Martines, Ø.G. Sources of error in tetrapolar impedance measurements on biomaterials and other ionic conductors. Sources of error in tetrapolar impedance measurements on biomaterials and other ionic conductors. *J. Phys. D: Appl. Phys.* 40:9, 2007.

**14.**     Fakirov, S., Evstatiev M., Petrovich S. Microfibrillar reinforced composites from binary and ternary blends of polyesters and nylon 6. *Macromolecules*. 26:5219-5226, 1993.

**15.**     Jaffer, F.A., Vinegoni, C., John, M.C., Aikawa, E., Gold, H.K., Finn, A.V., Ntziachristos, V., Libby, P., Weissleder, R. Real-time catheter molecular sensing of inflammation in proteolytically active atherosclerosis. *Circulation*. 118:1802-1809, 2008.

**16.**     Koike, T., Liang, J., Wang, X., Ichikawa, T., Shiomi, M., Sun, H., Watanabe, T., Liu, G., Fan, J. Enhanced aortic atherosclerosis in transgenic Watanabe heritable hyperlipidemic rabbits expressing lipoprotein lipase. *Cardiovasc Res*. 65:524-534, 2005.

**17.**     Konings, M.K., Mali, W.P., Viergever, M.A. Development of an intravascular impedance catheter for detection of fatty lesions in arteries. *IEEE Trans Med Imaging*. 16:439-446, 1997.

**18.**     Levene, H. Robust tests for equality of variances. *In* Olkin I., Hotelling H., et al. Contributions to probability and statistics: essays in honor of Harold Hotelling. *Stanford University Press*. 278-292, 1960.

19.    Li, X., Ma, T., Tian, J., Han, P., Zhou, Q., Shung, K.K. Micromachined PIN-PMN-PT crystal composite transducer for high-frequency intravascular ultrasound (IVUS) imaging. *IEEE Trans Ultrason Ferroelectr Freq Control*. 61:1171-1178, 2014.

20.    Libby, P. Mechanisms of acute coronary syndromes and their implications for therapy. *N Engl J Med*. 368:2004-2013, 2013.

21.    Libby, P., Lichtman, A.H., Hansson, G.K. Immune effector mechanisms implicated in atherosclerosis: from mice to humans. *Immunity*. 38:1092-1104, 2013.

22.    Lin, J.C.H., Lam, G., Tai Y.C. Viscoplasticity of parylene-C film at body temperature. *IEEE 25th International Conference on Micro Electro Mechanical Systems*. 476-479, 2012.

23.    Ma, T., Zhang, X., Chiu, C.T., Chen, R., Kirk Shung, K., Zhou, Q., Jiao, S. Systematic study of high-frequency ultrasonic transducer design for laser-scanning photoacoustic ophthalmoscopy. *J Biomed Opt*. 19:16015, 2014.

24.    Ma, T., Yu, M., Li, J., Munding, C.E., Chen, Z., Fei, C., Shung, K.K., Zhou, Q. Multi-frequency intravascular ultrasound (IVUS) imaging. *IEEE Trans Ultrason Ferroelectr Freq Control*. 62:97-107, 2015.

25.    Marcu, L., Fishbein, M.C., Maarek, J.M., Grundfest, W.S. Discrimination of human coronary artery atherosclerotic lipid-rich lesions by time-resolved laser-induced fluorescence spectroscopy. *Arterioscler Thromb Vasc Biol*. 21:1244-1250, 2001.

26.    Pelias, M.Z. Classics in arteriosclerosis research: On experimental cholesterin steatosis and its significance in the origin of some pathological processes by N. Anitschkow and S. Chalatow, 1913. *Arteriosclerosis*. 3:178-182, 1983.

27.    Sevanian, A., Hwang, J., Hodis, H., Cazzolato, G., Avogaro, P., Bittolo-Bon, G. Contribution of an in vivo oxidized LDL to LDL oxidation and its association with dense LDL subpopulations. *Arterioscler Thromb Vasc Biol*. 16:784-793, 1996.

28.    Streitner, I., Goldhofer, M., Cho, S., Thielecke, H., Kinscherf, R., Streitner, F., Metz, J., Haase, K.K., Borggrefe, M., Suselbeck, T. Electric impedance spectroscopy of human

atherosclerotic lesions. *Atherosclerosis*. 206:464-468, 2009.

**29.** Streitner, I., Goldhofer, M., Cho, S., Kinscherf, R., Thielecke, H., Borggrefe, M., Suselbeck, T., Streitner, F. Cellular imaging of human atherosclerotic lesions by intravascular electric impedance spectroscopy. *PloS one*. 7:e35405, 2012.

**30.** Suselbeck, T., Thielecke, H., Kochlin, J., Cho, S., Weinschenk, I., Metz, J., Borggrefe, M., Haase, K.K. Intravascular electric impedance spectroscopy of atherosclerotic lesions using a new impedance catheter system. *Basic Res Cardiol*. 100:446-452, 2005.

**31.** Worthley, S.G., Helft, G., Fuster, V., Fayad, Z.A., Shinnar, M., Minkoff, L.A., Schechter, C., Fallon, J.T., Badimon, J.J. A novel nonobstructive intravascular MRI coil: in vivo imaging of experimental atherosclerosis. *Arterioscler Thromb Vasc Biol*. 23:346-350, 2003.

**32.** Xiao, H., Lu, M., Lin, T.Y., Chen, Z., Chen, G., Wang, W.C., Marin, T., Shentu, T.P., Wen, L., Gongol, B., Sun, W., Liang, X., Chen, J., Huang, H.D., Pedra, J.H., Johnson, D.A., Shyy, J.Y. Sterol regulatory element binding protein 2 activation of NLRP3 inflammasome in endothelium mediates hemodynamic-induced atherosclerosis susceptibility. *Circulation*. 128:632-642, 2013.

**33.** Yeo, W.H., Kim, Y.S., Lee, J., Ameen, A., Shi, L., Li, M., Wang, S., Ma, R., Jin, S.H., Kang, Z., Huang, Y., Rogers, J.A. Multifunctional epidermal electronics printed directly onto the skin. *Adv Mater*. 25:2773-2778, 2013.

**34.** Yu, F., Dai, X., Beebe, T., Hsiai, T., 2011a. Electrochemical impedance spectroscopy to characterize inflammatory atherosclerotic plaques. *Biosens Bioelectron*. 30:165-173, 2011.

**35.** Yu, F., Li, R., Ai, L., Edington, C., Yu, H., Barr, M., Kim, E.S., Hsiai, T.K. Electrochemical impedance spectroscopy to assess vascular oxidative stress. *Ann Biomed Eng*. 39:287-296, 2011.

**36.** Yu, F., Lee, J., Jen, N., Li, X., Zhang, Q., Tang, R., Zhou, Q., Kim, E.S., Hsiai, T.K. Elevated electrochemical impedance in the endoluminal regions with high shear stress: implication for assessing lipid-rich atherosclerotic lesions. *Biosens Bioelectron*. 43:237-244, 2013.

**37.** Zeibig, S., Li, Z., Wagner, S., Holthoff, H.P., Ungerer, M., Bultmann, A., Uhland, K.,

Vogelmann, J., Simmet, T., Gawaz, M., Munch, G. Effect of the oxLDL binding protein Fc-CD68 on plaque extension and vulnerability in atherosclerosis. *Circ Res*. 108:695-703, 2011.

**CHAPTER FIVE**

**Absolute quantitation of myocardial blood flow in human subjects with or without myocardial ischemia using dynamic Flurpiridaz F 18 positron emission tomography**

Packard R.R.S., Huang S.-C., Dahlbom M., Czernin J., Maddahi J.

**ABSTRACT**

Absolute quantitation of myocardial blood flow (MBF) by positron emission tomography (PET) is an established method of analyzing coronary artery disease (CAD) but subject to the various shortcomings of available radiotracers. Flurpiridaz F 18 is a novel PET radiotracer which exhibits properties of an ideal tracer. A new absolute perfusion quantitation method with Flurpiridaz was developed, taking advantage of the early kinetics and high first-pass extraction by the myocardium of this radiotracer, and the first in human measurements of MBF performed in 7 normal subjects and 8 patients with documented CAD. PET images with time-activity curves were acquired at rest and during adenosine stress. In normal subjects, regional MBF between coronary artery territories did not differ significantly, leading to a mean global MBF of 0.73 mL/min/g at rest and 2.53 mL/min/g during stress, with a mean global myocardial flow reserve (MFR) of 3.70. CAD vascular territories with <50% stenosis demonstrated a mean MBF of 0.73 at rest and 2.02 during stress, leading to a mean MFR of 2.97. CAD vascular territories with ≥50% stenosis exhibited a mean MBF of 0.86 at rest and 1.43 during stress, leading to a mean MFR of 1.86. Differences in stress MBF and MFR between normal and CAD territories, as well as between <50% and ≥50% stenosis vascular territories, were significant ($P<0.01$). Absolute quantitation of MBF in humans with the novel PET radiotracer Flurpiridaz is feasible over a wide range of cardiac flow in the presence or absence of stress-inducible myocardial ischemia. The significant decrease in stress MBF and ensuing MFR in CAD territories allows a clear distinction between vascular territories exhibiting stress-inducible myocardial ischemia and those with normal perfusion.

**INTRODUCTION**

Absolute quantitation of myocardial blood flow (MBF) by positron emission tomography (PET) has a significant role in the clinical evaluation of epicardial and microvascular coronary artery disease (CAD), endothelial dysfunction due to various insults such as dyslipidemia and smoking, and the structural and functional manifestations of metabolic disorders such as diabetes mellitus (*1*). In addition, the noninvasive assessment of regional MBF at rest and during stress is valuable for the early diagnosis of CAD. Although the clinical value of the absolute quantitation of MBF by PET is well recognized, this technique is not often used due to certain practical limitations of currently available PET radiotracers (*2*).

PET radiotracers such as Rb82 chloride, N13 ammonia, and O15 water have been utilized to quantitate absolute MBF. Due to their short half-lives, O15 is limited to facilities with an onsite cyclotron whereas N13 requires either an onsite or nearby cyclotron. Rb82 is generator-produced and is approved for the clinical assessment of myocardial perfusion. However, its very short half-life affects image quality with noisy time-activity curves (TAC) reducing the tracer's ability to quantify myocardial perfusion. A desirable myocardial perfusion agent should have a very high first-pass extraction fraction and track regional myocardial blood flow over a wide range, permitting accurate determination of absolute MBF. The agent should exhibit excellent target-to-non-target uptake ratios, with high uptake in the myocardium and low uptake or rapid clearance from adjacent organs. Furthermore, it should be available as a unit dose from regional cyclotrons, obviating the need for on-site cyclotrons or costly Rb82 generators (*2*).

Flurpiridaz is a novel PET myocardial perfusion imaging (MPI) agent labeled with F 18. It is a structural analog of the insecticide pyridaben, a known inhibitor of the NADH:ubiquinone oxidoreductase also known as mitochondrial complex-1 (MC-1) of the electron transport chain (*3*). Flurpiridaz inhibits MC-1 by competing for binding with ubiquinone without affecting the

viability of cardiomyocytes. This radiotracer exhibits a rapid uptake and slow washout from cardiomyocytes (*3*). Experimental PET imaging in rats, rabbits and nonhuman primates demonstrates a high and sustained cardiac uptake which is proportional to blood flow (*4*). In rats, the first-pass extraction fraction of Flurpiridaz by the myocardium is 94% (*5*). This is a result of the high density of mitochondria in cardiac muscle (which comprise 20-30% of the myocardial intracellular volume) doubled by the lipophilicity of the compound and its high binding affinity to MC-1 (*4*). The flow-independent extraction fraction of Flurpiridaz implies a linear relationship between uptake and MBF, an important attribute for stress MBF measurements (*5*). In a pig model, Flurpiridaz exhibits higher activity ratios of the myocardium vs. the blood, liver and lungs compared to N13 ammonia (*6*). Moreover, Flurpiridaz has an excellent correlation with radioactive microspheres in assessing absolute quantitation of regional MBF over flow ranges from 0.1 – 3.0 mL/min/g (*6*) (*7*). This radiotracer also permits evaluation of myocardial infarction size in rats (*8*). Importantly, the isotope F 18 has a 110min half-life, making delivery of unit doses from regional cyclotrons feasible.

Use of this compound in human studies (*2*) (*9*) (*10*) demonstrated excellent quality myocardial images in addition to exhibiting many desirable properties of an ideal myocardial perfusion tracer including high myocardial uptake, slow myocardial clearance, and high myocardial-to-background contrast (*3*) (*4*) (*5*). In the present study, we sought to perform the absolute quantitation of MBF and derive the MFR using this compound in a group of normal subjects and CAD patients.

Methods to use Flurpiridaz for the quantitation of myocardial perfusion have been proposed and validated in a pig model (*6*) in which a 2-tissue compartmental model was used to fit myocardial kinetics of 10 or 20 minutes and to estimate myocardial perfusion. The modeling approach was similar to the one for N13 ammonia cardiac PET studies, except labeled metabolites in the blood were ignored and the tracer binding deemed irreversible. This approach is susceptible to potential

161

variations in labeled metabolites in the blood and subject movement which is a major concern with the high spatial imaging resolution of current PET/CT scanners. Others proposed using a static scan to simplify the quantitation procedure (*7*). They found that in the pig model the MFR obtained with the static scan approach matched the value obtained with microspheres, provided the scan time is from 5 to 10 min and the value is normalized by the blood pool activity in the 0 to 3 min image. The approach, however, still required the subject to be scanned starting with tracer injection time, and it did not provide accurate values for MBF.

In this study, we employ a quantitation method that can provide quantitative MBF using Flurpiridaz F 18. The method utilizes the early kinetics of myocardial uptake of the tracer . It takes advantage of the high first-pass extraction fraction of the tracer (*5*), i.e. no compartmental modeling is required and is less dependent on the assumptions necessitated by other proposed approaches discussed above. Since the method depends only on the dynamic images of a very short early time (less than two minutes), it is not as sensitive to subject movements. The method was applied both to normal subjects with low likelihood of myocardial ischemia and CAD patients with stress-inducible myocardial ischemia.

**METHODS**

**Human Subject/Patient Selection**

Patients included in the present study participated in the phase II clinical trial analyzing the characteristics of Flurpiridaz in PET MPI (clinicaltrials.gov identifier: NCT00849108), with inclusion/exclusion criteria previously detailed (*10*). All the patients included in the present study were enrolled at the Ronald Reagan UCLA Medical Center and signed an informed consent approved by the local institutional review board. There were a total of 7 normal subjects and 8 CAD patients **(Table 1)**. Participants were instructed to have no caffeine intake for 24h prior to pharmacological stress testing. As previously described (*9*) (*10*), normal subjects were recruited on the basis of their low likelihood of having myocardial ischemia based on a standard questionnaire which includes age, sex, presence or absence of angina pectoris and characteristics of anginal symptoms, when present. None of the normal subjects underwent coronary angiography. In patients who underwent coronary angiography (CAD patients), vascular territories were separated based on a diameter stenosis < 50% or ≥ 50%. For each participant, two Flurpiridaz PET studies were performed, one at rest and one with adenosine stress.

**Preparation of Flurpiridaz F 18**

The radiotracer Flurpiridaz was prepared by Lantheus according to a procedure published previously (*9*).

**PET Imaging Procedures**

Two Flurpiridaz PET imaging sessions were performed in each subject/patient. The first was done at rest, and either on the same day or the following day, the PET imaging was repeated under stress with adenosine infused at a rate of 140 mcg/kg body weight/min for 6 minutes, starting at 3 minutes before the injection of the tracer. 11 of the PET studies (6 normal and 5 CAD) were done using a same-day protocol, and 4 (1 normal and 3 CAD) were done using a 2-

day protocol.  For the same day studies, the rest study was performed first, and the stress study was performed 52.9 ± 11.2min later, as previously reported (*10*).  At 60min after the rest injection, the tracer distribution in the heart did not change much over a 5min period, and the TAC values measured before the stress injection were averaged and subtracted from the stress TAC before the modeling analysis was performed.  There was no significant increase in noise in the TACs when using the subtraction procedure in the same-day protocol as compared with the 2-day protocol.  For each imaging session, the subject was positioned supine in a PET/CT scanner (Biograph 64, Siemens Inc.).  Following CT imaging of the chest, Flurpiridaz (5 mCi) was administered IV as a slow bolus over 10 sec followed by a 5-10 mL saline flush.  PET imaging was started concomitantly to Flurpiridaz injection and list mode data were collected for 10 minutes.  Thereafter, the list mode data were framed into a scan sequence of 12x10, 4x30, 1x60, and 1x300 sec.  Images were reconstructed using a 2D OSEM iterative algorithm (8 subsets and 21 iterations).  No post reconstruction filtering was applied, resulting in a spatial resolution of 6.5 mm FWHM (full width at half maximum).

**Image Analysis**

The dynamic transaxial images were first reoriented into short axis slices.  These were then used to produce dynamic polar maps, where the sampling points were defined on a 6 minute summed framed at the end of the acquisition.  Regions of Interest (ROI) corresponding to the three coronary territories were defined on the dynamic polar maps.  A polar map was used to normalize the size and shape of hearts from different individuals and allow ROI to be obtained more consistently and objectively.  Using these ROI, tissue time-activity-curves (TACs) were generated from the dynamic polar maps.  A blood pool TAC was generated by placing a small ROI in the center of the left ventricle of the last frame of the dynamic short axis images.  This procedure was applied to both the rest and stress data (*11*).

## Absolute Quantitation of Myocardial Blood Flow

Quantitative myocardial perfusion in each perfusion territory was estimated using the tracer uptake kinetics within the first 90 seconds post tracer injection. Within this period, the tracer was assumed to be taken up by the myocardium without significant clearance, and with very few if any labeled metabolites contained in the blood during this early time period. Therefore, the radioactivity concentration in myocardial segment i can be described by Eq. 1 below.

$$C_i(t) = F_i \int_0^t C_p(\tau)d\tau + V_{bi}C_p(t), \quad \text{for i} = 1, 2, 3 \qquad \text{Eq. 1}$$

where the subscripts i=1, 2, and 3 indicate, respectively, the myocardial activities in the three perfusion territories (i.e., LAD, LCx, RCA), $C_p(t)$ is the radioactivity concentration in blood, and $V_{bi}$ is the vascular volume in that myocardial segment. Due to the partial volume effect and the spillover of activities between myocardium and blood pool, the measured radioactivity concentration in the blood pool ($C_p(t)$ ) and in the myocardial regions of the three perfusion territories ($C_i(t)$ , for i=1,2,3) from the dynamic PET images can be described by the following equations.

$$C_p(t)_{measured} = RC_{bp} \times C_p(t) + \sum_{i=1}^{3} SPF_{mbi} \times C_i(t)$$

$$C_i(t)_{measured} = RC_i \times C_i(t) + SPF_{bmi} \times C_p(t), \quad \text{for } i = 1, 2, 3 \qquad \text{Eq, 2}$$

$$= RC_i \times F_i \int_0^t C_p(\tau)d\tau + (V_b + SPF_{bmi}) \times C_p(t), \quad \text{for } i = 1, 2, 3$$

where RC is the recovery coefficient due to the partial volume effect (of the myocardium or the blood pool); SPF is the spillover fraction (the subscript bmi denotes the spillover from blood pool to myocardium region i, and mbi denotes the spillover fraction from myocardium segment i to the blood pool ROI).

Equation 2 was used to fit the measured myocardial TACs. With the approximation that $RC_{bp}$ = 0.95 and $SPF_{mbi}$ = 0.05/3 (i=1, 2, and 3), blood pool TAC ($C_p(t)$) was calculated from the measured blood pool TAC and the myocardial TACs directly, as

$$C_p(t) = \frac{1}{RC_{bp}} \times [C_p(t)_{measured} - \sum_{i=1}^{3} SPF_{mbi} \times C_i(t)]$$

$$= \frac{1}{0.95} \times [C_p(t)_{measured} - \sum_{i=1}^{3} (0.05/3) \times C_i(t)]$$

Eq. 3

Furthermore, the spillover fraction from blood pool to myocardium plus the vascular volume was approximated as 1.0 minus the RC of the corresponding myocardial segment. That is,

$(SPF_{bmi} + V_{bi}) = 1.0 - RC_i$     for i=1, 2, and 3.      Eq. 4

An iterative procedure in which the measured TAC of each perfusion territory was regressed one at a time, with the estimated $C_p(t)$ fixed from a previous iteration. After each round of regression of the measured TACs of the three perfusion territories, $C_p(t)$ was updated (with Eq. 3). The procedure was then repeated. Usually, the estimated values of $F_i$ and $RC_i$ converged within ~3 iterations.

Global myocardial perfusion ($C_g(t)_{measured}$) was estimated from the weighted average of the TACs of the three territories (weighted by their approximate areas on the polar map). That is,

$C_g(t)_{measured}$ = (7 $C_1(t)_{measured}$ +5 $C_2(t)_{measured}$ + 5 $C_3(t)_{measured}$)/17.      Eq. 5

The equation used for estimating the global myocardial perfusion is the same as those for each myocardial segment (i.e., Eq. 2), except that the $C_p(t)$ estimated at the end of the regression for individual myocardial segment was used for estimating the global myocardial perfusion.

After $F_i$ was determined, myocardial blood flow (MBF) was obtained by assuming a first-pass extraction fraction of 0.94 (*5*). That is,

$$MBF_i = F_i / 0.94. \hspace{4cm} \text{Eq. 6}$$

The units of $MBF_i$ are in (mL of blood)/min/(g of myocardium), assuming that the specific density of myocardium is ~ 1.0 g/mL. Since the kinetic data were corrected for partial volume, spillover, and vascular activity, the MBF value obtained corresponded to the blood perfusion value in myocardium with blood in the vasculature removed.

**Calculation of Myocardial Flow Reserve**

Myocardial flow reserve for each myocardial segment was calculated as the ratio of the segment's MBF value with adenosine infusion to the MBF value at rest.

$$MFR = (\text{MBF during adenosine infusion})/(\text{MBF at rest}) \hspace{2cm} \text{Eq. 7}$$

**Statistical Analysis**

All results are expressed as means and standard deviations. An analysis of variance and repeated measures analysis was performed. The natural logarithm of the territories was used in the repeated measures analysis for variance stability and sphericity assumption. A Bonferroni multiple comparison adjustment was performed. A P-value of less than 0.05 was considered

statistically significant.  IBM SPSS Statistics for Windows, Version 20.0 was used for the statistical

analyses.

**RESULTS**

A representative polar map depicting relative perfusion in a CAD patient with stress-inducible ischemia is shown, demonstrating a reversible defect mostly in the LAD distribution **(Fig. 1)**. The tracer kinetics in a normal myocardial region along with the blood pool time-activity curve (TAC) is illustrated **(Fig. 2)**. The model fitted curves at the end of the MBF estimation are also shown.

The MBF in each vascular territory of normal subjects with low likelihood of myocardial ischemia under rest and stress conditions with ensuing myocardial flow reserve is depicted as means ± standard deviations **(Fig. 3)**. There were no significant differences in flow between the LAD, LCx and RCA territories in each condition, with P-values of 0.70 for resting myocardial blood flow (RMBF), 0.11 for stress myocardial blood flow (SMBF) and 0.99 for MFR. For each vascular territory, there was a significant difference between RMBF and SMBF, RMBF and MFR, SMBF and MFR with P-values < 0.001.

The regional MBF in the LAD, LCx and RCA territories as well as global MBF derived from weighted contributions from each vascular territory (Eq. 5) in normal subjects with low likelihood of myocardial ischemia compared to regional MBF in < 50% stenosis and ≥ 50% stenosis vascular territories is detailed **(Table 2)**. In low likelihood territories, mean ± standard deviation of global MBF was 0.73 ± 0.13 mL/min/g at rest and 2.53 ± 0.48 mL/min/g at stress, leading to a MFR of 3.70 ± 0.39. In < 50% stenosis vascular territories, mean ± standard deviation of MBF was 0.73 ± 0.09 at rest and 2.02 ± 0.40 at stress, leading to a MFR of 2.97 ± 0.76. In ≥ 50% stenosis vascular territories, mean ± standard deviation of MBF was 0.86 ± 0.21 mL/min/g at rest and 1.43 ± 0.31 mL/min/g at stress, leading to a MFR of 1.86 ± 0.59. There was no significant difference in rest MBF in global or regional vascular flow between the low likelihood and < 50% stenosis (P=0.97) or ≥ 50% stenosis (P=0.73) vascular territories. Differences in stress MBF (P=0.004) and MFR (P=0.003) between global flow in low likelihood and <50% vascular territories were

significant. Similarly, differences in stress MBF (P=0.001) and MFR (P=0.001) between global flow in low likelihood and ≥ 50% vascular territories were significant. Differences were also significant when comparing individual vascular territories from normal subjects to individual vascular territories with < 50% stenosis or ≥ 50% stenosis from CAD patients (data not shown). Finally, comparing < 50% stenosis to ≥ 50% stenosis vascular territories, there was no significant difference in rest MBF (P=0.073) but there was a significant difference in stress MBF (P<0.001) and MFR (P<0.001).

The regional MBF and MFR in the vascular territories of normal subjects with low likelihood of myocardial ischemia (n=21 territories) vs. the vascular territories of CAD patients with < 50% stenosis (n=12 territories) and ≥ 50% stenosis (n=12 territories) is illustrated further and presented as means ± standard deviations **(Fig. 4)**. There was no significant difference in RMBF between conditions. As detailed above, SMBF and MFR was significant when comparing low likelihood to < 50% stenosis, low likelihood to ≥ 50% stenosis and < 50% stenosis to ≥ 50% stenosis vascular territories.

The scatterplot of the MFR obtained from each individual territory in normal subjects with low likelihood of myocardial ischemia compared to < 50% stenosis and ≥ 50% stenosis territories in CAD patients is illustrated in detail **(Fig. 5)**. Horizontal bars represent the respective mean values: 3.70 in low likelihood, 2.97 in < 50% stenosis and 1.86 in ≥ 50% stenosis. Differences were significant when comparing the MFR from low likelihood to < 50% stenosis (P=0.003), low likelihood to ≥ 50% stenosis (P=0.001) and < 50% stenosis to ≥ 50% stenosis vascular territories (P<0.001).

**DISCUSSION**

The present study is the first in human analysis of the absolute quantitation of MBF using Flurpiridaz PET. Analyses were performed in both normal subjects and CAD patients providing MBF data over a wide range of conditions. The importance of the absolute quantitation of MBF and its prognostic implication in the presence of abnormal MFR has been previously established. O15 water PET accurately detects CAD (*12*) and N13 ammonia MFR has a strong association with prognosis (*13*) (*14*). Rb82 MBF and MFR correctly detects 3-vessel CAD (*15*) and predicts adverse cardiovascular events (*16*) beyond relative MPI and the sum stress score (*17*). Moreover, absolute quantitation of MBF with Rb82 is an independent predictor of cardiac mortality in patients with known or suspected CAD and provides incremental risk stratification over established clinical variables and relative MPI (*18*).

Flurpiridaz exhibits many advantages over existing PET radiotracers, and meets the conditions of an ideal perfusion tracer (*2*). Flurpiridaz has a high extraction fraction by the myocardium, a short positron range providing high-resolution images, and a relatively long half-life of 110 minutes allowing it to be produced at regional cyclotrons. This novel PET radiotracer is compatible with both pharmacological and exercise stress imaging.

The present study demonstrates the feasibility of absolute quantitation of MBF with Flurpiridaz. Since no reference standard was used in the present study, the accuracy of the quantitation values reported is subject to caution. The population was too small to use invasive angiography as a reference standard. All MBF quantitation processes involve some assumptions, with potential errors introduced cancelling out when calculating MFR. Our results suggest that MBF obtained through Flurpiridaz is in a similar range as those measured with other radiotracers such as Rb82 chloride, N13 ammonia and O15 water. Most of the experience and literature pertains to N13 and Rb82 (*1*). Previous reference values using these radiotracers reported a rest MBF of

0.62 – 0.92 mL/min/g and a stress MBF of 1.97 – 3.55 mL/min/g in normal subjects, usually leading to a MFR of 3.5 – 4.0. Patients with CAD display a significantly lower stress MBF typically leading to a MFR of 2.0 – 2.5 in borderline abnormal studies and < 2.0 in frankly abnormal studies (1). MFR cutoffs for abnormal studies vary somewhat depending on the radiotracer used as well as the reference gold standard (fractional flow reserve during cardiac catheterization or ≥ 50% vs. ≥ 70% diameter stenosis during angiography) (19). Importantly however, our results obtained with Flurpiridaz do not necessitate a correction such as that often utilized in the case of Rb82 for example (20). This is due to the sigmoid-shaped cardiac extraction fraction of Rb82 leading to low extraction fractions at elevated myocardial blood flows. Future studies will be conducted to provide values of absolute myocardial blood flow and ensuing myocardial flow reserve with cutoffs below which the presence of CAD, whether epicardial or microvascular, may be predicted in a clinically useful manner.

Importantly, regional perfusion and myocardial uptake measurements are feasible with Flurpiridaz PET imaging. In normal subjects, a uniformity of MBF was observed at rest and during adenosine stress in the LAD, LCx and RCA territories. Similar results have been observed with other radiotracers (21) (22).

Interestingly, CAD vascular segments with <50% stenosis exhibited stress MBF and MFR values between those from vascular segments with ≥50% stenosis and those from normal subjects. Consistent with previous reports, this suggests that despite being labeled as angiographically non-significant, these territories are not normal and exhibit hemodynamic and metabolic abnormalities. Previously suggested mechanisms include abnormalities of endothelium-dependent and/or smooth muscle cell-dependent vasomotion, with these patients being at increased risk of future cardiovascular events (1).

The MBF quantitation procedure we adopted only uses the Flurpiridaz kinetics of the first 1.5 minutes. The procedure does not require taking blood samples from the patients to provide the input function, and thus does not need cross-calibration of the PET measurement with other devices such as well counters that frequently introduce large errors in practical situations. The procedure is based on a few assumptions that are supported by known kinetics of Flurpiridaz in blood and myocardium. First, it assumes that within the first 1.5 minutes post tracer injection there are few if any F 18 labeled metabolites in the blood. This is supported by results in animal and human studies. Another assumption is that, after myocardial uptake of Flurpiridaz, the compound is not cleared from the myocardium in a significant amount within 1.5 minutes. This is corroborated by animal and human studies demonstrating that the clearance rate constant of the compound in the myocardium was measured in hours (*3*) (*4*) (*5*) (*6*) (*9*) and no additional clearance component (e.g., due to the interstitial space) of faster clearance rate was observed in the kinetics of the first-pass extraction fraction measurements (*5*). Thus the modeling of the myocardial uptake of Flurpiridaz as an irreversible process (Eq. 1) is quite valid. The two assumptions made here were also made by Sherif et al (*7*) in their calculations of MFR and the tracer retentions in the myocardium of pig models, except that they calculated the retentions using a longer period of scan time (5-10 min for myocardial activity and 0-3 min for area under the blood TAC). The longer times made the assumptions less valid. Although the errors created were somewhat cancelled when calculating the MFR (as a ratio of stress and rest retentions), the retention measurements they obtained did not correlate well with the MBF determined by microspheres.

Another reason for their retention measurements failing to match the microsphere-measured perfusion is that their retention measurements did not consider partial volume and spillover effects in their calculations. In the procedure used in the present study, the partial volume effect and spillover of activities were explicitly accounted for (Eq. 2), although some assumptions and

approximations (Eqs. 3 and 4) were employed to simplify the procedure and make the estimation of myocardial perfusion more tractable and robust. The approach proposed by Nekolla et al (*6*) using a 2-tissue compartment did account for the partial volume effect and spillover fraction similar to our procedure. However, their approach using ten or twenty minutes of kinetics (0-10 or 0-20 min) is susceptible to subject movement during the imaging time that is difficult to avoid, especially for stress studies. Also, the assumption of having negligible labeled metabolites in the blood is no longer valid for Flurpiridaz over such a long time period.

A potential disadvantage of using short kinetics to quantitate perfusion is the lack of adequate count statistics to give a reliable assessment, such as with Rb82 determined MBF. However, due to the high first-pass extraction fraction of Flurpiridaz by the myocardium, the dynamic PET images of the heart in the first 2 minutes were of adequate quality and allowed measuring kinetics in myocardial regions well **(Fig. 2)**. The use of modeling fitting to the measured kinetics rather than just using a single integrated value also maximizes the value of the available data for estimation of myocardial perfusion. In the current study, the relative small variability of the MBF estimates obtained under both rest and stress conditions in normal subjects and in the  myocardial segments of <50% stenosed CAD patients clearly demonstrate the stability of the measurements based on the 1.5-min short kinetics and support the robustness of the quantitation procedure used.

In our MBF quantitation procedure, we also used a fixed value of 0.94 for the first-pass extraction fraction. This first-pass extraction fraction value was previously determined in a Langendorff preparation of rat heart (*5*) and was found to be independent of perfusion flow. Although the first-pass extraction fraction was taken directly from an animal study, its use in the present study gives human MBF values comparable to the commonly accepted values obtained by other methods. Even though the extraction fraction in humans may deviate slightly from 0.94, the resulting MBF

would not change significantly. In addition, a high first-pass extraction fraction is not significantly dependent on perfusion, and hence the conversion of tracer uptake to MBF can be greatly simplified (Eq. 6).

Certain aspects of the current MBF quantitation procedure, however, can be further improved to make it more useful in the clinical setting. For example, the extension of the method for generating MBF parametric images could take the quantitation to a level usable for routine clinical studies. Subsequent studies will measure MBF over finer coronary segments such as the standardized 17-segment left ventricular myocardial model which may be of greater clinical use. In the present study, normal subjects were recruited on the basis of their low likelihood of having myocardial ischemia. Given the presence of classic cardiovascular risk factors **(Table 1)** in this group, and despite their absence of angina, anginal equivalent or evidence of stress-inducible ischemia by electrocardiogram or PET MPI, this group may have had subclinical coronary artery disease. This may theoretically have led the stress MBF in the group of normal subjects to be lower than in a group of young subjects with complete absence of cardiovascular risk factors which were not included in the present study. Also, comparison of MBF measurements obtained through Flurpiridaz with those currently accepted using N13 ammonia PET in the same subjects is expected to provide further validation or improvement of the quantitative MBF method reported in this study, e.g. confirmation of the first-pass extraction fraction of 0.94.

Using a robust perfusion quantitation procedure, absolute quantitation of MBF using Flurpiridaz F 18 cardiac PET imaging is feasible in both normal subjects with low likelihood of myocardial ischemia and CAD patients. No significant differences in MBF (either at rest or with adenosine stress) and MFR were found among the three coronary perfusion territories in subjects with no stress-inducible ischemia. In CAD patients, diseased vascular segments had significantly lower MBF in response to adenosine stress and thus a reduced MFR. Future studies will determine

cutoff values for stress MBF and MFR in patients with CAD for direct clinical applicability. We believe patient risk stratification using PET imaging will be feasible in a broad clinical setting both by utilizing relative perfusion as well as through the absolute quantitation of MBF. These initial results suggest that Flurpiridaz, which is not yet approved by the United States Food and Drug Administration as a PET MPI agent, is uniquely poised as a radiotracer to fulfill all these requirements.

**FIGURES AND TABLES**

A            B            C

D            E            F
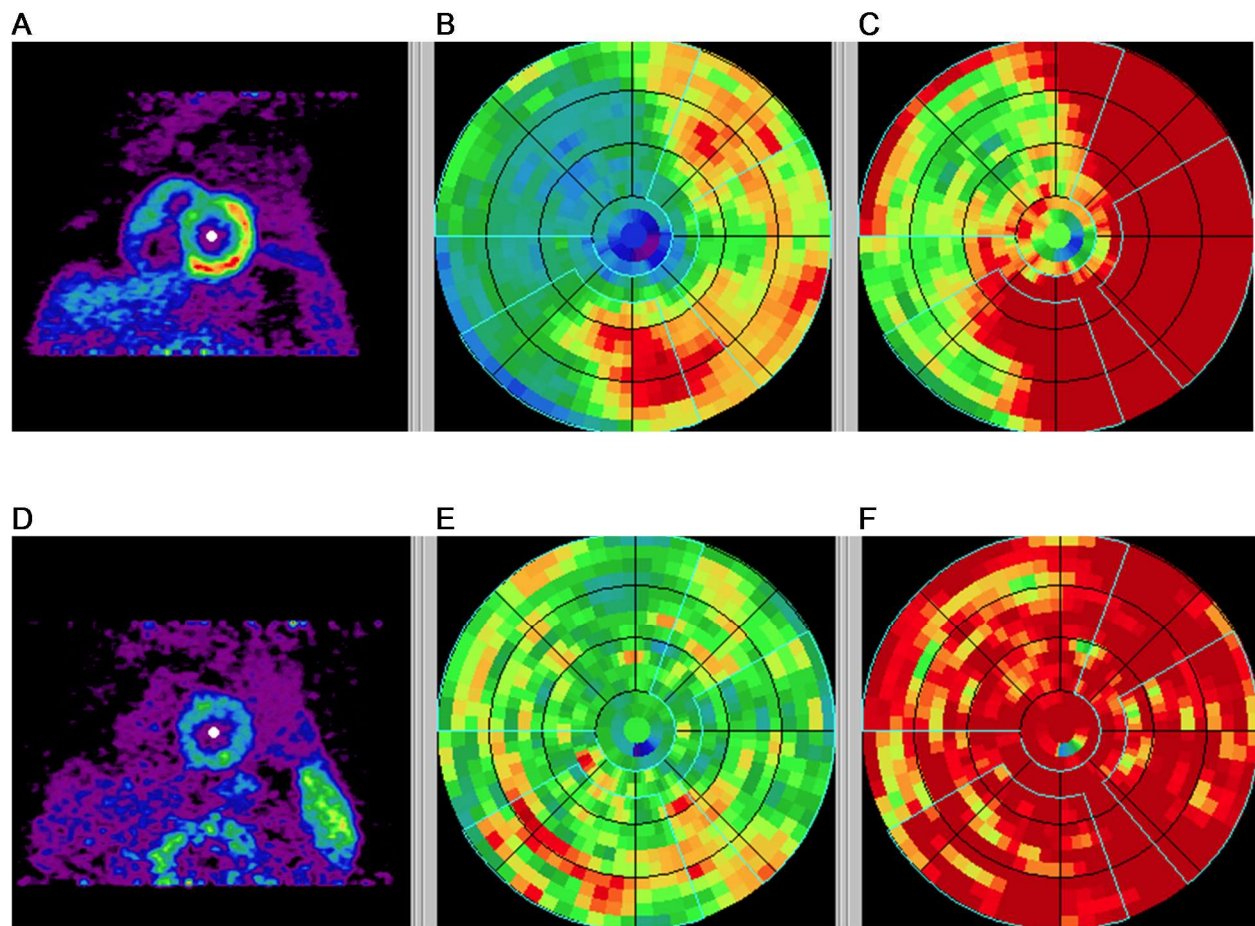


**Figure 1.** Polar maps in a CAD patient with stress images (A-C) and rest images (D-F) demonstrating a reversible defect affecting mostly the LAD territory. Early summed images (0.5-2 min) were re-oriented into short-axis views (A, D), polar maps generated (B, E), and normalized based on averages of normal subjects (C, F). The vascular territories and the left ventricular chamber were defined on the polar map automatically.
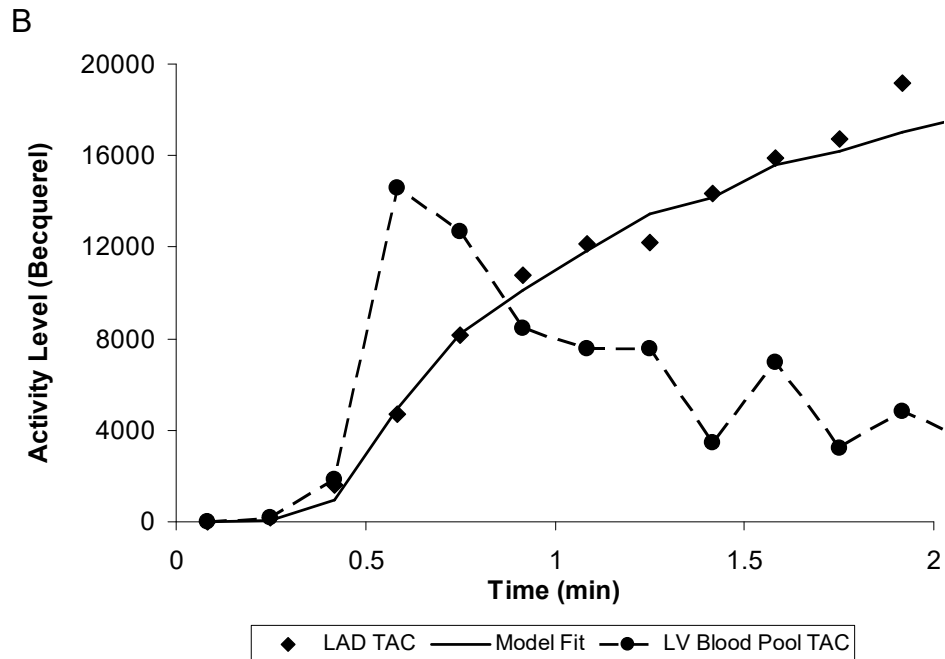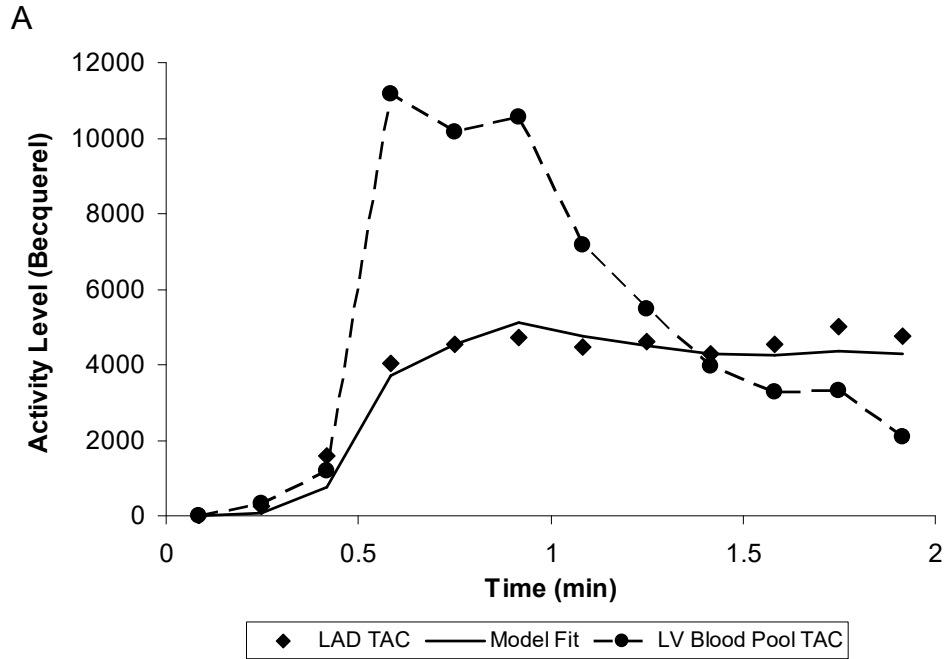
**Figure 2.** Left ventricular blood pool time-activity curve (TAC) (circle symbols) and Left Anterior Descending Artery TAC (lozenge symbols) obtained from predefined vascular ROI on the polar map during rest (A) and with adenosine stress (B) in a normal subject. The solid curve is the model fit to the vascular territory myocardial TAC based on a single-compartment model.

178
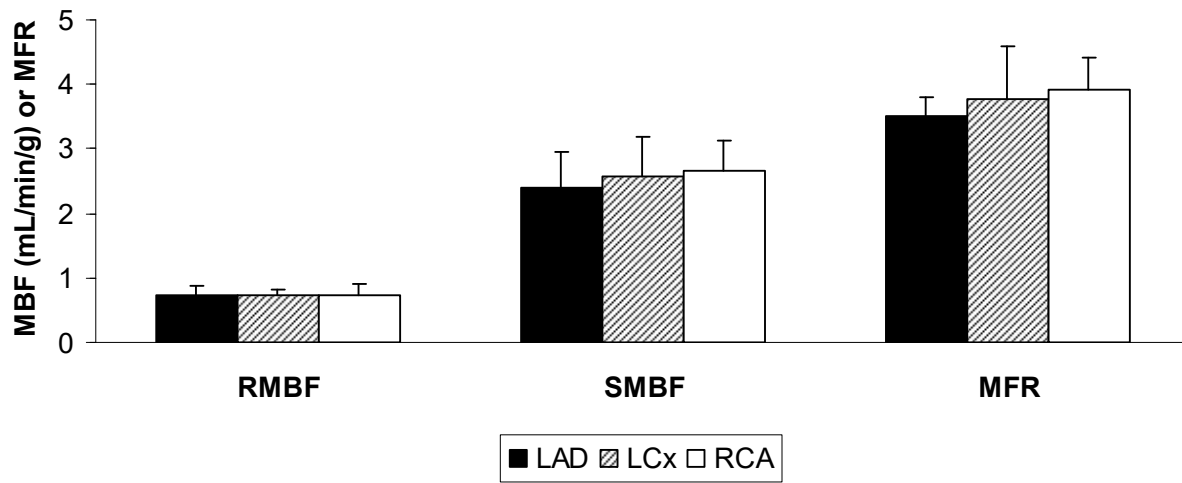
**Figure 3**.  Regional MBF at rest (RMBF) and during adenosine stress (SMBF) and MFR in the 3 vascular territories of normal subjects.
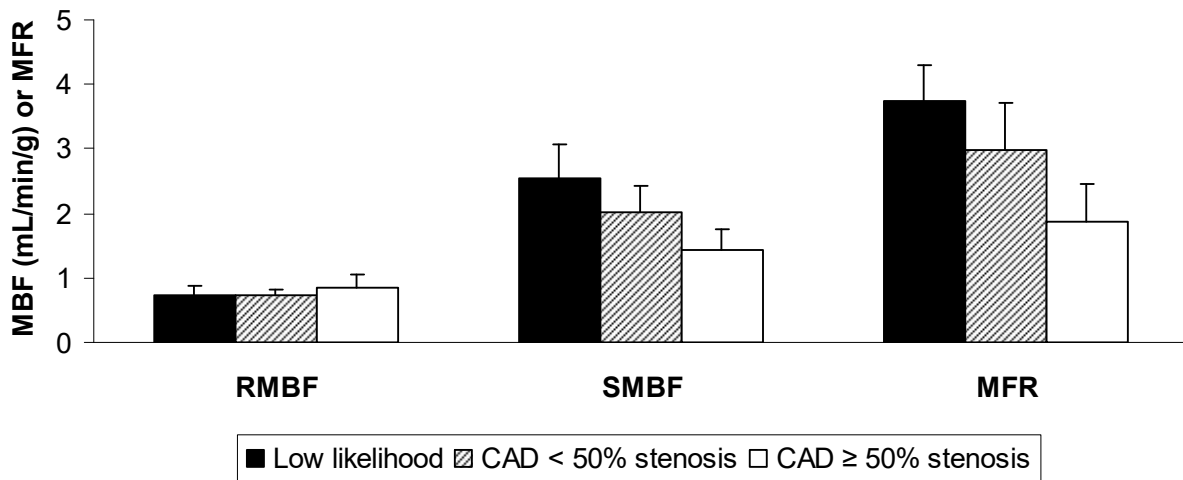
**Figure 4.** Regional MBF at rest (RMBF) and during adenosine stress (SMBF) and MFR in vascular territories of normal subjects with low likelihood of myocardial ischemia vs. vascular territories of CAD patients with < 50% stenosis and ≥ 50% stenosis.
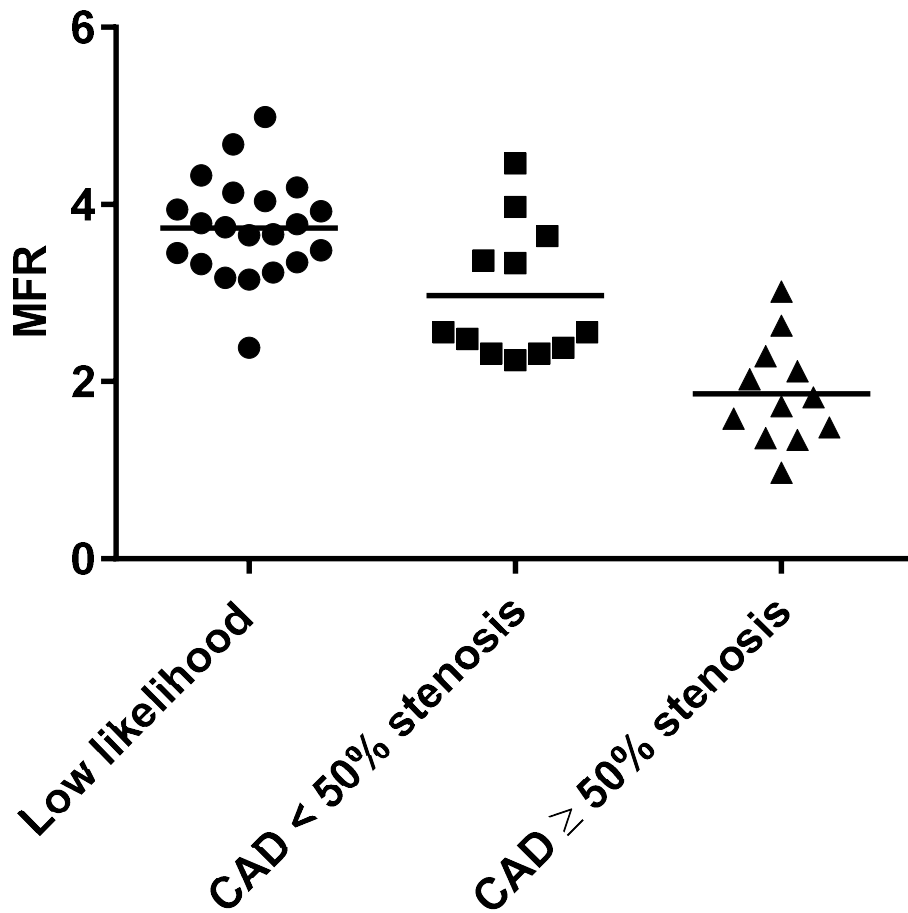
**Figure 5.** Scatterplot of the MFR obtained from each individual territory in normal subjects with low likelihood of myocardial ischemia vs. CAD patients with < 50% stenosis and ≥ 50% stenosis.

|  | Normal subjects (n = 7) | CAD patients (n = 8) |
|---|---|---|
| Age (years) | 66 | 68 |
| Sex (%) | | |
| Male | 86 | 100 |
| Female | 14 | 0 |
| BMI (kg/m$^2$) | 28 | 27 |
| Cardiovascular risk factors (%) | | |
| Hypertension | 43 | 75 |
| Diabetes mellitus | 0 | 50 |
| Dyslipidemia | 71 | 88 |
| Tobacco use - current | 0 | 0 |
| Tobacco use - former | 43 | 75 |
| Tobacco use - never | 57 | 25 |
| Labs (mg/dL) | | |
| LDL | 97 | 86 |
| HDL | 52 | 44 |
| Creatinine | 1.0 | 1.0 |
| Medications (%) | | |
| Antiplatelet agent | 86 | 88 |
| Statin | 71 | 88 |
| ACEI/ARB | 43 | 63 |
| Betablocker | 57 | 75 |

**Table 1.** Baseline characteristics of normal subjects with low likelihood of myocardial ischemia and CAD patients. Values are expressed as means or percentages. CAD: coronary artery disease. LDL: low density lipoprotein. HDL: high density lipoprotein. ACEI: angiotensin converting enzyme inhibitor. ARB: angiotensin receptor blocker.

| | Low likelihood (n=21 territories from 7 subjects) | | | | < 50% stenosis (n=12 territories from 8 patients) | ≥ 50% stenosis (n=12 territories from 8 patients |
|---|---|---|---|---|---|---|
| | **LAD** | **LCx** | **RCA** | **Global** | | |
| **RMBF** | 0.73 ± 0.15 | 0.73 ± 0.09 | 0.74 ± 0.17 | 0.73 ± 0.13 | 0.73 ± 0.09 | 0.86 ± 0.21 |
| **SMBF** | 2.41 ± 0.54 | 2.58 ± 0.60 | 2.67 ± 0.46 | 2.53 ± 0.48 | 2.02 ± 0.40 | 1.43 ± 0.31 |
| **MFR** | 3.50 ± 0.29 | 3.77 ± 0.82 | 3.93 ± 0.47 | 3.70 ± 0.39 | 2.97 ± 0.76 | 1.86 ± 0.59 |

**Table 2.** MBF and MFR in vascular territories characterized by low likelihood of myocardial ischemia, < 50% stenosis and ≥ 50% stenosis. Values are expressed as means ± standard deviation. RMBF: rest MBF. SMBF: adenosine stress MBF. MFR: myocardial flow reserve.

**REFERENCES**

**1.** Schindler TH, Schelbert HR, Quercioli A, Dilsizian V. Cardiac PET imaging for the detection and monitoring of coronary artery disease and microvascular health. *JACC Cardiovasc Imaging.* 2010;3:623-640.

**2.** Maddahi J. Properties of an ideal PET perfusion tracer: new PET tracer cases and data. *J Nucl Cardiol.* 2012;19 Suppl 1:S30-37.

**3.** Yalamanchili P, Wexler E, Hayes M, et al. Mechanism of uptake and retention of F-18 BMS-747158-02 in cardiomyocytes: a novel PET myocardial imaging agent. *J Nucl Cardiol.* 2007;14:782-788.

**4.** Yu M, Guaraldi MT, Mistry M, et al. BMS-747158-02: a novel PET myocardial perfusion imaging agent. *J Nucl Cardiol.* 2007;14:789-798.

**5.** Huisman MC, Higuchi T, Reder S, et al. Initial characterization of an 18F-labeled myocardial perfusion tracer. *J Nucl Med.* 2008;49:630-636.

**6.** Nekolla SG, Reder S, Saraste A, et al. Evaluation of the novel myocardial perfusion positron-emission tomography tracer 18F-BMS-747158-02: comparison to 13N-ammonia and validation with microspheres in a pig model. *Circulation.* 2009;119:2333-2342.

**7.** Sherif HM, Nekolla SG, Saraste A, et al. Simplified quantification of myocardial flow reserve with flurpiridaz F 18: validation with microspheres in a pig model. *J Nucl Med.* 2011;52:617-624.

**8.** Sherif HM, Saraste A, Weidl E, et al. Evaluation of a novel (18)F-labeled positron-emission tomography perfusion tracer for the assessment of myocardial infarct size in rats. *Circ Cardiovasc Imaging.* 2009;2:77-84.

**9.** Maddahi J, Czernin J, Lazewatsky J, et al. Phase I, first-in-human study of BMS747158, a novel 18F-labeled tracer for myocardial perfusion PET: dosimetry, biodistribution, safety, and imaging characteristics after a single injection at rest. *J Nucl Med.* 2011;52:1490-1498.

**10.** Berman DS, Maddahi J, Tamarappoo BK, et al. Phase II safety and clinical comparison

with single-photon emission computed tomography myocardial perfusion imaging for detection of coronary artery disease: flurpiridaz F 18 positron emission tomography. *J Am Coll Cardiol.* 2013;61:469-477.

**11.** Schindler TH, Zhang XL, Vincenti G, et al. Diagnostic value of PET-measured heterogeneity in myocardial blood flows during cold pressor testing for the identification of coronary vasomotor dysfunction. *J Nucl Cardiol.* 2007;14:688-697.

**12.** Kajander S, Joutsiniemi E, Saraste M, et al. Cardiac positron emission tomography/computed tomography imaging accurately detects anatomically and functionally significant coronary artery disease. *Circulation.* 2010;122:603-613.

**13.** Tio RA, Dabeshlim A, Siebelink HM, et al. Comparison between the prognostic value of left ventricular function and myocardial perfusion reserve in patients with ischemic heart disease. *J Nucl Med.* 2009;50:214-219.

**14.** Herzog BA, Husmann L, Valenta I, et al. Long-term prognostic value of 13N-ammonia myocardial perfusion positron emission tomography added value of coronary flow reserve. *J Am Coll Cardiol.* 2009;54:150-156.

**15.** Parkash R, deKemp RA, Ruddy TD, et al. Potential utility of rubidium 82 PET quantification in patients with 3-vessel coronary artery disease. *J Nucl Cardiol.* 2004;11:440-449.

**16.** Fukushima K, Javadi MS, Higuchi T, et al. Prediction of short-term cardiovascular events using quantification of global myocardial flow reserve in patients referred for clinical 82Rb PET perfusion imaging. *J Nucl Med.* 2011;52:726-732.

**17.** Ziadi MC, Dekemp RA, Williams KA, et al. Impaired myocardial flow reserve on rubidium-82 positron emission tomography imaging predicts adverse outcomes in patients assessed for myocardial ischemia. *J Am Coll Cardiol* 2011. 2011;58:740-748.

**18.** Murthy VL, Naya M, Foster CR, et al. Improved cardiac risk assessment with noninvasive measures of coronary flow reserve. *Circulation.* 2011;124:2215-2224.

**19.** Johnson NP, Gould KL. Integrating noninvasive absolute flow, coronary flow reserve, and

ischemic thresholds into a comprehensive map of physiological severity. *JACC Cardiovasc Imaging.* 2012;5:430-440.

**20.**     Saraste A, Kajander S, Han C, Nesterov SV, Knuuti J. PET: Is myocardial flow quantification a clinical reality? *J Nucl Cardiol.* 2012;19:1044-1059.

**21.**     Czernin J, Muller P, Chan S, et al. Influence of age and hemodynamics on myocardial blood flow and flow reserve. *Circulation.* 1993;88:62-69.

**22.**     Nagamachi S, Czernin J, Kim AS, et al. Reproducibility of measurements of regional resting and hyperemic myocardial blood flow assessed with PET. *J Nucl Med.* 1996;37:1626-1631.

**CHAPTER SIX**

**Cardiac PET perfusion tracers: current status and future directions**

Maddahi J., <u>Packard R.R.S.</u>

## ABSTRACT

Positron emission tomography (PET) myocardial perfusion imaging (MPI) is increasingly used for non-invasive detection and evaluation of coronary artery disease (CAD). However, the widespread use of PET MPI has been limited by shortcomings of the current PET perfusion tracers. Availability of these tracers is limited by need for an on-site ($^{15}$O water and $^{13}$N ammonia) or nearby ($^{13}$N ammonia) cyclotron or commitment to costly generators ($^{82}$Rb). Due to short half-lives ranging from 76sec for $^{82}$Rb, to 2.1min for $^{15}$O water and 10min for $^{13}$N ammonia, their use in conjunction with treadmill exercise stress testing is either not possible ($^{82}$Rb and $^{15}$O water) or is not practical ($^{13}$N ammonia). Furthermore, the long positron range of $^{82}$Rb makes image resolution suboptimal and its low extraction limits its defect resolution.

In recent years, development of an $^{18}$F labeled PET perfusion tracer has gathered considerable interest. The longer half-life of $^{18}$F (108 minutes) would make the tracer available as a unit dose from regional cyclotrons and allow use in conjunction with treadmill exercise testing. Furthermore, the short positron range of $^{18}$F would result in better image resolution. $^{18}$F flurpiridaz is by far the most thoroughly studied in animal models, and is the only F18-based PET MPI radiotracer currently undergoing clinical evaluation. Pre-clinical and clinical experience with $^{18}$F flurpiridaz demonstrated a high myocardial extraction fraction, high image and defect resolution, high myocardial uptake, slow myocardial clearance, and high myocardial-to-background contrast which was stable over time – important properties of an ideal PET MPI radiotracer. Pre-clinical data from other $^{18}$F labeled myocardial perfusion tracers are encouraging.

**INTRODUCTION**

Currently, single photon emission computed tomography (SPECT) myocardial perfusion imaging (MPI) remains the mainstay of risk stratification of coronary artery disease (CAD). However, several factors affect the accuracy of this test, in particular uncorrected non-uniform attenuation and photon scatter from extra-cardiac sources, particularly the liver. Attenuation artifacts are frequently observed due to the diaphragm as well as in obese patients and female patients. Positron emission tomography (PET) cardiac imaging has inherent attenuation correction and has superior spatial and temporal resolution compared to SPECT. This has led to the growing use of PET MPI in clinical practice. However, several limitations of the currently available PET perfusion tracers have hampered their widespread use. The short half-life of these tracers necessitates either the availability of an on-site cyclotron or costly generators. This has also rendered exercise treadmill testing impractical in routine streamlined clinical practice. Ensuingly, academic and biotechnology industry researchers over the last decade exhibited a growing interest in the development of an ^{18}F-based radiotracer in an effort to take advantage of the much longer 108min half-life of [18]F. This has led to a sharp growth in recent years in the development and experimental animal testing of ^{18}F-based PET MPI radiotracers (*1*) (*2*) (*3*). The present article will review currently available PET MPI tracers and will revisit some of the more thoroughly studied ^{18}F-based radiotracers at the basic and translational level.

**Current myocardial perfusion PET tracers**

Three PET myocardial perfusion tracers are currently available for clinical use: $^{15}$O water, $^{13}$N ammonia, and $^{82}$Rubidium. These tracers are different from one another with respect to their myocardial uptake, myocardial extraction fraction, positron range, half-life, production and use in the clinical setting, points that are discussed below.

**$^{15}$O water**

Myocardial uptake of $^{15}$O water is through passive diffusion (*4*). The physical half-life of this tracer is 2.06 minutes (*5*). As such its production requires an on-site cyclotron **(Table 1)**. Image resolution of PET tracers depends on their positron energy. Tracers that emit a higher energy positron have a lower image resolution because their high energy positron travels a longer distance away from the organ before they annihilate. In other words, the higher the energy of the emitted positron, the longer the positron range and the lower the image resolution **(Fig. 1)**. $^{15}$O has a 4.14 mm positron range (*5*) resulting in an intermediate image resolution **(Fig. 1)**.

Perfusion defect contrast is influenced by the myocardial extraction fraction of the myocardial perfusion tracer that is used for imaging. **Fig. 2** illustrates conceptually the relationship between myocardial blood flow (x-axes) and myocardial tracer uptake (y-axes) at baseline and at peak hyperemia. In these examples, myocardial blood flow (MBF) in a region supplied by a normal coronary artery increases to 2.4 ml/min/g, while in the region subtended by a moderately narrowed coronary artery it increases to only 1.8 ml/min/g (25% less than the normal region). The myocardial extraction fraction of $^{15}$O water is 100% (*6*). When this tracer is used for imaging, the difference in myocardial tracer uptake would be directly proportional to the difference in flow. In other words, tracer uptake in the under-perfused region would be 25% lower than that in the normal region (estimated 1.8 versus 2.4) **(Fig. 2A)**. Nevertheless, myocardial perfusion image quality with $^{15}$O water is suboptimal due to a low myocardial-to-background count ratio.

Due to its very short half-life, stress imaging with $^{15}$O water is only feasible in conjunction with pharmacologic stress, not treadmill exercise. The imaging protocol consists of injection of 24-30 mCi (900-1100 MBq) of the tracer at rest followed by dynamic imaging for 4-5min (14x5sec, 3x10sec, 3x20sec, and 4x30sec) (7).  Pharmacological stressor administration may begin shortly after completion of rest image acquisition, due to the short half-life of $^{15}$O water. Again, 24-30 mCi (900-1100 MBq) of the tracer is injected, this time at peak hyperemia, followed by dynamic imaging for 4-5min (7).

$^{15}$O water has been validated and extensively used for quantitation of MBF and coronary flow reserve (CFR) (4) (6) (8) (9).  However, $^{15}$O water is not approved by the FDA for clinical use and is not reimbursed by third party payers. The current clinical use of $^{15}$O water is primarily for measuring MBF in research studies and in the academic setting.

**$^{13}$N ammonia**

This tracer is taken up by the myocardium by passive free diffusion across cell membranes as ammonia ($NH_3$) where it equilibrates with its charged form ammonium ($NH_4$) and gets trapped inside the cell by conversion through glutamine synthase to $^{13}$N-glutamine (10) (11) (12).  The physical half-life of $^{13}$N ammonia is 9.96 minutes (5).  As such, its production has required an on-site cyclotron **(Table 1)**. Due to the 9.96 minute half-life of $^{13}$N ammonia, production and delivery of this tracer from a cyclotron a few miles away has been shown to be feasible. More recently, small, single site $^{13}$N ammonia cyclotrons have been developed *(Ionetix)* that allow on-site production and unit dose use of $^{13}$N ammonia in the clinical setting.  However research reports with this product are lacking at present.  The positron range of $^{13}$N ammonia is 2.53 mm (5) resulting in an intermediate-high image resolution as compared to other PET MPI tracers **(Fig. 1)**. The myocardial extraction fraction of $^{13}$N ammonia is is approximately 80% **(Table 1)**. Therefore, there is less difference in tracer uptake in the under-perfused versus normally perfused regions

as compared to $^{15}O$ water **(Fig. 2B)**. In other words the under-perfused to normal hyperemic blood flow ratio of 0.75 (1.8/2.4) would result in a tracer uptake ratio of 0.84 (1.3/1.55). Therefore, tracer uptake in the under-perfused region would be 16% below that of the normal region.

Since the physical half-life of $^{13}N$ ammonia is longer than those of $^{15}O$ water and $^{82}Rb$, it is feasible to use $^{13}N$ ammonia in conjunction with supine bicycle exercise (*13*) (*14*) or treadmill exercise (*15*). This approach, however, is not practical for routine clinical use. $^{13}N$ ammonia has been validated and extensively used for quantitation of MBF and coronary flow reserve in a variety of clinical conditions with a standard clinical protocol involving injection of 20 mCi (740 MBq) of $^{13}N$ ammonia at rest followed by a 10min image acquisition protocol, 30min after which a pharmacological stress is performed and a second 20 mCi (740 MBq) injection of $^{13}N$ ammonia performed and images acquired (*9*) (*16*) (*17*) (*18*) (*19*) (*20*). This tracer is approved by the FDA for clinical use and is reimbursed by third party payers.

## $^{82}Rb$

This tracer is taken up by the myocardium as a potassium analog through active transport by the $Na^+/K^+$ ATPase-pump (*21*) (*22*) (*23*). The physical half-life of $^{82}Rb$ is 1.25 minutes (*5*) and can be produced by a relatively small on-site generator **(Table 1)**. Availability of $^{82}Rb$ generators have been hampered by limited availability of $^{82}Sr$ and a single supplier for $^{82}Rb$ generators. Recently however, a new $^{82}Rb$ generator delivery system has been developed, comprised of a $^{82}Sr/^{82}Rb$ generator and an elution system that may offer improvement in safety *(Jubilant/DraxImage)*. This system is available in Canada and is currently under review by the US FDA. The positron range of $^{82}Rb$ is 8.6 mm (*5*) resulting in low image resolution as compared to other PET MPI tracers **(Fig. 1)**. The myocardial extraction fraction of $^{82}Rb$ is lower than the other PET perfusion tracers **(Table 1)**. Therefore, there is less difference in tracer uptake in the under-perfused versus normally perfused regions **(Fig. 2C)**: the same stress response would result in tracer uptake of 1.0 in the

normally perfused bed and 0.9 in the bed served by the stenotic vessel. Therefore, tracer uptake in the under-perfused region would be only 10% below that of the normal region.

The clinical imaging protocol for $^{82}$Rb starts with initial scout and transmission CT scans obtained for orientation and attenuation correction. Beginning with the intravenous bolus administration of 50 mCi (1850 MBq) of $^{82}$Rb, serial dynamic images are acquired for 6 min (14x5sec, 6x10sec, 3x20sec, 3x30sec and 1x90sec). Rapidly after completion of the rest study, a standard intravenous vasodilator infusion is administered. At peak hyperemia, a second 50 mCi (1850 MBq) dose of $^{82}$Rb is injected, and images recorded in the same manner (*24*) (*25*). Although the low myocardial extraction fraction of $^{82}$Rb does not render it ideal for absolute quantitation of MBF and CFR, this tracer has been extensively validated for this purpose (*23*) (*26*) (*27*) (*28*) and has provided useful information in the clinical setting (*29*) (*30*) (*31*) (*32*)

**Future directions**

Over the past few years, several $^{18}$F labeled myocardial perfusion PET tracers have been developed. Among these tracers, $^{18}$F flurpiridaz, formerly BMS-747158 or 2-*tert*-butyl-4-chloro-5-[4-(2-($^{18}$F)fluoroethoxymethyl)-benzyloxy]-*2H*-pyridazin-3-1, has entered phase 3 multicenter clinical trials and will be discussed in more detail. Data on other new $^{18}$F labeled tracers that are in pre-clinical investigation, such as fluorodihydrorotenone (F18-FDHR), p-fluorobenzyl triphenyl phosphonium cation (F18-FBnTP) and 4-fluorophenyl triphenyl phosphonium ion (F18-FTPP), will also be reviewed. Additional novel $^{18}$F labeled PET MPI radiotracers based on various iterations of triphenyl phosphonium salts are currently being studied (*33*), (*34*), (*35*), (*36*). Given these are mostly at preliminary stages of development, they will not be discussed below.

**$^{18}$F flurpiridaz**

$^{18}$F flurpiridaz is a novel PET MPI tracer which is a structural analog of the insecticide pyridaben, a known inhibitor of the NADH:ubiquinone oxidoreductase also known as mitochondrial complex-

1 (MC-1) of the electron transport chain (*37*).  Flurpiridaz inhibits MC-1 by competing for binding with ubiquinone without affecting the viability of cardiomyocytes.  Uptake and washout kinetics of Flurpiridaz in rat cardiomyocytes demonstrated a very rapid uptake with a time to ½-maximal uptake of 35sec, and slow washout with an efflux ½-time greater than 120min.  *In vivo* biodistribution studies in mice demonstrated that Flurpiridaz had the highest accumulation in the heart, with a substantial myocardial uptake of 9.5% injected dose per gram at 60min with very favorable heart-lung and heart-liver ratios of 14.1 and 8.3, respectively (*37*).  Mouse microPET images acquired from 5-15min and from 55-65min demonstrated clear visualization of the left ventricular myocardium with minimal background activity.  Importantly, cardiomyocyte toxicity was not observed when cells were incubated for 18h at concentrations up to 1umol/L.  Importantly, the highest concentration of Flurpiridaz used in studies did not exceed 200 nmol/L with a maximal incubation time of 45min, permitting to safely conclude that cardiomyocyte viability is not affected.

Further experimental PET imaging in rats, rabbits and rhesus monkeys demonstrated a high and sustained cardiac uptake which was proportional to blood flow (*38*).  In rats, heart-lung ratio was 9.5 at 15min with ^{18}F flurpiridaz compared to 2.0 with ^{99m}Tc sestamibi, whereas heart-liver ratio was 2.6 at 15min with ^{18}F flurpiridaz compared to 1.9 for ^{99m}Tc sestamibi.  Ratios at 60min were also more favorable to ^{18}F flurpiridaz.  In isolated rabbit hearts, the net ^{18}F flurpiridaz uptake increased proportionally at blood flow rates of 1.66 – 5.06 mL/min/g of left ventricular weight, achieving a slope of 0.47.  In comparison, ^{201}Tl and ^{99m}Tc sestamibi achieved a slope of 0.10 and 0.08, respectively. MicroPET images acquired in rats, rabbits and rhesus monkeys from 5-15min and from 55-65min demonstrated clear visualization of the myocardium with negligible background activity.  Percent change in tracer activity in the heart was determined in 5 rhesus monkeys at 10min intervals following the initial injection, with essentially constant levels in the heart after 60min.  The left coronary was ligated in rat hearts to visualize myocardial perfusion deficits with blue dye injection used as the reference.  The no-flow region by PET matched the

one with absence of dye histologically.  In a pig model, $^{18}$F flurpiridaz exhibits significantly higher activity ratios of the myocardium vs. the blood, liver and lungs compared to $^{13}$N ammonia  (*39*). A small increase in myocardial tracer uptake was noted from 10–40min, both at rest and adenosine stress, suggesting the presence of tracer metabolites.

Finally, this radiotracer also permits evaluation of myocardial infarction (MI) size in rats (*40*).  Left coronary arteries were ligated either permanently – inducing transmural MI's - or transiently for 30min – inducing subendocardial MI's - and triphenyltetrazolium chloride staining of tissue samples used as a reference of infarct size.  The animals were imaged 24h thereafter.  There was an excellent correlation of the defect size by microPET imaging with the MI size both after permanent (r=0.88) and transient (r=0.92) LAD ligation.

Imaging characteristics and potential clinical advantages of $^{18}$F flurpiridaz are described below:

**Unit dose availability:** $^{18}$F flurpiridaz has a half-life of 108 minutes and may be produced at regional cyclotrons and delivered to imaging centers in much the same way as $^{18}$F-labeled fluorodeoxyglucose (FDG), thus obviating the need for an on-site cyclotron **(Table 1)**.

**High image resolution:** The positron range of $^{18}$F is 1.03 mm and is shorter than those of $^{82}$Rb (8.6 mm), $H_2{}^{15}O$ (4.14 mm), and $^{13}NH_3$ (2.53 mm) (*5*) **(Table 1, Fig. 1)**.  Image resolution of $^{18}$F flurpiridaz PET is also better than $^{99m}$Tc SPECT. It is expected that improved image resolution leads to improved image quality and confidence of interpretation. In Phase II clinical trials (*41*), image qualities of rest and stress images obtained by $^{18}$F flurpiridaz PET and $^{99m}$Tc SPECT were compared by blinded observers in the same patients undergoing both studies. A higher percentage of images were rated as excellent/good by PET versus SPECT on stress (99.2% vs. 88.5%, p < 0.01) and rest (96.9% vs. 66.4, p < 0.01) images. Diagnostic certainty of interpretation

195

(define as percentage of cases with definitely abnormal/normal interpretation) was higher for PET versus SPECT (90.8% vs. 70.9%, p < 0.01).

**High extraction fraction and perfusion defect resolution:** The first-pass extraction fraction of ^{18}F flurpiridaz by the myocardium was determined in isolated rat hearts perfused with the Langendorff method (*42*). The radiotracer demonstrated an elevated – 94% – and flow-independent extraction fraction of ^{18}F flurpiridaz, implying a linear relationship between uptake and MBF, an important attribute for stress MBF measurements. In comparison, ^{13}N ammonia has an extraction fraction of 82% at rest and [82]Rb chloride one of 42% with a significant roll-off phenomenon, i.e. low extraction at high flows. The 94% extraction fraction of ^{18}F flurpiridaz did not change significantly at flows ranging from 5.0 – 16.6 mL/min which were achieved using adenosine stress. This is a result of the high density of mitochondria in cardiac muscle (which comprise 20-30% of the myocardial intracellular volume) doubled by the lipophilicity of the compound and its high binding affinity to MC-1 (*38*). The primary route of excretion of the compound is renal, consistent with a rapid decrease in activity of the radiotracer in the kidneys. Higher myocardial extraction facilitates detection of milder perfusion defects, as shown in **Fig. 2** (*43*). With a high-extraction radiotracer such as flurpiridaz, a substantial difference in tracer uptake is expected in normal versus under-perfused regions. With the same stress response illustrated in **Fig. 2D** (MBF increases to 2.4 ml/min/g in the normal vascular bed and to 1.8 ml/min/g in the bed served by the stenotic vessel), tracer uptake is estimated to be 2.0 and 1.6, respectively. Therefore, tracer uptake in the under-perfused region would be 20% below that of the normal region **(Fig. 2D)**. In Phase 2 clinical trials, the magnitude of reversible defects was greater with PET than SPECT (p = 0.008) in patients who had CAD on invasive coronary angiography.

**Low radiation exposure:** In Study 101 (*44*), the mean effective dose (ED) of $^{18}$F flurpiridaz injected at rest was very similar to that of FDG, with a much lower exposure to the critical organ by a factor of 2.5. In Study 102 (*45*), dosimetry of $^{18}$F flurpiridaz was evaluated in patients who were injected at rest and on a second day, at peak adenosine stress or at peak treadmill exercise. Excellent image quality was noted with both forms of stress imaging. Dosimetry results suggest that injection of up to 14 mCi (518 MBq) of $^{18}$F flurpiridaz during a rest-stress protocol would provide a clinically acceptable ED at 6.4 mSv. This is significantly lower than ED's of stress-redistribution $^{201}$Tl imaging (26 mSv) and rest-stress $^{99m}$Tc SPECT imaging (11.5 mSv). $^{18}$F flurpiridaz radiation exposure is 6.3 mSv, which is approximately one half of $^{99m}$Tc SPECT MPI and is similar to that of $^{82}$Rb 3D imaging (4.3 mSv).

**Feasibility of rest-treadmill exercise imaging:** The longer half-life of $^{18}$F also ensures that the radiotracer is present long enough to allow a patient injected at peak treadmill exercise to move to the camera and still be effectively imaged. Feasibility of rest-treadmill exercise $^{18}$F flurpiridaz was initially shown in Phase 1 clinical trials *(44, 45)*.  A very high target-to-background ratio was noted when $^{18}$F flurpiridaz was injected at peak treadmill exercise. Using the relationship between rest-stress contamination and dosing, it was determined that for a same-day rest-exercise protocol, a minimum dose ratio of 3.0 was needed, with a 60-minute waiting time between the 2 injections. For an optimum same-day rest-adenosine stress protocol, on the other hand, a dose ratio of 3 with a 30-minute waiting time between the 2 injections was required *(44, 45)*. These protocols were successfully implemented in the Phase 2 and Phase 3 clinical trials of $^{18}$F flurpiridaz.

**Peak stress function imaging:** Kinetic studies in Phase 1 trials (*45*) have shown that imaging may begin 2min following injection of $^{18}$F flurpiridaz during pharmacological stress. With treadmill exercise protocol, imaging may begin as soon as the patient is moved under the PET imaging

device following completion of exercise. Using $^{18}$F flurpiridaz, post stress imaging is, therefore, very close to peak stress and has a higher chance of detecting stress induced wall motion abnormalities. This is in contrast with $^{99m}$Tc SPECT MPI protocol in which post stress images are obtained 30-45min following stress.

**Diagnostic accuracy for detection of CAD:** In the Phase 2 trial (*41*) of $^{18}$F flurpiridaz, diagnostic performance of this tracer was compared to $^{99m}$Tc SPECT MPI for detection of CAD defined as ≥50% stenosis by invasive coronary angiography (ICA). 143 patients from 21 centers underwent rest-stress PET and $^{99m}$Tc SPECT MPI. In 86 patients who underwent ICA, sensitivity of PET was higher than SPECT (78.8% vs. 61.5%, respectively, p = 0.02). Specificity was not significantly different (PET: 76.5% vs. SPECT: 73.5%). Receiver-operating characteristic curve area was 0.82 ± 0.05 for PET and 0.70 ± 0.06 for SPECT (p = 0.04) **(Fig. 3)**. Normalcy rate was 89.7% with PET and 97.4% with SPECT (p = NS). **Fig. 4** illustrates a patient who underwent $^{99m}$Tc labeled SPECT MPI and $^{18}$F flurpiridaz MPI who was subsequently found to have normal coronary arteries on invasive coronary angiography. The SPECT MPI was a false positive due to the presence of a reversible inferior wall defect. $^{18}$F flurpiridaz MPI showed uniform distribution of activity throughout the myocardium and therefore was truly negative. The patient shown in **Fig. 5** had a normal SPECT MPI. $^{18}$F flurpiridaz MPI, however, showed reversible anterolateral defects that correlated with the presence of significant left circumflex coronary disease on ICA.

**Absolute quantitation of myocardial blood flow:** The importance of absolute quantitation of myocardial flow, above and beyond relative perfusion imaging, has been well established and is progressively entering routine clinical practice (*46*) (*47*) (*9*). $^{13}$N ammonia CFR increases diagnostic sensitivity (*48*) and has a strong association with prognosis (*49*) (*50*). $^{82}$Rb MBF and CFR correctly detects 3-vessel CAD (*51*) and predicts adverse cardiovascular events (*29*) beyond relative MPI (*30*) (*31*). Most importantly, absolute quantitation of MBF with $^{82}$Rb is a strong and

independent predictor of cardiac mortality in patients with known or suspected CAD, providing incremental risk stratification over established clinical variables and relative MPI (*32*).

The elevated extraction fraction of ^{18}F flurpiridaz at different flow rates makes it an optimal candidate for absolute MBF quantitation.  In an initial study, Nekolla and associates used a 3-compartmental modeling approach in a pig model for quantitation of MBF with ^{18}F flurpiridaz (*39*). In this 3-compartment kinetic model, k1 was the extraction from the arterial blood to the interstitium, essentially representing MBF; k2 the reverse diffusion of the radiotracer from the interstitium to the vascular space; and k3 represented the binding of the radiotracer from the interstitium to the cardiomyocyte MC-1.  k4, theoretically describing the reverse diffusion of the radiotracer from the cardiomyocyte MC-1 to the interstitium was set at zero given the very high retention rate of ^{18}F flurpiridaz.  Given the single-pass extraction fraction was known to be 94%, no correction for flow-dependent extraction was applied.  With the use of adenosine stress and LAD constriction, regional flow values ranged from 0.1 – 3.0 mL/min/g.  Results of the 3-compartment model fitting were 80% over a 10min and 84% over a 20min acquisition period. There was overall significant agreement between the kinetic modeling and MBF measured by microspheres, with a modest underestimation of MBF using this model leading to a slope=0.84 and r=0.88.  The underestimation of MBF was more accentuated in LAD constriction, with a slope=0.61 and r=0.93.

Another simplified method of absolute flow quantitation utilizing ^{18}F flurpiridaz and allowing radiotracer injection outside the PET scanner was proposed in a pig model (*52*).  Here, the authors posited that myocardial retention and standardized uptake values (SUV) based on late uptake could provide estimates of CFR.  These represent simplified methods, given radiotracer retention is a model-free approach in which tracer uptake is calibrated with myocardial radiotracer delivery, and given SUV represents myocardial uptake calibrated with the patient's dose and weight.

Radioactive microspheres were injected concomitantly to $^{18}$F flurpiridaz in the left atrium. Myocardial retention and SUV of $^{18}$F flurpiridaz were calculated using the averaged myocardial activity concentration. Myocardial retention was measured by averaging regional myocardial activities at various time-points. This average was subsequently normalized to the area under the blood curve in the 1$^{st}$ 3min after injection. SUVs were also calculated at various time-points at rest and stress. Both showed the best correlation with the 3-compartment kinetic model or microspheres at 5-12min after injection. However, at later intervals of 5-15min, 10-15min and 10-20min after injection, both retention and SUV underestimated MBF. The authors then calculated the ratios of stress and rest values of CFR-retention and CFR-SUV which were then compared to CFR-$^{18}$F flurpiridaz and CFR-microspheres. For CFR-retention vs. CFR-microspheres, the slope=0.63 and r=0.92 at 5-12min after injection. For CFR-SUV vs. CFR-microspheres, the slope=1.13 and r=0.95 5-12min after injection. At later time points, both CFR-retention and CFR-SUV values had poor concordance with either CFR-$^{18}$F flurpiridaz or CFR-microspheres. Given the good correlation of CFR-retention and particularly of CFR-SUV following radiotracer injection with measured absolute quantitation methods at 5-12min, and given that SUV measurement does not require tracer input function and hence could be measured even when the radiotracer is injected outside the PET scanner, the authors conclude that this approach would permit combination of flow quantitation with exercise treadmill protocols.

Our group recently completed the first in human absolute quantitation of MBF with $^{18}$F flurpiridaz (*53*). Study patients were participants in the phase II clinical trial of $^{18}$F flurpiridaz at the University of California, Los Angeles (UCLA) *(41)*. Analyses were performed in both normal subjects and CAD patients providing MBF data over a wide range of conditions. Our approach does not necessitate compartmental modeling. Dynamic polar maps were obtained and time-activity-curves generated. Quantitative myocardial perfusion was estimated using the tracer uptake kinetics within the first 90 seconds post tracer injection. Within this period, the tracer was

assumed to be taken up by the myocardium without significant clearance, and with very few if any labeled metabolites contained in the blood. Since the kinetic data were corrected for partial volume effect, spillover of activities between myocardium and blood pool, and vascular activity, the MBF value obtained corresponded to the blood perfusion value in the myocardium with blood in the vasculature removed. We found that CFR in patients with a low likelihood of CAD and territories supplied by normal coronary arteries was 3.7$\pm$ 0.39, while CFR was significantly lower in myocardial regions supplied by diseased coronary arteries (1.86$\pm$ 0.59). Although the first-pass extraction fraction was taken directly from an animal study, its use in our approach gives human MBF values comparable to the commonly accepted values obtained by other methods. Indeed, our results are in a similar range as those measured with other radiotracers such as $^{82}$Rb chloride, $^{13}$N ammonia and $^{15}$O water. Moreover, our results obtained with $^{18}$F flurpiridaz do not necessitate a correction such as that often utilized in the case of Rb82 for example (*54*).


**Fluorodihydrorotenone ($^{18}$F-FDHR)**

Rotenone is a neutral lipophilic compound that also binds to complex I in the mitochondrial electron transport chain (*55*). Rotenone is an inhibitor of MC-I and competitively inhibits the enzyme by competing for binding with ubiquinone. The exact characteristic of fluorodihydrorotenone's binding has not been fully evaluated. Isolated rabbit hearts were perfused and radiotracer kinetics assessed at flow rates ranging from 0.3 – 3.5 mL/min/g of left ventricle. The radioagent was not studied using a microPET imaging system, but rather myocardial extraction, retention and washout were computed from the venous outflow curves with the multiple-indicator technique and spectral analysis. Results were compared to $^{201}$Tl and to the vascular reference tracer $^{131}$I-albumin. The mean extraction fraction of $^{18}$F-FDHR and $^{201}$Tl were similar; however the initial extraction fraction of $^{18}$F -FDHR declined with flow. Overall, the investigators observed that the myocardial retention was higher and less affected by flow than

that of $^{201}$Tl, leading to superior correlation with flow 1min and 15min after radiotracer injection. Unfortunately, no followup studies with $^{18}$F-FDHR were conducted.

**p-Fluorobenzyl triphenyl phosphonium cation ($^{18}$F-FBnTP)**

$^{18}$F-FBnTP is a lipophilic cation. The delocalized positive charge of the compound allows it to cross the lipid bilayer by passive diffusion and accumulate in cells in a membrane potential-dependent manner. Due to its greater membrane potential, the radiotracer accumulates mainly in the mitochondria (*56*). The main clearance route is renal. The metabolic stability, uptake kinetics in isolated myocytes and in dog myocardium, as well as the myocardial and whole-body distribution in dogs were analyzed (*57*). In isolated myocytes, $^{18}$F-FBnTP results in rapid accumulation and prolonged retention, reaching 91% of the mean plateau activity after 15min, and 88% of control activity after 60min and 85% after 120min, respectively. Similar results are observed *in vivo*, with the radiotracer reaching a plateau in the left ventricular myocardium within 5min of administration, and a prolonged retention time up to 90min observed. In dogs, the metabolite fraction analyzed by high-performance liquid chromatography of plasma comprises <5% of total activity in blood at 5min, <9% at 10min and gradually increases to 24% at 30min after injection. However, the absolute concentration of metabolites in the blood is very low, around 3% after 20min, due to rapid tissue accumulation of the radiotracer. Whereas blood pool and lung activity decreases over time, leading to favorable uptake ratios to the heart, the ration of heart to liver is 1.2 after 60min. Despite this, high-quality cardiac images are produced with visualization of anatomic details including papillary muscles and atria. Similar radiotracer activity is observed in all quadrants. Whole body distribution of $^{18}$F-FBnTP demonstrates that the kidney cortex is the major target organ, followed by the heart and the liver.

In a followup study, the authors investigated the ability of $^{18}$F-FBnTP PET vs. $^{99m}$Tc-tetrofosmin SPECT to assess the severity of coronary artery stenosis in dogs with various degrees of stenosis

in the left anterior descending (LAD) and left circumflex coronary (LCx) arteries in an acute model of ischemia with intact myocardial viability (*58*). The authors utilized radioactive microspheres as the gold standard to determine true myocardial blood flow and Monastral blue staining to assess the risk area. $^{18}$F-FBnTP myocardial regional activity was measured *ex vivo* by direct tissue ☐-well counting and *in vivo* by dynamic PET imaging. The LAD or LCx arteries were dissected free 1-2cm from the origin and a cuff occluder placed around the artery. The authors demonstrated that $^{18}$F-FBnTP PET was superior to $^{99m}$Tc-tetrofosmin SPECT in assessing mild or severe stenosis compared to normal territories, with a flow defect contrast that was 2.7 times greater in favor of $^{18}$F-FBnTP. In both stenotic and normal vascular beds, peak $^{18}$F-FBnTP activity was obtained within 10-20sec after injection, and a near-plateau concentration observed within the following 10-20sec. This plateau activity was retained throughout the scanning time of up to 60min. The mean risk area by $^{18}$F-FBnTP PET was 84% of the true extent measured by Monastral blue-stained cardiac sections. The underestimation of the risk area is far less than that reported for technetium complexes which are typically in the 30% range. Finally, the authors note that in patients with chronic ischemia, either in the setting of repetitive stunning or myocardial infarction, the effect of tissue viability, mitochondrial bioenergetics and membrane potential – the driving force of $^{18}$F-FBnTP uptake by the myocardium – were not assessed.

In a similar followup study in rats, the investigators analyzed the ability of $^{18}$F-FBnTP to delineate the ischemic area after transient coronary occlusion in rats and assessed the presence of tracer washout and redistribution (*59*). Rats underwent thoracotomy and a 2min occlusion by suture against a snare of the left coronary artery was conducted at which time the radiotracer was injected, followed by reperfusion which was obtained by release of the snare. 1min prior to sacrifice, the animals underwent repeat occlusion of the left coronary artery by repositioning the snare with concomitant injection of Evans blue dye to determine the ischemic territory. $^{18}$F-FBnTP demonstrated stable ischemic defects at all time points (5min, 45min, and 120min) following

radiotracer injection and excellent correlation with the Evans blue dye determined histological ischemic area ($R^2=0.94$). A comparison was conducted at each time-point with $^{201}$Tl which exhibited redistribution and hence absence of significant defect after 120min – a known phenomenon with this SPECT tracer. The lack of redistribution for at least 45min of $^{18}$F-FBnTP should permit development of clinically feasible protocols. Interestingly, $^{18}$F-FBnTP also detects apoptosis and has a strong negative correlation with the Bax (pro-apoptotic) – to – Bcl-2 (anti-apoptotic) ratio ($R^2 = 0.83$) and release of the apoptogen cytochrome c ($R^2 = 0.92$) in breast cancer cells. This additional property is described in detail elsewhere (*60*).

**4-Fluorophenyl triphenyl phosphonium ion ($^{18}$F-FTPP)**

A related lipophilic cationic radiotracer but differing structurally and in electronic charge distribution, 4-fluorophenyl triphenyl phosphonium ion ($^{18}$F-FTPP), also targets the mitochondria and accumulates in the mitrochondrial matrix due to the relatively high mitochondrial interior membrane potential. $^{18}$F-FTPP was evaluated as a potential PET MBF agent (*61*). Biodistribution studies were performed in normal rats at 5, 30 and 60min and in rabbits before and after occlusion of the LAD accomplished by tightening of a snare around the artery in the setting of thoracotomy. Results were compared with $^{13}$N ammonia. Uptake was highest in the kidneys at all time points. Heart uptake was 1.5% of the injected dose per gram. MicroPET imaging demonstrated an initial spike of activity corresponding to blood flow followed by rapid washout and a plateau after 1-2min. After 5min, ratios were 11 for heart/blood, 2 for heart/lung and 5 for heart/liver. After 30min, these ratios were 75, 5 and 8 respectively and remained in a similar range at 60min. Images in the regions of interest and corresponding time-activity curves obtained following LAD occlusion were of similar quality between $^{18}$F-FTPP and $^{13}$N-ammonia.

**CONCLUSION**

For decades, PET MPI was mostly limited to academic research centers and large hospital systems while SPECT MPI remained the default approach in routine clinical practice by which patients underwent cardiac risk stratification and evaluation of stress-inducible myocardial ischemia. The enhanced sensitivity and specificity of PET radiotracers compared to SPECT radiotracers, as well as their inherent attenuation correction and ability to quantitate flow in an absolute manner further increases the value of a PET based approach. The major Achilles heel of routine PET MPI however has been the availability of radiotracers, with current requirement for either onsite or very nearby cyclotrons or costly generators. In this context $^{18}$F-based PET radiotracers, taking advantage of the radioisotope's 108min half-life, have garnered significant interest and have been developed by academic centers and biotechnology companies. Of the reported $^{18}$F-based PET MPI radiotracers, only $^{18}$F flurpiridaz is in advanced clinical evaluation with encouraging results.

**FIGURES AND TABLE**

| | ¹⁵O water | ¹³N ammonia | ⁸²Rb | ¹⁸F flurpiridaz |
|---|---|---|---|---|
| **Positron range (mm)** | 4.14 | 2.53 | 8.6 | 1.03 |
| **End point coordinate** | | | | |
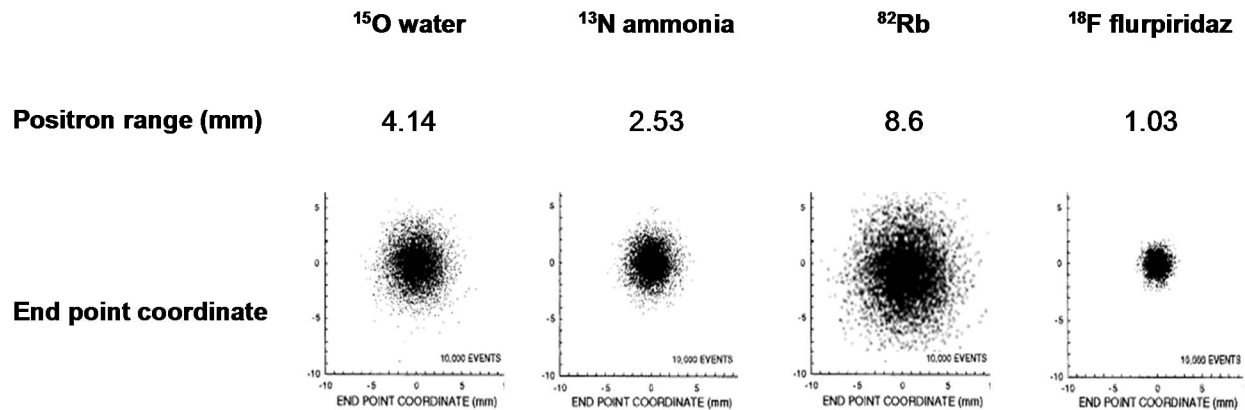


**Figure 1.** Positron range and end point coordinates are shown for various myocardial perfusion PET tracers. The higher the energy of the emitted positron, the longer it travels away from the source before annihilation and the worse the resolution of the imaged target. In this figure, end point coordinates are similar to point source images obtained from a given PET tracer.
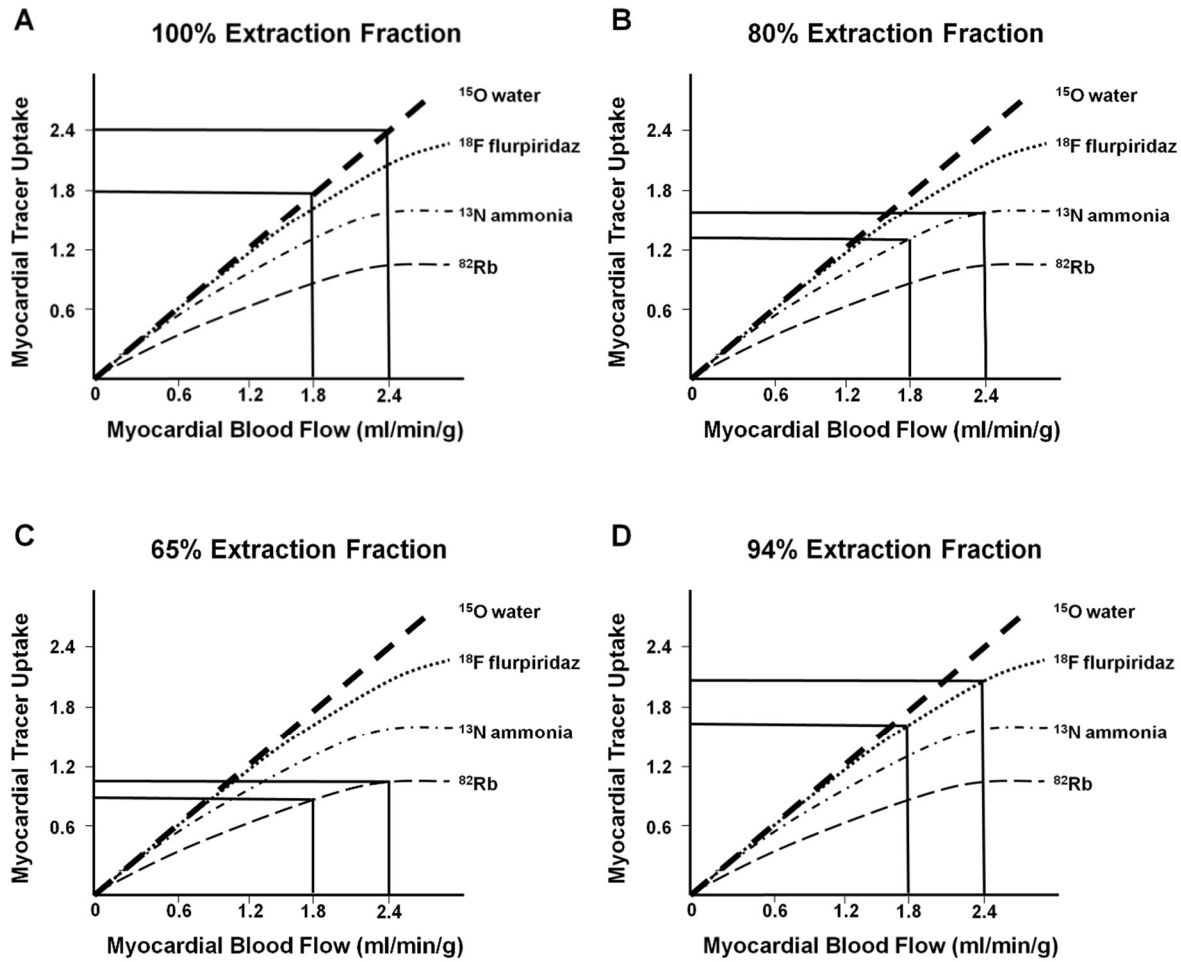
**Figure 2.** Conceptual effect of radiotracer extraction fraction on detection of myocardial perfusion defect severity. Myocardial uptake of various PET tracers (y-axes) are shown when myocardial blood flow (x-axes) increases by a greater increment in a vascular bed supplied by a normal coronary artery versus a lower increment in the myocardial region supplied by a narrowed coronary artery. The differences in myocardial uptake of various tracers are illustrated for $^{15}$O water (Figures 2a), $^{13}$N ammonia (Figures 2b), $^{82}$RB (Figure 2c) and $^{18}$F flurpiridaz (Figures 2d). *See text for detailed explanation*
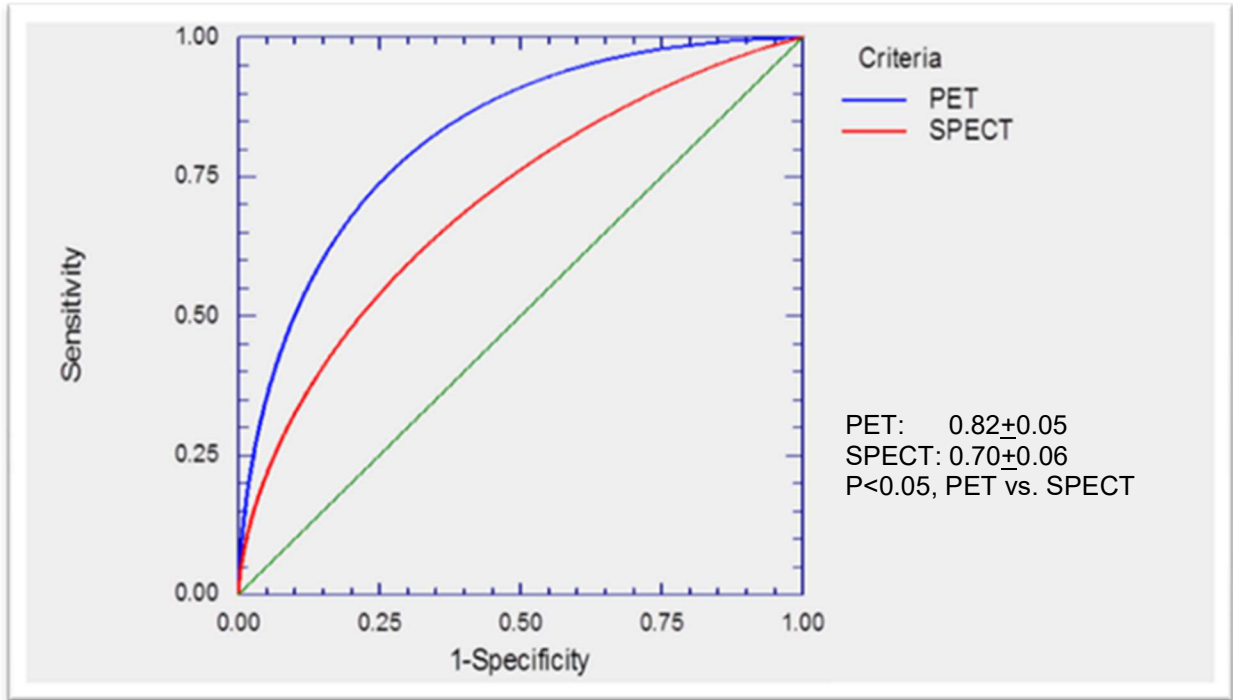
**Figure 3.** Receiver Operating Curves (ROC) for $^{18}$F flurpiridaz (blue) and $^{99m}$Tc labeled SPECT (red) for detection of coronary artery disease in Phase 2 $^{18}$F flurpiridaz multicenter study. The area under the ROC curve for $^{18}$F flurpiridaz was significantly better than that of $^{99m}$Tc labeled SPECT (p<0.05).
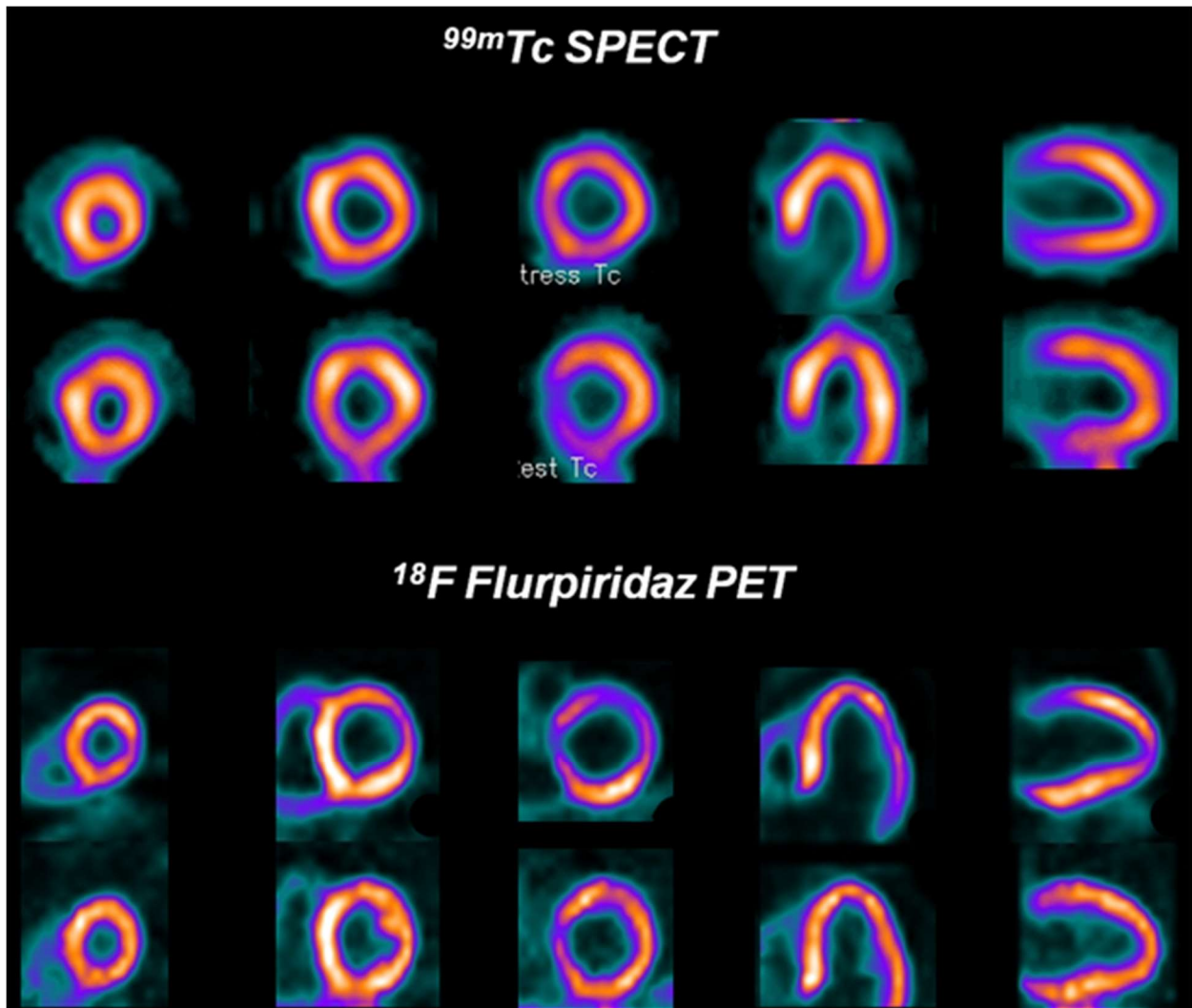
**Figure 4.** 99mTc SPECT and 18F flurpiridaz PET images in a patient with significant disease in the left circumflex coronary artery. The overall quality of the 18F flurpiridaz PET images (lower rows) was superior to the 99mTc SPECT images (upper rows). 18F flurpiridaz PET images showed reversible anterolateral wall defects in the distribution of the diseased left circumflex coronary artery, but the 99mTc SPECT images were normal.
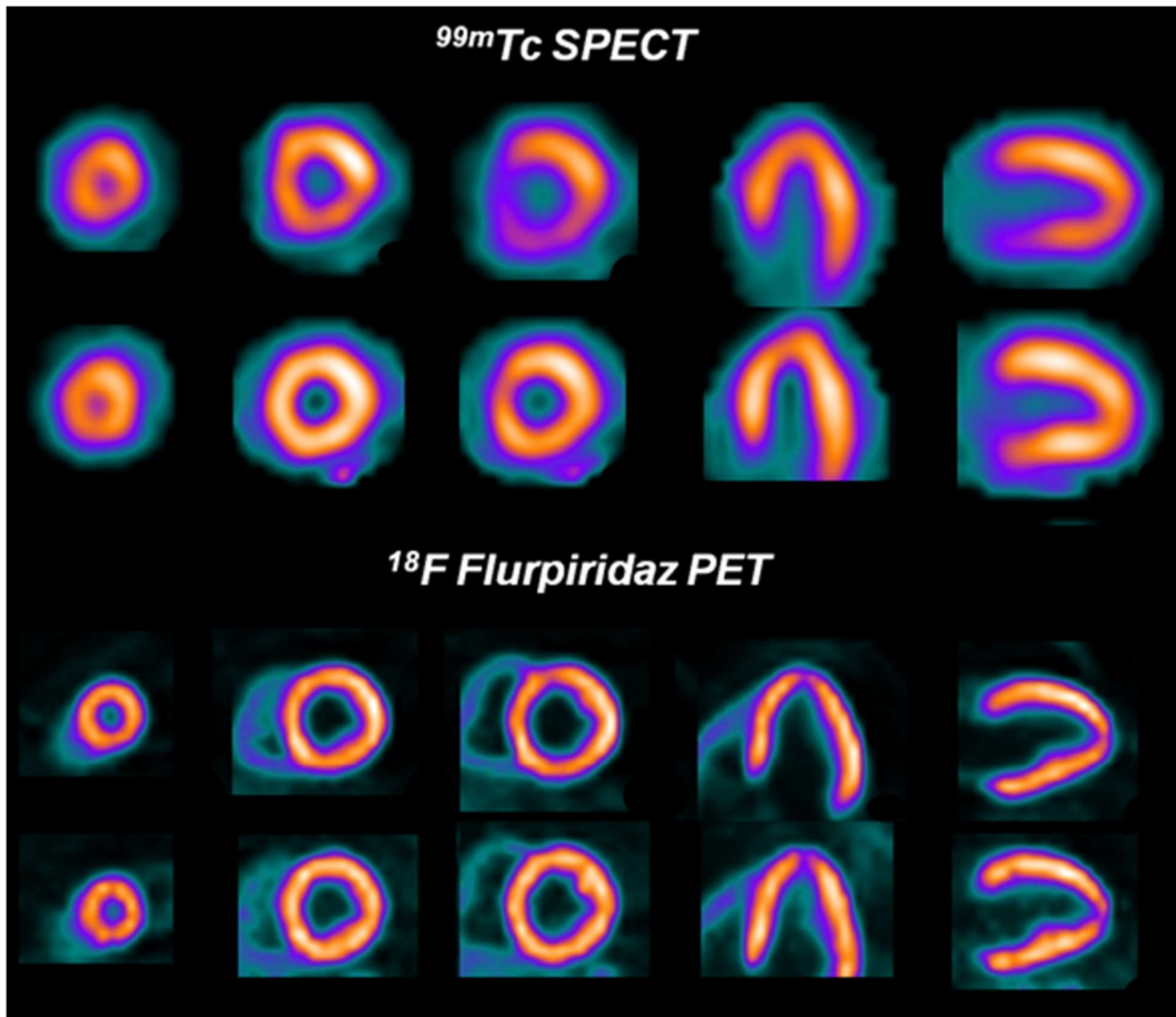
**Figure 5.** <sup>99m</sup>Tc SPECT images (upper rows) and flurpiridaz F 18 PET images (lower rows) from a patient with normal coronary arteries. A false positive reversible inferior defect is present on the <sup>99m</sup>Tc SPECT images due to shifting soft-tissue attenuation. The flurpiridaz F 18 PET study, however, provided superior image quality and was normal.

| | ¹⁵O water | ¹³N ammonia | ⁸²Rb | ¹⁸F flurpiridaz |
|---|---|---|---|---|
| **Half life (minutes)** | 2.06 | 9.96 | 1.25 | 109 |
| **Production** | On-site cyclotron | On-site or nearby cyclotron | Generator | Regional cyclotron |
| **Positron range (mm)** | 4.14 | 2.53 | 8.6 | 1.03 |
| **Image resolution** | Intermediate | Intermediate-high | Lowest | Highest |
| **Myocardial extraction fraction** | 100% | 80% | 65% | 94% |
| **Perfusion defect contrast** | Intermediate* | Intermediate | Lowest | Highest |
| **Pharmacological stress imaging protocol** | Feasible | Feasible | Feasible | Feasible |
| **Treadmill exercise Imaging protocol** | Not feasible | Feasible but not practical | Not feasible | Feasible |

**Table 1.** Characteristics of various cardiac PET perfusion tracers. * Theoretically 100% myocardial extraction fraction of ¹⁵O water should result in the highest perfusion defect contrast. However, poor myocardial-to-background ratio reduces defect contrast.

**REFERENCES**

1. Dilsizian V, Taillefer R. Journey in evolution of nuclear cardiology: will there be another quantum leap with the F-18-labeled myocardial perfusion tracers? *JACC Cardiovasc Imaging.* 2012;5:1269-1284.

2. Rischpler C, Park MJ, Fung GS, Javadi M, Tsui BM, Higuchi T. Advances in PET myocardial perfusion imaging: F-18 labeled tracers. *Ann Nucl Med.* 2012;26:1-6.

3. Nekolla SG, Saraste A. Novel F-18-labeled PET myocardial perfusion tracers: bench to bedside. *Curr Cardiol Rep.* 2011;13:145-150.

4. Bergmann SR, Fox KA, Rand AL, et al. Quantification of regional myocardial blood flow in vivo with H215O. *Circulation.* 1984;70:724-733.

5. Garcia EV, Galt JR, Faber TL, et al. Principles of nuclear cardiology imaging. In: Atlas of Nuclear Cardiology (4th edition), Vasken Dilsizian & Jagat Narula (eds). Chapter 1, pp 1-53, Springer Science, 2013.

6. Bol A, Melin JA, Vanoverschelde JL, et al. Direct comparison of [13N]ammonia and [15O]water estimates of perfusion with quantification of regional myocardial blood flow by microspheres. *Circulation.* 1993;87:512-525.

7. Kajander SA, Joutsiniemi E, Saraste M, et al. Clinical value of absolute quantification of myocardial perfusion with (15)O-water in coronary artery disease. *Circ Cardiovasc Imaging.* 2011;4:678-684.

8. Nitzsche EU, Choi Y, Czernin J, et al. Noninvasive quantification of myocardial blood flow in humans. A direct comparison of the [13N]ammonia and the [15O]water techniques. *Circulation.* 1996;93:2000-2006.

9. Schindler TH, Schelbert HR, Quercioli A, et al. Cardiac PET imaging for the detection and monitoring of coronary artery disease and microvascular health. *JACC Cardiovasc Imaging.* 2010;3:623-640.

10. Bergmann SR, Hack S, Tewson T, et al. The dependence of accumulation of 13NH3 by

myocardium on metabolic factors and its implications for quantitative assessment of perfusion. *Circulation.* 1980;61:34-43.

**11.** Schelbert HR, Phelps ME, Huang SC, et al. N-13 ammonia as an indicator of myocardial blood flow. *Circulation.* 1981;63:1259-1272.

**12.** Krivokapich J, Huang SC, Phelps ME, et al. Dependence of 13NH3 myocardial extraction and clearance on flow and metabolism. *Am J Physiol.* 1982;242:H536-542.

**13.** Tamaki N, Yonekura Y, Senda M, et al. Myocardial positron computed tomography with 13N-ammonia at rest and during exercise. *Eur J Nucl Med Mol Imaging.* 1985;11:246-251.

**14.** Krivokapich J, Smith GT, Huang SC, et al. 13N ammonia myocardial imaging at rest and with exercise in normal volunteers. Quantification of absolute myocardial perfusion with dynamic positron emission tomography. *Circulation.* 1989;80:1328-1337.

**15.** Chow BJ, Beanlands RS, Lee A, et al. Treadmill exercise produces larger perfusion defects than dipyridamole stress N-13 ammonia positron emission tomography. *J Am Coll Cardiol.* 2006;47:411-416.

**16.** Czernin J, Muller P, Chan S, et al. Influence of age and hemodynamics on myocardial blood flow and flow reserve. *Circulation.* 1993;88:62-69.

**17.** Di Carli M, Czernin J, Hoh CK, et al. Relation among stenosis severity, myocardial blood flow, and flow reserve in patients with coronary artery disease. *Circulation.* 1995;91:1944-1951.

**18.** Schindler TH, Nitzsche EU, Olschewski M, et al. Chronic inflammation and impaired coronary vasoreactivity in patients with coronary risk factors. *Circulation.* 2004;110:1069-1075.

**19.** Prior JO, Quinones MJ, Hernandez-Pampaloni M, et al. Coronary circulatory dysfunction in insulin resistance, impaired glucose tolerance, and type 2 diabetes mellitus. *Circulation.* 2005;111:2291-2298.

**20.** Schindler TH, Cardenas J, Prior JO, et al. Relationship between increasing body weight, insulin resistance, inflammation, adipocytokine leptin, and coronary circulatory function. *J Am Coll Cardiol.* 2006;47:1188-1195.

**21.**     Love WD, Burch GE. A comparison of potassium 42, rubidium 86, and cesium 134 as tracers of potassium in the study of cation metabolism of human erythrocytes in vitro. *J Lab Clin Med.* 1953;41:351-362.

**22.**     Love WD, Romney RB, Burch GE. A comparison of the distribution of potassium and exchangeable rubidium in the organs of the dog, using rubidium. *Circ Res.* 1954;2:112-122.

**23.**     Selwyn AP, Allan RM, L'Abbate A, et al. Relation between regional myocardial uptake of rubidium-82 and perfusion: absolute reduction of cation uptake in ischemia. *Am J Cardiol.* 1982;50:112-121.

**24.**     El Fakhri G, Kardan A, Sitek A, et al. Reproducibility and accuracy of quantitative myocardial blood flow assessment with (82)Rb PET: comparison with (13)N-ammonia PET. *J Nucl Med*. 2009;50:1062-1071.

**25.**     Naya M, Murthy VL, Taqueti VR, et al. Preserved coronary flow reserve effectively excludes high-risk coronary artery disease on angiography. *J Nucl Med.* 2014;55:248-255.

**26.**     Goldstein RA, Mullani NA, Marani SK, et al. Myocardial perfusion with rubidium-82. II. Effects of metabolic and pharmacologic interventions. *J Nucl Med.* 1983;24:907-915.

**27.**     Huang SC, Williams BA, Krivokapich J, et al. Rabbit myocardial 82Rb kinetics and a compartmental model for blood flow estimation. *Am J Physiol.* 1989;256:H1156-1164.

**28.**     Herrero P, Markham J, Shelton ME, et al. Noninvasive quantification of regional myocardial perfusion with rubidium-82 and positron emission tomography. Exploration of a mathematical model. *Circulation.* 1990;82:1377-1386.

**29.**     Fukushima K, Javadi MS, Higuchi T, et al. Prediction of short-term cardiovascular events using quantification of global myocardial flow reserve in patients referred for clinical 82Rb PET perfusion imaging. *J Nucl Med.* 2011;52:726-732.

**30.**     Ziadi MC, Dekemp RA, Williams KA, et al. Impaired myocardial flow reserve on rubidium-82 positron emission tomography imaging predicts adverse outcomes in patients assessed for myocardial ischemia. *J Am Coll Cardiol.* 2011;58:740-748.

**31.** Farhad H, Dunet V, Bachelard K, et al. Added prognostic value of myocardial blood flow quantitation in rubidium-82 positron emission tomography imaging. *Eur Heart J Cardiovasc Imaging.* 2013;14:1203-1210.

**32.** Murthy VL, Naya M, Foster CR, et al. Improved cardiac risk assessment with noninvasive measures of coronary flow reserve. *Circulation.* 2011;124:2215-2224.

**33.** Kim DY, Kim HS, Le UN, et al. Evaluation of a mitochondrial voltage sensor, (18F-fluoropentyl)triphenylphosphonium cation, in a rat myocardial infarction model. *J Nucl Med.* 2012;53:1779-1785.

**34.** Kim DY, Kim HJ, Yu KH, et al. Synthesis of [18F]-labeled (2-(2-fluoroethoxy)ethyl)tris(4-methoxyphenyl)phosphonium cation as a potential agent for positron emission tomography myocardial imaging. *Nucl Med Biol.* 2012;39:1093-1098.

**35.** Kim DY, Kim HJ, Yu KH, et al. Synthesis of [18F]-labeled (6-fluorohexyl)triphenylphosphonium cation as a potential agent for myocardial imaging using positron emission tomography. *Bioconjug Chem.* 2012;23:431-437.

**36.** Kim DY, Kim HJ, Yu KH, et al. Synthesis of [(1)(8)F]-labeled (2-(2-fluoroethoxy)ethyl)triphenylphosphonium cation as a potential agent for myocardial imaging using positron emission tomography. *Bioorg Med Chem Lett.* 2012;22:319-322.

**37.** Yalamanchili P, Wexler E, Hayes M, et al. Mechanism of uptake and retention of F-18 BMS-747158-02 in cardiomyocytes: a novel PET myocardial imaging agent. *J Nucl Cardiol*. 2007;14:782-788.

**38.** Yu M, Guaraldi MT, Mistry M, et al. BMS-747158-02: a novel PET myocardial perfusion imaging agent. *J Nucl Cardiol.* 2007;14:789-798.

**39.** Nekolla SG, Reder S, Saraste A, et al. Evaluation of the novel myocardial perfusion positron-emission tomography tracer 18F-BMS-747158-02: comparison to 13N-ammonia and validation with microspheres in a pig model. *Circulation.* 2009;119:2333-2342.

**40.** Sherif HM, Saraste A, Weidl E, et al. Evaluation of a novel (18)F-labeled positron-emission

tomography perfusion tracer for the assessment of myocardial infarct size in rats. *Circ Cardiovasc Imaging.* 2009;2:77-84.

**41.** Berman DS, Maddahi J, Tamarappoo BK, et al. Phase II safety and clinical comparison with single-photon emission computed tomography myocardial perfusion imaging for detection of coronary artery disease: flurpiridaz F 18 positron emission tomography. *J Am Coll Cardiol.* 2013;61:469-477.

**42.** Huisman MC, Higuchi T, Reder S, et al. Initial characterization of an 18F-labeled myocardial perfusion tracer. *J Nucl Med.* 2008;49:630-636.

**43.** Maddahi J. Properties of an ideal PET perfusion tracer: new PET tracer cases and data. *J Nucl Cardiol.* 2012;19:S30-37.

**44.** Maddahi J, Czernin J, Lazewatsky J, et al. Phase I, first-in-human study of BMS747158, a novel 18F-labeled tracer for myocardial perfusion PET: dosimetry, biodistribution, safety, and imaging characteristics after a single injection at rest. *J Nucl Med.* 2011;52:1490-1498.

**45.** Maddahi J, Bengel F, Huang S-C, et al. Phase 1 rest-stress study of F-18 labeled BMS747158 myocardial perfusion PET tracer: Human safety, dosimetry, biodistribution, and myocardial imaging characteristics [abstract]. *J Nucl Med.* 2009;50:184.

**46.** Gould KL, Johnson NP, Bateman TM, et al. Anatomic versus physiologic assessment of coronary artery disease. Role of coronary flow reserve, fractional flow reserve, and positron emission tomography imaging in revascularization decision-making. *J Am Coll Cardiol.* 2013;62:1639-1653.

**47.** Johnson NP, Gould KL. Integrating noninvasive absolute flow, coronary flow reserve, and ischemic thresholds into a comprehensive map of physiological severity. *JACC Cardiovasc Imaging.* 2012;5:430-440.

**48.** Fiechter M, Ghadri JR, Gebhard C, et al. Diagnostic value of 13N-ammonia myocardial perfusion PET: added value of myocardial flow reserve. *J Nucl Med.* 2012;53:1230-1234.

**49.** Tio RA, Dabeshlim A, Siebelink HM, et al. Comparison between the prognostic value of

left ventricular function and myocardial perfusion reserve in patients with ischemic heart disease. *J Nucl Med.* 2009;50:214-219.

50.     Herzog BA, Husmann L, Valenta I, et al. Long-term prognostic value of 13N-ammonia myocardial perfusion positron emission tomography added value of coronary flow reserve. *J Am Coll Cardiol.* 2009;54:150-156.

51.     Parkash R, deKemp RA, Ruddy TD, et al. Potential utility of rubidium 82 PET quantification in patients with 3-vessel coronary artery disease. *J Nucl Cardiol.* 2004;11:440-449.

52.     Sherif HM, Nekolla SG, Saraste A, et al. Simplified quantification of myocardial flow reserve with flurpiridaz F 18: validation with microspheres in a pig model. *J Nucl Med.* 2011;52:617-624.

53.     Packard RR, Huang SC, Dahlbom M, et al. Absolute quantitation of myocardial blood flow in human subjects with or without myocardial ischemia using dynamic F18 flurpiridaz positron emission tomography. *J Nucl Med* 2014;55:1438-1444.

54.     Saraste A, Kajander S, Han C, et al. PET: Is myocardial flow quantification a clinical reality? *J Nucl Cardiol.* 2012;19:1044-1059.

55.     Marshall RC, Powers-Risius P, Reutter BW, et al. Kinetic analysis of 18F-fluorodihydrorotenone as a deposited myocardial flow tracer: comparison to 201Tl. *J Nucl Med.* 2004;45:1950-1959.

56.     Madar I, Ravert H, Nelkin B, et al. Characterization of membrane potential-dependent uptake of the novel PET tracer 18F-fluorobenzyl triphenylphosphonium cation. *Eur J Nucl Med Mol Imaging.* 2007;34:2057-2065.

57.     Madar I, Ravert HT, Du Y, et al. Characterization of uptake of the new PET imaging compound 18F-fluorobenzyl triphenyl phosphonium in dog myocardium. *J Nucl Med.* 2006;47:1359-1366.

58.     Madar I, Ravert H, Dipaula A, et al. Assessment of severity of coronary artery stenosis in a canine model using the PET agent 18F-fluorobenzyl triphenyl phosphonium: comparison with

99mTc-tetrofosmin. *J Nucl Med.* 2007;48:1021-1030.

**59.**    Higuchi T, Fukushima K, Rischpler C, et al. Stable delineation of the ischemic area by the PET perfusion tracer 18F-fluorobenzyl triphenyl phosphonium after transient coronary occlusion. *J Nucl Med.* 2011;52:965-969.

**60.**    Madar I, Huang Y, Ravert H, et al. Detection and quantification of the evolution dynamics of apoptosis using the PET voltage sensor 18F-fluorobenzyl triphenyl phosphonium. *J Nucl Med.* 2009;50:774-780.

**61.**    Shoup    TM,    Elmaleh    DR,    Brownell    AL,    et    al.    Evaluation    of    (4-[18F]Fluorophenyl)triphenylphosphonium ion. A potential myocardial blood flow agent for PET. *Mol Imaging Biol.* 2011;13:511-517.

**CHAPTER SEVEN**

**PET should replace SPECT in cardiac imaging for diagnosis and risk assessment of patients with known or suspected CAD - Pro**

Maddahi J., <u>Packard R.R.S.</u>

Review article, in press, ***Journal of Nuclear Cardiology.***

Manuscript reproduced with permission.

**INTRODUCTION**

Positron emission tomography (PET) myocardial perfusion imaging (MPI) has been performed for the better part of 3 decades. Initially limited to academic centers and viewed with skepticism, it has gained greater acceptance as a test with improved ability to detect coronary artery disease (CAD) and improve patient risk stratification. Here, we will review how PET fares better than single photon emission computed tomography (SPECT) by comparing technical and radiotracer characteristics as well as clinical data.

**PET imaging protocols are more rapid than SPECT MPI**

PET MPI rest/stress studies are performed faster than SPECT studies owing to the shorter half-life of the PET radiotracers (1), their rapid clearance from the background and higher photon sensitivity of PET scanners. More rapid imaging protocols lead to decreased patient motion artifacts and increased patient throughput. Given the 76 sec half-life of $^{82}$Rb, a rest/stress protocol can be completed in 30 minutes whereas $^{13}$N-ammonia with a half-life of 9.8 minutes typically requires a protocol of approximately 80 min (1). Other than in research settings, exercise MPI with current PET tracers is not routinely feasible. A recent radiotracer, $^{18}$F-flurpiridaz, currently undergoing phase III clinical investigation, has a half-life of 110 min and is suitable for both pharmacological and exercise stress (1-4). Initial protocols have used a 30 min interval between rest and stress for pharmacological stimulation and a 60 min interval when using exercise stress (3-5). All recent PET scanners operate in 3D mode, allowing the detection of coincident photons in all directions resulting in greater photon sensitivity (6). Indeed, the 3D PET sensitivity is at least an order of magnitude higher compared to cardiac SPECT owing in part to lack of physical collimators.

**PET MPI is associated with lower radiation dose to patients**

For $^{82}$Rb chloride, radiation doses have been estimated to be in the range of 2.4 – 3.7 mSv (7, 8) and approximately 2 mSv for $^{13}$N ammonia (9). This radiation burden, comparable to a 1 year background radiation (3 mSv), is sizably less than the average exposure from a rest-stress SPECT MPI scan which is approximately 12 mSv. It is important to note however that the recent introduction of new SPECT scanners using solid-state photon detectors as well as resolution recovery software allow clinically acceptable image counts with decreased injected dose and radiation exposure to patients (10). Use of stress only protocol has further reduces radiation exposure to patients. A higher percentage of truly normal patients may be identified as such with PET MPI due to routine use of attenuation correction with PET.

Radiation dosimetry of ^{18}F-flurpiridaz has been shown to be favorable (11, 12). In general, ^{18}F-flurpiridaz PET MPI is associated with about ½ of radiation dose to patients as compared to comparable Tc-99m labelled SPECT MPI rest-stress or stress only protocol (3,13).

**PET MPI has a higher sensitivity for detection of CAD**

A known limitation of SPECT agents is their underestimation of perfusion defect severity (2). In 2 large meta-analyses, PET outperformed SPECT MPI with higher sensitivity and specificity (PET sensitivity/specificity 90 – 93%/81 – 88% vs. SPECT sensitivity/specificity 85 – 88%/76 – 85%) (14, 15). The first phase 3 ^{18}F-flurpiridaz multi-center clinical trial has shown that PET MPI sensitivity and overall accuracy with PET MPI is superior to Tc-99m labelled SPECT MPI (3). Furthermore, the diagnostic performance of PET is superior to SPECT in specific patient subgroups such as females and obese patients using Rb-82 PET (16) and ^{18}F-flurpiridaz PET (3). The following factors contribute to improved sensitivity of PET MPI:

a. PET system resolution is higher: Reduced detector element sizes of the new PET scanners allow for high spatial resolution, which ranges from 4.4 – 4.8 mm in the center of the field of view (6). The picosecond timing resolution achievable by fast coincident electronics and fast scintillators allows implementation of time-of-flight (TOF) PET reconstruction algorithms. TOF PET considers the time difference between the arrival of the 2 annihilation photons at opposite detectors. The iterative reconstruction algorithms incorporate this information to determine the position of the positron annihilation more accurately, leading to improved contrast and signal-to-noise ratios (6).

b. PET radiotracers have higher myocardial extraction fraction: PET radiotracers have superior extraction fractions than SPECT agents. These are ~60% for [82]Rb-chloride, ~80% for

222

[13]N-ammonia and ~94% for ^{18}F-flurpiridaz (1, 17). The lower first-pass extraction of SPECT radiotracers and the more prominent non-linear myocardial uptake with increasing blood flow, termed the "roll-off phenomenon", results in relatively lower myocardial contrast resolution images when compared to PET MPI (1). The first-pass myocardial extraction fraction of ^{99m}Tc-tetrofosmin is ~54% and that of ^{99m}Tc-sestamibi is ~60% (1).

c. Peak stress imaging is feasible with PET MPI: An additional significant advantage of PET over SPECT MPI is the ability to measure left ventricular ejection fraction (LVEF) at true peak stress which in SPECT MPI is measured on post-stress images. Peak stress LVEF measurement with PET MPI improves evaluation of the magnitude of myocardium at risk and the extent of angiographic coronary artery disease (18).

d. Absolute quantitation of myocardial blood flow (MBF) and coronary flow reserve (CFR): In clinical practice, SPECT and PET MPI studies are evaluated visually by "relative" flow quantitation, i.e. myocardial regions with the highest tracer uptake are assumed to be supplied by normal or non-obstructive epicardial coronary arteries, leading to identification on stress MPI of only the most severe lesion in multivessel CAD. However, flow-limiting stenosis of the remaining vessels may go unnoticed by visual "relative" evaluation. These disadvantages may be resolved by the systematic addition of "absolute" flow quantitation by PET (19). Using kinetic modeling, myocardial blood flow (MBF) in absolute terms (mL/g/min) at rest and during vasomotor stress can be determined allowing the computation of coronary flow reserve (CFR) as an adjunct to the visual interpretation of myocardial perfusion studies. Accurate attenuation correction and simultaneous tomographic acquisition of counts in list mode and rapid flow quantitation using commercial software have moved absolute MBF and CFR determination from a predominantly research arena to clinical practice. Absolute quantification of MBF by various PET radiotracers has been validated against microsphere blood flow over a wide flow range from 0.5 – 5.0 mL/g/min

(1). Use of MBF and CFR allows detection of subclinical CAD, improved identification of the extent of multivessel CAD and assessment of balanced ischemia seen in severe 3-vessel disease or left main disease with a left-dominant system (20). A decreased CFR provides incremental diagnostic value (21) and a normal CFR effectively rules out high-risk CAD on angiography (22). Abnormal CFR cutoffs values may vary based on the PET radiotracer, however by and large a value < 2 is deemed abnormal (1, 17). This is further supported by recent work with the novel ^{18}F flurpiridaz which demonstrated an inverse relationship of CFR with incremental levels of CAD burden (23). In spite of preliminary reports, CFR may not be readily assessed by SPECT MPI due to multiple limitations (24).

In addition to its enhanced ability to detect CAD, absolute MBF quantitation allows determination of endothelial dysfunction / microvascular disease (17), a phenomenon which often precedes CAD and may lead to the development of anginal symptoms. Hence, an abnormal PET CFR is usually a manifestation of macrovascular disease, microvascular disease, or a combination of both. Of note, vasodilator CFR predominantly is a measure of endothelium-independent coronary flow abnormalities, and to a lesser extent endothelium-dependent flow abnormalities. Coronary angiography may be necessary to differentiate between epicardial CAD, microvascular disease, or a combination of both.

**PET MPI has a higher specificity for detection of CAD**

A key advantage of PET compared to SPECT is that attenuation correction is an integral part of image acquisition and processing. Attenuation correction is performed in a very small percentage of SPECT MPI studies. Attenuation correction leads to improved specificity and superior diagnostic and prognostic performance of PET MPI in women and obese patients for (16, 25, 26).

**PET MPI improves risk stratification in patients suspected of having CAD**

All recent PET scanner allow list-mode acquisition leading to reconstruction of dynamic perfusion data and absolute MBF quantitation. Screening for subclinical atherosclerosis by PET CFR may aid in supplementing current global risk assessment approaches. A large body of evidence has established the additive information gained by absolute flow quantitation and CFR above and beyond relative perfusion assessment. Abnormal CFR values with both ^{13}N-ammonia (27) and [82]Rb-chloride (28, 29) have been associated with cardiovascular events. Over the last years, several studies (30-33) have documented the incremental prognostic value of PET CFR over clinical factors and beyond perfusion defect size with a cardiac mortality 5.6 fold higher in patients with the lowest tertile of CFR (< 1.5) compared to the highest tertile of CFR in multivariate analysis (31). Importantly, a normal CFR conferred protection from a subsequent cardiovascular events even in the presence of abnormal relative perfusion or a rest LVEF < 40%. CFR has been shown to result in a substantial improvement in risk discrimination and reclassification ability. Notably, among intermediate-risk patients, the use of CFR is associated with a net reclassification improvement of 55% (31). Diabetics without epicardial CAD but with impaired CFR were found to have an annual cardiac mortality similar to diabetics with known CAD (32). Interestingly, CFR is associated with cardiovascular events independently of luminal angiographic severity (33). Apart from the ability to identify high-risk individuals in whom the majority of events occur, a normal CFR confers a very low risk of cardiovascular events and mortality.

**CONCLUSION**

Detection of CAD and assessment of disease severity by PET MPI with addition of CFR to detect angiographically significant as well as subclinical atherosclerosis, provides the clinician with an integrated view of the disease state and subsequent risk.  CFR, representing a final common pathway of multiple pathophysiological processes which affect the macro- and microvasculature, is a powerful diagnostic and prognostic tool.  Based on clinical equipoise, contemporary CAD treatment approaches should prioritize strategies based on PET MPI and CFR with its superior accuracy and prognosis compared to SPECT.  Given its inherent limitations, SPECT MPI may be tied to more testing and downstream costs.  Finally, we would like to end this debate with a question:  "Would you be more reassured about a patient's CAD burden and prognosis if the SPECT MPI were negative or if the PET MPI and CFR were negative?"  Based on existing and emerging data, we believe the choice to be evident.

| Clinical advantages of PET MPI | Contributing factors |
|---|---|
| Shorter imaging protocol | Shorter half-lives of tracers<br>More rapid background clearance<br>Higher photon sensitivity of scanners |
| Lower radiation dose to patients | Shorter half-lives of tracers<br>More favorable radiation dosimetry |
| Higher sensitivity for CAD detection | Higher PET system resolution<br>Higher myocardial extraction fraction of tracers (except for Rb-82)<br>Peak stress imaging of LV function<br>Absolute quantitation of MBF and CFR |
| Higher specificity for CAD detection | Routine attenuation correction |
| Improved CAD risk stratification | Higher sensitivity and specificity for ischemia detection<br>Absolute quantitation of MBF and CFR |

**Table 1.** Clinical advantages of PET vs. SPECT MPI and contributing factors.

**REFERENCES**

**1.**     Maddahi J, Packard RR. Cardiac PET perfusion tracers: current status and future directions. *Seminars in Nuclear Medicine* 2014;44:333-43.

**2.**     Maddahi J. Properties of an ideal PET perfusion tracer: new PET tracer cases and data. *Journal of Nuclear Cardiology* 2012;19 Suppl 1:S30-7.

**3.**     Maddahi J, Udelson J, Heller GV, Lazewatsky J, Orlandi C. The first phase 3 international multicenter clinical trial of Flurpiridaz F 18, a new radiopharmaceutical for PET Myocardial perfusion imaging (abstract). *Journal of Nuclear Cardiology* 2015.

**4.**     Maddahi J, Huang SC, Schiepers C, Bengel F, Czernin J, Schelbert HS, et al. Same day rest-stress protocols for PET imaging with the new F-18 labeled BMS747158 myocardial perfusion tracer. *Journal of Nuclear Medicine* 2009;50(2):1173

**5.**     Berman DS, Maddahi J, Tamarappoo BK, Czernin J, Taillefer R, Udelson JE et al. Phase II safety and clinical comparison with single-photon emission computed tomography myocardial perfusion imaging for detection of coronary artery disease: flurpiridaz F 18 positron emission tomography. *Journal of the American College of Cardiology* 2013;61:469-77.

**6.**     Slomka PJ, Berman DS, Germano G. New cardiac cameras: single-photon emission CT and PET. *Seminars in Nuclear Medicine* 2014;44:232-51.

**7.**     Kaster T, Mylonas I, Renaud JM, Wells GA, Beanlands RS, deKemp RA. Accuracy of low-dose rubidium-82 myocardial perfusion imaging for detection of coronary artery disease using 3D PET and normal database interpretation. *Journal of Nuclear Cardiology* 2012;19:1135-45.

**8.**     Senthamizhchelvan S, Bravo PE, Esaias C, Lodge MA, Merrill J, Hobbs RF et al. Human biodistribution and radiation dosimetry of 82Rb. *Journal of Nuclear Medicine* 2010;51:1592-9.

**9.**     Knuuti J. Integrated positron emission tomography/computed tomography (PET/CT) in coronary disease. *Heart* 2009;95:1457-63.

**10.**     Einstein AJ. Effects of radiation exposure from cardiac imaging: how good are the data? *Journal of the American College of Cardiology* 2012;59:553-65.

**11.**     Maddahi J, Czernin J, Lazewatsky J, Huang SC, Dahlbom M, Schelbert H, et al. Phase I, first-in-human study of BMS747158, a novel 18F-labeled tracer for myocardial perfusion PET: dosimetry, biodistribution, safety, and imaging characteristics after a single injection at rest. *Journal of Nuclear Medicine* 2011;52(9):1490-8

**12.**     Maddahi J, Bengel F, Czernin J, Crane P, Dahlbom M, Schelbert, HS, et al. Dosimetry, biodistribution, and safety of flurpiridaz F 18 in healthy subjects undergoing 2-day rest-stress PET myocardial perfusion imaging (abstract). *Journal of Nuclear Cardiology* 2016

**13.**     Maddahi J, Lazewatsky J, Udelson J, Orlandi C. Radiation Dose to Patients in a Phase 3 Trial of Flurpiridaz F18, a New Radiopharmaceutical for PET Myocardial Perfusion Imaging (abstract) *Journal of Nuclear Cardiology* 2014

**14.**     Parker MW, Iskandar A, Limone B, Perugini A, Kim H, Jones C et al. Diagnostic accuracy of cardiac positron emission tomography versus single photon emission computed tomography for coronary artery disease: a bivariate meta-analysis. *Circulation Cardiovascular Imaging* 2012;5:700-7.

**15.**     Mc Ardle BA, Dowsley TF, deKemp RA, Wells GA, Beanlands RS. Does rubidium-82 PET have superior accuracy to SPECT perfusion imaging for the diagnosis of obstructive coronary disease?: A systematic review and meta-analysis. *Journal of the American College of Cardiology* 2012;60:1828-37.

**16.**     Bateman TM, Heller GV, McGhie AI, Friedman JD, Case JA, Bryngelson JR, et al. Diagnostic accuracy of rest/stress ECG-gated Rb-82 myocardial perfusion PET: Comparison with ECG-gated Tc-99m sestamibi SPECT. *Journal of Nuclear Cardiology* 2006;13 (1): 24-33

**17.**     Schindler TH, Schelbert HR, Quercioli A, Dilsizian V. Cardiac PET imaging for the detection and monitoring of coronary artery disease and microvascular health. *JACC Cardiovascular Imaging* 2010;3:623-40.

**18.**     Dorbala S, Vangala D, Sampson U, Limaye A, Kwong R, Di Carli MF. Value of vasodilator left ventricular ejection fraction reserve in evaluating the magnitude of myocardium at risk and the

extent of angiographic coronary artery disease: a 82Rb PET/CT study. *Journal of Nuclear Medicine* 2007;48:349-58.

19.     Bengel FM. Leaving relativity behind: quantitative clinical perfusion imaging. *Journal of the American College of Cardiology* 2011;58:749-51.

20.     Cremer P, Hachamovitch R, Tamarappoo B. Clinical decision making with myocardial perfusion imaging in patients with known or suspected coronary artery disease. *Seminars in Nuclear Medicine* 2014;44:320-9.

21.     Fiechter M, Ghadri JR, Gebhard C, Fuchs TA, Pazhenkottil AP, Nkoulou RN et al. Diagnostic value of 13N-ammonia myocardial perfusion PET: added value of myocardial flow reserve. *Journal of Nuclear Medicine* 2012;53:1230-4.

22.     Naya M, Murthy VL, Taqueti VR, Foster CR, Klein J, Garber M et al. Preserved coronary flow reserve effectively excludes high-risk coronary artery disease on angiography. *Journal of Nuclear Medicine* 2014;55:248-55.

23.     Packard RR, Huang SC, Dahlbom M, Czernin J, Maddahi J. Absolute quantitation of myocardial blood flow in human subjects with or without myocardial ischemia using dynamic flurpiridaz F 18 PET. *Journal of Nuclear Medicine* 2014;55:1438-44.

24.     Ben-Haim S, Murthy VL, Breault C, Allie R, Sitek A, Roth N et al. Quantification of Myocardial Perfusion Reserve Using Dynamic SPECT Imaging in Humans: A Feasibility Study. *Journal of Nuclear Medicine* 2013;54:873-9.

25.     Kay J, Dorbala S, Goyal A, Fazel R, Di Carli MF, Einstein AJ et al. Influence of sex on risk stratification with stress myocardial perfusion Rb-82 positron emission tomography: Results from the PET (Positron Emission Tomography) Prognosis Multicenter Registry. *Journal of the American College of Cardiology* 2013;62:1866-76.

26.     Chow BJ, Dorbala S, Di Carli MF, Merhige ME, Williams BA, Veledar E et al. Prognostic value of PET myocardial perfusion imaging in obese patients. *JACC Cardiovascular Imaging* 2014;7:278-87.

**27.**     Herzog BA, Husmann L, Valenta I, Gaemperli O, Siegrist PT, Tay FM et al. Long-term prognostic value of 13N-ammonia myocardial perfusion positron emission tomography added value of coronary flow reserve. *Journal of the American College of Cardiology* 2009;54:150-6.

**28.**     Fukushima K, Javadi MS, Higuchi T, Lautamaki R, Merrill J, Nekolla SG et al. Prediction of short-term cardiovascular events using quantification of global myocardial flow reserve in patients referred for clinical 82Rb PET perfusion imaging. *Journal of Nuclear Medicine* 2011;52:726-32.

**29.**     Ziadi MC, Dekemp RA, Williams KA, Guo A, Chow BJ, Renaud JM et al. Impaired myocardial flow reserve on rubidium-82 positron emission tomography imaging predicts adverse outcomes in patients assessed for myocardial ischemia. *Journal of the American College of Cardiology* 2011;58:740-8.

**30.**     Dorbala S, Di Carli MF. Cardiac PET perfusion: prognosis, risk stratification, and clinical management. *Seminars in Nuclear Medicine* 2014;44:344-57.

**31.**     Murthy VL, Naya M, Foster CR, Hainer J, Gaber M, Di Carli G et al. Improved cardiac risk assessment with noninvasive measures of coronary flow reserve. *Circulation* 2011;124:2215-24.

**32.**     Murthy VL, Naya M, Foster CR, Gaber M, Hainer J, Klein J et al. Association between coronary vascular dysfunction and cardiac mortality in patients with and without diabetes mellitus. *Circulation* 2012;126:1858-68.

**33.**     Taqueti VR, Hachamovitch R, Murthy VL, Naya M, Foster CR, Hainer J et al. Global coronary flow reserve is associated with adverse cardiovascular events independently of luminal angiographic severity and modifies the effect of early revascularization. *Circulation* 2015;131:19-27.

**CHAPTER EIGHT**

**Fractional flow reserve by computerized tomography and subsequent coronary revascularization**

Packard R.R.S., Li D., Sayre J.W., Budoff M.J., Karlsberg R.P.

**ABSTRACT**

Fractional flow reserve by computerized tomography (FFR-CT) provides non-invasive functional assessment of the hemodynamic significance of coronary artery stenosis. We determined the FFR-CT values, receiver operator characteristic (ROC) curves and predictive ability of FFR-CT for *actual* standard of care guided coronary revascularization. Consecutive outpatients who underwent coronary CT angiography (coronary CTA) followed by invasive angiography over a 24-month period from 2012-2014 were identified. Studies that fit inclusion criteria (n=75 patients, mean age 66, 75% males) were sent for FFR-CT analysis, and results stratified by coronary artery calcium (CAC) scores. Coronary CTA studies were re-interpreted in a blinded manner, and baseline FFR-CT values obtained retrospectively. Therefore, results did not interfere with clinical decision-making. Median FFR-CT values were 0.70 in revascularized (n=69) and 0.86 in not revascularized (n=138) coronary arteries ($P$ <0.001). Using clinically established significance cutoffs of FFR-CT ≤0.80 and coronary CTA ≥70% stenosis for the prediction of clinical decision making and subsequent coronary revascularization, the positive predictive values were 74% and 88%, and negative predictive values 96% and 84%, respectively. The area under the curve (AUC) for all studied territories was 0.904 for coronary CTA, 0.920 for FFR-CT, and 0.941 for coronary CTA combined with FFR-CT ($P$ =0.001). With increasing CAC scores, the AUC decreased for coronary CTA but remained higher for FFR-CT ($P$ <0.05). The addition of FFR-CT provides a complementary role to coronary CTA and increases the ability of a CT-based approach to identify subsequent standard of care guided coronary revascularization.

**INTRODUCTION**

Previous observations demonstrated the need for improved risk stratification and increased yield of patients who undergo invasive coronary angiography and subsequent revascularization.[1] Mounting evidence over recent years supports the use of coronary computerized tomography angiography (coronary CTA) as an attractive non-invasive approach that may fulfill this gatekeeper role.[2,3] However, coronary artery calcium (CAC) significantly reduces the diagnostic specificity[4,5] and overall accuracy[6] of coronary CTA.

Coronary CTA provides non-invasive assessment of CAD with a high correlation to invasive coronary angiography.[4,5] Recent large clinical trials[7,8] further support increased diagnostic certainty and improved efficiency of triage to invasive coronary angiography when using coronary CTA. Despite these findings however, coronary CTA has not been widely adopted – in part due to its initial inability to determine the physiologic importance of CAD. Fractional flow reserve derived from coronary CTA (FFR-CT) enhances the accuracy of coronary CTA and has emerged as a potential tool to provide functional characterization of the hemodynamic significance of coronary artery stenosis with correlation to invasive FFR.[9] Furthermore, the accuracy of FFR-CT is superior to coronary CTA stenosis in the presence of calcification[10,11] thereby providing enhanced interpretation ability.

An ideal non-invasive strategy should go beyond the prediction of the anatomical narrowing of an artery and aggregate risk factor profiles, intrinsically reflect clinical parameters and predict the physiological need for coronary revascularization on a per vessel basis. Multiple studies have compared FFR-CT to coronary artery stenosis and invasive FFR,[12-14] and determined its ability to identify obstructive CAD during invasive angiography[15] with associated cost reduction.[16] Despite these studies analyzing CT functional imaging of coronary obstructions,[17] none have compared

FFR-CT to actual decision-making at the time of invasive coronary angiography while integrating all available parameters including risk factor profile, clinical presentation and anatomical findings.

Accordingly, in the present study we retrospectively determined whether FFR-CT predicts standard of care guided coronary revascularization in 'real world' clinical practice, above and beyond percent stenosis determination. We calculated the performance of coronary CTA alone, FFR-CT alone, or coronary CTA combined with FFR-CT to predict actual standard of care guided clinical decision making leading to medical management vs. coronary revascularization – integrating clinical presentation as well as clinical and diagnostic parameters with findings during invasive coronary angiography. In addition, we further established the range of FFR-CT values in patients who underwent coronary revascularization and analyzed the performance of FFR-CT and coronary CTA in studies with significant calcium burden.

**METHODS**

**Patient population**

Consecutive outpatients who underwent computerized tomography (CT) followed by invasive angiography (mean delay 45.8 days) over a 24-month period from 2012-2014 at the Cedars Sinai Heart Institute–Cardiovascular Medical Group of Southern California (Los Angeles) were identified using a retrospective approach. Patient characteristics **(Table 1)** at the time of coronary CTA were obtained through review of electronic medical records. The decision to obtain CT studies **(Table 1)** and to proceed with invasive coronary angiography was at the discretion of the care providers. The decision to advance to coronary revascularization was based on standard of care. This study was approved by the Institutional Review Board.

**Coronary CT angiography studies**

Coronary CTA images were acquired using a 64-slice multi-detector row Lightspeed VCT scanner (General Electric Healthcare). Patients received beta blockers to achieve a heart rate <60bpm. Following a scout X-ray of the chest, a timing bolus (10–20mL iodixanol [Visipaque], General Electric Healthcare) was performed to detect time to reach optimal contrast opacification in the axial image at a level immediately superior to the ostium of the left main coronary artery. Nitroglycerin was given prior to contrast administration. A triple phase contrast protocol was used during image acquisition: iodixanol (60mL), followed by a ½–½ mixture of iodixanol and normosaline (40mL), followed by a normosaline flush (50mL). The scan parameters were 64x0.625mm collimation, tube voltage 100 or 120kV, effective mA 350–780 and 512x512 matrix size. All coronary computerized tomography angiography (CTA) studies were transferred to a workstation (Vitrea–Vital Images, Toshiba).

**Coronary CT angiography interpretation**

The coronary CTA studies were re-interpreted separately by 2 readers (R.R.S.P. and R.P.K.) blinded to all patient characteristics, FFR-CT and invasive coronary angiography results. The coronary CTA readers were permitted to use any or all of the available post-processing image reconstruction algorithms, including 2-dimensional axial and 3-dimensional maximal intensity projection, multi-planar reformat, cross-sectional analysis, and volume-rendered technique. A semi-quantitative scale was used by the coronary CTA readers to grade the extent of luminal stenosis as a percentage of the vessel diameter. Stenosis severity was recorded in the following manner: 0%, 1-24%, 25-49%, 50-69%, 70-99%, and 100%. There was 95% overall inter-observer agreement of the 2 blinded readers. In the 4 cases with discrepant reads, consensus was reached by joint interpretation.

**FFR-CT studies**

CT studies that did not fit inclusion criteria (absence of coronary CT angiography, prior coronary revascularization, incomplete or suboptimal datasets) were excluded **(Fig. 1)**. The remaining studies (n=75) were sent for FFR-CT analysis (HeartFlow) which was performed as previously described.[15,18] Three-dimensional blood flow simulations in the coronary vasculature were performed using proprietary software, with qualitative and quantitative image analysis, image segmentation, and physiological modelling using principles of computational fluid dynamics.[9] Coronary blood flow was simulated under conditions that modelled coronary hyperemia to mirror pressure and flow data and the FFR values that would have been obtained during an invasive evaluation. Data provided to the investigators included the lowest FFR-CT value in each coronary distribution and a color-scale representation showing FFR-CT values in all vessels >1.8mm in diameter. FFR-CT values from left main coronary arteries were excluded due to inconsistent reporting when vascular territories were short, and FFR-CT values from chronic total occlusions (CTOs) were excluded to avoid skewing of the data and given this additional measure is of limited clinical utility. Baseline FFR-CT values were obtained retrospectively and therefore did not

237

interfere with clinical decision-making.  FFR-CT values were compared in revascularized (n=50 patients, n=69 arteries) and not revascularized arteries (n=138) **(Fig. 2, 3)**.

**Comparative performance of FFR-CT and coronary CTA**

The positive and negative predictive abilities for coronary revascularization of previously established and clinically used significance cutoffs of FFR-CT ≤0.80 and coronary CTA ≥70% stenosis were compared **(Table 2)**.  Receiver operator characteristic (ROC) curves for the prediction of coronary revascularization were determined for coronary CTA alone, FFR-CT alone, and coronary CTA combined with FFR-CT **(Fig. 4)**.  For the ROC curves, FFR-CT values were used as continuous variables ranging from 0.50–1.0, whereas the following discrimination thresholds were used for coronary CTA stenosis:  0%, 1-24%, 25-49%, 50-69% and 70-99%. ROC curves were analyzed in the entire population to determine global test performance and in the subgroups with a CAC score of >0, >200, >400, >600, >800, and >1000 **(Fig. 5)**.

**Statistical analyses**

Statistics were performed using the Mann-Whitney test for differences in median FFR-CT values, the Kolmogorov-Smirnov test for FFR-CT value distributions, and the c-statistic to compare the relative performance of FFR-CT and coronary CTA as well as to analyze significance of the ROC curves.  To test the significance of differences in areas under two independent ROC curves, Cochran's c-statistic was applied based on multiple comparisons, as previously described.[19]  To this end, we first calculated the areas under the ROC curve (AUC) for coronary CTA, FFR-CT and the combination of coronary CTA and FFR-CT.  Next, we used predictors with the SAS ROCcomp command to apply both nested and non-nested models.[20]  IBM SPSS version 20 and GraphPad version 6 were used to perform the statistical analyses.  A *P*-value <0.05 was considered statistically significant.

**RESULTS**

Over a 24-month period (2012-2014), 257 consecutive outpatients who had a CT followed by invasive coronary angiography were identified **(Fig. 1)**. Of the excluded studies, 60 did not have a coronary computerized tomography angiography (CTA) with either a non-contrast CAC (coronary artery calcium) score only, an aortogram, a pre-electrophysiological study, a TAVR (trans-catheter aortic valve replacement) or PE (pulmonary embolism) protocol; 62 had prior revascularization (given FFR-CT is not approved in patients with prior surgical or interventional revascularization) with 47 who had prior PCI (percutaneous coronary intervention) and 15 prior CABG (coronary artery bypass grafting); and 60 studies were excluded or rejected due to misregistrations such as a 'skip' in the axial data, motion artifact, or missing left ventricular segments. No studies were rejected due to blooming artifact.

All the remaining coronary CTA studies underwent successful FFR-CT analysis (n=75 patients, n=207 territories). Patient characteristics, medical history, medications and laboratory results are presented in **Table 1**. The 10-year ACC/AHA atherosclerotic cardiovascular disease (ASCVD) risk,[21] defined as coronary death or nonfatal myocardial infarction, or fatal or nonfatal stroke, of our study population was as follows: 27% had an ASCVD <7.5%, placing them in the low risk category, whereas 73% had an ASCVD ≥7.5%, categorizing them as high risk. None of the patients had a previous myocardial infarction. Indications for the coronary CTA studies are detailed in **Table 1**. Of the patients who underwent a coronary CTA study, 64% were symptomatic with 19% experiencing typical angina and 45% reporting atypical anginal symptoms. In the remaining 36% of patients who were asymptomatic, coronary CTA was used as a screening tool for the determination of underlying CAD burden and severity. 8% of patients had previously identified CAD by coronary CT or invasive angiography, and 28% had significant CAD risk factors. The mean CAC score was 705.

Baseline FFR-CT distributions (median, 25th–75th percentile) **(Fig. 2)** in revascularized 0.70 (0.62–0.75) compared to not revascularized territories 0.86 (0.82–0.91) displayed significantly different medians (*P* <0.001) and value distributions (*P* <0.001). We retrospectively analyzed the proportion of cases in which FFR-CT recapitulated the clinical decision-making process to medically manage or revascularize coronary territories **(Fig. 3)**. Concordance was observed in 90% of the territories whereas 10% were discordant. 58% of territories (n=120) had a FFR-CT >0.80 and were managed medically, whereas 32% of territories (n=66) had a FFR-CT ≤0.80 and were revascularized. 1% of the territories (n=3) had a FFR-CT >0.80 but were revascularized, with review of cases illustrating coronary stenoses ≥50% and presence of typical anginal symptoms. Invasive FFR was not obtained in these cases. Of the 9% territories (n=18) in which an FFR-CT ≤0.80 was reported but were medically managed, the following contributing factors were observed; invasive coronary stenosis <25% (n=8), invasive coronary stenosis 25-50% (n=3), discrepancy with an invasive FFR >0.80 during cardiac catheterization (n=5) or significant stenosis deemed too distal and not amenable to intervention (n=2). In addition, the above patients with invasive coronary stenoses <25% or 25-50% underwent invasive coronary angiography following coronary CTA falsely concerning for significant stenoses which were obtained in the setting of known CAD, CAD screening, or atypical symptoms **(Table 1)**.

Next, we sought to compare the discriminative ability of FFR-CT compared to coronary CTA in the prediction of standard of care guided coronary revascularization **(Table 2)**. To this end, clinically accepted and routinely used significance cutoffs were studied, i.e. FFR-CT ≤0.80 and coronary CTA stenosis ≥70%. The overall accuracies for the prediction of revascularization were similar – 86% for FFR-CT and 85% for coronary CTA. Importantly, a significant complementary role for these 2 strategies was observed, with coronary CTA having a superior positive predictive value of 88% and a positive likelihood ratio of 14.3, whereas FFR-CT had a superior negative predictive value of 96% and a negative likelihood ratio of 0.09.

We further determined receiver operator characteristic (ROC) curves for the comparison of 3 strategies: coronary CTA alone, FFR-CT alone, and coronary CTA combined with FFR-CT for the prediction of subsequent coronary revascularization in the entire study population **(Fig. 4)**. Using continuous variables portrayed in the ROC curves, the global statistical accuracy was not used to test the study properties of coronary CTA vs. invasive coronary angiography, but the overall ability of coronary CTA vs. FFR-CT to predict actual clinical decision-making, i.e. medical management vs. coronary revascularization. The reference group was coronary CTA alone (AUC, 95% CI): 0.904 (0.863–0.944), with the ROC curve demonstrating the strong performance of this test by itself. FFR-CT alone (AUC, 95% CI): 0.92 (0.883–0.957), had a greater AUC than coronary CTA which did not achieve significance ($P$ = 0.4). However, combining coronary CTA with FFR-CT (AUC, 95% CI): 0.941 (0.911–0.971) had the highest AUC for the prediction of subsequent revascularization and was significant ($P$ = 0.001). In addition, we identified from the ROC curve the optimal FFR-CT cut-off value to predict downstream revascularization may be a lower FFR-CT value of 0.76, and not 0.80.[22] In order to test the performance of this FFR-CT cutoff value, a comparison of ROC curves (on a per-patient basis) was applied, yielding an AUC of 0.842 for an FFR-CT cut-off of 0.76 and an AUC of 0.829 for an FFR-CT cutoff of 0.80 ($P$ = 0.043).

AUCs were also stratified according to increasing CAC burden categories and demonstrated the increasing contribution of FFR-CT to overall accuracy with worsening calcification **(Fig. 5)**. Whereas coronary CTA AUC progressively decreased with worsening calcification burden, ranging from 0.90 (CAC>0) to 0.71 (CAC>1000), this phenomenon was less observed in the FFR-CT AUC which remained more stable in its discriminative ability, ranging from 0.92 (CAC>0) to 0.86 (CAC>1000) ($P$ <0.05, FFR-CT combined with coronary CTA vs. coronary CTA alone for all CAC scores).

241

A case example of a patient with short clinical vignette comparing coronary CTA, FFR-CT and

invasive coronary angiography results is illustrated **(Fig. 6)**.

**DISCUSSION**

The management of patients with stable coronary artery disease (CAD) has evolved significantly[23-25] with efforts to determine which coronary stenoses cause myocardial ischemia. A strategy of artery-specific flow-guided revascularization was explored in the FAME trials.[26,27] In stable CAD patients, routine measurement of invasive FFR during coronary angiography significantly reduces death and non-fatal myocardial infarction compared to an angiographically driven approach when stenting of indicated lesions only if the FFR is ≤0.80.[26] Conversely, similar patients with an FFR >0.80 should receive medical therapy alone to improve outcomes.[27] Thus, the routine measurement of FFR is supported by large clinical trials and integrated into American[28] and European guidelines[29] recommending the use of FFR with a cutoff of 0.80 to guide the decision to medically manage or revascularize patients with stable CAD.[30]

FFR-CT may offer a noninvasive equivalent to invasive FFR.[17] FFR-CT provides functional characterization of the hemodynamic significance of coronary artery stenosis without changes in acquisition, medication, contrast or radiation.[9,18] FFR-CT computation is based on calculations of coronary flow and pressure fields from anatomic data, in particular construction of an anatomic model of the coronary arteries, a mathematical model of coronary physiology to derive boundary conditions representing cardiac output, aortic pressure, microcirculatory resistance, and their combination with fluid dynamics principles which relate to conservation of mass and balance of momentum.[18]

The present study sought to take findings beyond previous reports[12-14] by predicting not just the significance of coronary artery narrowing, but also establishing the distribution of FFR-CT values, inclusive of studies with high calcium scores, in an integrated manner to predict coronary revascularization behavior in patients commonly treated with standard of care in a large urban Cardiology practice. We applied this measure to consecutive outpatients over a 24-month period

243

who had previously undergone invasive coronary angiography following a coronary CTA study. Given baseline FFR-CT values were obtained retrospectively, results did not interfere with clinical decision-making. We determined baseline FFR-CT values in patients undergoing coronary revascularization and those treated with optimal medical therapy, establishing significant differences in median values (0.70 vs. 0.86, respectively). A comparison of accepted and routinely used clinical significance cutoffs of FFR-CT ≤0.80 and coronary CTA stenosis ≥70%[26-29] highlighted important different behaviors of these 2 tests. Indeed, a coronary CTA approach had a significant positive predictive value and positive likelihood ratio, indicating that in the presence of an angiographically significant stenosis, the odds of having a downstream revascularization were high, reflecting the ability of coronary CTA to identify high-risk patients. In contrast, an FFR-CT approach had a significant negative predictive value and negative likelihood ratio, supporting the hypothesis that in the presence of a hemodynamically insignificant FFR-CT value >0.80, the odds of having downstream revascularization were low, thereby reflecting the ability of FFR-CT to exclude high-risk patients. With the use of FFR-CT values as continuous variables and incremental discrimination thresholds for coronary CTA stenoses, we further established global performance measures of these tests in the prediction of coronary revascularization. Accordingly, our data demonstrate that even though coronary CTA alone had a high predictive ability of subsequent coronary revascularization, FFR-CT alone performed better, and the combination of coronary CTA and FFR-CT performed best, particularly in patients with advanced disease and elevated CAC scores. In addition, our findings suggest that the best cut-off value for the prediction of downstream revascularization may be a lower FFR-CT value of 0.76, and not 0.80 as reported with invasive FFR.

Previous CT trials determined the diagnostic characteristics of coronary CTA compared to invasive coronary angiography – i.e. % angiographic stenosis by CT vs. % angiographic stenosis by cardiac catheterization,[4,5,31] a correlation dependent on target lesion, coronary calcium score,

and vessel diameter.  In these coronary CTA validation studies, coronary artery segments <2 mm in diameter were not evaluated.[32]  In the present study, we examined the ability of coronary CTA alone, FFR-CT alone, or coronary CTA combined with FFR-CT to integrate all available parameters including clinical presentation, laboratory findings, non-invasive imaging workup, and findings on invasive coronary angiography with actual clinical decision-making regarding medical management vs. coronary revascularization on a per-vessel basis.  The difference in approach we adopted with an endpoint consisting of standard of care guided clinical decision-making to manage with optimal medical therapy or revascularize coronary territories, as opposed to previous studies where the endpoint consisted of anatomic findings during cardiac catheterization,[4,5,31] explain differences in the observed predictive abilities of coronary CTA and FFR-CT we illustrate. Our study has several limitations.  This was a single center retrospective study.  We analyzed FFR-CT only in patients who had a coronary CTA followed by invasive angiography.  The decision to proceed with revascularization was at the discretion of the primary cardiologist, based on medical history, clinical presentation, non-invasive imaging tests and findings during angiography. We believe however these limitations also constitute a strength of our study population which is representative of 'real world' patient care and may avoid the patient selection bias of clinical trials.

**CONCLUSIONS**

FFR-CT predicts standard of care guided coronary revascularization and provides additive predictive value to coronary CTA, improving overall accuracy, particularly in territories with significant calcification. Future studies are needed to validate these observations prospectively and to determine the optimal FFR-CT cutoff for the prediction of coronary revascularization. Our results suggest that coronary CTA combined with FFR-CT allows individual patient-level, artery-specific decision making, thereby enhancing the gatekeeping function of coronary CTA and increasing the diagnostic and therapeutic yield of invasive coronary angiography.

**FIGURES AND TABLES**

| Patient Characteristics | |
|---|---|
| Age, years | 66 ± 10 |
| Gender, male | 56 (75) |
| **Medical History** | |
| LVEF, % | 60 ± 8 |
| Hypertension | 41 (55) |
| Dyslipidemia | 59 (79) |
| Diabetes mellitus | 8 (11) |
| Tobacco use | |
|     Current | 10 (14) |
|     Former | 25 (33) |
|     Never | 40 (53) |
| Family history of CAD | 40 (53) |
| **Medications** | |
| Aspirin | 45 (60) |
| Second antiplatelet agent | 6 (8) |
| Betablocker | 22 (29) |
| ACE-I/ARB | 32 (43) |
| Statin | 42 (56) |
| Fish oil | 9 (12) |
| Ezetimibe | 8 (11) |
| **Laboratory Results** | |
| Creatinine, $\mu$mol/L | 87 (77 – 99) |
| GFR, mL/min/1.73 m$^2$ | 75 (63 – 86) |
| Glucose, mmol/L | 5.4 (4.9 – 5.9) |
| HbA1C, % | 5.6 (5.4 – 5.9) |
| Total cholesterol, mmol/L | 4.6 (4.0 – 5.5) |
| LDL cholesterol, mmol/L | 2.8 (2.2 – 3.7) |
| HDL cholesterol, mmol/L | 1.3 (1.1 – 1.5) |
| Triglycerides, mmol/L | 1.3 (0.8 – 1.7) |
| **Coronary CTA Indication** | |
| Symptomatic with typical angina | 14 (19) |
| Symptomatic with atypical angina | 34 (45) |
| Asymptomatic with known CAD * | 6 (8) |
| Asymptomatic with CAD risk factors | 21 (28) |

**Table 1.** Patient characteristics and coronary CTA indication

Values are mean ± standard deviation, n (%), or median (interquartile range).  * Known CAD defined as previous CAD identification by invasive angiography or coronary CT angiography. ACE-I: angiotensin-converting enzyme inhibitor.  ARB: angiotensin receptor blocker.  GFR: glomerular filtration rate.  HbA1C: hemoglobin A1C.  HDL: high density lipoprotein.  LDL: low density lipoprotein.  LVEF: left ventricular ejection fraction.

|  | FFR-CT ≤ 0.80 | | Coronary CTA ≥ 70% | |
|---|---|---|---|---|
|  |  | *P*-value |  | *P*-value |
| **Accuracy** | 86% | <0.001 | 85% | <0.001 |
| **Positive predictive value** | 74% (63–83%) | <0.001 | 88% (75–95%) | <0.001 |
| **Positive likelihood ratio** | 5.6  (3.8–8.1) | <0.001 | 14.3 (6.4–32.0) | <0.001 |
| **Negative predictive value** | 96% (91–99%) | <0.001 | 84% (77–89%) | <0.001 |
| **Negative likelihood ratio** | 0.09 (0.04–0.2) | <0.001 | 0.39 (0.29–0.53) | <0.001 |

**Table 2.** FFR-CT vs. coronary CTA analyses using routine clinical significance cut-offs and subsequent coronary revascularization.

Values in parentheses depict the 95% confidence intervals.
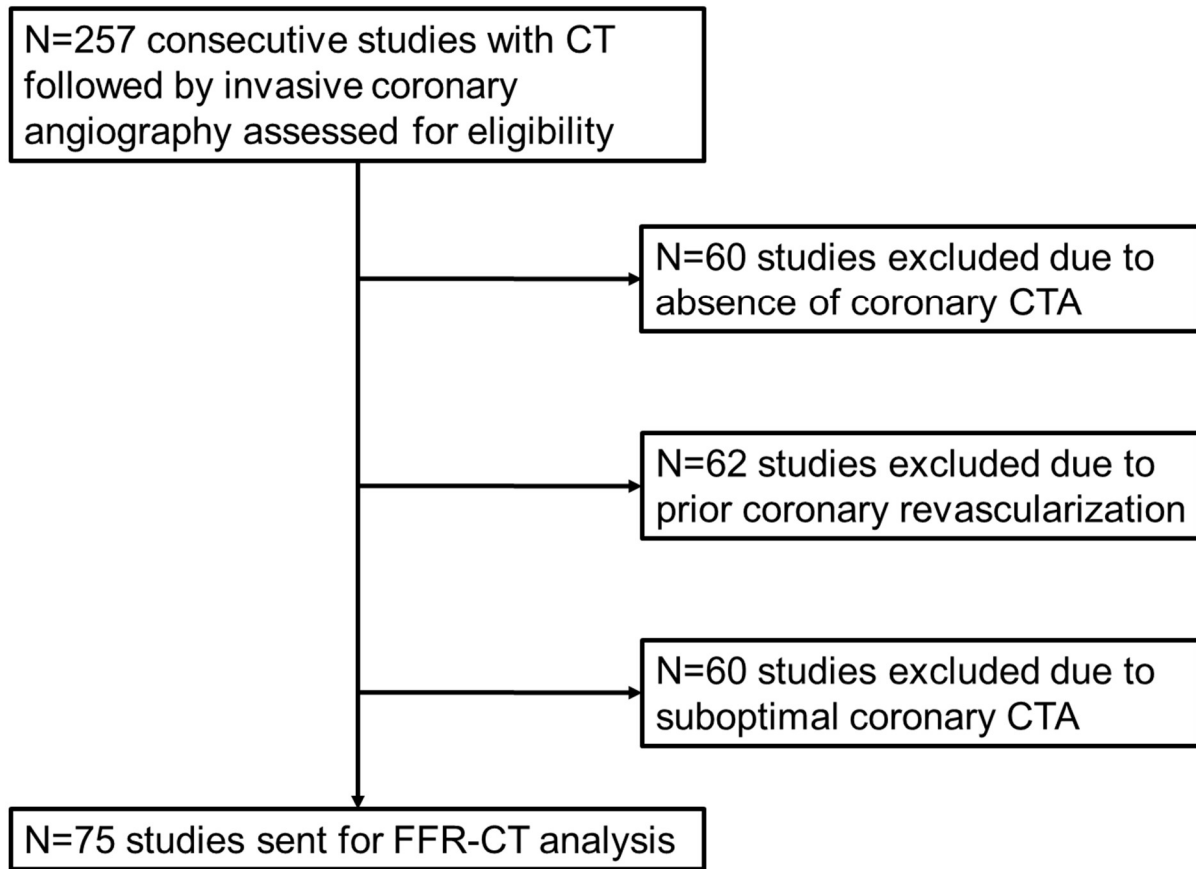
**Figure 1.** Study flowchart.
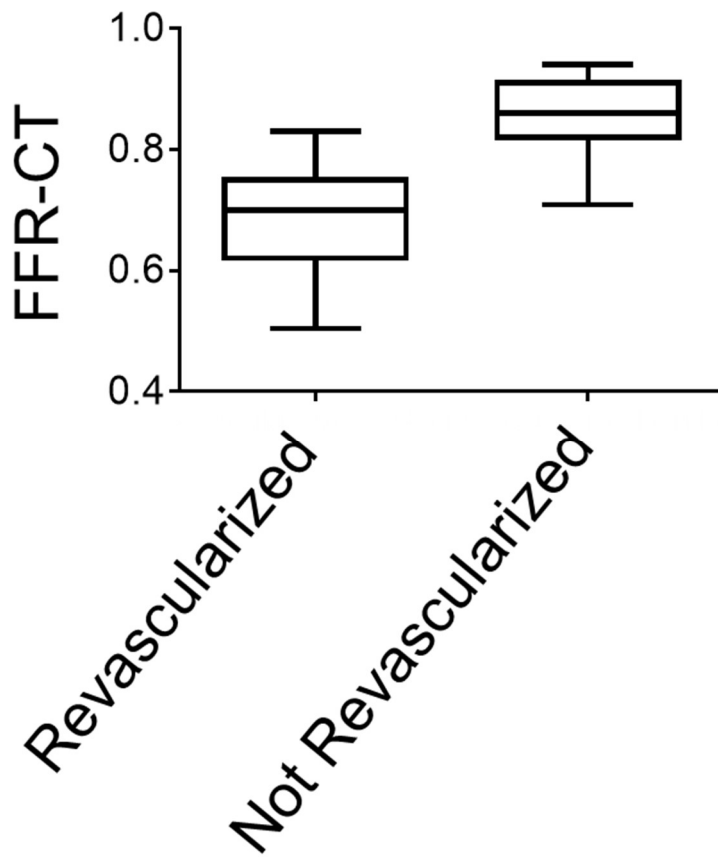
**Figure 2.** FFR-CT distributions in revascularized vs. not revascularized coronary arteries.

Bow and whisker plots with the boxes depicting the $25^{th}$–$75^{th}$ percentile and the whiskers the $5^{th}$–$95^{th}$ percentile of data distribution.
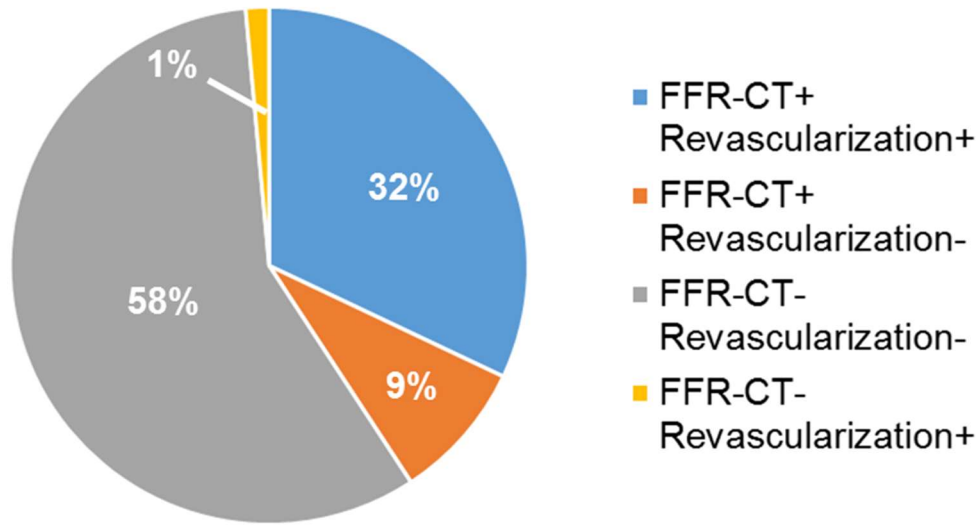
**Figure 3.** FFR-CT and clinical decision of CAD management.

Concordance between FFR-CT findings and clinical management was observed in 90% of the coronary territories (n=186) whereas 10% were discordant (n=21).
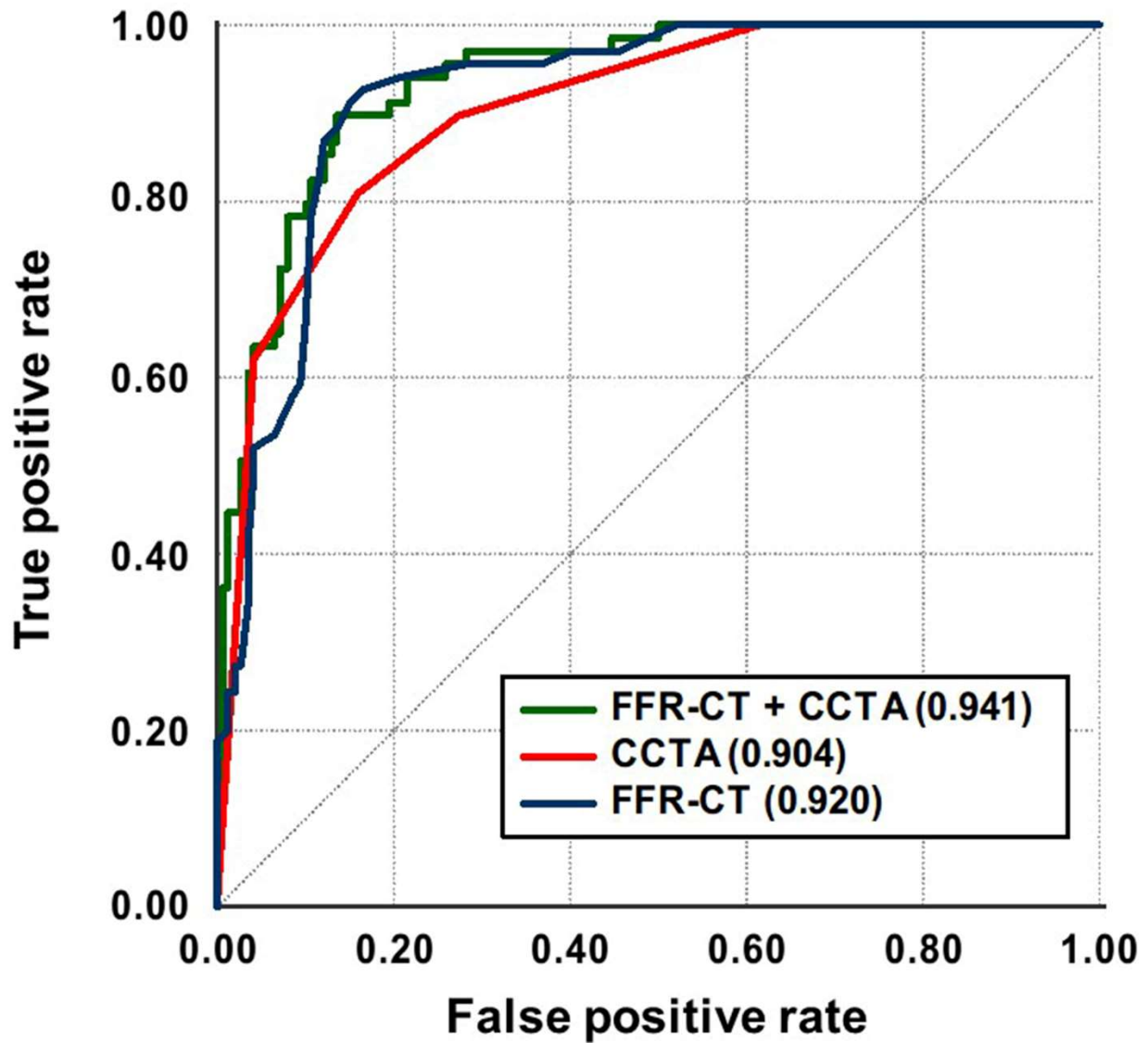
**Figure 4.** Receiver operator characteristic curves of coronary CTA, FFR-CT, or coronary CTA + FFR-CT to predict subsequent coronary revascularization.

Coronary CTA alone was the reference group and had an AUC of 0.904, whereas FFR-CT alone had an AUC of 0.92 and combining coronary CTA with FFR-CT had the highest AUC of 0.941.
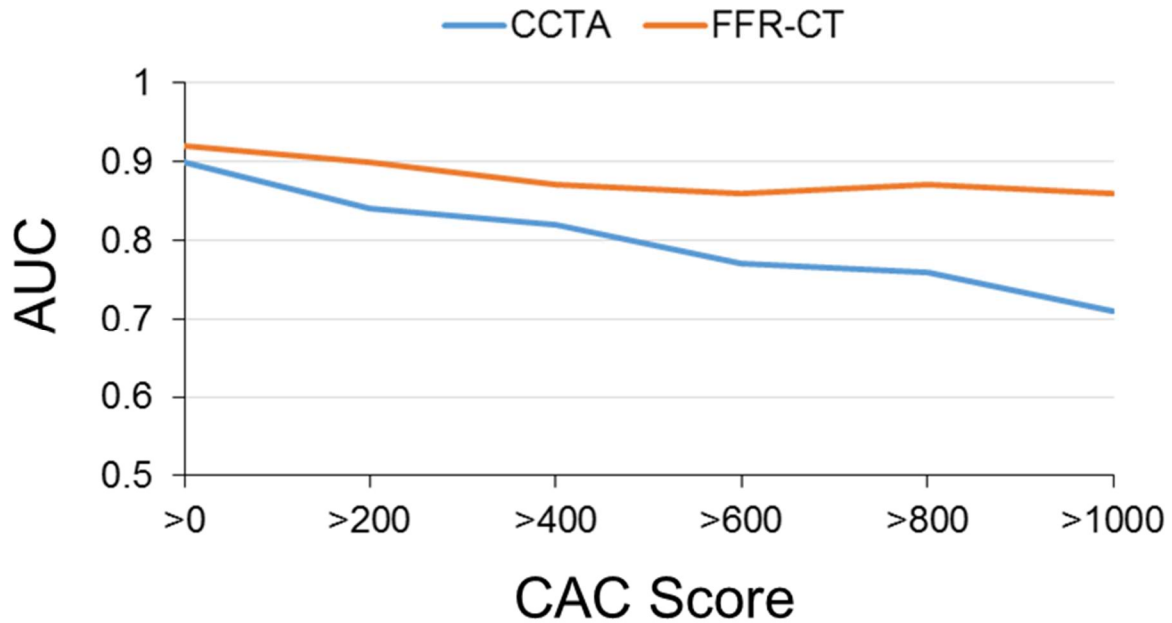
**Figure 5.** AUC plots of coronary CTA vs. FFR-CT according to increasing CAC scores for the prediction of subsequent revascularization.

AUC plots depicting relative performance of coronary CTA vs. FFR-CT in territories with increasing calcification burden ranging from CAC score >0 to >1000 demonstrate a superior performance of FFR-CT at all levels of coronary artery calcification compared to coronary CTA.

AUC: area under the curve.  CAC: coronary artery calcium.
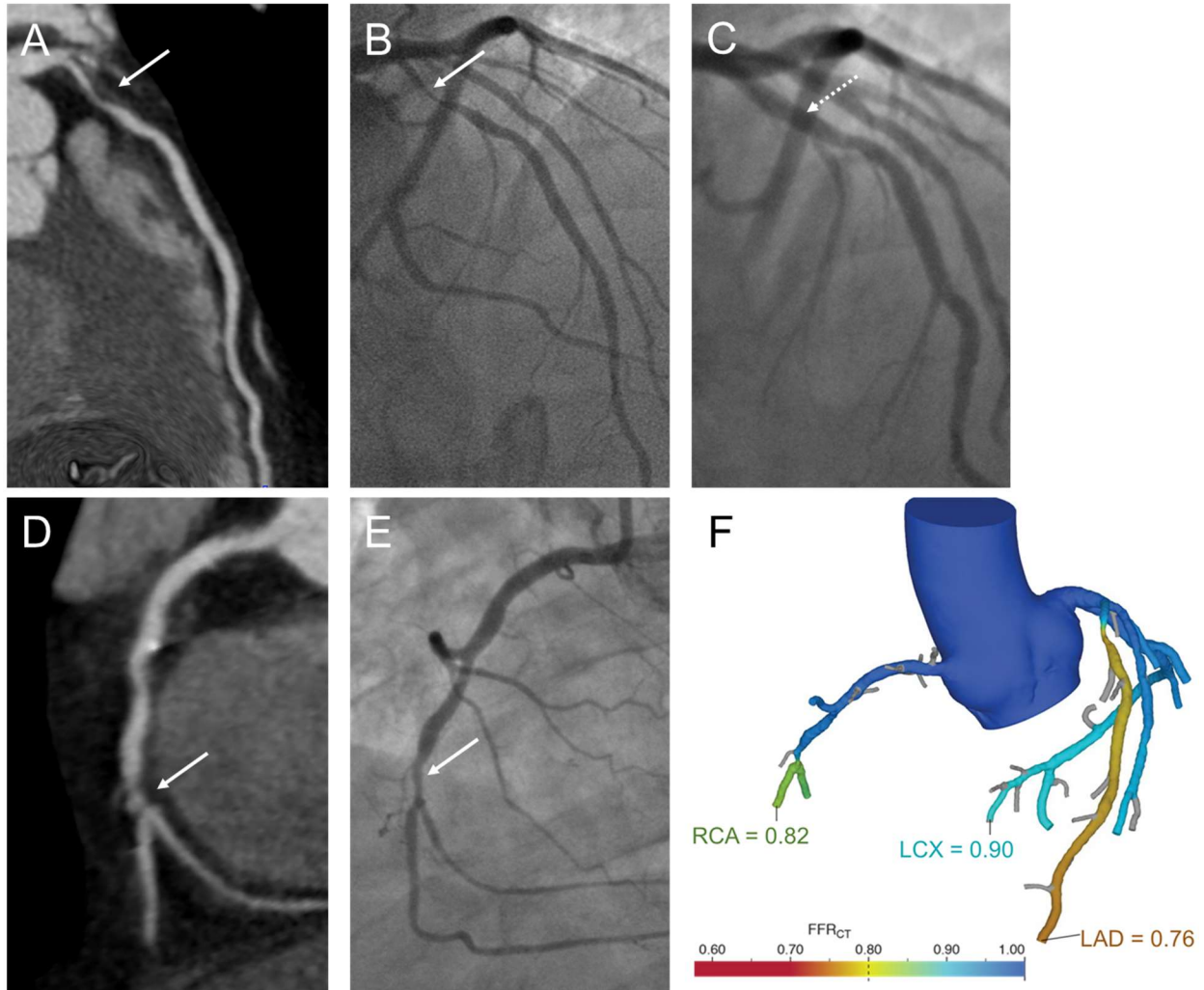
**Figure 6.** Case example comparing coronary CTA, FFR-CT and invasive angiography results. A 71 year old male presented with exertional chest pain. He exercised for 10 minutes on a Bruce protocol, experienced reproducible chest pain but had no significant ECG changes. He underwent coronary CTA which showed a 70-95% ostial left anterior descending (LAD) coronary artery narrowing (A). Invasive angiography confirmed the 70-95% ostial LAD narrowing (B) and the artery was stented (C). The coronary CTA also showed a 25-49% mid right coronary artery (RCA) narrowing followed by a 70-95% distal narrowing (D). The mid RCA narrowing was judged minimal on invasive angiography and the distal RCA a 50% narrowing that did not undergo stenting (E). FFR-CT was 0.76 in the LAD that underwent stenting and 0.82 in the RCA that did

not undergo stenting (F), predicting decision-making in the cardiac catheterization laboratory.  The

patient was asymptomatic at 2-year followup.   The solid white arrows represent the stenotic

segments identified on coronary CTA (A, D) or invasive angiography (B, E).  The dashed white

arrow represents the revascularized LAD stenotic segment (C).  The FFR-CT values in each

coronary territory are depicted in color scale, and the numerical values of the worst FFR-CT

determined in distal segments provided (F).   A color scale graph of FFR-CT values is also

presented (F).  LCX = left circumflex coronary artery.

**REFERENCES**

**1.**     Patel MR, Peterson ED, Dai D, Brennan JM, Redberg RF, Anderson HV, et al. Low diagnostic yield of elective coronary angiography. *N Engl J Med* 2010;362:886-95.

**2.**     Karlsberg RP, Budoff MJ, Thomson LE, Friedman JD, Berman DS. Integrated coronary computed tomographic angiography in an office-based cardiology practice. *Rev Cardiovasc Med* 2009;10:194-201.

**3.**     Shaw LJ, Hausleiter J, Achenbach S, Al-Mallah M, Berman DS, Budoff MJ, et al. Coronary computed tomographic angiography as a gatekeeper to invasive diagnostic and surgical procedures: results from the multicenter CONFIRM (Coronary CT Angiography Evaluation for Clinical Outcomes: an International Multicenter) registry. *J Am Coll Cardiol* 2012;60:2103-14.

**4.**     Budoff MJ, Dowe D, Jollis JG, Gitter M, Sutherland J, Halamert E, et al. Diagnostic performance of 64-multidetector row coronary computed tomographic angiography for evaluation of coronary artery stenosis in individuals without known coronary artery disease: results from the prospective multicenter ACCURACY (Assessment by Coronary Computed Tomographic Angiography of Individuals Undergoing Invasive Coronary Angiography) trial. *J Am Coll Cardiol* 2008;52:1724-32.

**5.**     Meijboom WB, Meijs MF, Schuijf JD, Cramer MJ, Mollet NR, van Mieghem CA, et al. Diagnostic accuracy of 64-slice computed tomography coronary angiography: a prospective, multicenter, multivendor study. *J Am Coll Cardiol* 2008;52:2135-44.

**6.**     Kruk M, Noll D, Achenbach S, Mintz GS, Pregowski J, Kaczmarska E, et al. Impact of coronary artery calcium characteristics on accuracy of CT angiography. *JACC Cardiovasc Imaging* 2014;7:49-58.

**7.**     Douglas PS, Hoffmann U, Patel MR, Mark DB, Al-Khalidi HR, Cavanaugh B, et al. Outcomes of anatomical versus functional testing for coronary artery disease. *N Engl J Med*;372:1291-300.

**8.**     investigators S-H. CT coronary angiography in patients with suspected angina due to

257

coronary heart disease (SCOT-HEART): an open-label, parallel-group, multicentre trial. *Lancet* 2015;385:2383-91.

9.     Min JK, Taylor CA, Achenbach S, Koo BK, Leipsic J, Nørgaard BL, et al. Noninvasive Fractional Flow Reserve Derived From Coronary CT Angiography: Clinical Data and Scientific Principles. *JACC Cardiovasc Imaging* 2015;8:1209-22.

10.     Min JK, Koo BK, Erglis A, Doh JH, Daniels DV, Jegere S, et al. Effect of image quality on diagnostic accuracy of noninvasive fractional flow reserve: results from the prospective multicenter international DISCOVER-FLOW study. *J Cardiovasc Comput Tomogr* 2012;6:191-9.

11.     Nørgaard BL, Gaur S, Leipsic J, Ito H, Miyoshi T, Park SJ, et al. Influence of Coronary Calcification on the Diagnostic Performance of CT Angiography Derived FFR in Coronary Artery Disease: A Substudy of the NXT Trial. *JACC Cardiovasc Imaging* 2015;8:1045-55.

12.     Koo BK, Erglis A, Doh JH, Daniels DV, Jegere S, Kim HS, et al. Diagnosis of ischemia-causing coronary stenoses by noninvasive fractional flow reserve computed from coronary computed tomographic angiograms. Results from the prospective multicenter DISCOVER-FLOW (Diagnosis of Ischemia-Causing Stenoses Obtained Via Noninvasive Fractional Flow Reserve) study. *J Am Coll Cardiol* 2011;58:1989-97.

13.     Nakazato R, Park HB, Berman DS, Gransar H, Koo BK, Erglis A, et al. Noninvasive fractional flow reserve derived from computed tomography angiography for coronary lesions of intermediate stenosis severity: results from the DeFACTO study. *Circ Cardiovasc Imaging* 2013;6:881-9.

14.     Nørgaard BL, Leipsic J, Gaur S, Seneviratne S, Ko BS, Ito H, et al. Diagnostic performance of noninvasive fractional flow reserve derived from coronary computed tomography angiography in suspected coronary artery disease: the NXT trial (Analysis of Coronary Blood Flow Using CT Angiography: Next Steps). *J Am Coll Cardiol* 2014;63:1145-55.

15.     Douglas PS, Pontone G, Hlatky MA, Patel MR, Nørgaard BL, Byrne RA, et al. Clinical outcomes of fractional flow reserve by computed tomographic angiography-guided diagnostic

strategies vs. usual care in patients with suspected coronary artery disease: the prospective longitudinal trial of FFRct: outcome and resource impacts study. *Eur Heart J* 2015;47:3359-67.

**16.** Hlatky MA, De Bruyne B, Pontone G, Patel MR, Nørgaard BL, Byrne RA, et al. Quality of Life and Economic Outcomes of Assessing Fractional Flow Reserve With Computed Tomography Angiography: The PLATFORM Study. *J Am Coll Cardiol* 2015;66:2315-23.

**17.** de Feyter PJ. CT functional imaging using intracoronary gradient analysis: an indispensable boost for CT coronary angiography. *Eur Heart J Cardiovasc Imaging* 2012;13:971-2.

**18.** Taylor CA, Fonte TA, Min JK. Computational fluid dynamics applied to cardiac computed tomography for noninvasive quantification of fractional flow reserve: scientific basis. *J Am Coll Cardiol* 2013;61:2233-41.

**19.** Hanley JA, McNeil BJ. A method of comparing the areas under receiver operating characteristic curves derived from the same cases. *Radiology* 1983;148:839-43.

**20.** DeLong ER, DeLong DM, Clarke-Pearson DL. Comparing the areas under two or more correlated receiver operating characteristic curves: a nonparametric approach. *Biometrics* 1988;44:837-45.

**21.** Stone NJ, Robinson JG, Lichtenstein AH, Bairey Merz CN, Blum CB, Eckel RH, et al. 2013 ACC/AHA guideline on the treatment of blood cholesterol to reduce atherosclerotic cardiovascular risk in adults: a report of the American College of Cardiology/American Heart Association Task Force on Practice Guidelines. *J Am Coll Cardiol* 2014;63:2889-934.

**22.** Faraggi D, Reiser B. Estimation of the area under the ROC curve. *Stat Med* 2002;21:3093-106.

**23.** Boden WE, O'Rourke RA, Teo KK, Hartigan PM, Maron DJ, Kostuk WJ, et al. Optimal medical therapy with or without PCI for stable coronary disease. *N Engl J Med* 2007;356:1503-16.

**24.** Group BDS, Frye RL, August P, Brooks MM, Hardison RM, Kelsey SF, et al. A randomized

trial of therapies for type 2 diabetes and coronary artery disease. *N Engl J Med* 2009;360:2503-15.

**25.**     Velazquez EJ, Lee KL, Deja MA, Jain A, Sopko G, Marchenko A, et al. Coronary-artery bypass surgery in patients with left ventricular dysfunction. *N Engl J Med* 2011;364:1607-16.

**26.**     Tonino PA, De Bruyne B, Pijls NH, Siebert U, Ikeno F, van' t Veer M, et al. Fractional flow reserve versus angiography for guiding percutaneous coronary intervention. *N Engl J Med* 2009;360:213-24.

**27.**     De Bruyne B, Fearon WF, Pijls NH, Barbato E, Tonino P, Piroth Z, et al. Fractional flow reserve-guided PCI for stable coronary artery disease. *N Engl J Med* 2014;371:1208-17.

**28.**     Levine GN, Bates ER, Blankenship JC, Bailey SR, Bittl JA, Cercek B, et al. 2011 ACCF/AHA/SCAI Guideline for Percutaneous Coronary Intervention. A report of the American College of Cardiology Foundation/American Heart Association Task Force on Practice Guidelines and the Society for Cardiovascular Angiography and Interventions. *J Am Coll Cardiol* 2011;58:e44-122.

**29.**     Task Force M, Montalescot G, Sechtem U, Achenbach S, Andreotti F, Arden C, et al. 2013 ESC guidelines on the management of stable coronary artery disease: the Task Force on the management of stable coronary artery disease of the European Society of Cardiology. *Eur Heart J* 2013;34:2949-3003.

**30.**     Pijls NH, Tanaka N, Fearon WF. Functional assessment of coronary stenoses: can we live without it? *Eur Heart J* 2013**;**34:1335-44.

**31.**     Miller JM, Rochitte CE, Dewey M, Arbab-Zadeh A, Niinuma H, Gottlieb I, et al. Diagnostic performance of coronary angiography by 64-row CT. *N Engl J Med* 2008;359:2324-36.

**32.**     Sandfort V, Lima JA, Bluemke DA. Noninvasive Imaging of Atherosclerotic Plaque Progression: Status of Coronary Computed Tomography Angiography. *Circ Cardiovasc Imaging* 2015;8:e003316.

**CHAPTER NINE**

**Integrating FFR$_{CT}$ into routine clinical practice: a solid PLATFORM or slippery slope?**

Packard R.R.S., Karlsberg R.P.

Coronary computed tomography angiography (CTA) is being used increasingly in patient care despite the highest standard ever set for adoption of a noninvasive imaging test for diagnosing coronary artery disease (CAD). Recent analyses from the SCOT-HEART (Scottish Computed Tomography of the HEART) trial, which randomized patients to standard of care with or without coronary CTA (1), demonstrated that following a coronary CTA, invasive angiograms are significantly more likely to show obstructive lesions, and appropriate therapy to be initiated, associated with halving of myocardial infarction occurrence (2). Combined with the recent PROMISE (Prospective Multicenter Imaging Study for Evaluation of Chest Pain) trial (3), these data supported this expanding role for coronary CTA in CAD management (4). Furthermore, coronary CTA may be used to monitor coronary plaque progression (5,6) and has an increasing role in patients with acute chest pain (7) presenting to the emergency department (8). These studies and others have fueled the proposal that coronary CTA is a highly competitive or superior modality as a gatekeeper to invasive angiography (9,10).

Complementing this role of coronary CTA, considerable effort has been devoted to assess the physiologic significance of stenosis burden by different CT-based approaches, including transluminal attenuation gradient (TAG) (11,12), contrast density difference (13), CT vasodilator-induced stress myocardial perfusion imaging (14,15), and fractional flow reserve CT (FFR$_{CT}$), the most rigorously studied parameter of functional CAD assessment (16-22). Moreover, FFR$_{CT}$ has demonstrated additive value in what remains an Achilles' heel of coronary CTA: decreased accuracy in the setting of significant calcification (23-25).

In this issue of the *Journal* (16), Douglas et al. present the 1-year follow-up of the previously reported 90-day quality of life (QOL) and economic impact (17) of the PLATFORM (Prospective Longitudinal Trial of FFRCT Outcome and Resource Impacts) trial (18). In an elegant editorial

that accompanied the 90-day trial results (19), Hulten and Di Carli reviewed the history and evolution of CAD testing and changing clinical trends as well as pivotal $FFR_{CT}$ trials (20-22). They concluded that randomized trials comparing $FFR_{CT}$, coronary CTA, and stress testing were needed to further evaluate changes in cost and outcomes with $FFR_{CT}$ (19). The authors also noted that translating $FFR_{CT}$ results from a clinical trial population to routine clinical practice patients might prove challenging.

In their 1-year follow-up study, Douglas and colleagues concluded that there were no meaningful differences in QOL in the planned noninvasive and invasive arms other than by 1 isolated metric; however, addition of $FFR_{CT}$ led to increased cost in the planned noninvasive arm but a significant decrease in the planned invasive arm. In the planned invasive arm, regardless of the angina type experienced, an $FFR_{CT}$-guided strategy was beneficial, with a substantial 60% reduction in invasive coronary angiography (ICA), the main driver of economic impact. Additionally, $FFR_{CT}$ led to a significant 61% decrease in the finding of obstructive CAD at the time of ICA. The study was underpowered to test whether this decrease in ICA led to significant differences in 'hard' cardiovascular events such as fatal myocardial infarction, acute coronary syndromes, or urgent revascularizations.

The following caveats should be noted: the study was conducted in European centers and reflect local practice patterns, which cannot be assumed to be identical to American centers. Moreover, as PLATFORM was not a randomized trial, the decision to medically manage or directly send patients to the cardiac catheterization laboratory must be examined more closely. In the planned invasive cohort, many patients would not likely be chosen to directly proceed to ICA in many cardiology centers under current guidelines. Conversely, American patterns of noninvasive

imaging tests have had disquieting percentages of normal studies, raising questions about the appropriateness of our patient selection process (26).

The decision to proceed with ICA in PLATFORM was unclear. Only ~50% of the usual care and $FFR_{CT}$-guided arms had noninvasive testing – the results of which were not reported – before the decision to proceed to ICA, an approach at odds with current guidelines (27). As an extreme example, in some cardiology environments patients with angina are offered ICA only after failed medical therapy and/or abnormal noninvasive testing demonstrating large areas of reversible ischemia on myocardial perfusion imaging (28). Certainly there was room for additional testing using current routine modalities prior to and/or other than $FFR_{CT}$ in the planned invasive arm of the PLATFORM study.

Another significant drawback to the routine use of $FFR_{CT}$ is the lack of advantage in the noninvasive arm. Costs were higher in the planned noninvasive cohort, even when $FFR_{CT}$ was assigned a cost weight equal to coronary CTA, emphasizing that $FFR_{CT}$ should not be universally proposed to patients during CAD work-up but considered in patients designated to ICA. Importantly, 297 patients in both study arms underwent coronary CTA. Of those, 201 studies showed stenoses ≥30% with subsequent submission for $FFR_{CT}$ analyses. Of those, 177 were actually analyzed and $FFR_{CT}$ values provided to clinicians. In other words, $FFR_{CT}$ values were available in only 58% of noninvasive and 60% of invasive arm cases, respectively, for clinical decision making. More than likely, a proportion of the decisions not to proceed with ICA might have been done on the basis of coronary CTA alone. In fact, observational studies suggest coronary CTA alone can dramatically reduce by almost half the incidence of ICA in controlled clinical environments (9).

The major advantage of FFR$_{CT}$ above other methods of physiologic assessment resides in its direct reference to invasive FFR. An invasive FFR-guided method of artery-specific revascularization of stable CAD patients was addressed in the FAME (Fractional Flow Reserve Versus Angiography for Multivessel Evaluation) trials (29,30) and led American (31) and European (32) guidelines to recommend routine use of FFR with a cutoff of 0.80 to guide the decision to medically manage or revascularize patients. Furthermore, FFR$_{CT}$ has now undergone testing and validation against invasive FFR in multiple clinical trials (20-22), leading to its approval by the U.S. Food and Drug Administration (FDA). In the PLATFORM cases where invasive FFR was performed (50 vessels in 29 patients), FFR$_{CT}$ had an overall accuracy of 84%. An additional advantage of FFR$_{CT}$ is that it can be added onto coronary CTA for artery-specific physiological measurement when deemed necessary, with no need for repeat acquisition and, hence, no additional radiation or contrast administration.

As perceived by Hulten and Di Carli (19), introducing FFR$_{CT}$ into the real world was challenging. We performed the first 100 U.S. studies after FDA release and likely have one of the largest volumes in clinical practice currently (25,33). In our environment, when not enrolled in a clinical trial, patients had to pay for the test out of pocket. This required a detailed, understandable explanation with supplemental written and video material. It also meant many patients could not get the test. Hospital and office administrators needed to be convinced of the value proposition, especially with no insurance reimbursement. In the early stages, sole reliance on FFR$_{CT}$ was not routinely accepted; therefore, multimodality noninvasive testing was requested by other health care team members, patients, or both. There was concern about the 'black box' nature of the measurement, given the unclear contributions of the CT angiogram versus the segmentation and computational fluid dynamics modeling leading to the final FFR$_{CT}$ value, the skill of the personnel performing the interpretation/segmentation/modeling, the effects of noncalcified plaque on the modeling, concern about a sole commercial vendor and concern about nonconcordance with

clinical features and other noninvasive testing. FFR$_{CT}$ provided a convenient 'second opinion' on the coronary CTA interpretation with additive functional assessment, which was confirming in some cases, challenging in others. Clinical care had to adjust to the changing paradigm of FFR$_{CT}$ with values provided not only at the distal tip of the arteries, but also the capability of measurements at any level of the artery and across a narrowing. Despite these limitations, we found that FFR$_{CT}$ implemented in a routine clinical practice predicted artery-specific revascularization behavior better than coronary CTA alone (33), particularly in cases with heavy calcification (25).

For FFR$_{CT}$ to gain broader use, outcomes trials similar to the FAME trials should be performed to unequivocally demonstrate the central role this technology can play in managing patients with CAD; currently, FFR$_{CT}$ is only being used as a 'surrogate' to invasive FFR. We should not assume this surrogate measure has the same outcome associations as invasive FFR until these measures meet the same standards in similarly designed rigorous trials. Nonetheless, the enhanced role FFR$_{CT}$ provided in patients with planned ICA in PLATFORM is noteworthy.

This trial further expanded the "PLATFORM" of coronary CTA by providing an additional tool to enhance our ability to refer the right patients for ICA. Obviously, it would have been more powerful if PLATFORM was a randomized trial, if the workup of the population agreed with current guidelines, and if FFR$_{CT}$ results were compared to coronary CTA alone and provocative stress testing. This is particularly the case given previous single-center observational studies as well as registry data proposed CTA – without FFR$_{CT}$ – as a gatekeeper to ICA (9,10). However, while the exact role of FFR$_{CT}$ in managing patients with CAD continues to be explored, either complementary to or in replacement of other noninvasive strategies, the present effort by Douglas

et al. analyzing the 1-year follow-up of the PLATFORM trial provides 1 more step in our understanding of the growing role of coronary CTA in patient care.

## REFERENCES

**1.** [No authors listed]. CT coronary angiography in patients with suspected angina due to coronary heart disease (SCOT-HEART): an open-label, parallel-group, multicentre trial. *Lancet* 2015;385:2383-91.

**2.** Williams MC, Hunter A, Shah AS, et al. Use of Coronary Computed Tomographic Angiography to Guide Management of Patients With Coronary Disease. *J Am Coll Cardiol* 2016;67:1759-68.

**3.** Douglas PS, Hoffmann U, Patel MR, et al. Outcomes of anatomical versus functional testing for coronary artery disease. *N Engl J Med* 2015;372:1291-300.

**4.** Fordyce CB, Newby DE, Douglas PS. Diagnostic Strategies for the Evaluation of Chest Pain: Clinical Implications From SCOT-HEART and PROMISE. *J Am Coll Cardiol* 2016;67:843-52.

**5.** Zeb I, Li D, Nasir K, et al. Effect of statin treatment on coronary plaque progression – a serial coronary CT angiography study. Atherosclerosis 2013;231;198-204

**6.** Sandfort V, Lima JA, Bluemke DA. Noninvasive Imaging of Atherosclerotic Plaque Progression: Status of Coronary Computed Tomography Angiography. *Circ Cardiovasc Imaging* 2015;8:e003316.

**7.** Nieman K, Hoffmann U. Cardiac computed tomography in patients with acute chest pain. *Eur Heart J* 2015;36:906-14.

**8.** Cheezum MK, Blankstein R. Coronary computed tomographic angiography: its role in emergency department triage. *Circulation* 2014;130:2052-56.

**9.** Karlsberg RP, Budoff MJ, Thomson LE, Friedman JD, Berman DS. Reduction in downstream test utilization following introduction of coronary computed tomography in a cardiology practice. *Int J Cardiovasc Imaging* 2010;26:359-366.

**10.** Shaw LJ, Hausleiter J, Achenbach S, et al. Coronary computed tomographic angiography as a gatekeeper to invasive diagnostic and surgical procedures: results from the multicenter

CONFIRM (Coronary CT Angiography Evaluation for Clinical Outcomes: an International Multicenter) registry. *J Am Coll Cardiol* 2012;60:2103-14.

11.	Steigner ML, Mitsouras D, Whitmore AG, et al. Iodinated contrast opacification gradients in normal coronary arteries imaged with prospectively ECG-gated single heart beat 320-detector row computed tomography. *Circ Cardiovasc Imaging* 2010;3:179-86.

12.	Choi JH, Min JK, Labounty TM, et al. Intracoronary transluminal attenuation gradient in coronary CT angiography for determining coronary artery stenosis. *JACC Cardiovasc Imaging* 2011;4:1149-57.

13.	Hell MM, Dey D, Marwan M, Achenbach S, Schmid J, Schuhbaeck A. Non-invasive prediction of hemodynamically significant coronary artery stenoses by contrast density difference in coronary CT angiography. *Eur J Radiol* 2015;84:1502-8.

14.	George RT, Silva C, Cordeiro MA, et al. Multidetector computed tomography myocardial perfusion imaging during adenosine stress. *J Am Coll Cardiol* 2006;48:153-60.

15.	Blankstein R, Shturman LD, Rogers IS, et al. Adenosine-induced stress myocardial perfusion imaging using dual-source cardiac computed tomography. *J Am Coll Cardiol* 2009;54:1072-84.

16.	Douglas PS, De Bruyne B, Pontone G, et al. One-Year Clinical, Economic, and Quality-of-Life Outcomes of FFRCT-Guided Care in Patients With Suspected Coronary Artery Disease: The PLATFORM Study. *J Am Coll Cardiol* 2016;68:435-45.

17.	Hlatky MA, De Bruyne B, Pontone G, et al. Quality of Life and Economic Outcomes of Assessing Fractional Flow Reserve With Computed Tomography Angiography: The PLATFORM Study. *J Am Coll Cardiol* 2015;66:2315-23.

18.	Douglas PS, Pontone G, Hlatky MA, et al. Clinical outcomes of fractional flow reserve by computed tomographic angiography-guided diagnostic strategies vs. usual care in patients with suspected coronary artery disease: the prospective longitudinal trial of FFRct: outcome and resource impacts study. *Eur Heart J* 2015;47:3359-67.

**19.**     Hulten E, Di Carli M. FFRCT Solid PLATFORM or Thin Ice? *J Am Coll Cardiol* 2015;66:2324-8.

**20.**     Koo BK, Erglis A, Doh JH, et al. Diagnosis of ischemia-causing coronary stenoses by noninvasive fractional flow reserve computed from coronary computed tomographic angiograms: results from the prospective multicenter DISCOVERFLOW (Diagnosis of Ischemia-Causing Stenoses Obtained Via Noninvasive Fractional Flow Reserve) study. *J Am Coll Cardiol* 2011;58:1989-97.

**21.**     Nakazato R, Park HB, Berman DS, et al. Noninvasive fractional flow reserve derived from computed tomography angiography for coronary lesions of intermediate stenosis severity: results from the DeFACTO study. *Circ Cardiovasc Imaging* 2013;6:881-9.

**22.**     Nørgaard BL, Leipsic J, Gaur S, et al., for the NXT Trial Study Group. Diagnostic performance of noninvasive fractional flow reserve derived from coronary computed tomography angiography in suspected coronary artery disease: the NXT trial (Analysis of Coronary Blood Flow Using CT Angiography: Next Steps). *J Am Coll Cardiol* 2014;63:1145–55.

**23.**     Min JK, Koo BK, Erglis A, et al. Effect of image quality on diagnostic accuracy of noninvasive fractional flow reserve: results from the prospective multicenter international DISCOVER-FLOW study. *J Cardiovasc Comput Tomogr* 2012;6:191-9.

**24.**     Nørgaard BL, Gaur S, Leipsic J, et al. Influence of Coronary Calcification on the Diagnostic Performance of CT Angiography Derived FFR in Coronary Artery Disease: A Substudy of the NXT Trial. *JACC Cardiovasc Imaging* 2015;8:1045-55.

**25.**     Packard RR, Nakanishi R, Li D, Budoff M, Karlsberg RP. Fractional Flow Reserve Computerized Tomography Outperforms Coronary CT Angiography in Calcified Arteries and Predicts Subsequent Coronary Revascularization: A Real-World Experience. *J Cardiovasc Comput Tomogr*. 2016;10(3S):S21.

**26.**     Rozanski A, Gransar H, Hayes SW, et al. Temporal trends in the frequency of inducible myocardial ischemia during cardiac stress testing: 1991 to 2009. *J Am Coll Cardiol* 2013;61:1054-65.

**27.**     Fihn SD, Gardin JM, Abrams J, et al. 2012 ACCF/AHA/ACP/AATS/PCNA/SCAI/STS Guideline for the diagnosis and management of patients with stable ischemic heart disease. *J Am Coll Cardiol* 2012;60:e44-e164.

**28.**     Hachamovitch R, Rozanski A, Shaw LJ, et al. Impact of ischaemia and scar on the therapeutic benefit derived from myocardial revascularization vs. medical therapy among patients undergoing stress-rest myocardial perfusion scintigraphy. *Eur Heart J* 2011;32:1012-24.

**29.**     Tonino PA, De Bruyne B, Pijls NH, et al. Fractional flow reserve versus angiography for guiding percutaneous coronary intervention. *N Engl J Med* 2009;360:213-24.

**30.**     De Bruyne B, Fearon WF, Pijls NH, et al. Fractional flow reserve-guided PCI for stable coronary artery disease. *N Engl J Med* 2014;371:1208-17.

**31.**     Levine GN, Bates ER, Blankenship JC, et al. 2011 ACCF/AHA/SCAI Guideline for Percutaneous Coronary Intervention. A report of the American College of Cardiology Foundation/American Heart Association Task Force on Practice Guidelines and the Society for Cardiovascular Angiography and Interventions. *J Am Coll Cardiol* 2011;58:e44-122.

**32.**     Montalescot G, Sechtem U, Achenbach S, et al. 2013 ESC guidelines on the management of stable coronary artery disease: the Task Force on the management of stable coronary artery disease of the European Society of Cardiology. *Eur Heart J* 2013;34:2949-3003.

**33.**     Packard RR, Li D, Budoff MJ, Karlsberg RP. Fractional flow reserve computerized tomography and subsequent coronary revascularization. *J Am Coll Cardiol* 2016;67(13_S):1670.